ULTRACOLD ION-ATOM SCATTERING

by

Niranjan Myneni

A thesis submitted to

Jawaharlal Nehru University

for the degree of

Doctor of Philosophy

Light and Matter Physics Group

Raman Research Institute

Bangalore – 560 080 (INDIA)

December 2021

Declaration

I hereby declare that except where specific reference is made to the work of others, the contents of this dissertation are original and have not been submitted in whole or in part for consideration for any other degree or qualification in this, or any other university. This dissertation is my own work and contains nothing which is the outcome of work done in collaboration with others, except as specified in the text and Acknowledgments. I also declare that I have run it through **Turnitin** plagiarism detection software.

Niranjan Myneni

Countersigned:

Prof. Sadiq Rangwala

Light and Matter Physics Group

Raman Research Institute

Bengaluru - 560080

Thesis Certificate

This is to certify that the thesis titled **"Ultracold ion-atom scattering"** submitted by Niranjan Myneni for the award of the degree of Doctor of Philosophy of Jawaharlal Nehru University is a bona-fide work. This has not been submitted to any other university for any other degree, diploma or title.

Prof. Sadiq Rangwala
(Thesis Supervisor)
Light and Matter Physics Group
Raman Research Institute
Bangalore-560 080

Prof. Sridhar S

Director

Raman Research Institute

Bangalore-560 080

Acknowledgments

I wish to express my thanks to Dr. Sadiq Rangwala for giving me the opportunity to work in his group, and also for his constant supervision and guidance of my thesis work. I gratefully acknowledge his support and contribution towards the completion of this work .

My sincere thanks to Olivier Dulieu, Laboratoire Aime Cotton, France and Robin Cote, Boston University USA, for useful discussions and collaborations. I thank Dr. Andal Narayanan and Dr. Usha Devi for their support and for conducting the annual review of my thesis work. I wish to thank Prof. E. Krishnakumar, Dr. Saptarishi Chauduri and Prof. Reji Philip, who were approachable for discussions regarding our experiments and also shared some lab supplies and equipment.

I thank senior lab members Tridib, Jyothi, Sourav, Rahul and Bhargav, the current lab members Nishant, Anand, Sreyas, Subodh and Vardhan, and ex-lab members Sagar and Sayan for providing a nice working environment in the lab, and for sharing instruments and knowledge.

I acknowledge the technical support by Md. Ibrahim, N. Narayanaswamy, Achan, Anand and all the other members of the precision and general workshops. I sincerely thank Sujatha, Meena, Mukundan and Dorababu for crucial support with electronics.

I wish to thank Harini and Savitha for their help. Shiva and Manju are acknowledged for all their support and hard work. I thank all the Library staff, canteen, E and B, computer department and other administrative staff at RRI for providing a pleasant environment throughout my PhD work.

Lastly, I am grateful to have continued support from my family and I would like to explicitly regard the support from my wife Sapna.

Synopsis

The study of the physics of controllable and isolated systems with long range binary interactions is of great importance for understanding complex systems and their interactions with environments, in the quantum regime. Hybrid ion-atom systems have allowed the studies of the nature of binary interactions in dilute systems in regimes where semi-classical formalism is adequate to explain the results [1-4]. Despite the challenge of using ions, which apply repulsive forces on each other and are highly sensitive to any electromagnetic fields, in the presence of cold atoms, stabilization, thermalization and cooling has been shown [5-11]. This process of cooling has been shown to not work until the ions attain temperatures as low as the ultracold atoms, due to limitations arising from the mechanism of trapping the ions. However, both theoretical studies computing observable phenomena at ultracold temperatures and experimental efforts to enable measurement of these phenomena are being actively pursued.

At ultracold temperatures, quantum nature of interactions dominate the properties of scattering of ions in a cloud of cold-atoms. As the ion-atom collision energies are lowered, only one or few partial waves would be sufficient to describe the phenomenon. At these temperatures, the nature of scattering or diffusion would be very different from the classical counterpart of such a system. The physics of ultracold collisions is further enriched when the colliding partners have an identity interchange symmetry. This symmetry, allows for a resonant charge exchange (RCE) channel in addition to the direct elastic (DE) channel in ion-atom collisions [12]. While separate evaluation and measurement of collision cross section in each channel is possible with some high energy approximations, the collision in any specific instance is indistinguishable between the DE and RCE channels, due to symmetry.

Choice of the System

The estimate for how low a temperature is required to see the fully distinct quantum scattering is the s-wave limit, which is the temperature below which the scattering cross section is dominated by just one ($l = 0$) partial wave. In other words, the s-wave limit is the temperature equivalent of the angular momentum barrier energy height of the $l = s1$ partial wave. For ion-atom collisions, this energy barrier height is inversely proportional to square of the reduced mass. The realization of an ultra-cold ion-atom mixture in the s-wave collision limit has been a major direction in Atomic Physics since the late 2000's. Given the challenge in cooling ions to temperatures where quantum effects dominate its interactions with the atom, it is important to identify a system with a high s-wave limit so that experiments in the quantum collision regime are feasible. Lithium, which is light and can be laser cooled is a popular choice as the atom for this reason. However, the ion of lithium cannot be laser cooled and thus ion-atom experiments probing effects of identity interchange symmetry at ultracold temperatures have not been possible so far despite great interest. We emphasize on this symmetry and even propose exploiting this symmetry to attain lower ion temperatures in a homo-nuclear atomic cloud, thus our choice for the ion also is lithium. Since we forego any ability to optically image ions, we have used a destructive detection scheme for the ions as will be described below.

Collision cross sections

The scattering potential for ion-atom collision is the molecular ion potential energy curve (PEC) for the electronic states with asymptotic equivalence to the internal states of the ion and the atom. Computation of the precise PECs and their manipulation to obtain scattering potentials is briefly described. For low energy elastic collisions, the participating PECs are the ground and the first excited states. The total elastic cross section is evaluated via full quantum treatment for homo-nuclear, ion-atom collisions without any high energy approximations. We show the disagreements with both semi-classical calculations and approximate quantum calculations. Further, the collision rates and diffusion cross sections which determine the charge mobility and transport are

presented.

Atom-Cavity Coupling

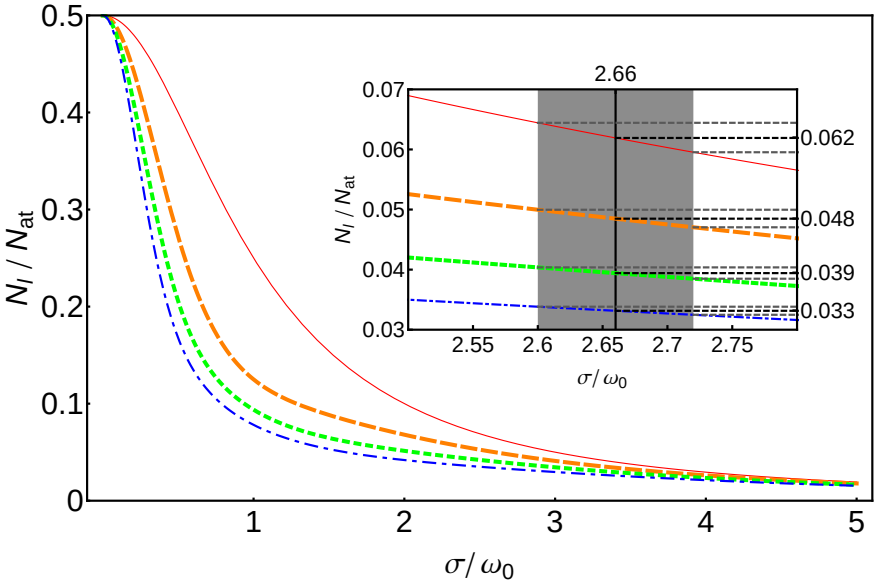

Figure 1: As a function of size of MOT with respect to the cavity waist, the ratio of atoms coupled to the 00, 10, 20 and 30 modes is plotted in Red, Orange, Green and Blue respectively. Inset shows the result close to the size of the MOT which was used.

As a possible strategy to detect a small number of dark ions, we nevertheless explored possibility of optical detection. It is realized that it is necessary to work with small ion numbers to observe these phenomena. A cavity based detection technique was explored for detecting interaction of ions with cold atoms. Although a cavity is shown to be a tool to detect the change in number of trapped cold atoms, it was found that it lacks the necessary sensitivity to measure the effects of small number of ions [7]. We have expanded on earlier investigations to then explore the possibility of detection via higher order cavity modes, so that spatial information can be obtained. Cold atoms in a magneto-optical trap (MOT) have been coupled to a medium finesse cavity to perform this experiment. We have established atom-cavity coupling as a tool to determine the density distributions and thus any changes to the location and density profiles of cold atoms, see figure 1 [13]. However such effects are not expected to be pronounced in interaction with small ion numbers and thus we choose not to integrate a cavity with this system.

Experimental Design

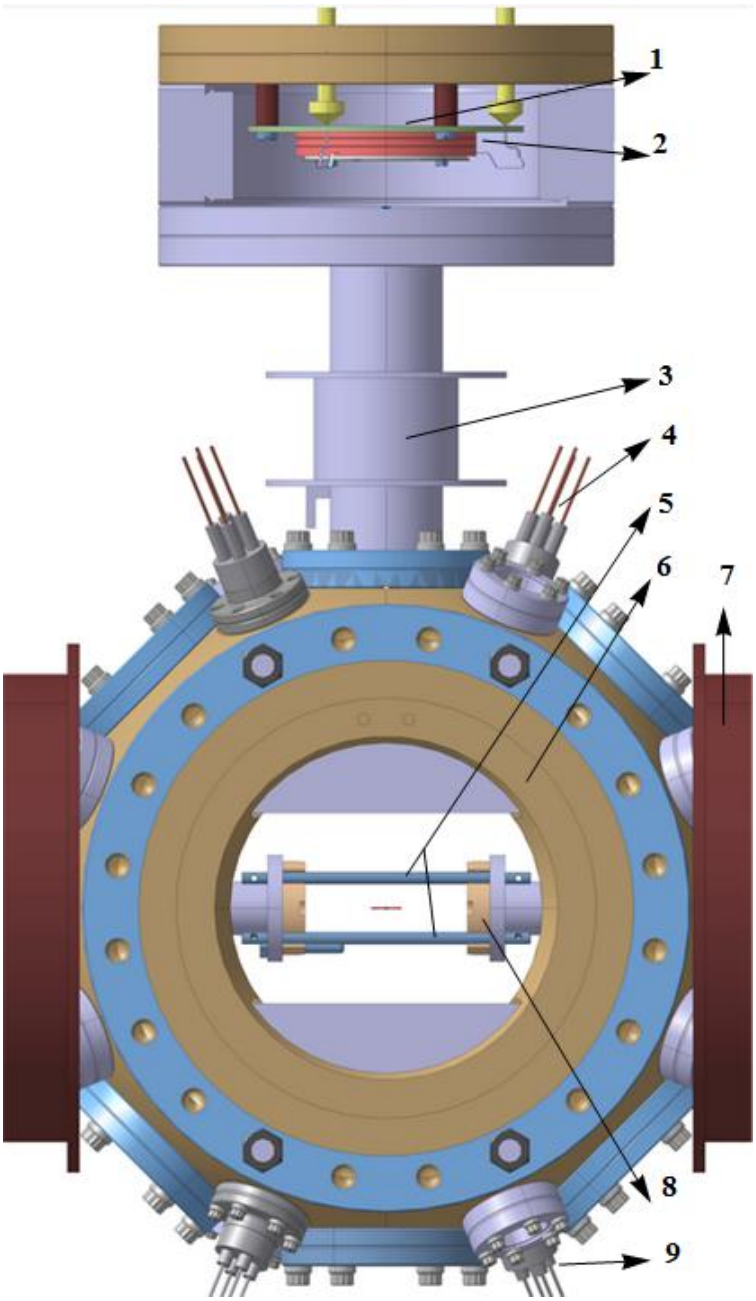

Figure 2: 1. Phosphor screen, 2. Micro channel plate, 3. coil for lensing ion extraction trajectories, 4. Feed through to grid and deflection plates, 5. Ion trap Radio frequency electrodes, 6. MOT coils, 7. Helmholtz coils, 8. Ion trap end caps, 9. Feed through to Li and Ca dispensers.

Given the difficulties in the cavity based experiment for sensitive ion-atom interaction detection, we designed a new experiment to enable the measurement of atom-ion interactions. We use a micro channel plate for studying ion diffusion with enhanced position resolution. The robust and reliable simulations to validate the physics and numerical estimation which resulted in identification of parameter space to work in have been successful. We have examined a few possible alternatives, performed simulations and zeroed down on this particular scheme. The experiment corresponding to the calculations has been completely designed and built to measure the charge diffusion of a very cold ion in a cloud of low temperature atoms, see figure 2. In the experiment we have the possibility of working with the ions of Ca and Li. Few preliminary experiments to identify working aspects and ways to integrate the mentioned methods will be presented.

Charge Hopping

At very low temperatures, collisions are not the only means for charge transport in an ultracold gas cloud. The position uncertainty ascribed by quantum mechanics, given by the thermal de Broglie wavelength along with the identity exchange symmetry leads to a spontaneous relocation of the charge. We describe this phenomenon of charge hopping homo-nuclear cold atomic clouds [14]. We calculate the hop rates relevant for experimentally realizable conditions and identify parameter space for hop rate to be higher than collision rates. In such situations, we show that localized cloud of atoms can cause the charge to be contained within it, forming a trap for the ions due to density gradient of the atomic cloud. The ability of such a system to tolerate static stray fields is shown. In regimes where transport is dominated by hopping, the mobility and possible emergent symmetry are discussed.

Emergent Symmetry

From the scattering potentials, collision rates and hop rates calculation discussed above, we determine the ion-atom interactions in the low temperature limit. The ion-ion interactions for a static ion number is repulsive $1/r$, while the ion-atom hopping interaction is dominated by the exchange

interaction and the delocalizations. Assuming a homogenous and isotropic density distribution of randomized atoms, we track the evolution of a small number of initially localized ions. Simulations using a model show localization and thermalization of ions in a cloud of ultra-cold atoms. Given the strong tendency to thermalize, we propose this system as a direct strategy to cool the ions to temperatures which common methods for trapping and cooling ions, cannot attain due to constrains from the trapping mechanisms. Since the RCE collisions have been seen to be more effective than the DE collisions, in removing energy from the ions it is expected to be favourable. Simulations have also shown that the localized ions form steady state symmetric structures irrespective of their relative positions at the time of creation. Effect of a finite magnetic field to increase the localization and possibility of realizing lower dimensions has been investigated. The cross sections evaluated for lithium ion-atom collisions are used and the competing effect of direct elastic collisions is discussed.

Conclusions

In conclusion, this thesis describes the physical phenomena relevant to ultracold ion-atom scattering and all other significant charge transport processes that can be realized at low temperatures. The rich physics of systems with identity exchange where the individual components can be trapped probed and detected, and the nature of interactions be tuned by parameters has been explained. The different identified processes and phenomenon have been described and attempts have been made to observe them with a carefully designed experimental setup. The discussion and future directions with a number of interesting observable phenomena are presented.

References

1. Michaland Tomza et al. "Cold hybrid ion-atom systems". In: *Reviews of Modern Physics* 91.3 (July 2019). ISSN: 0034-6861. DOI: 10.1103/revmodphys.91.035001.

2. Leon Kapra et al. "Suppression of Ion Transport due to Long-Lived Subwavelength Local-

ization by an Optical Lattice". In: *Phys. Rev. Lett.* 111.16 (Oct. 2013), p. 163002. DOI: 10.1103/PhysRevLett.111.163002.

3. David R Leibrandt et al. "Cavity Sideband Cooling of a Single Trapped Ion". In: *Phys. Rev. Lett.* 103.10 (Aug. 2009), p. 103001. DOI: 10.1103/PhysRevLett.103.103001.

4. Felix H.J. Hall et al. "Light-assisted cold chemical reactions of barium ions with rubidium atoms". In: *Molecular Physics* 111.12-13 (July 2013), pp. 1683-1690. ISSN: 00268976. DOI: 10.1080/00268976.2013.770930.

5. K Ravi et al. "Cooling and stabilization by collision in a mixed ion-atom system". In: *Nature Communications* 3.1 (2012), p. 1126. ISSN: 2041-1723. DOI:10.1038/ncomms2131.

6. Marko Cetina et al. "One-dimensional array of ion chains coupled to an optical cavity". In: *New Journal of Physics* 15.5 (2013), p. 53001.

7. Sourav Dutta and S A Rangwala. "Nondestructive detection of ions using atom-cavity collective strong coupling". In: *Phys. Rev. A* 94.5 (Nov. 2016), p. 053841. DOI: 10.1103/PhysRevA.94.053841.

8. Vladan Vuletìc et al. "External-feedback laser cooling of molecular gases". In: *Physical Review A - Atomic, Molecular, and Optical Physics* 75.5 (2007), pp. 1-4. ISSN: 10502947. DOI: 10.1103/PhysRevA.75.051405.

9. Ziv Meir et al. "Dynamics of a Ground-State Cooled Ion Colliding with Ultracold Atoms". In: *Physical Review Letters* 117.24 (Dec. 2016). DOI: 10.1103/PhysRevLett.117.243401.

10. Felix H.J. Hall et al. "Ion-neutral chemistry at ultralow energies: Dynamics of reactive collisions between laser cooled Ca+ ions ans Rb atoms in an ion-atom hybrid trap". In: *Molecular Physics* 111.14-15 (2013), pp.2020-2032. ISSN: 00268976. DOI: 10.1080/00268976.2013.780107.

11. Marko Cetina, Andrew T. Grier, and Vladan Vuletìc. "Micromotion-induced limitto atom-ion sympathetic cooling in Paul traps". In: *Physical Review Letters* 109.25 (Dec. 2012). ISSN: 00319007. DOI: 10.1103/PhysRevLett.1090253201.

12. D.S.F. Crothers. "Nonadiabatic Charge Transfer". In: *Advances in Atomic and Molecular Physics* 17 (Jan. 1982), pp. 55-98. ISSN: 0065-2199. DOI: 10.1016/S0065-2199(08)60067-6.

13. M. Niranjan et al. "Measuring spatially extended density profiles using atom-cavity collective strong coupling to higher-order modes". In: *Physical Review A* 99.3 (Mar. 2019). ISSN: 24699934. DOI: 10.1103/PhysRevA.99.033617.

14. Robin Côtè. "From Classical Mobility to Hopping Conductivity: Charge Hopping in an Ultracold Gas". In: *Phys. Rev. Lett.* 85.25 (Dec. 2000), pp. 5316-5319. DOI: 10.1103/PhysRevLett.85.5316.

Publications

- **M. Niranjan**, S. Dutta, T. Ray and S. A. Rangwala
  "*Measuring spatially extended density profiles using atom-cavity collective strong coupling to higher order modes*"
  Phys. Rev. A 99, 033617 (2019); https://link.aps.org/doi/10.1103/PhysRevA.99.033617

- A. Pandey, **M. Niranjan**, N. Joshi, S. A. Rangwala, R. Vexiau and O. Dulieu
  "*Interaction potentials and ultracold scattering cross sections for the $^7Li^+$–^7Li ion-atom system*"
  Phys. Rev. A 101, 052702 (2020); https://link.aps.org/doi/10.1103/PhysRevA.101.052702

- **M. Niranjan**, Anand Prakash and S. A. Rangwala
  "*Analysis of Multipolar Linear Paul Traps for Ion–Atom Ultracold Collision Experiments*"
  Atoms 2021, 9(3), 38; https://doi.org/10.3390/atoms9030038

- N. Joshi, **M. Niranjan**, A. Pandey, S. A. Rangwala, and O. Dulieu
  "*Homonuclear ion-atom collisions: application to Li^+-Li*"
  Phys. Rev. A 105, 063311 (2022); https://link.aps.org/doi/10.1103/PhysRevA.105.063311

- **M. Niranjan**, N. Joshi, A. Pandey, S. A. Rangwala, and O. Dulieu
  "*Quantum exchange symmetry induces charge diffusion and trapping in ultracold gases*" - (under communication)

Prof. Sadiq Rangwala (Thesis supervisor) Niranjan Myneni

Table of Contents

Acknowledgments . . . . . **v**

Synopsis . . . . . **vii**

Publications . . . . . **xv**

List of Tables . . . . . **xxiii**

List of Figures . . . . . **xxv**

1 Introduction **1**

1.1 Background 1

1.2 Motivation: a complete understanding of ion-atom interaction 3

1.3 Objectives 5

1.4 Organization of the thesis 6

2 Mechanisms for Trapping Cold Atoms and Ions **9**

2.1 Laser cooling 10

2.2 Magneto optical trap . . . 12

2.3 Dark-MOT and other traps . . . 15

2.4 Paul traps . . . 16

2.5 Hybrid traps . . . 19

2.6 Optical cavities coupled with ultracold atoms/ions . . . 20

3 Collective Strong Coupling of Atoms to Cavity . . . 23

3.1 Modes of a Fabry-Pérot cavity . . . 24

3.2 Strong coupling of 2 level atoms . . . 28

3.3 Experimental details and methods . . . 31

3.4 Results for VRS with different modes . . . 37

3.5 Discussion and applications . . . 39

4 Theory for Ultracold Homonuclear Ion-Atom Collision and Interaction . . . 41

4.1 Cold collisions . . . 42

4.2 Li molecular ion potential energy curves . . . 44

4.2.1 *Ab initio Born-Oppenheimer PECs* . . . 45

4.2.2 Determination of asymptotic extension of PEC's . . . 48

4.2.3 Criterion for bounds on the scattering parameters . . . 51

4.3 Collision cross sections . . . 53

4.4 Experimentally relevant collision parameters . . . 62

4.4.1 Collision rates . . . 62

4.4.2 Collisions limited ion diffusion . . . 63

4.5 Summary . . . 64

5 Charge Hopping in Ion-Atom Systems and its Consequences for Charge Diffusion . . 66

5.1 Formalism for charge hopping . . . 68

5.1.1 Probabilistic instantaneous separation . . . 69

5.1.2 Charge hop rate . . . 72

5.2 Charge hopping in a uniform and continuous distribution of atoms . . . 74

5.3 Charge hopping in discrete cloud of atoms . . . 79

5.4 Charge trapping in density gradient of Gaussian atom distribution . . . 80

5.5 Effect of a small electric field . . . 90

5.6 Discussion . . . 90

6 Virial Analysis for Linear Multipole Ion Traps . . . 93

6.1 Scope and utility of linear Paul traps . . . 94

6.2 Microscopic detail of ultracold ion-atom collision . . . 96

6.3 Ion trap configurations . . . 99

6.4 Virial theorem for 2k-pole traps . . . 100

6.5 Results . . . 102

6.5.1 Dynamics of an Ion in a 2k-Pole Trap . . . 103

6.5.2 Comparison of ion cooling efficiency . . . 112

6.6 Inferences from the computation analysis . . . 114

7 The Experiment for Ion Transport Studies . . . 119

7.1 Goals and the approach for measurement . . . 119

7.2 Essentials and requisites for DiLi+hium experiment . . . 121

7.2.1 Vacuum constraints . . . 121

7.3 Vacuum System for UHV . . . 122

7.3.1 Pumps and plumbing . . . 123

7.3.2 Magnetic coils and final assembly . . . 124

7.4 Creation, trapping and detection of ions . . . 127

7.4.1 Ion trap assembly and mounting . . . 134

7.4.2 Ion extraction and detection assembly . . . 136

7.4.3 Feedthroughs and electrical connections . . . 136

7.5 Laser systems and control . . . 137

7.6 Characterization and results . . . 143

7.7 Concluding remarks . . . 146

8 Summary and Future Prospects . . . 147

8.1 Summary of results . . . 147

8.2 Future prospects . . . 148

Appendix A Near neighbor distances for discrete distributions 149

Appendix B Mechanical drawings 153

Appendix C Mathematica code for charge hop rates 159

References 193

List of Tables

4.1 Dissociation limit, E_∞, its convergence with basis sets, ΔE_∞, total energy E_e at R_e, its convergence with basis sets, ΔE_e, equilibrium distance, R_e, well depth, D_e, and repulsive wall position R_{in} of the $X^2\Sigma_g^+$ and $A^2\Sigma_u^+$ PECs of $^7Li_2^+$. Results for various basis sets aug-cc-pCVXZ, with X ≡ D, T, Q, 5 are displayed. 46

4.2 Fundamental spectroscopic constants of the $X^2\Sigma_g^+$ and $A^2\Sigma_u^+$ PECs for Li_2^+. The label Exp. refers to the best available experimental determination, while the numbered Th labels refer to various theoretical determinations. 52

4.3 $^7Li^+$-^7Li scattering lengths for the modeled $X^2\Sigma_g^+$:ΔR = $\pm r_g$, $X^2\Sigma_g^+$:ΔR = 0 and $A^2\Sigma_u^+$:ΔR = $\pm r_u$, $A^2\Sigma_u^+$:ΔR = 0 curves are listed. For direct comparison with Zhang *et al.* [171] and Schmid *et al.* [17], the values obtained from X/A:ΔR = 0 are appropriate. 59

6.1 Virial analysis of $2k$-pole traps in normal operation. Results for the coefficient ν, from simulated trajectories using various appropriate potentials are shown which illustrate the compliance with equation 6.8. The average values are computed over several macromotion cycles and the standard deviation is shown as the error. 104

List of Figures

1 As a function of size of MOT with respect to the cavity waist, the ratio of atoms coupled to the 00, 10, 20 and 30 modes is plotted in Red, Orange, Green and Blue respectively. Inset shows the result close to the size of the MOT which was used. . . ix

2 1. Phosphor screen, 2. Micro channel plate, 3. coil for lensing ion extraction trajectories, 4. Feed through to grid and deflection plates, 5. Ion trap Radio frequency electrodes, 6. MOT coils, 7. Helmholtz coils, 8. Ion trap end caps, 9. Feed through to Li and Ca dispensers. x

2.1 Schematic figure for laser cooling in 1d using counter propagating red detuned beams of equal intensity. 10

2.2 Illustration of the laser cooling frequencies and the Doppler shifts. 11

2.3 Panel (a) illustrates the lifting of degeneracy for hyperfine levels due to applied gradient magnetic field, the detunings due to Doppler effect and magnetic fields, and the effectively resonant cooling transitions. The schematic for implementing a MOT is shown in panel (b). 13

2.4 Transverse image of a bright MOT with $^{8}5$Rb atoms taken using an infrared CMOS camera. 14

2.5 A schematic of linear Paul trap configurations is shown and the voltages applied on each electrode are specified. 17

2.6 The first parameter region for stable trapping of ions in an ideal Paul trap obtained from simulations is shown. 17

2.7 A typical ion trajectory in a linear quadrupole Paul trap is shown to exemplify the constituent macro and micromotion. 18

2.8 The profiles and electromagnetic field functions of the various TEM modes in a cylindrically symmetric optical Fabry Pérot cavity, the Laguerre Gauss ($LG_{l\,m}$) modes are shown. 21

3.1 Theoretical mode profile functions and images of transverse LG modes of the empty cavity, measured by imaging the probe light transmitted through the cavity. The continuous red curve is for $LG_{0\,0}$ mode, the dashed orange curve is for $LG_{1\,0}$ mode, the dotted green curve is for $LG_{2\,0}$ mode and the dot-dashed blue curve is for $LG_{3\,0}$ mode. 27

3.2 Ratio of atoms coupled to the $LG_{l\,0}$ cavity mode, N_l and the total number of atoms in the MOT N_{at} for different sizes of MOT's co-centered with the cavity. The continuous red curve is for $LG_{0\,0}$ mode, the dashed orange curve is for $LG_{1\,0}$ mode, the dotted green curve is for $LG_{2\,0}$ mode and the dot-dashed blue curve is for $LG_{3\,0}$ mode. Inset shows zoomed in version of the same curves around the value of σ/ω_0 measured from CCD1 image of the bright-MOT, 2.66$\pm$0.06 29

3.3 Theoretical estimation of VRS due to bright MOT as the MOT is shifted radially by distance a. The continuous red curve is for 00 mode, the dashed orange curve is for 10 mode, the dotted green curve is for 20 mode and the dot-dashed blue curve is for 30 mode. 30

3.4 Schematic of experiment. MML is a mode matching lens used for coupling of light to the FP cavity, F is an optical bandpass filter to block any stray light of frequencies far from ω_a, BS is a beam splitter, PMT1 and PMT2 are photomultiplier tubes and CCD1 and CCD2 are imaging cameras. The cavity resonant frequency ω_c of a particular transverse mode is matched with ω_a by adjusting the cavity length using the annular PZT and the cavity probe laser frequency ω_p is scanned around ω_a. Inset: The contour plot for the density distribution of the ^{85}Rb MOT atoms which fluoresce with natural transition frequency ω_a are imaged by CCD1. 33

3.5 The relevant ^{85}Rb energy levels and the transitions used in the experiment are illustrated. In the figure, CL is the cooling laser, RLB and RLD are the repumping laser for the bright-MOT and the dark-MOT respectively. The probe lasers for the bright-MOT and the dark-MOT VRS, PLB and PLD, are scanned across the identified transitions. 34

3.6 a. Empty cavity transmission for LG_{00} cavity mode. b. Transmission through cavity with co-centered bright-MOT atoms. The continuous blue curve shows VRS for LG_{00} cavity mode and the dashed pink curve showing VRS for LG_{30} cavity mode. The VRS signal for LG_{00} mode has larger width and exhibits features of slight non-linearity due to higher peak intensity as a result of smaller mode cross section. . . . 35

3.7 VRS for different LG modes due to bright-MOT measured on the F = 3 to F′ = 4 transition. Blue circles are experimental values of measured VRS and the blue error bars are one standard deviation. The red squares are calculated values of VRS, using N_{at} measured by PMT1 signal and σ obtained from the Gaussian fit to CCD1 image of the MOT, for different cavity modes. The red error bars include estimated errors in calculated VRS due to statistical and least count errors in measured N_{at} and σ. . . 37

3.8 VRS with a Dark-MOT for different LG modes measured on the F = 2 to F′ = 3 transition. Blue circles are from experimental measurement of VRS and the blue error bars are one standard deviation on either sides of the mean value of corresponding measurements. 38

4.1 Li_2^+ potential energy curves $X^2\Sigma_g^+$ and $A^2\Sigma_u^+$, computed in the present work (MRCI-SD with aug-cc-pCV5Z basis set), and respectively denoted as XTh_1 and ATh_1 are shown. The energy differences ΔE with the curves calculated using the approach of (denoted by XTh_2 and ATh_2), are shown in the inset. 44

4.2 The asymptotically extended PECs $X^2\Sigma_g^+$ (full red line) and $A^2\Sigma_u^+$ (full blue line) of Li_2^+ are shown. The asymptotic induction and exchange functions, V_{ind}^a(R) and V_{exch}^a(R), the computed induction and exchange functions, V_{ind}^c(R) and V_{exch}^c(R), are plotted for the comparison. The first derivatives of $X^2\Sigma_g^+$ and $A^2\Sigma_u^+$ PEC's, and V_{ind}^c(R) are drawn in the inset. 49

4.3 Potential energy curves near the repulsive wall (see insets) for $X^2\Sigma_g^+$ (a) and $A^2\Sigma_u^+$ (b), computed using basis sets aug-cc-pCVXZ with X ≡ D, T, Q, 5 and corresponding position R_{in} of their inner turning point at the dissociation limit E_∞ ((c) and (d)). The selected ranges ΔR for the variation of the repulsive wall of the aug-cc-pCV5Z calculations mimicking possible inaccuracies for cross section calculations are shown: ΔR = $\pm r_{g,u}$ with r_g = 0.01 a_0 and r_u = 0.02 a_0 for $X^2\Sigma_g^+$ and $A^2\Sigma_u^+$ respectively. 50

4.4 Quantum (modulo π) and semi-classical phase shifts as functions of the partial waves ℓ, for a collision along the $X^2\Sigma_g^+$:ΔR = 0 and $A^2\Sigma_u^+$:ΔR = 0 curves for the collision energies (a) 10^{-5} a.u., and (b) 10^{-6} a.u. The lines joining the points are a guide to the eye. 53

4.5 Quantum phase shift (modulo π) of the $X^2\Sigma_g^+$:ΔR = $\pm r_g$ and $X^2\Sigma_g^+$:ΔR = 0 curves as a function of the collision energy for the partial waves (a) $\ell = 0$, and (b) $\ell = 1$. At low energies, the change in the phase shifts for different PEC models are significant only for ℓ = 0. 54

4.6 (a) S_g(E) for the generated $X^2\Sigma_g^+$:ΔR = $\pm r_g$, and $X^2\Sigma_g^+$:ΔR = 0 curves are plotted. (b) S_u(E) for the $A^2\Sigma_u^+$:ΔR = $\pm r_u$ and $A^2\Sigma_u^+$:ΔR = 0 are plotted. In (a),(b), the semi-classical cross section, 2826×$E^{-1/3}$, is shown. 55

4.7 S_{ce}(E) for the two bounding modifications of PEC's, $X^2\Sigma_g^+$:ΔR = +r_g, $A^2\Sigma_u^+$:ΔR = +r_u and $X^2\Sigma_g^+$:ΔR = -r_g, $A^2\Sigma_u^+$:ΔR = -r_u, are shown along with the S_{ce} for $X^2\Sigma_g^+$:ΔR = 0, $A^2\Sigma_u^+$:ΔR = 0 curves. Langevin and Langevin/4 are also plotted for comparison. 56

4.8 The total collision cross section, σ_{tot}(E), of the $^7Li^+$-^{7}Li system in its first asymptotic state, which involves the electronic states $X^2\Sigma_g^+$ and $A^2\Sigma_u^+$ are shown for the modified PECs X/A:ΔR = $\pm$(r_g,r_u), and X/A:ΔR = 0. The semi-classical cross section, 2826$\times E^{-1/3}$ and the centrifugal barrier energies for ℓ = 1-5 are also shown. 58

4.9 σ_{tot} obtained from partial wave method (full quantum treatment), is plotted along with the high energy approximate $\tilde{\sigma}_{tot}$, and the semi-classical result for ion-atom collision cross section for both $^7Li^+$-^{7}Li and $^6Li^+$-^{6}Li systems. 60

4.10 The comparison of the diffusion cross section obtained from partial wave method (full quantum treatment), with the twice of S_{ce} as done conventionally for high energy collisions, Langevin, Langevin/4, and classical high energy expression for exchange form is shown for the $^7Li^+$-^{7}Li system in panel (a), and for the $^6Li^+$-^{6}Li system in panel (b). 61

4.11 Figure shows the collision rate coefficient for $^7Li^+$-^{7}Li and $^6Li^+$-^{6}Li systems over a range of temperatures. 63

4.12 Figure shows the plot for ion diffusion coefficient due to ion-atom collisions times the atom number density as a function of temperature. 64

5.1 Panel (a) illustrates the condition where $\lambda_T \ll L$, where charge hopping is very unlikely as the atom and ion are well separated and although cold and delocalized, present a very small probability for charge hopping. Panel (b) illustrates the case when $\lambda_T \leq L$ where the delocalized ion and atom start overlapping and the charge hop becomes probable. The blue and red dot represents the instantaneous positions of the ion and atom at the time of charge hop, while their average separation is L. The bottom frame shows the post hop atom and ion. In panel (c) the sequential charge hops in a cloud of atoms is illustrated. In this situation charge hop with many nearby atoms is probable leading to charge transport. In successive frames in (c), the atoms are depicted in relative motion and therefore show small displacement and reordering. The symbols are self explanatory and are used in the mathematical development below. 69

5.2 Panel (a) shows the average hop rate between an ion-atom pair of ^{7}Li as a function of their mean separation, L, plotted for different temperatures, T. The top ticks mark the L for which the condition L = λ_T is satisfied. In the inset, average hop rates for a fixed separation L= 1μm (green solid curve), L = 0.5 μm (blue dot-dashed curve), L= 0.2μm (red dashed curve) and the limiting case, L$\approx$ 0 (black dotted curve) are plotted as a function of T with the vertical grid-lines marking the $L = \lambda_T$ condition. This illustrates that the temperature range where hop rates are significant and the range where the low temperature limit holds revealing that hop rates diminish for $L > \lambda_T$. Panel (b) shows the same plots for ^{6}Li$^+$-^{6}Li system. . . . 73

5.3 Figure illustrates the comparison of collision rates normalized by atom density k_{coll}, total hop rates per atom density for continuous atom density distribution, $\bar{v}_{tot}^{con}$ and the total hop rates per atom density for discrete atom density distribution, $\bar{v}_{tot}$ for both $^7Li^+$-^7Li and $^6Li^+$-^6Li systems, evaluated for atom densities $n_1 = 10^{19}$ m^{-3}, $n_2 = 10^{18}$ m^{-3} and $n_3 = 10^{17}$ m^{-3} as a function of temperature T are shown. This illustrates the large temperature where the hop rates exceed the collision rates. The corresponding free space degenerate gas transition temperatures are shown by the vertical bars. 76

5.4 Panel (a) shows the diffusion coefficients for the, collision mediated ion transport D_{coll}, hop mediated charge transport for continuous density distribution of atoms D_h^{con} and the hop mediated charge transport for discrete density distribution of atoms D_h for ^7Li-^7Li system as function of temperature T. In both panels, $n_1 = 10^{19}m^{-3}$ and $n_2 = 10^{18}m^{-3}$. Panel (b) shows the same plots for $^6Li^+$-^6Li system. This shows that a temperatures of few μK and densities higher than 10^{18} m^{-3} will be needed to observe the dominance of hop mediated diffusion over collisional diffusion, which is a much smaller parameter space than the one in which hop rates are higher than collision rates. 78

5.5 The diffusion coefficients of a single ion starting at the centre of a Gaussian distribution of atoms of peak density $n_0 = 10^{19}$ m^{-3} and $\sigma = 100\mu$m is shown in panel (a). The collisional diffusion (large dashed, green) moves the ion away from the trap centre monotonically. The hopping diffusion coefficient (small dashed, blue) first causes the ion to move outward for $r_I < 1.24\sigma$, and inwards for $r_I \geq 1.24\sigma$. The net diffusion coefficient of the ion (thick yellow) is a result of the combination of these two distinct processes. It make two intercepts at zero diffusion coefficient, one at 1.25σ and the other at 2.48σ. A thermal ion starting at $r_I < 2.48\sigma$ will move to stabilize at $\approx 1.25\sigma$ and an ion beyond 2.48σ will escape. This shows that there is a shell of diffusive stability for a ion. Panel (b) is a contour plot of the total diffusion coefficient in a plane and the red arrows show the direction and magnitude of average diffusion at each point in the plane. Here, the shell of stable equilibrium is shown by the black circle and the orange circle shows the radius beyond which inward diffusion is not likely. This shows that the presence of the hopping mechanism results in ion trapping by a gradient atom distribution and charge localization to a spherical shell. This provides a very clear experimental signature of charge hopping. 82

5.6 Figure illustrates the Monte-Carlo hopping trajectory calculations for 100 instances of an ion starting at the origin. The statistical average values of $\overline{r}_I$ over all trajectories, are represented by filled blue circles, and the error bars denoting one standard deviation. It is clear that the ion localizes at $\overline{r}_I \approx 1.25\sigma_G$, for long hold times. The dashed red curve is the ballistic trajectory with average thermal velocity, the thick yellow curve is the theoretical mean trajectory $\overline{r}_I(t)$ incorporating both collisional and hopping diffusion and the thin green curve is the theoretical mean trajectory $\overline{r}_I(t)$ with just the collisional diffusion coefficient. The insets show these curves in their small and large hold time limits. 83

5.7 For a $^{7}Li^{+}$-^{7}Li system with different conditions mentioned in the panels, the collisional diffusion coefficient (brown), hopping based diffusion coefficient (dashed blue) and their sum (thick yellow) are plotted. In the insets, the corresponding theoretical mean trajectories due to these diffusion coefficients are shown in similarly styled curves along with the ballistic trajectory with mean velocity (dotted red). It is clear that ^{7}Li system offers a few more temperature and atom number density choices to observe charge trapping due to hopping in a spherical shell. Larger the gap between the green and red vertical lines, the more stable the radial charge confinement. 85

5.8 For a $^{7}Li^{+}$-^{7}Li system under conditions mentioned in the panels, the mean of 100 simulated trajectories with charge hopping is plotted as blue circles and the error bars represent the standard deviation. The dotted red curve is the ballistic trajectory with average thermal velocity, the thick yellow curve is the theoretical mean trajectory with the sum of collisional and hopping diffusion coefficients, the dashed dark blue curve is the average theoretical trajectory with just charge hopping and the thin brown curve is the upper limit to ion mobility allowed by just collisions. The insets show the same curves in their small hold time limits. 86

5.9 For a $^{6}Li^{+}$-^{6}Li system with different conditions mentioned in the panels, the collisional diffusion coefficient (brown), hopping based diffusion coefficient (dashed blue) and their sum (thick yellow) are plotted. In the insets, the corresponding theoretical mean trajectories due to these diffusion coefficients are shown in similarly styled curves along with the ballistic trajectory with mean velocity (dotted red). . . . 87

5.10 For a $^6Li^+$-^6Li system under conditions mentioned in the panels, the average of 100 simulated trajectories with charge hopping is plotted as blue circles and the error bars represent the standard deviation. The dotted red curve is the ballistic trajectory with average thermal velocity and the thick yellow curve is the theoretical mean trajectory with the sum of collisional and hopping diffusion coefficients. In panel (a), the thin brown curve represents the mean trajectory with just collisional diffusion. Whereas in panel (b), the brown curve is the thin brown curve is the upper limit to ion mobility allowed by just collisions. The physical meaning of the result of same equation (the brown curves), changes as the thermal velocities become lower than the corresponding collisional mobility limit. The insets show the same curves in their small hold time limits. 88

5.11 The panels show the ballistic trajectory (red, dotted) of a single ion starting at the origin at $t = 0$, the Monte-Carlo hopping trajectory calculations for 100 instances (light blue) and the survival probability (purple) of the ion within 3σ of the Gaussian atomic distribution discussed in figure 5.5. The three panels show these for different values of a constant electric field E_s imposed on the system. This is the experimentally realistic case, and once again illustrates that the prolonged survival of the ion within the atomic ensemble is the testable signature of charge hopping due to exchange symmetry. 89

6.1 Electrode potential configuration for normal operation of (**a**) a 4-pole trap, (**b**) a 6-pole trap, (**c**) an 8-pole trap and (**d**) a 12-pole trap, where $V(t) = V_0 \sin \omega t$. We keep the parameters r_0 and a fixed for all the trap configurations. Note that the 12-pole trap in (**d**) is also equivalent to the superposition of three quadrupole traps. 94

6.2 The time domain collision between a trapped and compensated stationary ion, initially located at the center of a quadrupole (**a**) and octupole (**b**) trap, with a stationary atom in its vicinity is shown. The calculation is two-dimensional. As a result of the mutual attraction of the trapped ion with the atom, in the presence of the trapping field, post collision, both the ion and the atom gain kinetic energy. The amount of kinetic energy gained in the collision in (**a**,**b**) is illustrated in (**c**,**d**), respectively. . . 97

6.3 The change in the energy of the Ca ion-atom system, initially at rest, with the ion at the trap center post collision is presented. The results for the quadrupole and octopole trap configurations are shown. The energy gained is plotted against the phase of the electric field at the time of ion-atom's closest approach. 98

6.4 The real space trajectories for the mentioned initial position (r=0.1r_0, $\theta = 0, \pi/4 and \pi/2k$ respectively) of creation of ion in 4 and 6 pole trap configurations is shown. 106

6.5 The real space trajectories for the mentioned initial position (r=0.1r_0, $\theta = 0, \pi/4 and \pi/2k$ respectively) of creation of ion in 8 and 12 pole trap configurations is shown. 107

6.6 Probability distribution of finding the ion at a radial distance r from the center of the trap in 2-dimensional 4 and 6 pole traps, for an ion created at $r(0) = 0.1r_0$ and angular coordinate θ. The inset2s show the phase space trajectories associated with the respective trapping configurations and the computed value of ν, specific to each case, is shown in the panels. 108

6.7 Probability distribution of finding the ion at a radial distance r from the center of the trap in 2-dimensional 8 and 12 pole traps. The insets show the phase space trajectories associated with the respective trapping configurations and the computed value of ν, specific to each case, is shown in the panels. 109

6.8 Panel (**a**) shows the probability distribution for an ion created at radial distance of 0.1 r_0, with random angular coordinate θ for various $2k$-pole traps. Panel (**b**) shows the probability distribution for an ion created with a Gaussian distribution of width $0.05r_0$, centered with the ion trap for various $2k$-pole traps. The insets show the corresponding density distribution. 111

6.9 The temperature of an ion held in ideal 4-pole and 8-pole trapping potentials are shown with constant damping (blue points) and without damping (red points). The variation of cooling rates in both trap potentials with the parameter q_r can be seen. The damping coefficient is equivalent to the best achievable laser cooling for a $^{40}Ca^{+}$ ion, in all panels. 112

6.10 The temperature of an ion held in 4-pole and 8-pole trapping potentials, generated using SIMION software are shown with constant damping (blue points) and without damping (red points). 113

6.11 Alternate trap configurations for using an 8-pole or 12-pole setup as a modified quadrupole are shown. Panel (**a**) is an 8-pole structure with alternate electrodes explicitly grounded. Panel (**b**) shows a skewed quadrupole trap. Panel (**c**) shows an effective quadrupole trap with an 8-pole setup, where successive electrodes are at a phase difference of Pi/2. Finally, panel (**d**) shows a 12-pole structure, with a quadrupole field configuration and multiple shielding electrodes. 117

7.1 The illustration of position sensitive ion destruction is shown. For different positions of the ion at the center of the trapping region, the position of hit on the micro channel detector plane varies accordingly. The readout of the position of hit on the detector plate can be mapped to the ion position, prior to extraction. 120

7.2 The schematic of the full vacuum setup showing the components exterior to the vacuum chamber is shown. The mounting sites of vacuum pump, Li dispensers, all the magnetic coils, and the MCP detector is shown to clarify the geometry of various ports discussed in the main text. 124

7.3 Schematic showing the mounting for axial coils, MOT coils, detector tube within the space constraints of the setup. 126

7.4 This is an illustration of the geometric constraints relating the beam diameters taken here as 16.4 mm, the outer diameter of the end caps d_{out} and the end-cap to end-cap distance l_{min}. 129

7.5 This is a design render of the functional elements of the Paul trap with optimized dimensions for the purpose of our hybrid ion-atom experiments. The various parts have been labelled and the electrode voltages to be applied in the normal operation are mentioned. 130

7.6 A rendered image of the assembled ion detector with 2 MCPs in Chevron configuration and P43 phosphor screen mounted on a CF100 flange with CF63 glass window to image the phosphor screen. 132

7.7 Circuit diagram for appending the detector power supply to provide electronic signal for ion time of arrival measurement. 132

7.8 schematic showing the designed elements of the hybrid ion-atom trap, the assembled ion detector along with the components for ion extraction. 133

7.9 The full mounting assembly of the ion trap to the main chamber is shown. The ion trap electrodes are held by the two central Macor plates, which also insulate all of the electrodes from each other. The wider mounting rods connect to the rear side of the end caps (see Figure B.2 in Appendix B) through the Macor plates. These mounting rods are held without touching the mounting plates by use of another set of similar design Macor plates, behind the mounting plates. Finally the whole assembly mounts to the grooves on the chamber with the help of the groove grabbers attached to the mounting plates. 134

7.10 A photograph showing the schematic of the home-built laser mounts for high temperature ECDL application. The components are labelled and the mechanical drawings for the parts are provided in Appendix B. 138

7.11 Figure shows the saturation absorption spectrum for ^{7}Li obtained using home-built lasers. The setup involves a hollow cathode lamp which results a different spectrum from the ones obtained using heat pipes. We do not see any pronounced ground state cross over peaks. The excited state hyperfine levels are unresolved. 139

7.12 The atomic levels relevant for ^{7}Li MOT are shown with the various level seperations labelled and the measured values of cooling and repumper MOT laser beams, on our wavemeter are also given. 140

7.13 A photograph of the lasers on the optical table, taken in our lab. 141

7.14 A photograph of the experimental chamber and the associate optical circuitry on the optical table, taken in our lab. 142

7.15 Panel (a) and (b) show intensity profiles measured by the CMOS camera pixels in the two directions x and z, along with the obtained best fits for a Gaussian of widths $\sigma_x = 1.04$ mm and $\sigma_z = 0.95$ mm respectively. Panel (c) is the full gray scale image of the MOT from the from the camera. Panel (d) shows a photograph of the ^{7}Li MOT fluorescing red light, taken with a handheld mobile camera through one of the CF16 view ports. Since the wavelength emitted by lithium is visible red, one can directly see such a MOT without much difficulty. 144

7.16 The top panel shows the image of the electronic readout from the MCP detector illustrating the pulses obtained for each ion hit and the availability of the ions' time of arrival information and ion count. The bottom panel shows a long time integrated image of the phosphor screen behind the detector, that replicates the MOT atom density profile as it is an overlap of glows from hits of multiple ions originating from different regions of the MOT. 145

B.1 Laser mount showing diode and grating mounts. 153

Chapter 1

Introduction

1.1 Background

Over the last few decades, propelled by the developments in lasers and their manipulation of cold, dilute gases of atoms [1–6] as well as ions [7–12], exciting new possibilities have emerged. The precision with which single atoms and ions can be trapped and addressed is such that quantum states and their superpositions are accessible in the optical domain where both the motional and internal states can be controlled [13–19]. Atoms and ions offer a unique advantage when quantum systems are concerned, since they are identical by their very nature and so no investment in preparation of the basics system is required.

The advantage that a dilute gas of atoms or ions offers, is that it comprises identical quantum systems. While the study of individual quantum systems is well advanced both theoretically and experimentally, interacting quantum systems serve up a number of challenges to our understanding. Even simply stated problems which concern interacting quantum systems (such as atoms, which are individually well understood) throw up surprises and require vigorous theoretical and experimental investigation. This is where trapped, cold and state prepared atoms and ions come into their own, since they are individually identical and they can be identically manipulated [13, 14, 20–23]. In such a tailored system of identical particles, quantum effects which result from their

interactions can be measured and studied in detail. The ability to produced tailored ensembles in such systems, allows precise measurements of interactions between the constituents.

Of the variety of species which can be laser cooled, Group I atoms (alkali) are most amenable for laser cooling and have resulted in a variety of experimental and theoretical studies [24–26]. For atomic ions, the species most amenable for laser cooling are singly charged ions of Group II elements (alkaline earth). In both cases, the atom/ion presents itself with one electron in the outermost shell, a configuration which is found to be generically, the simplest to effectively laser cool. Recent experimental investigations, led by the advances in trapping, cooling, manipulation and readout of single atoms and ions have pushed the boundaries of control and precision [13, 16–18, 20–22, 27–31]. This provides new insight into the quantum theory of matter and matter-light interactions, which is crucial for the progress of many areas of physics as well as future quantum technologies.

Many successes have resulted in the field of cold and ultracold matter, ever since the development of methods to cool and trap neutral atoms with laser light [6, 24, 32]. These discoveries led to the first observation of Bose-Einstein condensation in dilute atomic gases in 1995 by Eric A. Cornell, Wolfgang Ketterle, and Carl E. Wieman [9, 33] and the study of ultracold collisions [34]. Furthermore, experiments using optical lattices [35], with perfect periodic potential for the atoms with variable geometry and dimensionality, connect quantum optics and atomic physics with condensed-matter and solid state physics [35–39], along with their implementation for quantum information processing [40–42], and metrology [43, 44].

Historically ions were cooled and trapped before atoms and laser cooling was demonstrated on trapped ions long before atoms were lasers cooled [1, 3, 7]. Initial studies with trapped ions were focused on mass spectrometry, ion-neutral chemistry and metrology, and with the advent of laser cooling it developed into ion clocks [43, 45–47] and crystals of trapped ions were synthesized [10, 20, 48–51]. In the early to mid nineties, the Cirac-Zoller proposal [52] for quantum computing with trapped ions resulted in the rapid growth of ion trap experiments with laser cooling and over the years these systems are the most evolved precision quantum computing and quantum simulation platforms [22, 30, 31, 42, 53–57].

Laser cooled and trapped atoms, though a step behind chronologically, grew with startling speed once the initial laser cooled atoms were observed. In no time, experiments with optical lattices were performed and within the decade, cold dilute gas Bose Einstein Condensate was realized [33, 58]. The milestones are too numerous to enumerate, but this was followed by quantum degeneracy for Fermi gases [59], the control of interactions using Feshbach processes [60–62] and its consequent science, the BEC-BCS crossover [63–66], optical lattice based quantum simulators, quantum metrology and computing platforms [35, 39, 40, 67–69].

Ultracold atoms, which are highly controllable and scalable, typically are limited to short-range van der Waals interactions [36]. Interactions among ultracold atoms can be described in terms of a scattering length, that is tunable typically via magnetically scanning across Feshbach resonances. Enhanced dipole-dipole interactions can be introduced, by means of Rydberg excitations [23, 70], or confinement-induced resonances [71].

Investigation of longer range interactions in the quantum domain have been opened with the realization of more complex systems such as ultracold molecules [72–74]. Combining trapped ultracold atoms and ion(s) with spatial overlap allows for the study of well characterised ion-atom interactions ($\approx 1/r^4$). Hybrid ion-atom experiments have an advantage of both subsystems being independently controllable and addressable for position and/or state readout. The long coherence times in scalable and reproducible atomic systems, along with intermediate-range and tunable ion-atom interactions show new emerging features. To fully benefit from such advantages, however, it is essential to understand the fundamental collisional properties and other charge transport phenomena of ions in ultracold atoms, since they determine the prospects for decoherence and atom/ion number losses in ultracold ensembles.

1.2 Motivation: a complete understanding of ion-atom interaction

In a dilute thermal gases, the chemical and transport phenomena like reaction rates, diffusion, viscosity, etc., depend primarily on binary interactions. Experiments with cold trapped ions and atoms, provide the ability to measure their respective loss rates, positions, other measurables, and

thereby obtain a quantitative measurement of the interactions [14, 75–79]. A single ion can also be employed as a probe to investigate local properties of an atomic cloud.

At high temperatures the interaction of ion(s) with atoms is limited to collisions, which are consistent with the classical description of point particles with an attractive force ($\propto 1/r^5$) corresponding to the ion-atom interaction potential ($\propto 1/r^4$). As we lower temperatures, the number of collisional channels that remain probable get limited due to reduction of collision energy. At even lower temperatures, the classical and even the semiclassical approximations breakdown and the partial wave scattering solution is required. Therefore at ultracold temperatures, the quantum nature of collisions will manifest in the measurable charge transport.

In a system with like ion and atom, which is referred to as a daughter-parent ion-atom pair, the interaction is complicated by the involvement of the interchange symmetry. For example, a parent atom (A) losing an electron to a positively charged daughter ion (A^+) becomes an elastic process, with no change in energy. This charge exchange symmetry in an ion-atom system [80] is analogous to spin exchange symmetry [19, 81] in like atom-atom systems (where the two like atoms are in different spin states and same electronic states) or excitation exchange symmetry in like atoms in different electronic states [82]. The models used by most researchers nowadays for computing effects of collisional interactions and compare with experimental results, include the effect of the exchange symmetry. However, while the theory of atom-ion collisions is well established for high collision energies [70, 83], the theoretical descriptions used in the ultracold domain still exhibits inconsistencies.

Ultracold dilute gases are characterized by large thermal de Broglie wavelengths, which is the extent of delocalization of each particles. As a result of which, there can be a finite overlap of particles' positions. This can lead to a new kind of exchange symmetry mediated ion-atom interaction, which we call "charge hopping mechanism" which is operational only at ultralow temperatures as opposed to the collisional interactions. The transport due to charge hopping is analogous to charge conductivity and the collisional ion transport is analogous to the much slower electron mobility in conductors [84–86].

Ions are much more susceptible to small electric fields, than neutral atoms, which poses a chal-

lenge with respect to the lowest temperatures at which ion-atom systems can be operated. The challenges of measuring these intriguing phenomena in experiments have to be overcome by identifying the better suited experimental scheme and parameters of choice. As ultracold temperatures are not approachable with more than a few ions, experimental schemes which offer the resolution to measure the effect of a very small number of ions in an ensemble of atoms have to be identified.

1.3 Objectives

The present thesis aims to create a platform for experimental study of ultracold ion-atom interactions. In order to do this, we have already given an overview of the state of the art in atom-ion hybrid trap physics at the time of starting the thesis. Clearly both trapped atoms and trapped ions need to be worked with. We start by making a MOT of cold atoms and measuring the spatial properties of the MOT using atom-cavity strong coupling. This would provide the basis for extending the use of an optical cavity as a non-destructive probe for ion-atom interactions.

Earlier, several experiments had been done in our group to understand ion-atom interaction at higher ion temperatures [14, 75–78, 87–89] where we show stability and cooling of ions due to interaction with ultracold atoms. However, this ion cooling is not expected to persist up to ultracold ion temperatures in presence of the ion trap fields [90]. For this new experiment we would like to evaluate the prospects of studying the effects of ultracold ion-atom interactions. We then explore how to mitigate the heating by asking the question: is there a better design for the ion trap than the linear quadrupole design? In order to study atom-ion interactions, we then work towards a consistent scheme of measuring charge transport, using position sensitive destructive ion detection, through which the ion-atom scattering and overall interaction can be obtained at ultracold temperatures. The theoretical description of scattering and charge hop process needed to be consistent with the experimental domain and design optimization has been presented. Preliminary results with the new experiment built to address the problems outlined above are then presented. The main sections of this thesis are:

- To study collective strong coupling of ultracold atoms to an optical Fabry-Pérot cavity. To develop an optical cavity as a diagnostic tool for atom number distributions. To evaluate the prospects of resolving the effect of interactions of few ions with the atoms in cavity based measurements.

- To revisit the theory for like (homonuclear) ion-atom scattering at ultralow energies and obtain the theoretical estimates for measurable quantities. To obtain bounds on the scattering cross sections to estimate the result of possible inaccuracy in the best scattering potentials we used.

- To provide a formalism for the charge hopping process in experimentally realizable conditions. Using this to obtain the charge diffusion due to charge hopping and simulate for the resulting charge transport. To use numerical simulations of transport to identify the signatures of the experimental evidence for charge hopping process.

- To design an ion trap which is optimized to assist in the various possible experimental routes to achieve the necessary conditions, as suggested by the above theoretical estimations.

- To design, build, assemble the experiment in which measuring charge transport, using position sensitive destructive ion detection, can be done with the resolution to measure the results as expected above.

1.4 Organization of the thesis

In the second chapter, we discuss the conceptual background of all the experiments that constitute this thesis. A brief introduction to laser cooling, magneto-optical trap and ion trapping is provided. At the end, we provide an understanding of combining these traps to make a hybrid ion-atom trap.

In the third chapter, we describe our endeavors to use mode dependent, collective atom-cavity coupling to measure atom density profiles, in addition to the total atom numbers. The scope of this technique as a versatile tool and its limitations are explored.

In the fourth chapter, the theory for homonuclear ion-atom scattering is worked out from first principles, being consistent with ultracold temperatures. We detail our method for estimating the possible range for scattering parameters, subject to possible future improvements of potentials.

The fifth chapter is dedicated for the charge hopping mechanism, its formalism and characterization. We simulate the trajectories of an ion, that undergoes stochastic charge hopping in a cloud of ultracold thermal atoms. We find distinguishable signatures of the charge hopping mechanism in a practical experiment. This sets the paradigm for the experiment, in the scheme of measurement, the optimal operating parameters and the expected results.

In the sixth chapter, we compare the trapped ion kinetics in a quadrupole trap to other higher order linear Paul trap configurations. We present a comprehensive analysis of the merits and demerits of a higher order multipole trap for different applications.

In the seventh chapter, we elaborately go through the design optimization for all components of the apparatus, that is built to meet all the criteria set by the results of previous chapters. The fabrication and assembly of all devices is explained in great detail. The detail of the lasers used for the experiments and the optical setup are also discussed. Finally we demonstrate the working of various constituents of the experiment and present some initial results.

We conclude the thesis by summarizing the work and the future prospects of research with homonuclear ion-atoms in ultracold regime experiments using such a hybrid apparatus, some of which will be implemented as continuation of this line of work in our lab.

Chapter 2

Mechanisms for Trapping Cold Atoms and Ions

In order to study interactions between individual particles or ensembles of atoms, ions, molecules, etc., which arise due to the intrinsic properties of such particles, it is necessary to achieve conditions where the effects of thermal motion are minimum. At typical real world temperatures, thermal properties and behaviour of gases is fairly well described by the kinetic theory of gases [91, 92]. Hard sphere treatment of collisions between individual gas particles, subject to the available degrees of freedom, determine the macroscopic properties of the gas. The specific, fine details of the interaction between the colliding partners, which is masked by the kinetics at higher energies, start to play a crucial role at low energies. Further, the role of quantum behaviour, interaction with fields, and the statistics obeyed by the particles of interest can be studied. To enable just this, experiments have to be carried out at very low energies.

This is difficult to engineer for pairs of single particles, in part because the retrieval of signals from single interacting systems is very challenging. Such studies are therefore done with trapped dilute gas ensembles, which are laser cooled to and trapped at, their limiting temperatures. Such studies have been enabled by the established techniques of trapping and cooling of atoms and ions [6, 9, 24, 26, 32, 33, 44, 67, 93]. In this chapter, we describe the mechanisms including a brief description of the theoretical concepts of cooling and trapping atoms, trapping charged particles which are

crucial for pursuing the experiments in this thesis.

2.1 Laser cooling

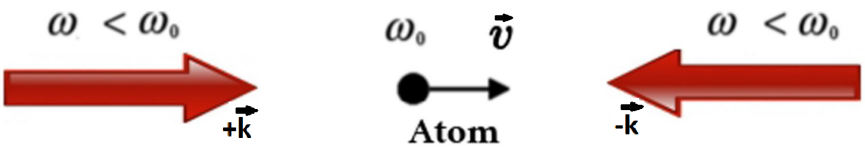

Figure 2.1: Schematic figure for laser cooling in 1d using counter propagating red detuned beams of equal intensity.

Since photons have momentum, a particle which absorbs or emits a photon, undergoes a momentum change equal to the momentum of the photon. When we have a scenario where a particle continuously absorbs photons from a resonant unidirectional beam and emits photons spontaneously in random directions, the particle gains momentum in the direction of the beam of photons as the average momentum change due to all the photon emissions due to spontaneous emission, which is random in direction, is zero. This is known as radiation force. The trick to achieve cooling using such forces is to use pairs of counter propagating laser beams, with equal intensity, such that both beams have a frequency slightly lower than the resonant frequency of the atom/ion that needs to be cooled. This way, the beam propagating opposite to the direction of motion of the atom/ion will be seen closer to atomic resonance by the atom/ion than the beam propagating along the direction of motion of the atom/ion by it, due to Doppler effect, see figure 2.1. As a result, the absorption of photons from the counter-propagating beam is more frequent than from the co-propagating beam and therefore laser beams can be used to provide a velocity dependent force in order to slow down atoms, ions, etc (laser cooling).

To understand the process of laser cooling, let us consider a simple case of a two level atom in one dimension moving with an initial velocity $\vec{v}$. For slowing down the velocity of an atom, the atom

should absorb a photon with wavevector, $\vec{k}$ opposite in direction to $\vec{v}$. Also, since the beam has to be resonant with the atom moving opposite to its direction, the beam's has to be red detuned with respect to the resonant frequency of the two level atom. A counter propagating pair of red detuned laser beams with equal intensity is used, such that an atom moving in either direction always sees the laser beam with wavevector opposite to its velocity, Doppler shifted closer to resonance than the laser beam with wavevector along its velocity direction, see figure 2.2.

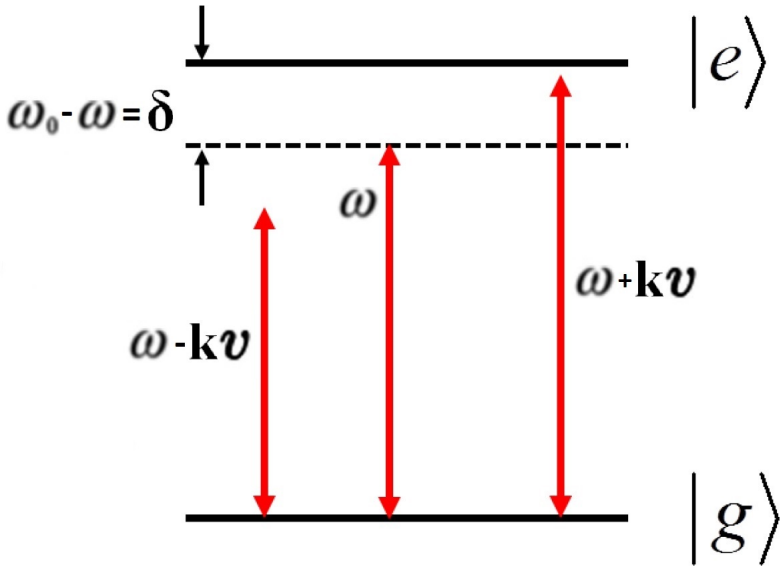

Figure 2.2: Illustration of the laser cooling frequencies and the Doppler shifts.

The red detuning is kept larger than the Doppler shift due to a velocity $\vec{v}$. As a result, the atom preferentially absorbs photons from the opposing beam and its velocity slows down over time. The spontaneous isotropic emission results in a random walk and cancels out on average over many cycles. The forces due to the two counter propagating beams $\vec{F}_+$ and $\vec{F}_-$ on the atom from photons of momentum $\pm\hbar\vec{k}$ is given by [32, 67, 94]

$$\vec{F}_\pm = \pm\frac{\hbar\Gamma}{2}\frac{\frac{I}{I_{sat}}}{1+\frac{I}{I_{sat}}+4\frac{(\delta\mp kv)^2}{\Gamma^2}}\vec{k}\,, \tag{2.1}$$

where I is the laser light intensity in each beam, I_{sat} is the saturation intensity for the transition given by $I_{sat} = \pi hc\Gamma/3\lambda^3$, c is the speed of light in free space, λ is the wavelength and k is the magnitude of the wavevector of the detuned laser light, Γ is the natural linewidth of the excited state of the two level atom and δ is the detuning of the laser from the resonant frequency. The net

force $\vec{F}_{total} = \vec{F}_{+} + \vec{F}_{-}$ on the atom is simplified to the first order in $\vec{v}$ to obtain [67]

$$\vec{F}_{total} = -\frac{8\hbar k^2 \delta}{\Gamma} \frac{\frac{I}{I_{sat}}}{(1 + \frac{I}{I_{sat}} + 4\frac{\delta^2}{\Gamma^2})^2} \vec{v} \equiv -\beta \vec{v} \,. \tag{2.2}$$

For small atomic velocities, the force by the laser beams is opposite in direction to and proportional to the atom velocity, which results in viscous damping of the atoms velocity. This setup of two counter propagating beams ensures that cooling continues even in the event of reversal of the atoms velocity due to some stochastic absorption-emission cycles. The root mean square (rms) momentum gain is not zero, which results in random walk in momentum space, giving a finite temperature $\hbar\Gamma/(2\,k_B)$ for the atom and is called the Doppler cooling limit [67, 95].

The above idea can be extended to real experiments in three dimensions by applying 3 sets of counter propagating, mutually orthogonal, pairs of beams, such that all the six beams of equal intensity intersect in a volume where laser cooling is functional. This technique, called optical molasses, can cool the atoms in the intersection of the 3 pairs of beams but the atoms' diffusive motion prevents it from remaining perpetually in the intersection region.

Using carefully designed magnetic fields, it is possible to engineer radiation forces which can achieve some of the desired tasks like (i) to cool atoms from very high initial velocities to the Doppler cooling limit (Zeeman slower), (ii) to confine the atoms to a small region (trap) along with cooling them (which is explained below).

2.2 Magneto optical trap

The magneto optical trap (MOT) uses a combination of magnetic field and particular optical fields to cool and trap the atoms [96]. The MOT requires an inhomogeneous magnetic field which is produced by a pair of matched coils in anti-Helmholtz configuration. For simplicity, once again let us consider a two level atom with angular momentum of the ground state F_g = 0 and the excited state F_e = 1, moving in one dimension ($\hat{z}$) with a velocity $\vec{v}$ in the presence of counter propagating laser beams. In a position dependent magnetic field of magnitude $B(z)$, the atomic

level degeneracy is lifted by $\Delta E_{|F,m_F\rangle} = \mu_B\, g_F\, m_F\, B(z)$ due to linear Zeeman effect and the levels are labelled by the magnetic quantum number, m_F = 0, ± 1. Here μ_B is the Bohr magneton and g_F is the Lande g factor. The dipole allowed transitions can occur from $0 \leftrightarrow 0, \pm 1$ by absorbing a π, $\sigma^{\pm}$ polarized photons respectively.

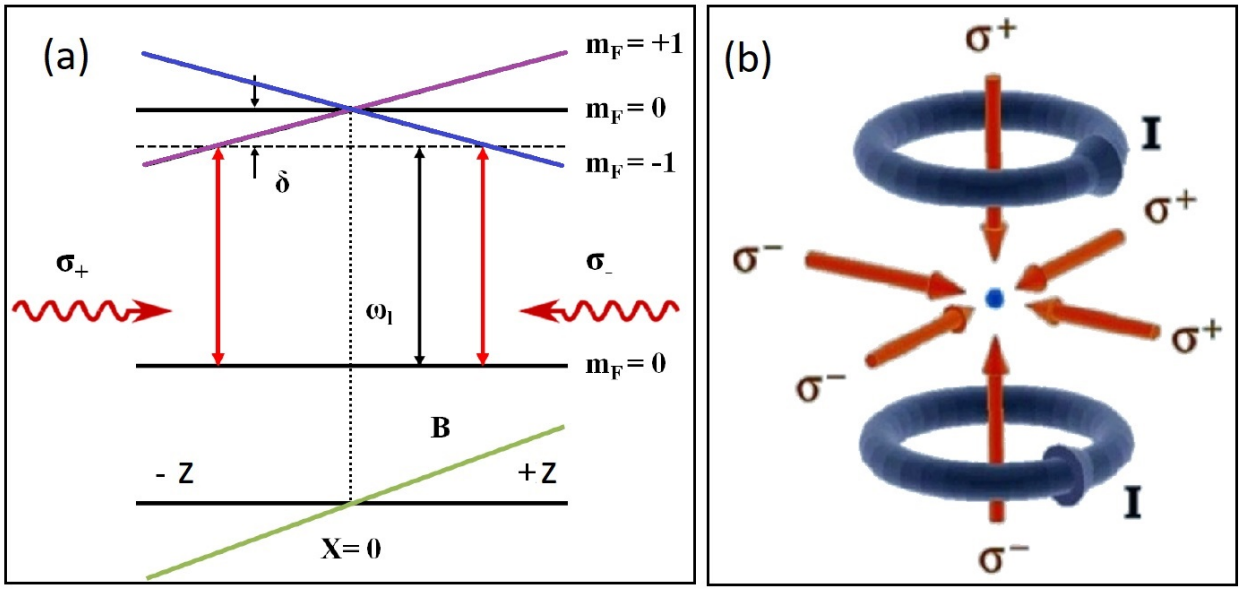

Figure 2.3: Panel (a) illustrates the lifting of degeneracy for hyperfine levels due to applied gradient magnetic field, the detunings due to Doppler effect and magnetic fields, and the effectively resonant cooling transitions. The schematic for implementing a MOT is shown in panel (b).

For positions z $>$ 0, the field due to the matched pair of coils in anti-Helmholtz configuration, B(z) is positive and the energy of the state m_F = +1 is shifted higher linearly with z and the energy of the state m_F = -1 is shifted lower with respect to the level, m_F = 0 which is not shifted in energy. Hence an atom in this region with a velocity in $+\hat{z}$ direction, sees the red detuned light of the beam with wave vector -$\vec{k}$ as more resonant to the closest m_F = -1 level than the light of the beam with wavevector $\vec{k}$. Therefore the application of $\sigma^{\pm}$ polarized lights respectively in $\pm\vec{k}$ direction will cause the atoms to preferentially absorb from the oppositely propagating laser beam. The exact opposite is true for an atom in this region moving in -$\hat{z}$ direction. This gives rise to a position dependent force which drives the atoms towards the spatial centre. Figure 2.3.a illustrates the hyperfine levels, the detunings due to Doppler effect and magnetic fields, and the effectively resonant cooling transitions. The schematic for a MOT is shown in figure 2.3.b. The

force on the atom from the counter propagating beams can be expressed as [32]

$$\vec{F}_{\pm} = \pm\frac{\hbar\Gamma}{2}\frac{\frac{I}{I_{sat}}}{(1+\frac{I}{I_{sat}}+4\frac{\delta\mp kv\pm\mu'\frac{dB}{dz}z/\hbar}{\Gamma^2})}, \tag{2.3}$$

where $\mu' \equiv (g_e M_e - g_g M_g)\mu_B$ is called the effective magnetic moment for the transition, where M_g and M_e are the magnetic quantum number of the ground and excited states. The net force is

$$\vec{F} = -\beta\vec{v} - \eta\vec{r}, \tag{2.4}$$

where $\eta = \mu' B_0\beta/\hbar k$ and β is defined in equation 2.2. The position dependence of the force expressed in equation 2.3, is such that the atom is pushed to the point of zero magnetic field. Thus atoms get cooled and trapped simultaneously in a MOT.

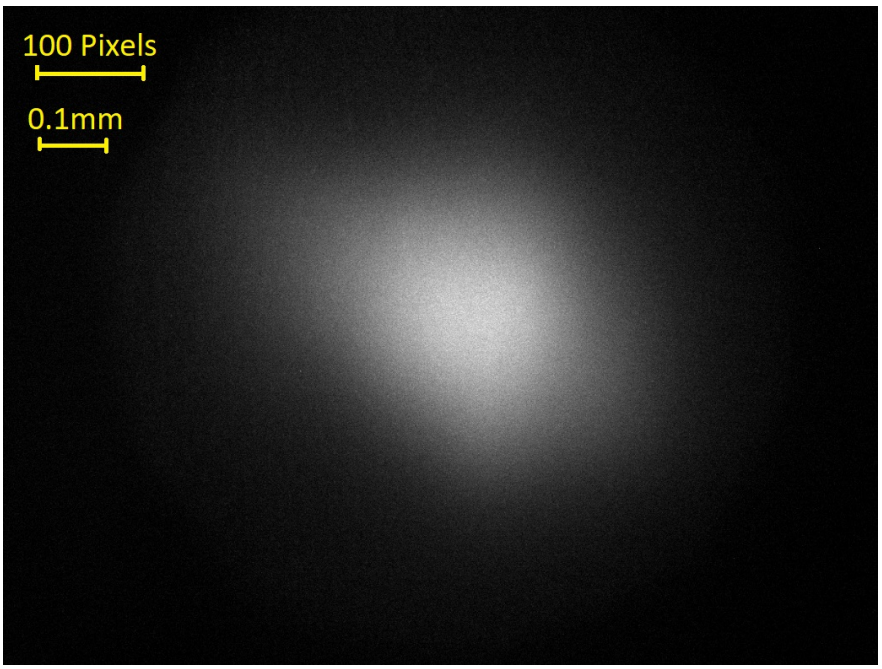

Figure 2.4: Transverse image of a bright MOT with $^{8}5$Rb atoms taken using an infrared CMOS camera.

The MOT has an important feature that the same magnetic field can be used for different atomic species with their corresponding resonant lasers to simultaneously trap the mixture. This is because it depends on the magnetic moment of the electron for single electron atoms. Since we deal mostly with alkali atoms this far, although the MOT concept extends for all atoms [97–101]. Also,

MOTs can be loaded directly from background gas in the apparatus as long as there is are significant number of atoms in velocity class that can be captured by it. This feature makes the use of MOT, as one of the first steps in making more challenging colder or/and denser traps, prominent. Figure 2.4 shows a picture of ^{85}Rb MOT captured by a CMOS camera. In experiments where large atom numbers and dense MOTs are desired to start with, a precursor cooling step in the form of a Zeeman slower or a 2D MOT is used [102, 103].

2.3 Dark-MOT and other traps

In experiments with real atoms, it is necessary to consider more than two levels. Typically, an atom in excited state due to a photon absorption from the ground state, has a finite probability of de-exciting into another lower energy state different from the original ground state. When such a de-excitation happens either via photon emission or via inelastic collisions, the atom is no longer influenced by the cooling light field. An additional light field known as repumper field will be needed to bring such atoms back into the cooling cycle. This is done by mixing repumper beam(s) with either all 6, or a fraction of the cooling beams to keep a MOT operational. Typical decay rates from the first excited levels to the ground state, used for MOT transition in alkali atoms, range between 5-6 MHz. This is the most common kind of a MOT, which has a steady state atom population in each of the involved internal states, excited and ground. Also, since the mechanism for this trap involves emission of resonant photons, this fluorescence can be used to directly image the created cold atom ensemble, therefore it is called as a bright-MOT.

The fluorescence from one atom in the MOT, if absorbed by another MOT atom, can perturb the cooling mechanism. This prospect of re-absorption of an emitted photon poses limitations for achieving the desired high densities and low temperatures in a bright-MOT. Some variants of the mechanism of MOT are widely applied to overcome the limitations of a bright-MOT. One such variant of MOT incorporates a central dark spot in the repumper beams, thereby creating a small volume at the trap center which is devoid of the radiation pressure from the light field. This setup allows formation of a cold ensemble of atoms to due to the trap loading and cooling in the volume other than the dark spot. However, absence of radiation pressure in the actual region to

which majority of the trapped atoms are confined, allows the achievement of lower temperatures and/or higher densities. Since most atoms do not participate in the absorption-emission cycle, this kind of MOT known as a dark-MOT does not fluoresce and has mostly state selected, ground state atoms.

We have employed a dark-MOT in some of the experiments described in chapter 3, where we present a method to estimate the density profile of a dark-MOT [77, 104, 105]. Both the bright-MOT and the dark-MOT are steady state, perpetually operable traps, as they are continuously loading and shedding atoms. This allows the atom numbers, density, internal state population distribution and temperatures to attain a steady state. This is unlike a lot of other trap mechanisms in ultracold physics, which constantly lose atoms, such as a magnetic trap or an optical dipole trap. However, the atomic levels populated by the atoms in a bright-MOT are different from the one populated by the atoms in a dark-MOT, which makes the utility of dark-MOT different.

2.4 Paul traps

The motion of a charged particle is highly susceptible to electric and magnetic fields. An electrostatic potential minimum in three dimensional free space is not achievable (Earnshaw's theorem [106]). However, an oscillating electric field or a combination of static electric and magnetic fields can be used to trap the charged particle. Both these methods have their merits and challenges. In both these kind of traps, the charged particle(s) would be dynamically trapped and undergoes oscillatory motion with characteristic trap frequencies. The trap involving dc electric and magnetic fields is known as the Penning trap [107] and the one which involves an oscillating electric field is the Paul trap [108]. Early implementation of both these methods emphasized on shaping electrodes to match the desired equipotential surfaces. However, many configurations of Paul traps have been developed, subsequent to the invention of lasers, the configurations no longer need the geometric precision to attain the desired measurement precision. The additional integration of light field, is a necessary inclusion which helps in improving cooling, precision and control [17, 21, 28, 33, 44–46, 93, 108]. Figure 2.5 shows a linear Paul trap configuration which facilitates laser cooling of the trapped ions.

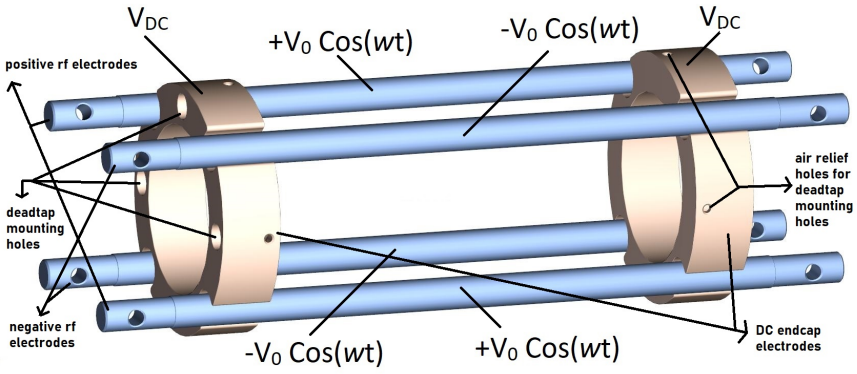

Figure 2.5: A schematic of linear Paul trap configurations is shown and the voltages applied on each electrode are specified.

As large uniform magnetic fields are required for the Penning trap, it is not suitable for certain hybrid trap configurations, which use neutral atom traps that need particular magnetic field profiles (like a MOT). Paul traps are shown to be stable against small magnetic fields, the likes of which are needed for a MOT [75, 109]. Also, several atypical configurations of Paul traps have been implemented where axial magnetic fields have been additionally introduced to aid the charge particle trapping in the transverse plane [110–112]. In view of these attributes, we have chosen to work with Paul traps for our ion-atom experiments described later.

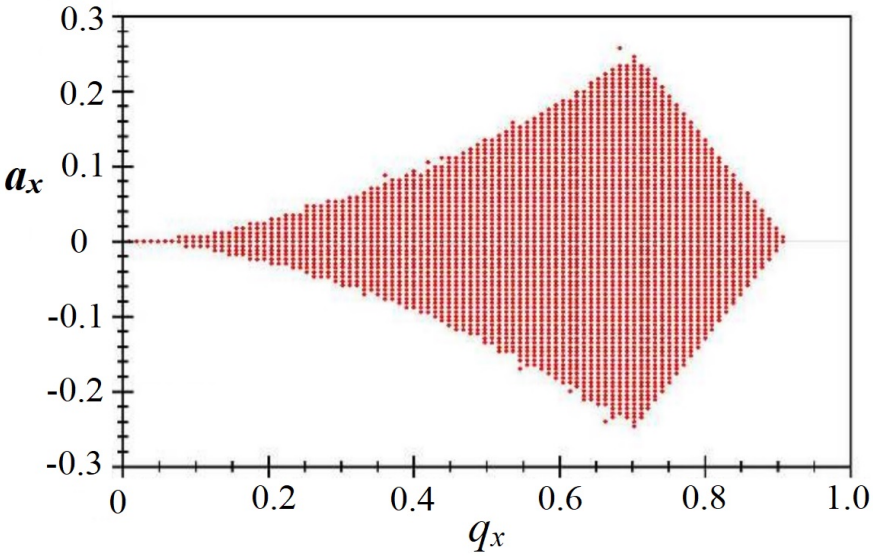

Figure 2.6: The first parameter region for stable trapping of ions in an ideal Paul trap obtained from simulations is shown.

In this section we will discuss the theory of ideal Paul trap and the specifics of the design optimization of the implemented trap for our goals will be presented in Chapter 6. The potential for an ideal 3D Paul trap [12] is given by,

$$V(x,y,z,t) = \left(\frac{U_0 + V_{rf}\cos 2\pi f t}{2d^2}\right)(2z^2 - x^2 - y^2). \tag{2.5}$$

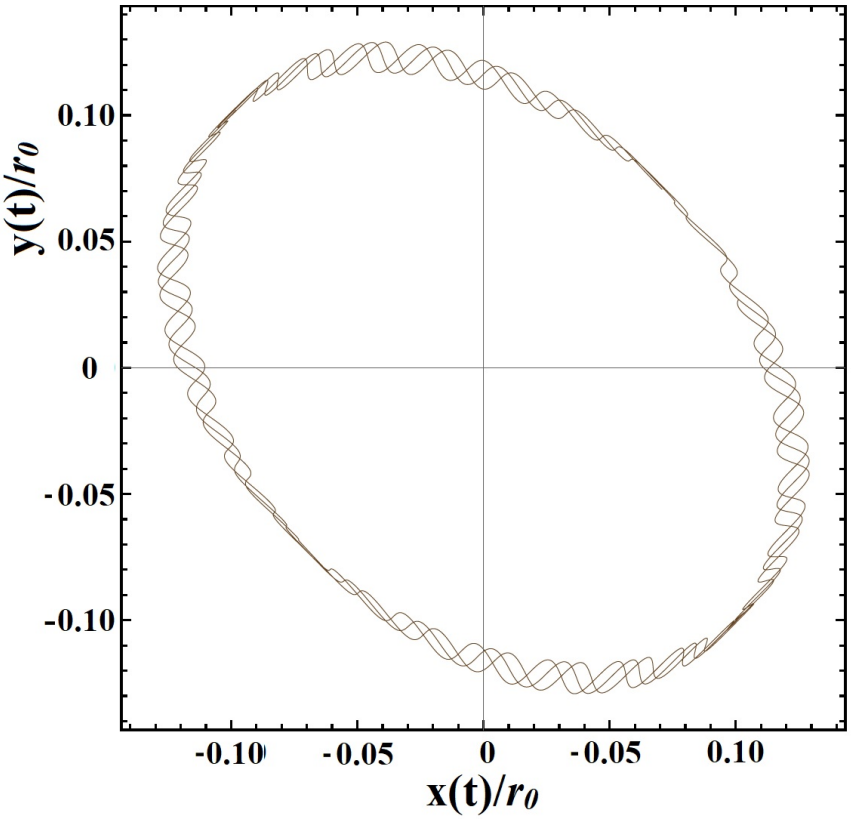

Figure 2.7: A typical ion trajectory in a linear quadrupole Paul trap is shown to exemplify the constituent macro and micromotion.

Here U_0 is the dc potential, V_{rf} is the magnitude of the oscillating potential at radio frequency (RF) f, d is a length scale signifying the extent of the trap, $\hat{z}$ is the axial direction in which DC field, via endcap electrodes is used to provide confinement and $\hat{x}$, $\hat{y}$ represent the transverse directions in which RF trapping is implemented. Using this potential, the equations of motion for the ion(s) are,

$$\frac{d^2x}{dt^2} + [a_x - 2q_x \cos 2\pi ft]x = 0\,, \tag{2.6}$$

$$\frac{d^2y}{dt^2} + [a_y - 2q_y \cos 2\pi ft]y = 0\,, \tag{2.7}$$

$$\frac{d^2z}{dt^2} + [a_z - 2q_z \cos 2\pi ft]z = 0\,, \tag{2.8}$$

where $a_x = a_y = -a_z/2 = \frac{-4QU_0}{m_i d^2(2\pi f)^2}$ and $q_x = q_y = -q_z/2 = \frac{2QV_{rf}}{m_i d^2(2\pi f)^2}$ are dimensionless parameters, m_i is the mass of the ion and Q is the charge of the ion. Parameters a_j and q_j for $j \equiv (x, y, z)$ are used to define the stability parameter region of the trap and only a small range of the combination of a_j and q_j provide stable trapping [11, 12], the first region of stability is shown in figure 2.6. Figure 2.7 shows the typical motion of an ion trapped in an ion trap, along each of the axes. It can be seen from the figure that there are two types of oscillatory motion in the ions trajectory, one is the low frequency harmonic motion, and the other is the fast oscillator motion on top of this harmonic motion. The harmonic part is called the secular motion or macromotion, and the high frequency part is called micromotion. The micromotion results from the response of the ion to the RF frequency, applied to the transverse electrodes, and its amplitude is proportional to the distance from the trap center, as this is the response of the ion to the ac electric field applied to the trap electrodes. In the limit $a, q \ll 1$, the motion of the ion simplifies to $x(t) = G(1 - 0.5q_x \cos 2\pi ft) \cos \omega_x t$, where G is a constant and $\omega_{x,y}/2\pi = 0.5\zeta_{x,y} f$ is the secular frequency. $\zeta_j = \sqrt{a_j^2 + 0.5q_j^2}$ is called the stability parameter.

2.5 Hybrid traps

It is possible to apply additional cooling techniques laser cooling, sympathetic cooling, etc, to trapped ions in a Paul trap. As mentioned earlier, the more modern implementations of linear Paul traps, allow more optical access which comes handy in implementing laser cooling and imaging of ions. Hybrid traps in which a continuously operated neutral atom trap and an ion trap are overlapped in the same spatial region are of particular interest for us because we intend to study ultracold ion-atom interactions. The stability, thermalization and efficient sympathetic cooling of

ions using ultracold atomic ensembles have been demonstrated earlier [14, 75, 77, 88, 89].

Ion traps designed using a hybrid of Paul and Penning trap designs are also known as hybrid traps, and we have made provision to implement some such arrangements in our experiment. The suitable electrode potentials of the linear Paul trap can create effective field free environments at the center at times when the Paul trap is not in operation. We present our arguments for making the choices design implementations in our experiment, which was built with the target to study ultracold ion atom scattering, in chapter 6.

2.6 Optical cavities coupled with ultracold atoms/ions

A Fabry-Pérot (FP) resonator for light, formed by placing two highly reflecting surfaces facing each other, can be used to dress and enhance certain properties of the light beam within it [113, 114]. Two symmetric convex dielectric mirrors placed at near con-focal configuration is a typical realization of this device. Electromagnetic fields in such a resonator are constrained by the interference of the input beam and the multiply reflected resonant beam, which forms a standing wave. When monochromatic light, of a specific frequency, is coupled into a FP cavity, only select lengths of the cavity will lead to resonant coupling. These select cavity lengths corresponding to the number of half wavelengths of the light supported within the cavity length. These resonant modes are known as the longitudinal modes of a FP cavity.

The beam size is minimum at the centre of the cavity and it increases on either sides towards the mirrors and beyond them. The boundary conditions at the surfaces of the mirrors constrain the beams transverse profile of the light coupled to the FP cavity. The expanding beam size and the curved mirror surfaces add curvature to the wavefronts of the beam at various positions and thus, the different resonant transverse beam profiles stipulate a corresponding additional position dependent Guoy phase for the beam. The interference condition mentioned above has to incorporate these additional Guoy phases and thus, each of these resonant transverse beam profiles corresponding to the same longitudinal mode, will be supported with slight variation in the cavity length. These are the transverse electromagnetic (TEM) modes.

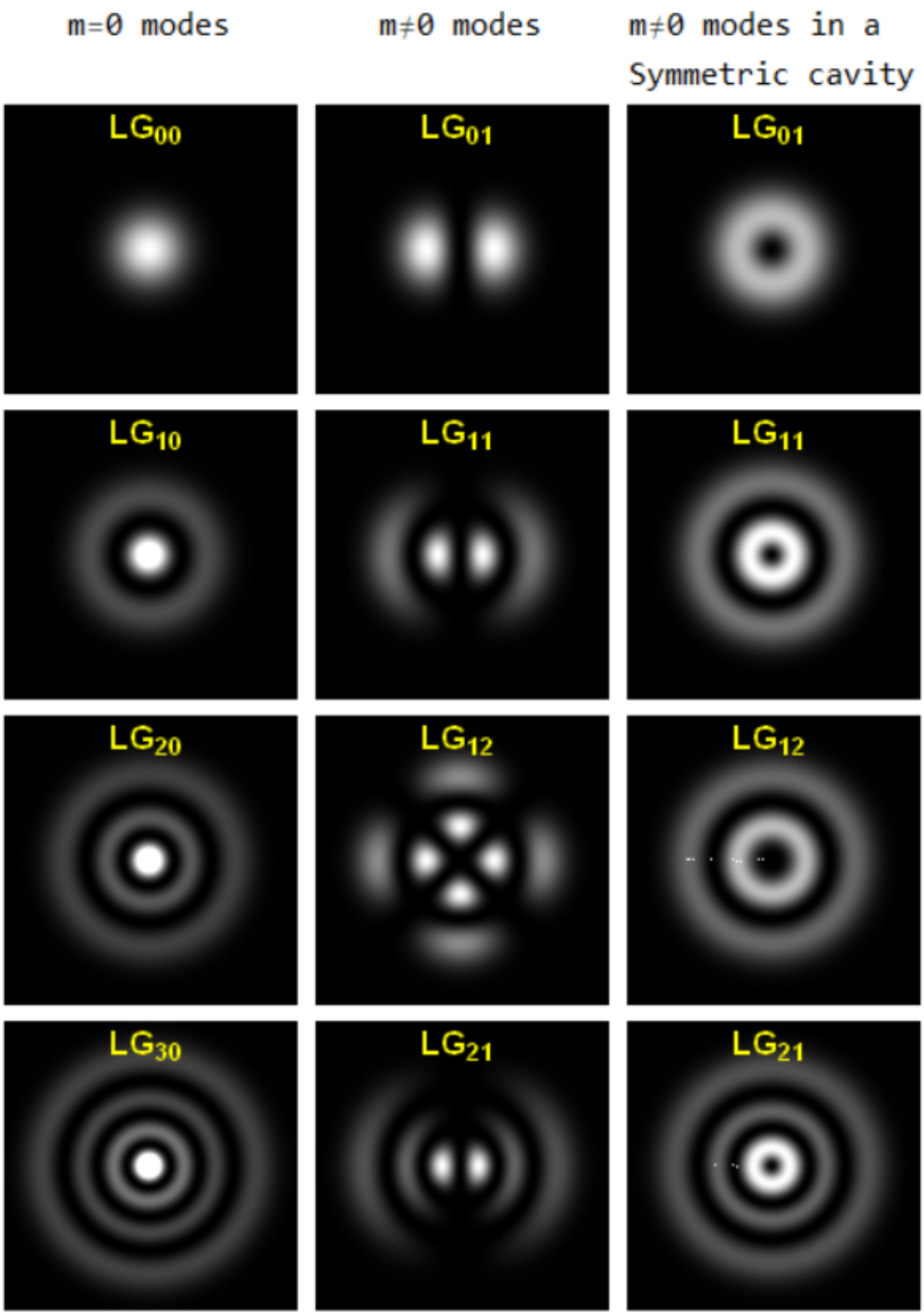

Figure 2.8: The profiles and electromagnetic field functions of the various TEM modes in a cylindrically symmetric optical Fabry Pérot cavity, the Laguerre Gauss ($LG_{l\,m}$) modes are shown.

The profiles of the TEM modes supported by a FP cavity will be determined by the symmetry with which the cavity is built. See figure 2.8 for an illustration of a few TEM modes, of a cavity with cylindrical symmetry, known as Laguerre Gauss ($LG_{l\,m}$) modes with the subscripts l and m denoting the number of radial and azhimuthal nodes in the transverse mode profile.

The modes with $m = 0$ are inherently cylindrically symmetric and can be directly observed with a symmetric cavity. The modes with $m \neq 0$, on the other hand need a deviation from cylindrical symmetry to specify the planes of the azhimuthal nodes. In the absence of any such specific aberrations, these modes appear as superposition of the mode profile rotated by all possible azimuth angles, in the transverse plane, which appear as the symmetrized mode profiles shown in the third column of figure 2.8.

These spatial properties of electromagnetic waves characterized by a FP cavity lead to their usage as a versatile tool. Light coupled into the cavity could be highly amplified in intensity inside the cavity volume due to the multiple reflections from the highly reflecting surfaces. This makes cavities useful when intense fields are needed [104, 115]. The standing wave formed by the field inside a cavity is used in many experiments to introduce periodic conditions with large field gradients for trapping atoms, ions or molecules [55, 116, 117]. The coupling of atoms in the cavity volume to cavity modes unravels many mechanisms of application for probing [41, 53, 118], trapping [27, 117, 119–121], controlling[55, 104, 122, 123] and reading out properties of atoms [77, 105, 124, 125] inside the cavity.

In chapter 3 of this thesis we will mention details about collective coupling of ultracold atoms to cavity modes. We present a novel method for comparing the collective coupling to a number of TEM modes with respective spatial profiles to determine information regarding spatial distribution of the coupled atoms. In cases where the spatial distribution is well known and cylindrically symmetric, the spatial distribution of interactions which the atom-cavity coupling is sensitive to, can be measured. This adds to the versatile utility of a FP cavity in ultracold systems with atoms and/or ions, the scope and limitations of which are discussed later.

Chapter 3

Collective Strong Coupling of Atoms to Cavity

We contemplate the possibility of an optical cavity mediated probe to ultracold ion-atom interactions. Such methods employ a cavity to measure specifics of the ultracold atom ensemble [77] and thereby infer the characteristics of the ions interacting with the ensemble. This ends up being a continuous, precise and controllable measurement, while being non-destructive for the ions as well. We first characterize coupling of ultracold atoms to optical cavity and using this to measure the atom number and density profile, and then evaluate the prospects of the relevance of this technique for ultra cold ion-atom experiments with a single or a few ions.

The confinement of light in optical cavities enables a variety of studies and allows a number of applications [126]. Optical Fabry-Pérot (FP) cavities, coupled with ultracold atoms, have been used to probe, manipulate, detect and trap atoms or molecules [26, 27, 68, 115, 120–122, 124, 127–137]. In many hybrid traps which employ an optical cavity [49, 50, 55, 68, 120, 122–124, 135, 138–144], which require entire ensembles of the trapped species to overlap with the cavity mode, the cavity mode volume is large. This is particularly true when continuously operable traps like a MOT are used, and the necessary optical access for laser beams, etc., limits the minimum cavity length. This results in a large mode volume, making it very challenging to achieve strong cavity coupling with a single atom or a few atoms, while collective strong coupling is achievable. For

ultra-cold trapped atoms, the Doppler line broadening due to atomic motion and trapping fields is narrow enough to allow the ensemble of cold atoms to couple effectively with an optical cavity of moderate finesse.

In our group, collective strong atom-cavity coupling, with the lowest order transverse mode has been used for diagnosing the number and temperature of MOT atoms co-centered with the cavity [89, 124] and for measuring ion-atom interactions [77], apart from realizing optical switching experiments. In addition theoretical and experimental exploration of the utility of a cavity measurement for measuring interactions has been explored [115]. This leads us to ask the question, about how useful extending cavity based measurements for ion-atom interactions can be, within the context of this thesis. From the discussion in the previous chapter on the coupling of atoms to cavities, it became clear that the effects of interactions as conceived in the latter part of the thesis is not compatible with the current cavity technology in the laboratory. Nevertheless this is an exceedingly interesting system for precision measurement of interactions and that is also the motivation for the present exploration of atom cavity interaction. Here, we have extended the use of an optical cavity and its higher order modes, for the diagnosis of atom density profiles along with the number of atoms. We make an estimate for change in collective atom-cavity coupling due to presence of an ion, and have measured this for multiple ions [115]. The prospect of using this for measurement of ultracold ion-atom interactions, with a hybrid ion atom trap co-centered with a cavity is discussed in the last section of this chapter.

3.1 Modes of a Fabry-Pérot cavity

Conditions for constructive superposition of light in a cavity, allow only certain specific modes of light to be resonant in an optical cavity [142]. There are two kinds of modes in an optical FP cavity, the longitudinal and the transverse modes. A particular longitudinal mode is defined by the number of harmonics of light, of the wavelength used, which are contained within the cavity length. Transverse modes are described by the spatial distribution of electric or magnetic fields of the beam of light passing through the cavity. Cavities made of curved mirrors, have cylindrical symmetry, and the theoretical description of cavity modes in such a case is as follows.

The wave equation which determines the electric field $\vec{E}(\vec{r},t)$ of an electromagnetic wave in free space is given by

$$\nabla^2 \vec{E}(\vec{r},t) = \frac{1}{c^2}\,\frac{\partial^2}{\partial t^2}\vec{E}(\vec{r},t)\,. \tag{3.1}$$

For a beam propagating in $\vec{z}$ direction the eigen modes for transverse electric field functions in cylindrical coordinates (with radial index r, azimuthal index ϕ and axial index z) can be expressed as

$$\vec{E}(r,\phi,z) \propto \Psi_{l\,m}(r,\phi,z)\,\hat{\epsilon}\,, \tag{3.2}$$

where $\hat{\epsilon}$ is the unit vector in the direction of polarization of the propagating beam. Under the assumption that the extent of the beam in the transverse (r,ϕ) plane is negligible compared to that in the direction of propagation $\vec{z}$, equation 3.1 can be replaced by the paraxial wave equation

$$(\nabla^2_{r,\phi} + 2i\,k_z\,\frac{\partial}{\partial z})\,\Psi(r,\phi,z) = 0\,. \tag{3.3}$$

Solving equation 3.3 using the form

$$\Psi(r,\phi,z) = U(r,\phi)\,e^{-ik_z z}\,, \tag{3.4}$$

we get the Laguerre-Gauss ($\mathrm{LG}_{l\,m}$) eigen functions [145], $\Psi_{l\,m}(r,\phi,z)$ as

$$\Psi_{l\,m}(r,\phi,z) = \frac{\omega(0)}{\omega(z)}\left(\frac{r\sqrt{2}}{\omega(z)}\right)^{|m|} e^{\left(\frac{-r^2}{\omega^2(z)}\right)}\,\mathbb{L}_l^{|m|}\left(\frac{2r^2}{\omega^2(z)}\right)\times e^{i(k_z z - m\phi)}\,e^{i\left(\frac{k_z r^2}{2R(z)}\right)}\,e^{-i(2l+|m|+1)\tan^{-1}(z/z_R)}\,, \tag{3.5}$$

where k is wave number, z_R is the Raleigh length, $\omega(z)$ is the waist of the $\Psi_{l\,m}$ at $z=0$, $R(z)$ is radius of curvature of the cavity beam wave-front and $\mathbb{L}_l^m$ is the Laguerre polynomial with radial index l and azimuthal index m, $\hat{z}$ is parallel to the optic axis of the cavity. The total electric field in the cavity, in the transverse plane is given by $\vec{E}_{cav}(r,\phi,z) = \vec{E}^{+}(r,\phi,z) + \vec{E}^{-}(r,\phi,z)$, which is the sum of the electric fields of the forward and reverse propagating beams in the cavity. These transverse cavity modes with $\vec{E}_{cav} \propto [\Psi_{l\,m}(r,\phi,z) + \Psi_{l\,-m}(r,-\phi,-z)]$ are called Laguerre-Gauss ($\mathrm{LG}_{l\,m}$) modes. The intensity in a transverse plane is proportional to $|\vec{E}_{cav}(r,\phi,z)|^2$, given by.

$$|\vec{E}_{cav}(r,\phi,z)|^2 \propto e^{(\frac{-2r^2}{\omega^2(z)})} \times \frac{(2\,r^2)^{|m|}}{\omega(z)^{2|m|+2}} (\mathbb{L}_l^{|m|}(\frac{2r^2}{\omega^2(z)}))^2 \times \cos^2\left(k_z z - m\phi + \frac{k_z r^2}{2R(z)} - (2l+|m|+1)\tan^{-1}\left(\frac{z}{z_R}\right)\right). \quad (3.6)$$

The first term on the right hand side of equation 3.6 represents the Gaussian transverse profile of the paraxial beam, which along with the second term corresponds to the cylindrically symmetric, Laguerre Gauss functions, based on the Laguerre polynomials and their corresponding beam size dependant spatial spread. Both radial and axial coordinate are seen in this term as the transverse extent of the beam depends on z and since the number of azimuthal nodes $|m|$ greatly influences the extent as well as the profile of each mode in the transverse plane. The third term shows the effective phase with the first part corresponding to the phase from Gaussian profile and the rest due to the Laguerre-Gauss mode's profile.

The solution for resonant cavity field must satisfy the boundary conditions at the cavity mirrors at $z = \pm$ L/2. This condition gives us that all $\mathrm{LG}_{l\,m}$ modes with equal value of $2l + |m|$ would be resonant for the same cavity length. Every $\mathrm{LG}_{l\,0}$ mode has l radial nodes. When $m \neq 0$, the total phase of the electric field is dependent on ϕ, leading to m angular nodes.

However, if the cavity is perfectly cylindrically symmetric, then no specific directions for the angular nodes can be stable. In this case, the effective $\mathrm{LG}_{l\,m}$ mode will be the superposition of all $\Psi_{l\,m}$ functions with the angular node in all angles. Thus the LG modes with $m \neq 0$ have an additional node at the center, $r = 0$ along with the l radial nodes at finite radii. The size of this central node and the radii of the radial nodes will be larger for higher values of m.

In practical cavities, the phase of different modes with the same $2l+|m|$ would be slightly different due to aberrations and imperfections, hence they would be resonant at slightly different cavity lengths [125] making it possible to stabilize any individual mode.

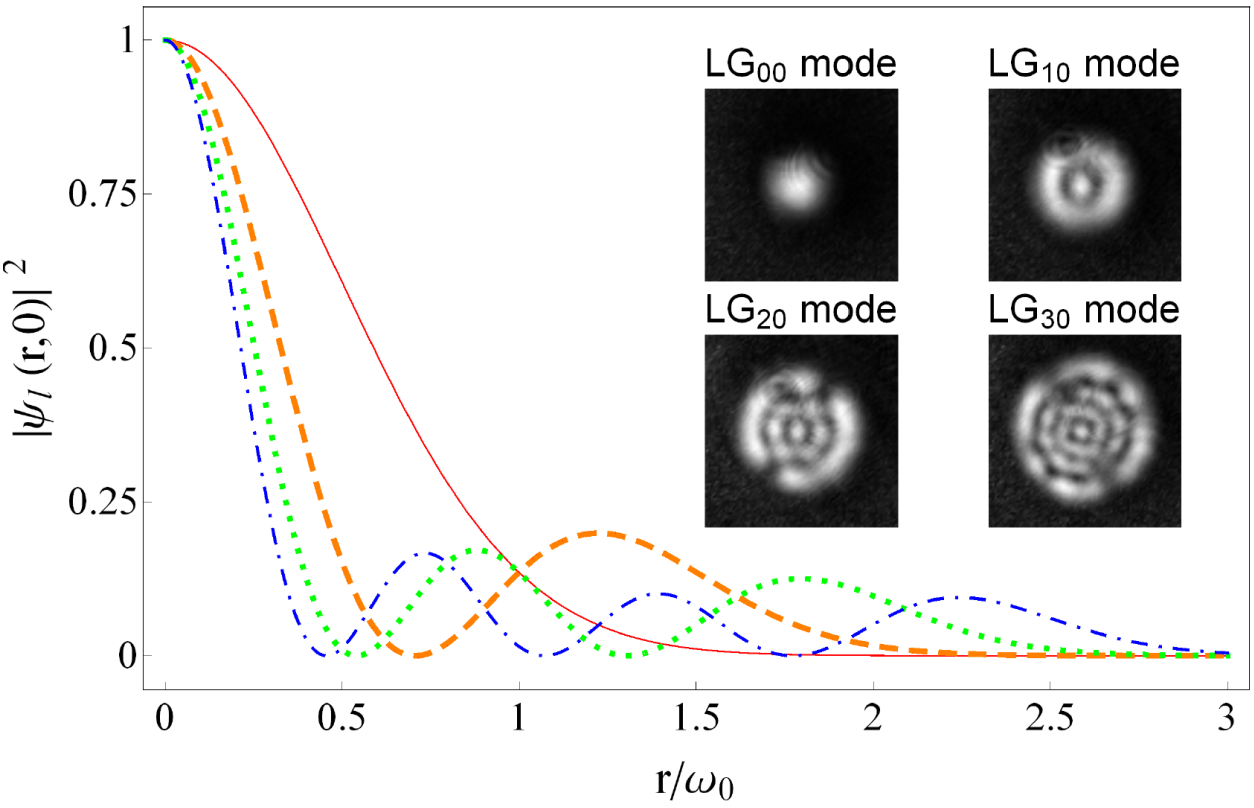

Figure 3.1: Theoretical mode profile functions and images of transverse LG modes of the empty cavity, measured by imaging the probe light transmitted through the cavity. The continuous red curve is for LG_{00} mode, the dashed orange curve is for LG_{10} mode, the dotted green curve is for LG_{20} mode and the dot-dashed blue curve is for LG_{30} mode.

In our experiment, we adjust the coupling of the input to the cavity to stabilize only $m0$ modes by monitoring the image of the cavity transmission intensity profile. We ensure that there is no central dark spot. This ensures that the cavity modes used in the present experiments have only the radial index l and the electric field inside the cavity is given by$E_{cav}(r,z) \propto \psi_l(r,z)\hat{\epsilon}$ where $\psi_l(r,z)$ is given by equation 3.7,

$$\psi_l(r,z) = \frac{\omega(0)}{\omega(z)}\, e^{(\frac{-r^2}{\omega^2(z)})}\, \mathbb{L}_l^0(\frac{2r^2}{\omega^2(z)})\cos(\, kz + \frac{kr^2}{2R(z)} - (2l+1)\tan^{-1}(\frac{z}{z_R})\,). \tag{3.7}$$

The experimental images with the radial functional form of the intensity of the modes are illustrated in figure 3.1.

3.2 Strong coupling of 2 level atoms

The interaction of the cavity and atomic state results in the lifting of the degeneracy between (a) the excited atom and the empty cavity mode, and (b) the ground state atom and the occupied cavity mode [146, 147]. The experimental manifestation of this phenomenon is seen as a frequency splitting about the atomic resonance, in the transmission of a weak probe beam. When the condition $g > \kappa, \gamma$, is satisfied, this splitting can be resolved in a measurement, and is known as vacuum Rabi splitting (VRS) [126, 140, 148]. Here, g is the rate at which the cavity mode and the atom exchange excitation, κ is the rate at which cavity mode loses photons and γ is the photon loss rate due to spontaneous emission from the atom coupled to the cavity. This has been observed both with single atoms [41, 125, 149–152] and with a collection of trapped atoms (or ions) [49, 50, 53, 123, 124, 139, 143, 144, 153] within a high finesse cavity. Collective strong coupling with higher order transverse electromagnetic (TEM) cavity modes in a multimode cavity has been demonstrated [143] earlier. In this study we use individual higher order LG modes with cylindrical symmetry within the cavity to make measurements on atom numbers and their density profiles.

The number of atoms that couple with a particular cavity mode is determined by the overlap integral of the square of mode function with the atomic density distribution. This is a fraction of the total atom number in the MOT, N_{at} and the fraction is dependent on the specific LG mode. The VRS due to collective strong coupling of atoms to $\mathrm{LG}_{l\,0}$ mode of a cavity is given by [148, 153]

$$2\hbar g_l = \mu_a \sqrt{\frac{2\hbar\omega_c N_l}{\epsilon_0 V_l}}, \tag{3.8}$$

where V_l is the mode volume and N_l is the number of atoms coupled to the l^{th} LG mode and are given by

$$N_l = \int_{r=0}^{\infty}\int_{z=-L/2}^{L/2}\int_{\phi=0}^{2\pi} \rho(r,\phi,z)|\psi_l(r,z)|^2 d^3r, \tag{3.9}$$

$$V_l = \int_{r=0}^{\infty}\int_{z=-L/2}^{L/2}\int_{\phi=0}^{2\pi} |\psi_l(r,z)|^2 d^3r. \tag{3.10}$$

By solving equation 3.10, mode volumes V_l of all LG modes are obtained to be identically equal to $\pi\omega(0)^2 L/4$ where L is the cavity length. Single atom-cavity coupling $\bar{g}$ is obtained by calculating g_l from equation 3.8 assuming $N_l = 1$. For our system, we calculate values of $\bar{g}$ to be 200.8 kHz for F = 3 to F′ = 4 transition (PLB) and 96.6 kHz for F = 2 to F′ = 3 transition (PLD) as the values of μ_a for these two cases are different.

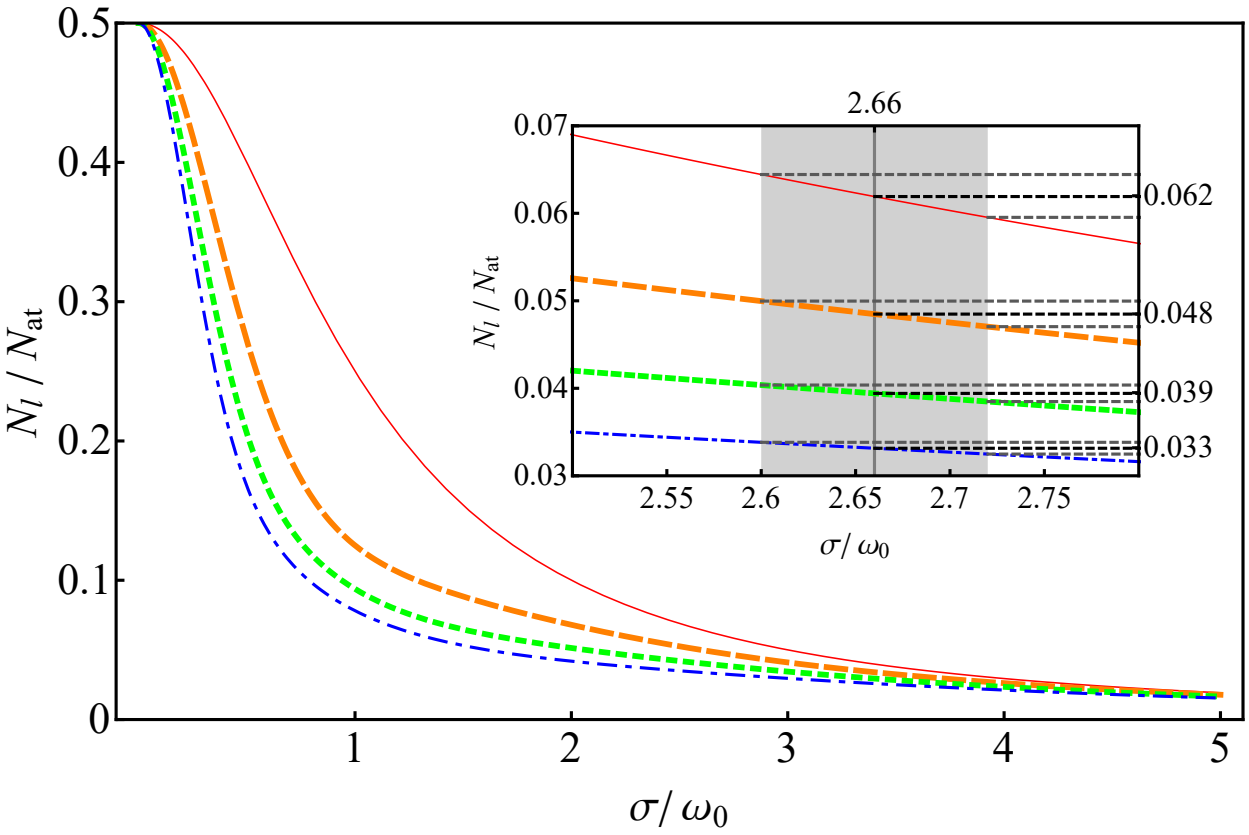

Figure 3.2: Ratio of atoms coupled to the LG_{l0} cavity mode, N_l and the total number of atoms in the MOT N_{at} for different sizes of MOT's co-centered with the cavity. The continuous red curve is for LG_{00} mode, the dashed orange curve is for LG_{10} mode, the dotted green curve is for LG_{20} mode and the dot-dashed blue curve is for LG_{30} mode. Inset shows zoomed in version of the same curves around the value of σ/ω_0 measured from CCD1 image of the bright-MOT, 2.66±0.06

In the case when the atomic density distribution, ρ is a constant the VRS, $\Delta\nu = 2\hbar g_l$ becomes independent of l, which implies that the coupling to every LG mode is equal [49]. Alternatively, when ρ is not uniform, VRS for different LG modes will be different. For a non-uniform, but regular density profile of atoms, such as Gaussian distribution co-centered with the cavity, with peak density ρ_0 and $1/e^2$ radius $\sigma \ll L$, $\rho(r,\phi,z) = \rho_0 \exp[-2(z^2+r^2)/\sigma^2]$, using equations 3.7-3.10

and using $\omega(z) = \omega(0)$ and $\bar{r} = 2r^2/\omega(0)^2$, we get

$$\frac{g_{l+1}}{g_l} = \sqrt{\frac{\int_0^\infty e^{-(1+\alpha)\bar{r}} \left[\mathbb{L}^0_{l+1}(\bar{r})\right]^2 d\bar{r}}{\int_0^\infty e^{-(1+\alpha)\bar{r}} \left[\mathbb{L}^0_{l}(\bar{r})\right]^2 d\bar{r}}} \,. \tag{3.11}$$

Both the integrands in equation 3.11 are positive definite, the integral in numerator is always smaller than that in the denominator, and for $\alpha = \frac{\omega_0^2}{4\sigma^2} \ll 1$ i.e., when $\omega_0 \ll 2\sigma$, $g_{(l+1)}/g_l \approx 1$, which is the uniform density of atoms case. A systematic decrease results in the VRS with higher order modes (with increase in the l index of the LG mode) for a Gaussian distribution when $\sigma \approx \omega_0$. So in this case of a Gaussian atomic distribution co-centered with the FP cavity, the change in the VRS with $\mathrm{LG}_{l\,0}$ can be used to measure the atom density distribution in the radial direction. The VRS with $\mathrm{LG}_{l\,0}$ mode is higher than VRS due to $\mathrm{LG}_{(l-1)\,2}$ mode, and so on for a Gaussian atomic density profile.

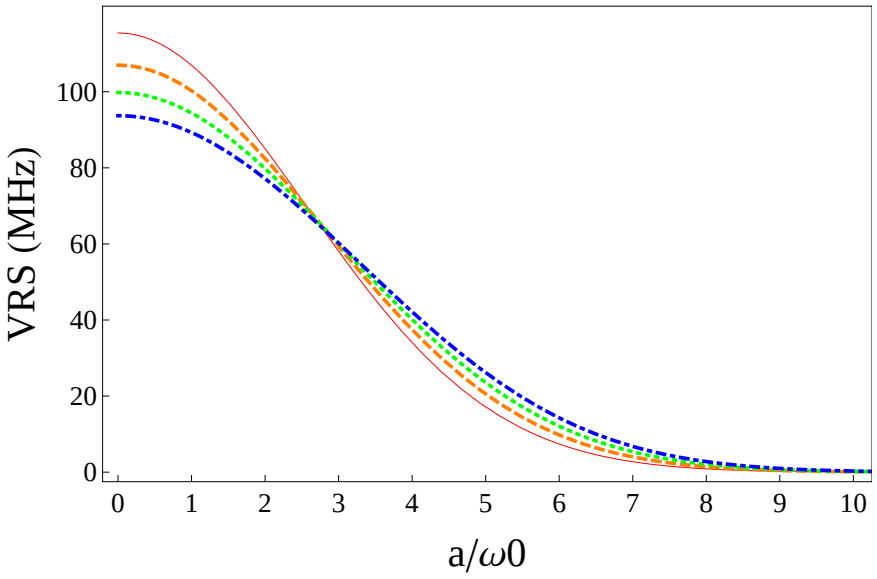

Figure 3.3: Theoretical estimation of VRS due to bright MOT as the MOT is shifted radially by distance a. The continuous red curve is for 00 mode, the dashed orange curve is for 10 mode, the dotted green curve is for 20 mode and the dot-dashed blue curve is for 30 mode.

For a Gaussian density of atoms shifted radially from the axis of the cavity by a distance a, the number of atoms coupled to $\mathrm{LG}_{l\,0}$ mode can be obtained by substituting the expression,

$\rho'(r,\phi,z) = \rho_0 exp[-((r-a)^2+z^2)/\sigma^2]$ in equation 3.8 and using $\bar{a} = 2(r-a)^2/\omega(0)^2$, which gives

$$N_l' \propto \int_0^\infty e^{-(\alpha\bar{a})} e^{-\bar{r}} \left[\mathbb{L}_l^0(\bar{r})\right]^2 d\bar{r}\,. \tag{3.12}$$

The integrand of equation 3.12 is positive definite and decreases as a increases. In this case the measured VRS due to the cavity coupled atoms reduces very quickly as the cloud of atoms is displaced radially from the axis of the cavity. In the case of a single atom in the cavity, $N_l = |\Psi_{l\,0}(r_a, z_a)|^2$ where (r_a, ϕ_a, z_a) are the coordinates of the atom's position. [127, 130, 131, 134, 151]

If the atomic ensemble is a uniform sphere of radius r_s and density ρ_s, which is co-centered with the cavity,

$$\frac{N_l}{N_{at}} = \frac{2\pi\rho_s \int_0^{r_s} r\sqrt{(r_s^2 - r^2)}\, e^{-\bar{r}} \left[\mathbb{L}_l^0(\bar{r})\right]^2 dr}{(4\pi\rho_s r_s^3/3)}\,, \tag{3.13}$$

where N_{at} is the total number of atoms. However when $L \gg r_s \gg \omega(0)$, for small values of l, we get $N_l = N_{at}$.

Thus from the above analysis, we conclude that it can be determined whether the density of atoms is uniform or a Gaussian distribution in an experiment which measures VRS. If the atomic ensemble is not radially symmetric, i.e. $\sigma_x \neq \sigma_y$, though the VRS with different LG modes can be numerically calculated, the ellipticity in the atomic density profile cannot be retrieved from the measured values of VRS with different modes. Thus we approximate the density of atoms to a spherical Gaussian distribution with $\sigma = (\sigma_x\sigma_y\sigma_z)^{1/3}$. For the bright-MOT case presented in this paper, we take $\sigma_z = \sigma_y$ as the magnetic field gradient in y and z directions is the same, as are the laser parameters, and we therefore use $\sigma = (\sigma_x\sigma_y^2)^{1/3}$.

3.3 Experimental details and methods

We prepare a magneto-optical trap (MOT) of ^{85}Rb (rubidium) atoms, which is well overlapped with the mode of a medium finesse, near con-focal FP cavity. The coupling of both a bright-MOT and a dark-MOT to the fundamental and higher order Laguerre-Gaussian (LG) mode, is studied

experimentally. The fluorescence of the bright-MOT is recorded on a calibrated photo multiplier tube (PMT1) and on a CCD camera, to determine the atom number and density distribution respectively.

The VRS calculated using the experimental density as input and the measured VRS for the different $LG_{l\,0}$ modes are in very good agreement. This validates the VRS measurement for the determination of the atomic density. On the other hand, the a toms in a dark-MOT are trapped and shelved in the lowest hyperfine F$= 2$ level and do not interact with the cooling or repumping laser beams, see figure 3.5. In this case, the in-situ atomic density cannot be determined via the above fluorescence measurements but the cavity measurement can be used to estimate the density. However, this requires the VRS measurement to be performed for different $LG_{l\,0}$ modes.

The atom-cavity coupling is investigated for the cylindrically symmetric Laguerre-Gauss $LG_{0\,0}$, $LG_{1\,0}$, $LG_{2\,0}$ and $LG_{3\,0}$ modes. As each of these modes has a different spatial distribution, the density variation of the trapped atoms integrated along the cavity axis can now be explicitly measured, assuming cylindrical symmetry. The dependence of VRS on the choice of the transverse mode of the cavity allows and extends the utilization of FP cavities for measurements.

In particular, the ability to estimate in-situ density profile of atoms (or molecules, or ions, in future experiments) in optically dark and steady state traps, while using minimal probe intensities can be used advantageously in hybrid trap experiments [41, 77, 135, 154]. In what follows, we first describe the experimental system and use the system specific numbers and atomic parameters to model the atom-cavity collective strong coupling as a function of different transverse modes, present the results of measurements and compare the experimental results with the theoretical model, which shows very good agreement.

The experiment has a near con-focal FP cavity with mirrors of radius of curvature 50 mm placed at a distance of $L = 45.7$ mm, which allows us to create a MOT within the cavity as shown in figure 3.4. The mode waist $\omega(0)$ for $LG_{0\,0}$ mode for the above parameters is 78 μm. The cavity has a finesse of $\mathcal{F} \approx 600$ and its length can be tuned across a few free spectral ranges (FSR) with a ring shaped piezoelectric transducer (PZT) on which, one of the cavity mirrors is mounted, see figure 3.4.

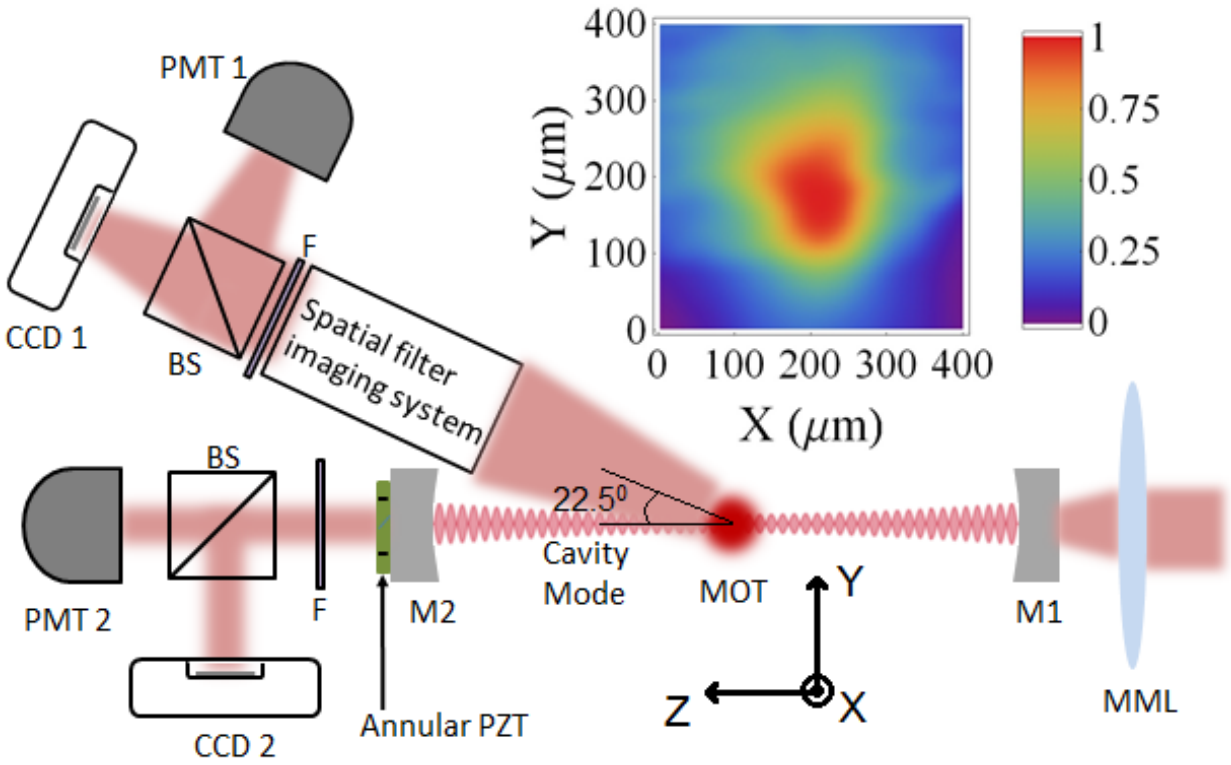

Figure 3.4: Schematic of experiment. MML is a mode matching lens used for coupling of light to the FP cavity, F is an optical bandpass filter to block any stray light of frequencies far from ω_a, BS is a beam splitter, PMT1 and PMT2 are photomultiplier tubes and CCD1 and CCD2 are imaging cameras. The cavity resonant frequency ω_c of a particular transverse mode is matched with ω_a by adjusting the cavity length using the annular PZT and the cavity probe laser frequency ω_p is scanned around ω_a. Inset: The contour plot for the density distribution of the ^{85}Rb MOT atoms which fluoresce with natural transition frequency ω_a are imaged by CCD1.

Details of the full hybrid trap arrangement can be found in previous experimental work [77, 88, 89, 104, 124, 143, 155]. The PZT allows tuning the resonant frequency of a particular LG mode of the cavity ω_c to the atomic transition frequency ω_a. The frequency of the cavity in-coupled probe light ω_p, is scanned across ω_a and the transmission signal of the probe light through the cavity is measured by a photo multiplier tube, PMT2. Although the cavity is not locked, the frequency scan of the probe frequency is much faster than the drift rate of the cavity, once the cavity resonance condition is manually set. The drift during one full set of measurement is calculated to be less than ± 1 MHz, which can effect the measured VRS by up to +0.5 MHz. This VRS drift is estimated using the formalism of J. Gripp et al. [156]. This effect is less than the natural linewidth of atoms and is smaller than the statistical error bars on measurements.

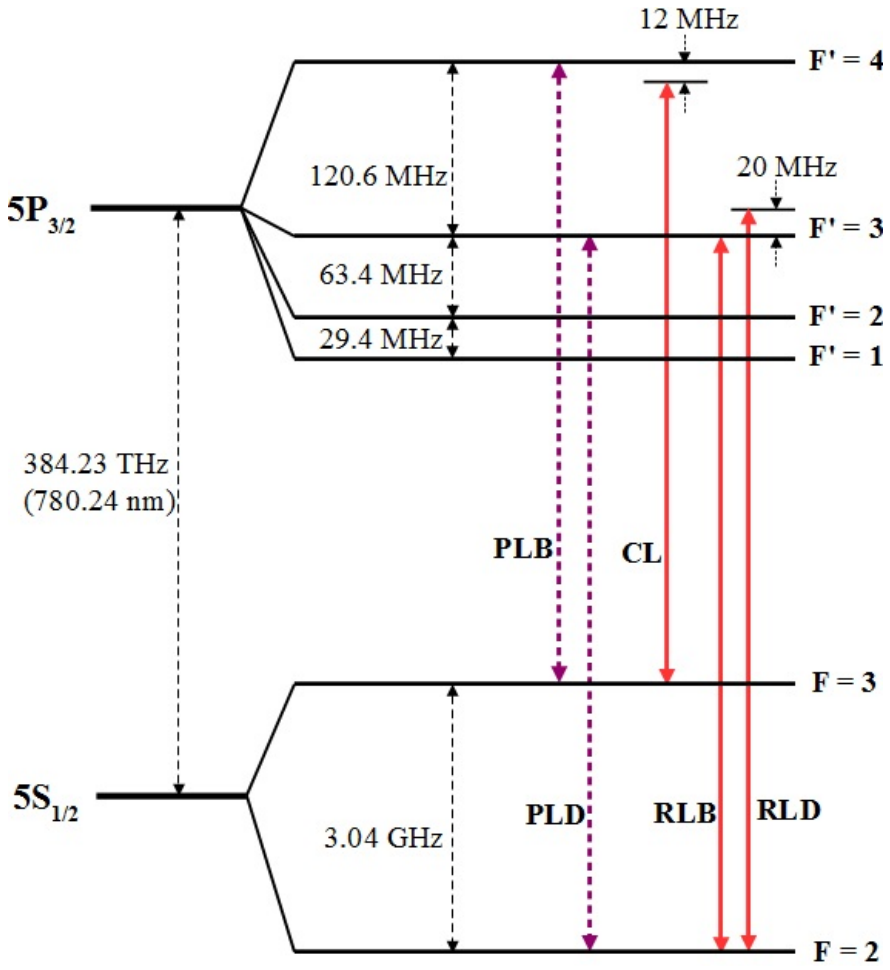

Figure 3.5: The relevant ^{85}Rb energy levels and the transitions used in the experiment are illustrated. In the figure, CL is the cooling laser, RLB and RLD are the repumping laser for the bright-MOT and the dark-MOT respectively. The probe lasers for the bright-MOT and the dark-MOT VRS, PLB and PLD, are scanned across the identified transitions.

The frequencies relevant to the experiment are illustrated in figure 3.5. The PMT measures a signal in the form of a single transmission peak at ω_c, when the cavity is empty while, with the MOT atoms in the cavity, the transmission is modified to shows two peaks, as shown in figure 3.6, separated by the VRS frequency interval given by $2\hbar g_{lm} \propto \sqrt{N_{lm}}$, where g_{lm} is the collective coupling of atoms and N_{lm} is the number of atoms coupled to the cavity mode LG_{lm}. Below we measure the VRS for the atomic distribution using the various LG_{l0} modes. [49, 93, 118, 124, 143, 147, 153].

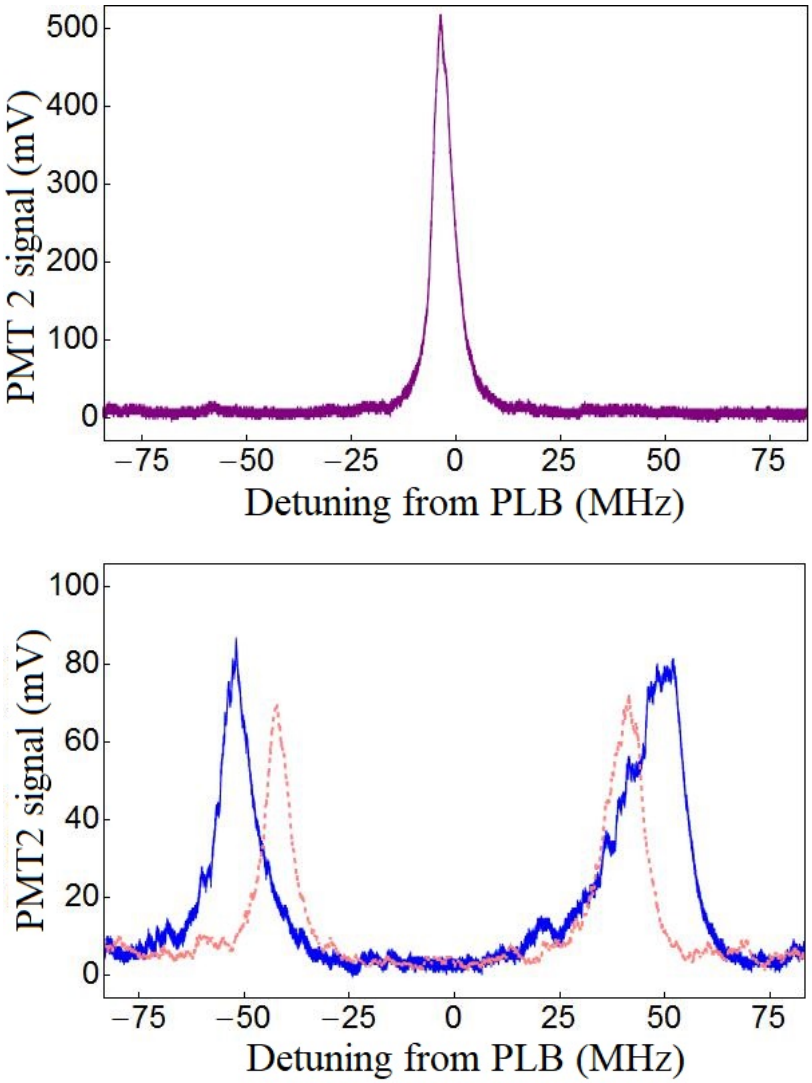

Figure 3.6: a. Empty cavity transmission for LG_{00} cavity mode. b. Transmission through cavity with co-centered bright-MOT atoms. The continuous blue curve shows VRS for LG_{00} cavity mode and the dashed pink curve showing VRS for LG_{30} cavity mode. The VRS signal for LG_{00} mode has larger width and exhibits features of slight non-linearity due to higher peak intensity as a result of smaller mode cross section.

For a bright-MOT (which has atoms in both the ground and electronically excited state at any instant), the repumping beams are combined with all the 6 cooling beams, and for the dark-MOT (where the central MOT atoms are not repumped and so are optically pumped into the dark ground state), 2 hollow repumping beams with a dark spot of diameter 2mm in the center, are combined with 2 of the horizontal cooling beams [77]. To measure VRS due to bright-MOT atoms, the cavity probe frequency ω_p is scanned across the F$= 3$ to F$' = 4$ atomic transition. On the other

hand, for measuring VRS due to dark-MOT atoms, ω_p is scanned across the F$=2$ to F$'=3$ transition. Different transitions are used to probe the atom-cavity coupling in the bright and dark MOT cases because the ground state population of the atoms is in different states. g_l depends on the dipole matrix element μ_a of the probed transition which is different for the bright-MOT and the dark-MOT cases [157]. The transition dipole moment with isotropic polarization for respective F and F' is the relevant μ_a and the measured VRS is independent of the polarization of the probe beam [124]. The characterization of the bright-MOT and the dark-MOT have been described in earlier work [77, 89, 104]. The VRS measurements with dark-MOT were performed by Dr. Sourav Dutta.

We have shown in earlier work that VRS measurements are independent of the polarization of the probe [124]. This is consistent with the present measurement. The in-situ measurement of the VRS directly for the bright-MOT atoms is complicated by the coupling of MOT light into the near resonant cavity mode [155]. Therefore, to measure the atom coupling variation with the probe light of specific spatial modes, we switch off the cooling lasers for 1 ms, keeping re-pumping lasers on, thereby optically pumping atoms into the F = 3 state and within 0.5 ms scan the probe laser back and forth across the atom-cavity resonance, long before the atoms leave the trap region. The ballistic expansion of the atomic cloud during this time has been determined in Ray et. al. [124] to be less than 1% of our MOT size. As the two VRS peaks occur at different times the effect would be different on each. However, no corrections for this expansion has been made while presenting results of this paper because this correction is substantially less than the statistical error of the measurements. For the dark-MOT, since the atomic fluorescence is severely suppressed, in-situ measurement of VRS can be done with the dark-MOT [77, 104].

The cavity probe light is taken from the output of a single mode, polarization maintaining fiber and has a Gaussian intensity profile. This $TEM_{0\,0}$ single mode beam has good mode matching with the $LG_{0\,0}$ cavity mode, and has poor mode matching with higher order $LG_{l\,0}$ cavity modes. Therefore higher input probe powers are required for obtaining a measurable VRS signal with higher order modes. This also limits the number of cavity modes up to which we can measure VRS. For the experiment the input light power is adjusted such that transmitted light output power through the empty cavity for different LG modes is constant and is sufficient to measure the VRS. We only

scan the cavity length holding to the best cylindrically symmetric LG_{00} mode. This ensures that the conditions for measurement with different modes do not change significantly, we also verify this by explicitly imaging the cavity output mode.

3.4 Results for VRS with different modes

The collective strong coupling of rubidium (Rb) atoms in a magneto-optical trap (MOT) to the Laguerre-Gaussian (LG) modes of a Fabry-Pérot cavity is investigated. Bright and dark ^{85}Rb MOT atoms are prepared at the geometric center of the cavity and the vacuum Rabi splitting (VRS) of the collectively coupled atom-cavity system is measured for LG_{l0} (l = 0,1,2,3) modes.

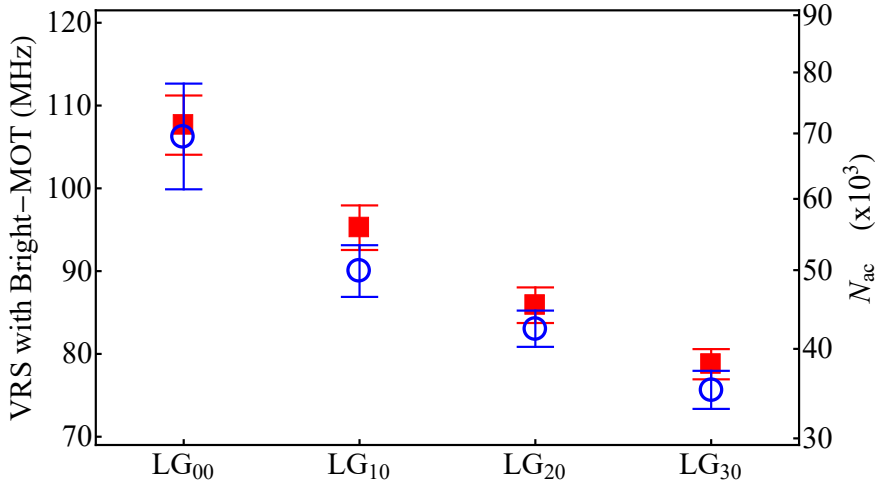

Figure 3.7: VRS for different LG modes due to bright-MOT measured on the F = 3 to F′ = 4 transition. Blue circles are experimental values of measured VRS and the blue error bars are one standard deviation. The red squares are calculated values of VRS, using N_{at} measured by PMT1 signal and σ obtained from the Gaussian fit to CCD1 image of the MOT, for different cavity modes. The red error bars include estimated errors in calculated VRS due to statistical and least count errors in measured N_{at} and σ.

The experimental results for the bright-MOT are shown in figure 3.7. Here we see the VRS signal measured with a bright-MOT and the effective number of atoms coupled to the cavity mode (N_l) as a function of changing LG modes. Care has been taken to ensure that the MOT is well centered, by maximizing the VRS signal with the LG_{00} mode while ensuring the MOT is symmetric. It is observed that the measured VRS decreases as l index increases, for identical initial MOT atom

number and MOT density profile. This matches the expected variation for a localized atomic ensemble with a three dimensional Gaussian distribution of atoms, as expressed in equation 3.11. Calculated values of densities are expected to be higher than measured values for two reasons. One, we have neglected MOT expansion before measurement of VRS and two, any finite amount of probe intensity leads to a reduced measure of VRS [104, 156, 158]. We have taken necessary measures to minimize these effects by optimizing the probe beam power and the measurement interval timing.

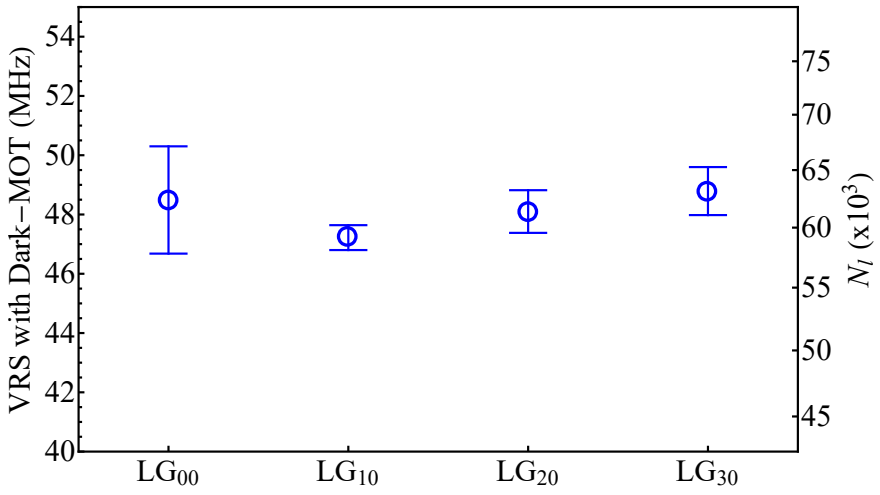

Figure 3.8: VRS with a Dark-MOT for different LG modes measured on the F = 2 to F′ = 3 transition. Blue circles are from experimental measurement of VRS and the blue error bars are one standard deviation on either sides of the mean value of corresponding measurements.

For the bright-MOT, the best fits for parameter $\sigma = (\sigma_x \sigma_y^2)^{1/3}$ from the MOT image is obtained to be 209.3 $\pm$3.9μm while the least count error due to the size of pixels in CCD1 is 4.6 μm. The total number of atoms in the MOT, $N_{at} = (1.16 \pm 0.03) \times 10^6$ is obtained from PMT1 signal. This gives the peak atom density to be $\rho_0 = (6.43 \pm 0.67) \times 10^{10}$ cm^{-3}. The VRS calculated for this values of N_{at} and σ using equation 3.8 are in good agreement and this can be seen in figure 3.7. The possible source of systematic errors in measurement of N_{at} due to cooling laser power fluctuations ($\pm$ 3%) is estimated to be less than 3%. However, accounting for a maximum possible error of $\pm$0.5 MHz in measurement of the detuning of the cooling beams, we get a maximum potential systematic error of $\pm$8% in the atom number measured through fluorescence. These errors have not been shown in figure 3.7, where only the statistical errors and least count errors are accounted for in

the displayed error bars. In principle, measurements can be made with MOT atoms whose center is displaced from the cavity axis. However, shifting the MOT atoms spatially with respect to the cavity axis, while maintaining the density profile is challenging. Such a measurement is much more amenable with dipole trapped atoms within the cavity mode.

In the case of the dark-MOT, atoms are optically pumped out of the cooling cycle, which allows for an in-situ detection of atoms of a dark-MOT using cavity coupling and VRS. For the dark-MOT, the VRS for the different $LG_{l\,0}$ modes used shows no statistically significant change, which is illustrated in figure 3.8. This is in stark contrast with the results for the bright-MOT, where monotonic decrease is seen in the VRS, with increase in the l index. The constant VRS measured as a function of the different LG modes is consistent with the constant density of atoms in the central region of the dark-MOT, within lengths of order of ω_0, as discussed earlier.

Although the dark-MOT cannot be imaged in-situ, the 2 hollow repumping beams can be quickly changed to non-hollow beams and the obtained PMT1 signal can be used to measure the total number of atoms in the dark-MOT. Applying this method, we obtain the number of atoms in our dark-MOT to be $\approx 1.4\times10^6$. The measurement in figure 3.8 is a direct in-situ measurement of dark-MOT atoms coupled to a cavity. The constant atom density is expected as the cooling in the central region of the dark-MOT stops, and the energy of the atoms is sufficient to distribute them uniformly in the dark spot region of the MOT. Assuming uniform atomic density ρ_s, within a sphere of radius r_s and by numerically solving equation 3.13, we calculate the size of dark-MOT, r_s to be 222$\pm$7 μm, and the density in the central region of the dark-MOT, ρ_s to be $3.1 \pm 0.3 \times 10^{10}$ cm^{-3}. The obtained value of r_s is $\approx$ 3 times $\omega(0)$ which is larger than the waist of the highest LG mode used.

3.5 Discussion and applications

The simple theoretical model for this process described earlier and the experimental measurements are found to be in close agreement with each other. We show that the density distributions of atoms, which are collectively strongly coupled to the cavity mode can be probed by varying

the cavity spatial mode. The method works for trapped and free flight atoms, as has been demonstrated. As different transverse modes have different spatial extents and spatial profiles, varying these directly samples the extended atomic distribution. Further, since the atoms are collectively strongly coupled to the cavity, the spatial measurement transforms into a frequency measurement, which is fast and robust in implementation. This is a robust method since sensitivity to the fluctuations in the atom number is suppressed due to the $\sqrt{N_c}$ dependence of the VRS. It should be kept in mind that if the density distribution is regular and cylindrically symmetric, then measurements with different transverse modes can measure the spatial density profile of the ensemble of atoms. In principle when the entire distribution is shifted off axis, the density distribution can still be measured, though conducting such measurements with a MOT is very intricate as the atomic density profile changes as we shift the MOT. However for dipole trapped atoms, this method would be effective. In the case when the ellipsoidal density distributions, the method does not apply. The method can be flexibly adapted to a wide variety of measurements in the future, expanding the tool-box of available techniques for the measurement of atoms coupled to a cavity.

In systems like a dark-MOT, this method can be used to measure in-situ density profiles which is challenging to measure in other available methods like absorption imaging where, the resonant light used can alter the state preparation instantaneously and can perturb the atomic density profile. Since the cavity transmission is suppressed for resonant light due to VRS, the probe does not interfere with the state preparation of the atomic ensemble. A combination of spatial mode dependent measurement with a number dependent frequency measurement can propel cavity based measurements into new applications.

In connection to our original quest of using optical cavity as a tool to investigate ultracold ion-atom interactions, we conclude that this method of probing lacks the necessary resolution. Cavity based non-destructive measurements to differentiate the effect of small interactions due to low number of ions may not be feasible. The scope for using higher order modes to our advantage is limited given that the atom cavity coupling is lower for these modes. The weak interaction with ground state ions poses difficulties for probing with any 2-photon Raman or electromagnetically induced transparency (EIT) processes as well, pointing to the need for an alternative destructive direct detection mechanism for the ions with the present technology.

Chapter 4

Theory for Ultracold Homonuclear Ion-Atom Collision and Interaction

In order to devise the experiment for understanding ion-atom interactions in the quantum regime, it is imperative to understand what the two body ion-atom interaction is theoretically. The interaction between the ion and atom is mediated by the molecular ion potential. The bound states represent the the molecular ion, while the continuum states represent the interaction between the free ion and atom. Hence the entire interaction between the ion and atom is determined by the molecular potential and its scattering states, the knowledge of this becomes imperative. In this chapter we calculate the molecular potential for the Li(Lithium) ion-atom system and the scattering cross sections for this system as a function of collisional energy.

While previous calculations existed, we chose to perform our own calculations of molecular potentials, since the cross sections determined from the earlier calculations showed large variations at the very low energies, where quantum effects manifest. This effort also helped us understand the nuances of these calculations so that we could then appreciate how interactions/collisions occur at the lowest energies, where quantum effects manifest. Once this is understood, knowledge of the transport properties of the positive ions in a gaseous medium can also be understood, using the binary ion-atom interaction as its underpinning. This calculation therefore also forms the basis for the understanding of many problems in charge dynamics. It is possible to independently

probe and detect the ion species in many experiments, and this enables the study of the interactions between charged particles and neutral particles. For an atomic ion in a dilute atomic gas, the ion atom collisions are an available mechanism of interaction at all temperatures. For high energy collisions, an ion-atom collision involves many partial waves ℓ, and the well defined long-range nature of their interaction [31, 92] allows a semi-classical description of the collision. Semiclassical theories for collisions can compute the various possible collision outcomes, both elastic and inelastic, for high temperatures or high collision energies [83, 84, 92]. In this case, the scattering cross section for each channel is independently obtained and the resulting effects can be quantified.

Assuming that collisions are instantaneous, scattering cross sections signify the probability of occurrence of the particular channel of collisions. Any measurable phenomena that depends directly on the rate of specific collisions, can be obtained from the scattering cross sections. If the collisions are isotropic, other many body properties like diffusion coefficient, viscosity coefficient, can be obtained as a function of this scattering cross section. However, when the collisions are not isotropic, the corresponding cross section that determines each of these phenomena will have to be modified, and are known as diffusion cross section and viscosity cross section respectively [159]. The formalism for these cross sections and the resultant observable properties is well established for thermal gases [91].

At low temperatures, as only low energy collisions are allowed, the number of collision outcomes possible get limited. The short range nature of scattering potential becomes increasingly significant and full quantum treatment becomes essential and will be discussed in this chapter. The case of homonuclear ion-atom collisions is enriched by the presence of a symmetry against interchange of the ion and the atom. The calculation of collisional properties for Li^+-Li system and the resultant measurable parameters will be presented in later parts of this chapter.

4.1 Cold collisions

Experimental research on ion-atom interactions in dilute, trapped gas systems at ultracold temperatures is rapidly evolving towards detailed investigation of the quantum dynamics of the re-

sulting outcomes [13, 14, 16, 18, 21, 54, 56, 57, 78, 81, 160–163]. One of the main goals of cooling an atomic ion using ultracold atomic gas with collisions has been realized in many experimental configurations [14–16, 56, 161]. An atom and an ion mutually interact at large internuclear distance, R, through an attractive potential behaving as $\sim -\alpha_d/(2R^4)$, where α_d, the static dipole polarizability depends on the internal electronic state of the atom. The origin of this potential is that the atom, although neutral, gains an induced dipole moment as a result of the electric field due to the charged ion. This induced dipole is then attracted by the charge. However, at smaller internuclear separations, the ion-atom potential depends on the interaction of the electronic cores of the ion and atom. This is given by the corresponding electronic state potential energy curves of the molecular ion formed by the combination of this ion and atom [19, 21, 57, 90].

Despite continuous progress towards precise control of the trapped ion motion, reaching the ultralow relative energy regime ($E/k_B \approx 1\mu$K or lower) for ion-atom collisions remains challenging experimentally. At these energies, only the first few partial waves contribute significantly to the collision. More importantly, the contribution of these first few partial waves differs significantly from their semiclassical equivalents obtained using just the well defined long range interaction potential. Due to the limitations of ion cooling using in the presence of ultracold atoms and trap imperfections in dynamical trapping, it is experimentally advantageous if the full quantum regime can be realised at the highest possible temperatures [57, 90].

The centrifugal barrier induced by the angular momentum term for the p-wave ($\ell = 1$), which has a height equal to $1/(2\mu^2\alpha_d)$ (in atomic units of energy), signifies the ultimate energy limit for quantum collisions regime. This limit represented as a temperature is known as the s-wave limit, as only the $l = 0$ partial wave contributes to the collisions. As the p-wave angular momentum barrier will be high for low reduced mass, μ, choice of low mass atom and/or ion enables the possibility to probe the quantum collision regime at relatively higher collision energies. For this reason, lithium is implemented in several ongoing experiments [13, 17, 22, 164]. Most hybrid ion-atom trapping experiments use an alkaline-earth ionic species suitable for laser cooling. Although this aids the realization of low ion-atom collision energies, the choice of a heteronuclear ion-atom combination excludes the resonant charge exchange (RCE) channel, where an electron of the atom can be transferred to the ion in an elastic collision [14, 83, 161, 165].

In previous experiments [14, 77], our group has consistently exploited the RCE in the study of ion-atom collisions. We therefore focus this study on the scattering properties of Li^+-Li in the quantum regime. We consider the ultracold Li atoms in the ground electronic state and ignore the hyperfine interaction. This leaves only the elastic collisions possible as there will not be enough energy in the collisions to change the internal energy state of either of the colliding particles.

4.2 Li molecular ion potential energy curves

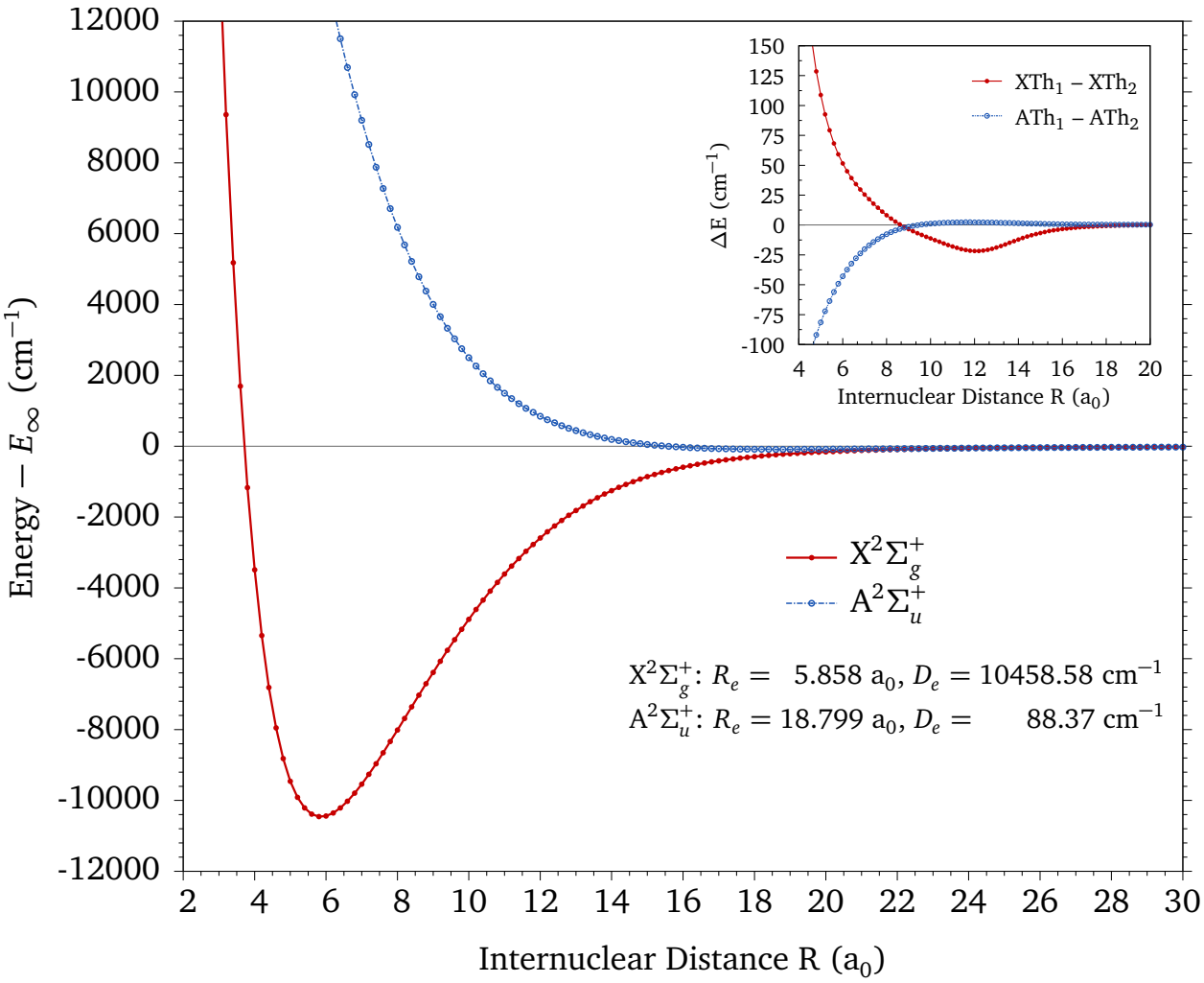

Figure 4.1: Li_2^+ potential energy curves $X^2\Sigma_g^+$ and $A^2\Sigma_u^+$, computed in the present work (MRCI-SD with aug-cc-pCV5Z basis set), and respectively denoted as XTh_1 and ATh_1 are shown. The energy differences ΔE with the curves calculated using the approach of (denoted by XTh_2 and ATh_2), are shown in the inset.

4.2.1 *Ab initio Born-Oppenheimer PECs*

We compute the *ab initio* potential energy curves (PECs) of the $X^2\Sigma_g^+$, the electronic ground state, and the $A^2\Sigma_u^+$, the first electronic excited state, of the Li_2^+ molecular ion using the MRCI method and the best available basis sets. The previous high quality calculations, report a significant discrepancy ($\approx$ factor of 2) between the calculations for a_g [17], the scattering length for the $X^2\Sigma_g^+$ state, which determines the low-energy ion-atom scattering cross section. These molecular ion *ab initio* PECs are smoothly matched to their physical asymptotic forms in the large-R range.

The $X^2\Sigma_g^+$ and $A^2\Sigma_u^+$ states of Li_2^+ under the Born-Oppenheimer approximation were calculated using the MOLPRO package [166]. This approach is variational and ensures convergence towards the best energies for both states with basis-set size. The PECs obtained with the largest available basis set, namely augmented Dunning correlation-consistent, polarized valence, 5-zeta basis set [aug-cc-pCV5Z] were calculated by Dr. Amrendra Pandey, who was a post-doctoral fellow in our group. The details of this calculation have been described in Pandey et. al [167]. While the PECs and phase shifts were calculated by Dr. Pandey, the entire problem was evolved and framed, and the potentials' asymptotic forms, the scattering formalism and computations were developed and done by me. Its consequences for the ion-atom collision problem was also studied by me.

The accuracy of the ultralow energy scattering parameters calculated using these PECs depends majorly on the precision of the PECs near the classical turning point. It has been inferred that the precision of the *ab initio* PECs in the small R regimes is questionable although their behaviour in this range is well captured. We have changed the classical turning point slightly to estimate the effect of the imprecise PECs. We assert that the maximum possible correction is the difference between the classical turning point obtained with the largest basis set (aug-cc-pCV5Z) and the smaller basis set (aug-cc-pCV3Z). We compute the resulting maximum inaccuracy in the scattering parameters calculation. Due to the large discrepancies between a_g values reported in the literature, we determine bounds for a_g so that the more precise calculations in the future should not supersede the conclusions drawn here.

Electronic State	E_∞ (a.u.)	ΔE_∞ (%)	E_e (a.u.)	ΔE_e (%)	R_e (a_0)	D_e (cm^{-1})	R_{in} (a_0)	aug-cc-pCVXZ basis sets, with X $\equiv$
$X^2\Sigma_g^+$	-14.73530934		-14.78224306		5.940	10300.76	3.758	D
	-14.75148110	0.1097	-14.79891577	0.1128	5.875	10410.70	3.723	T
	-14.75540520	0.0266	-14.80300996	0.0277	5.865	10448.03	3.715	Q
	-14.75673756	0.0090	-14.80438625	0.0093	5.858	10458.58	3.713	5
$A^2\Sigma_u^+$	-14.73530934		-14.73570944		18.939	87.81	15.630	D
	-14.75148110	0.1097	-14.75188381	0.1098	18.839	88.38	15.563	T
	-14.75540520	0.0266	-14.75580764	0.0266	18.818	88.32	15.545	Q
	-14.75673756	0.0090	-14.75714022	0.0090	18.799	88.37	15.540	5

Table 4.1: Dissociation limit, E_∞, its convergence with basis sets, ΔE_∞, total energy E_e at R_e, its convergence with basis sets, ΔE_e, equilibrium distance, R_e, well depth, D_e, and repulsive wall position R_{in} of the $X^2\Sigma_g^+$ and $A^2\Sigma_u^+$ PECs of $^7Li_2^+$. Results for various basis sets aug-cc-pCVXZ, with X $\equiv$ D, T, Q, 5 are displayed.

We then derive the phase-shifts characterizing the $^7Li^+$-^7Li collision as functions of the energy. The resulting scattering lengths a_g and a_u of the $X^2\Sigma_g^+$ and $A^2\Sigma_u^+$ states, respectively, are both computed to be positive with $a_g \gg a_u$. Our results are consistent with previous studies on the $X^2\Sigma_g^+$ and $A^2\Sigma_u^+$ PECs. We observe that the computed phase shifts are not as sensitive to many computational or second order corrections to the *ab initio* PECs as they are to the nature of curves in small-R region, due to the contribution of the core electrons. A convergence criterion is developed to bound the range of uncertainty within which the values of scattering lengths, a_g and a_u, are constrained. We then evaluate the total cross sections by computing the phase shifts, and finally provide recommended values for the cross sections and their bounds for the $^7Li^+$-^7Li system.

In order to provide a convergence criterion on potential energies, we compute the *ab initio* $X^2\Sigma_g^+$ and $A^2\Sigma_u^+$ PECs with a series of aug-cc-pCVXZ basis sets (with X $\equiv$ D, T, Q, 5) in the [2 a_0 - 50 a_0] internuclear distance range, with a 0.2 a_0 step. They correlate to the lowest asymptotic limit $Li^+(^1S_0)$ + $Li(^2S_{1/2})$. We report in table 4.1, the total potential energy at R $\rightarrow \infty$, i.e. dissociation limit, E_∞, and at the equilibrium distance, R_e, i.e. E_e, the well depth D_e = E_∞ - E_e, the position of the repulsive wall R_{in} at the dissociation limit. The relative change ΔE_∞ and ΔE_e of E_∞ and E_e with the increasing size of the basis set are also reported. The convergence of E_e for $A^2\Sigma_u^+$ curve is better than the one for $X^2\Sigma_g^+$ as they are computed at large internuclear separations where the electron correlation is better estimated even with smaller basis sets. The observed bound on the E_∞ indicates that molecular calculations of the Li_2^+ in the best limits will not result a bigger change in the well depth, D_e, of $X^2\Sigma_g^+$ than 10 cm^{-1} (difference between the D_e's obtained in X $\equiv$ Q and X $\equiv$ 5 cases) from the value obtained with aug-cc-pCV5Z basis set. Experimental value of the D_e, listed in table 4.2, also supports the above theoretical bound.

The *ab initio* $X^2\Sigma_g^+$ and $A^2\Sigma_u^+$ PECs, relative to E_∞ are shown in figure 4.1. The inset displays the difference between these PECs with the ones obtained from the method of based on the representation of the Li^+ cores by an effective core potential (ECP) and a core polarization potential (CPP) (referred as the Th_2 method), thus treating the Li_2^+ molecule as a one-electron system. The overall agreement is satisfactory between the two approaches, with the largest difference at 12 a_0 of about 1% in energy. Below 6 a_0, the difference is much larger, which can be understood as the ECP+CPP approach restrains the calculation from precisely representing the core-valence correlation at short

internuclear distances.

4.2.2 Determination of asymptotic extension of PEC's

The low-energy scattering wavefunctions need to be computed up to the large internuclear distances, with R $\gg \lambda$, where λ is the de Broglie wavelength of the colliding system (for $^7Li^+$-^{7}Li, 10 $a_0 < \lambda < 10^6$ a_0 for the collision energies 10^{-5}a.u. $> E > 10^{-15}$ a.u.). The *ab initio* PECs, in the large-R limit, become less accurate as the binding energy is comparable to the error in the absolute energy. Therefore we must use the asymptotic functional forms, $V_p^a(R)$, to extend the PEC's,

$$V_p^a(R) = V_{ind}^a(R) \mp V_{exch}^a(R); p \equiv \{g, u\}\,, \tag{4.1}$$

where g and u corresponds to $X^2\Sigma_g^+$ and $A^2\Sigma_u^+$ respectively. The asymptotic induction term, V_{ind}^a(R), contains the contribution of multipole interactions between Li^+ and Li and is expressed as

$$V_{ind}^a(R) = -\left[\frac{C_4}{R^4} + \frac{C_6}{R^6} + \frac{C_8}{R^8} + ...\right], \tag{4.2}$$

where C_4 = $\alpha_d/2$, C_6 = $\alpha_q/2$, C_8 = $\alpha_o/2$, with α_d, α_q, and α_o being the dipole, quadrupole, and octupole static polarizabilities of the ^{7}Li ground state atom. $\alpha_d = 164.161$ a.u., $\alpha_q = 1423.415$ a.u., and $\alpha_o = 39653.720$ a.u. The van der Waals interaction, varying as $1/R^6$, which is generally small for ion-atom cases, along with any other higher order effects, will be accounted for in the modified C_4 finally used in the scattering calculations.

The asymptotic exchange term reads,

$$V_{exch}^a(R) = \frac{1}{2}AR^\alpha e^{-\beta R}\Big[1 + \frac{B}{R} + \frac{C}{R^2} + ...\Big], \tag{4.3}$$

where the parameters $\alpha = 2.1774$ a.u., $\beta = 0.6294$ a.u., and $B = 0.5191$ a.u. are simple functions of the ^{7}Li ionization energy. The A and C parameters are obtained from the fits to the *ab initio* exchange energy, given by half of the difference of *ab initio* $A^2\Sigma_u^+$ and $X^2\Sigma_g^+$ PEC's with equation 4.3. The interval 23 a_0 < R < 28 a_0 is used in the fitting procedure, yielding $A = 0.133899$ a.u. and

$C = 27.7397$ a.u. This interval gives us the fit with the smallest relative residuals. The *ab initio* exchange energy intersects V^a_{exch}(R) at R = 25.6 a_0, which is selected as the point beyond which the asymptotic expansions of equations 4.2 and 4.3 are used.

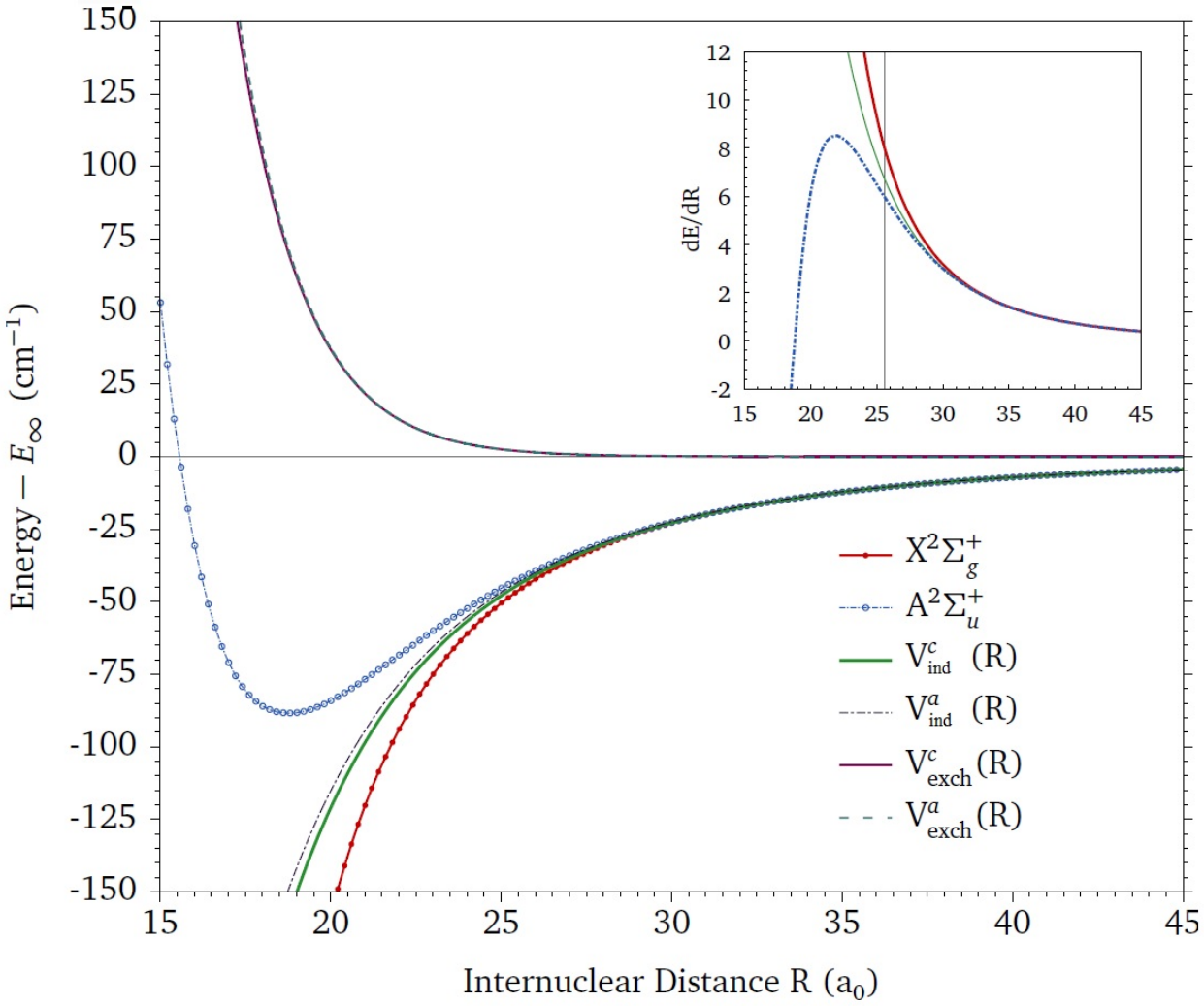

Figure 4.2: The asymptotically extended PECs $X^2\Sigma_g^+$ (full red line) and $A^2\Sigma_u^+$ (full blue line) of Li_2^+ are shown. The asymptotic induction and exchange functions, V^a_{ind}(R) and V^a_{exch}(R), the computed induction and exchange functions, V^c_{ind}(R) and V^c_{exch}(R), are plotted for the comparison. The first derivatives of $X^2\Sigma_g^+$ and $A^2\Sigma_u^+$ PEC's, and V^c_{ind}(R) are drawn in the inset.

V^a_{exch}(R) decays exponentially with R, and so in the large-R limit, only the contribution of V^a_{ind}(R) remains significant. Around 35 a$_0$, V^a_{exch}(R) becomes smaller than 0.1% of V^a_{ind}(R). Moreover, the contributions of the C_6/R^6 and C_8/R^8 terms become smaller than 1% of the induction energy beyond 29.5 a_0 and 12.5 a_0 respectively. E_∞ is obtained using a fit on the *ab initio* induction energy,

given by average of $A^2\Sigma_u^+$ and $X^2\Sigma_g^+$ PEC's, with the form given in the equation 4.2 using C_6 as a free parameter in the range 35-50 a_0. For a calculation with aug-cc-pCV5Z basis set, change in the E_∞ for different fit ranges, varying from 25-50 to 35-50 a_0, is ~ 0.02 cm^{-1}. After setting E_∞ as the origin of energies of the PECs, calculation of the extension of the potentials in the large R range is performed.

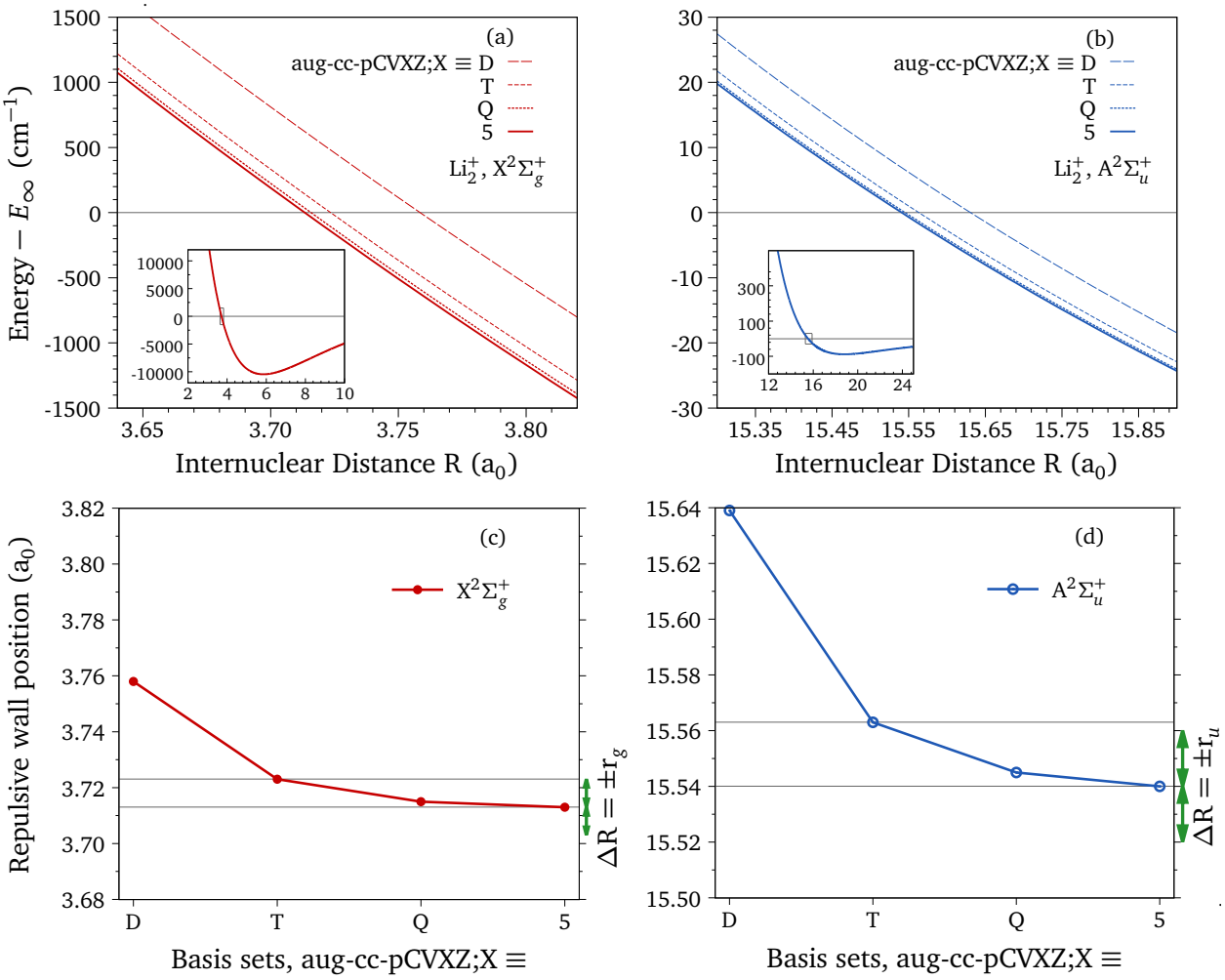

Figure 4.3: Potential energy curves near the repulsive wall (see insets) for $X^2\Sigma_g^+$ (a) and $A^2\Sigma_u^+$ (b), computed using basis sets aug-cc-pCVXZ with X ≡ D, T, Q, 5 and corresponding position R_{in} of their inner turning point at the dissociation limit E_∞ ((c) and (d)). The selected ranges ΔR for the variation of the repulsive wall of the aug-cc-pCV5Z calculations mimicking possible inaccuracies for cross section calculations are shown: $\Delta R = \pm r_{g,u}$ with r_g = 0.01 a_0 and r_u = 0.02 a_0 for $X^2\Sigma_g^+$ and $A^2\Sigma_u^+$ respectively.

In order to arrive at the large R extension of the potential, we work towards fulfillment of the following goals (i) keeping the PEC's and their derivatives continuous at R = 25.6 a_0, (ii) maintaining

half the difference of the PEC's equal to V^a_{exch}(R) for R≥25.6 a_0 and, (iii) as R $\rightarrow \infty$ the PEC's approach V^a_{ind}(R). First, a R dependent $1/R^4$ coefficient, C_4(R), is calculated using the *ab initio* PECs, C_6 and C_8 terms of V^a_{ind}(R) in the range 20 a_0 < R < 50 a_0, where the PECs can be well expressed as combinations of the asymptotic induction and exchange functions. Then, from the computed C_4(R), functional forms of the $\partial C_4/\partial$R, and C_4(R) are obtained.

The function C_4(R) in the large-R limit converges to the constant $C_4 = \alpha_d/2$. Also, the computed induction function, V^c_{ind}(R), with C_4(R) and $\partial C_4/\partial$R fitted to the *ab initio* PECs, implicitly includes the van der Waals dispersion contributions. The asymptotic induction and exchange functions, V^a_{ind}(R) and V^a_{exch}(R), the computed induction and exchange functions, V^c_{ind}(R) and V^c_{exch}(R), given by *ab initio* potentials for R≤ 25.6 a_0 and by their asymptotic extensions for R > 25.6 a_0 along with the extended potentials, V^c_g(R) and V^c_u(R), corresponding to $X^2\Sigma^+_g$ and $A^2\Sigma^+_u$ states, and their derivatives for the internuclear distance range 15-45 a_0 are shown in figure 4.2. The difference between V^a_{ind}(R), which uses a constant C_4, and V^c_{ind}(R), which uses a derived R-dependent function C_4(R), is quite evident in the 18-25 a_0 range (see figure 4.2). This procedure fixes in a consistent way the asymptotic form of the PEC's for reliable scattering calculations at extremely low energies.

4.2.3 Criterion for bounds on the scattering parameters

The large variation in the previously reported low energy ion-atom cross section values is indicative of it's strong sensitivity to the ab-initio PEC's. The low energy scattering solutions are found to be very sensitive to small changes in the repulsive wall of the molecular ion potential energy curves. To estimate this dependence a set of PECs for $X^2\Sigma^+_g$ and $A^2\Sigma^+_u$ are generated to estimate the uncertainty in the scattering parameters. The primary reason for small-R sensitivity is the increasing contribution of the core-electrons. For determining a set of PECs, the repulsive wall position of the $X^2\Sigma^+_g$ and $A^2\Sigma^+_u$ is used as a parameter for representing the change in the small-R region, i.e. $\forall$ R < R_e. The variation in the small-R region of the potentials as a function of the calculation accuracy can be estimated by comparing the D_e from the PECs obtained using different methods and basis sets (table 4.2), with our values computed with basis sets aug-cc-pCVXZ with X ≡ D, T, Q, 5 (table 4.1).

Table 4.2: Fundamental spectroscopic constants of the $X^2\Sigma_g^+$ and $A^2\Sigma_u^+$ PECs for Li_2^+. The label Exp. refers to the best available experimental determination, while the numbered Th labels refer to various theoretical determinations.

State: Work, Ref. No.	R_e (a_0)	D_e (cm^{-1})	ω_e (cm^{-1})	$\omega_e x_e$ (cm^{-1})	B_e (cm^{-1})
$X^2\Sigma_g^+$ state:					
Experiment [168, 169]	5.88	10464 ± 6	262.2 ± 1.5	1.7 ± 0.5	0.496 ± 0.002
This work, Th_1					
Theory [167]	5.858	10458.58	261.96	1.51	0.500
This work, Th_2					
Theory [167]	5.838	10515.76	262.54	1.50	0.503
Theory [170]	5.863	10439	262.58	1.58	–
Theory [171]	5.877	10457.7	261.6	1.47	–
Theory [172]	5.844	10498	263.39	–	–
Theory [173]	5.848	10475	264	1.94	0.506
Theory [17]	5.856	10441	263.76	1.646	0.5006
Theory [174]	5.826	10494	262.771	1.645	0.505
Theory [175]	5.899	10466	263.08	1.477	0.4945
Theory [176]	5.877	10457	266.2	–	0.4753
$A^2\Sigma_u^+$ state:					
This work, Th_1					
Theory [167]	18.799	88.37	16.15	0.84	0.0486
This work, Th_2					
Theory [167]	18.797	88.71	16.17	0.84	0.0486
Theory [170]	18.795	88	15.98	0.81	–
Theory [171]	18.798	88.4	16.63	1.05	–
Theory [172]	18.787	89	15.92	–	–
Theory [173]	18.729	88	15.81	0.74	0.049
Theory [17]	18.802	90	20.1	0.13	0.049
Theory [174]	18.763	89	16.312	0.750	0.0487
Theory [175]	18.899	90	16.01	0.79	0.049

Consequently, the difference between repulsive wall of PECs computed using aug-cc-pCV5Z and aug-cc-pCVTZ basis sets is taken as the permissible range of change in the wall positions of the PEC models with $\Delta R = \pm(r_g, r_u)$ with r_g = 0.01 a_0 for $X^2\Sigma_g^+$ and r_u = 0.02 a_0 for $A^2\Sigma_u^+$. The PECs for cross section bounds are created by linearly scaling the R coordinate of the *ab initio* curves, $\forall$ R $< R_e$, for the required change of ΔR = $\pm(r_g,r_u)$ at the repulsive wall position R_{in}. The scattering calculations are performed for the two bounding modifications to both $X^2\Sigma_g^+$ and $A^2\Sigma_u^+$ curves with suffixes ":ΔR = $\pm r_{g/u}$", and for *ab initio* curves denoted as ":ΔR = 0". In order to apply our methodology of bounds to scattering parameters, it is essential to perform the calculations in which all electrons of the molecular system are variationally optimized. Also, in ion-atom systems where next higher excited molecular ion PECs interact with the ground and first excited state, this interaction needs to be accounted for example for alkaline earth metal ions like Be, Ca, etc.

4.3 Collision cross sections

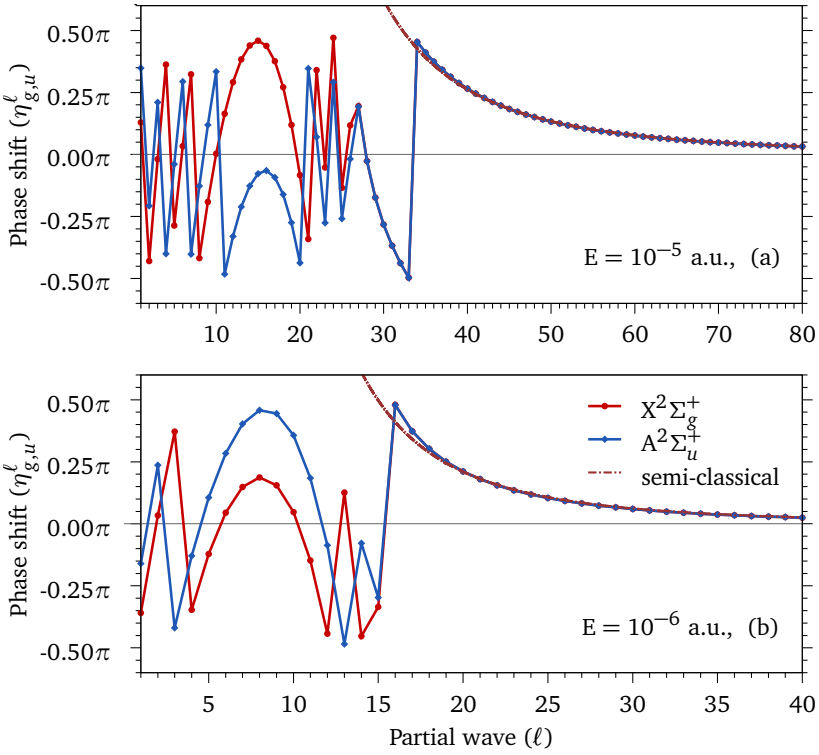

Figure 4.4: Quantum (modulo π) and semi-classical phase shifts as functions of the partial waves ℓ, for a collision along the $X^2\Sigma_g^+$:ΔR = 0 and $A^2\Sigma_u^+$:ΔR = 0 curves for the collision energies (a) 10^{-5} a.u., and (b) 10^{-6} a.u. The lines joining the points are a guide to the eye.

Applying standard scattering theory based on the partial wave expansion of the total wave function in R, the Schrödinger equation for a single partial wave, ℓ, at a collision energy $E = \hbar^2 k^2/(2\mu)$; $k = 2\pi/\lambda$ is

$$\left[-\frac{\hbar^2}{2\mu}\frac{d^2}{dR^2} + \frac{\hbar^2}{2\mu}\frac{\ell(\ell+1)}{R^2} + V_p^c(R) \right] y_p^{E,\ell}(R) \;=\; E\, y_p^{E,\ell}(R)\,, \tag{4.4}$$

where μ is the (^{7}Li$^+$-^{7}Li) Watson's charge-modified reduced mass, $p \equiv g, u$. The asymptotic form of the wave function $y_p^{E,\ell}$(R) is given by $y_p^{E,\ell}(\mathrm{R}) \simeq k\mathrm{R}[j_\ell(k\mathrm{R})cos(\eta_p^\ell) - n_\ell(k\mathrm{R})sin(\eta_p^\ell)]$, where $j_\ell(k\mathrm{R})$ and $n_\ell(k\mathrm{R})$ are the spherical Bessel functions, and η_p^ℓ is the quantum phase shift generated by the scattering potential V_p^c(R). Equation (4.4) is solved numerically, and η_p^ℓ is extracted at large distances, namely at R = 10λ as the asymptotic limit for low energies when $\lambda > 100\ a_0$, and at R = $1000\ a_0$ for higher energies when $\lambda < 100\ a_0$.

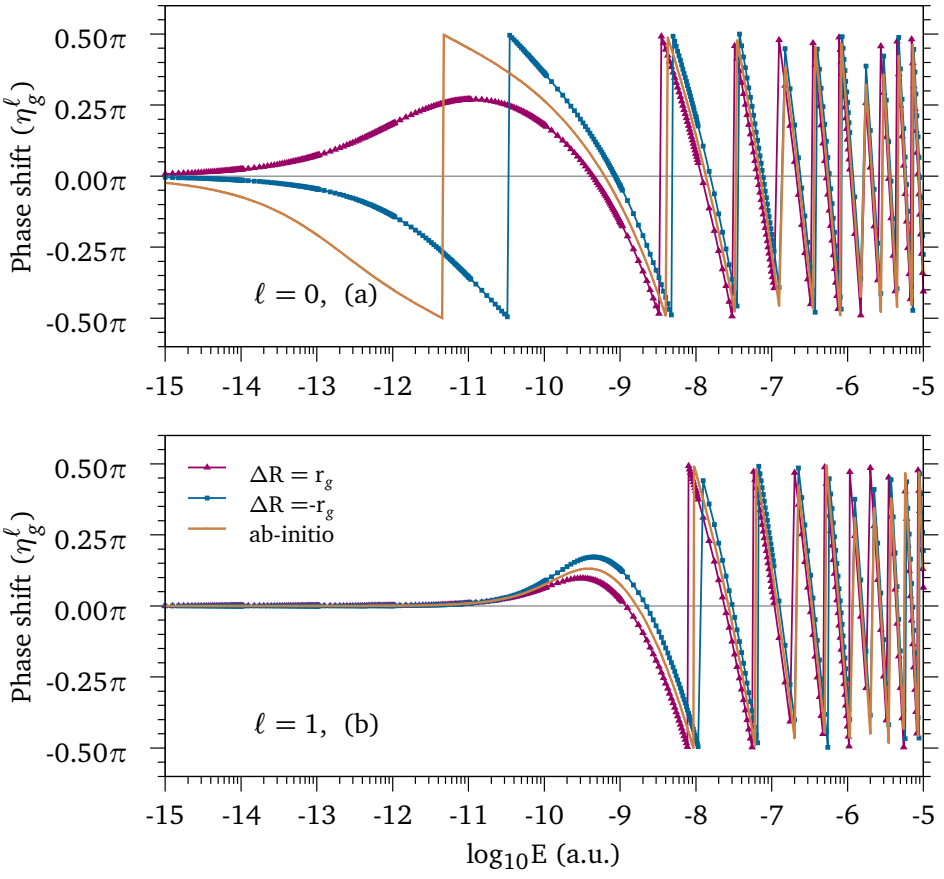

Figure 4.5: Quantum phase shift (modulo π) of the $X^2\Sigma_g^+$:ΔR = $\pm$r$_g$ and $X^2\Sigma_g^+$:ΔR = 0 curves as a function of the collision energy for the partial waves (a) $\ell = 0$, and (b) $\ell = 1$. At low energies, the change in the phase shifts for different PEC models are significant only for ℓ = 0.

In figure 4.5, the quantum phase shifts η_g^ℓ for $\ell = 0, 1$ are plotted as a function of the collision energy for the *ab initio* PEC and the generated PECs with shifted repulsive walls, $X^2\Sigma_g^+$:$\Delta R = \pm r_g$. At low energies, the effect is weak for $\ell > 0$ as the centrifugal barrier becomes dominant in the collision. Note that the s-wave ($\ell = 0$) phase shift changes sign when the repulsive wall is slightly shifted, indicating the presence of a pole where the scattering length diverges. As a result, the accuracy of the PEC becomes a major factor in determining the collision cross section. This is the primary motivation for the extreme care taken in determining the scattering potential in section 4.2.1.

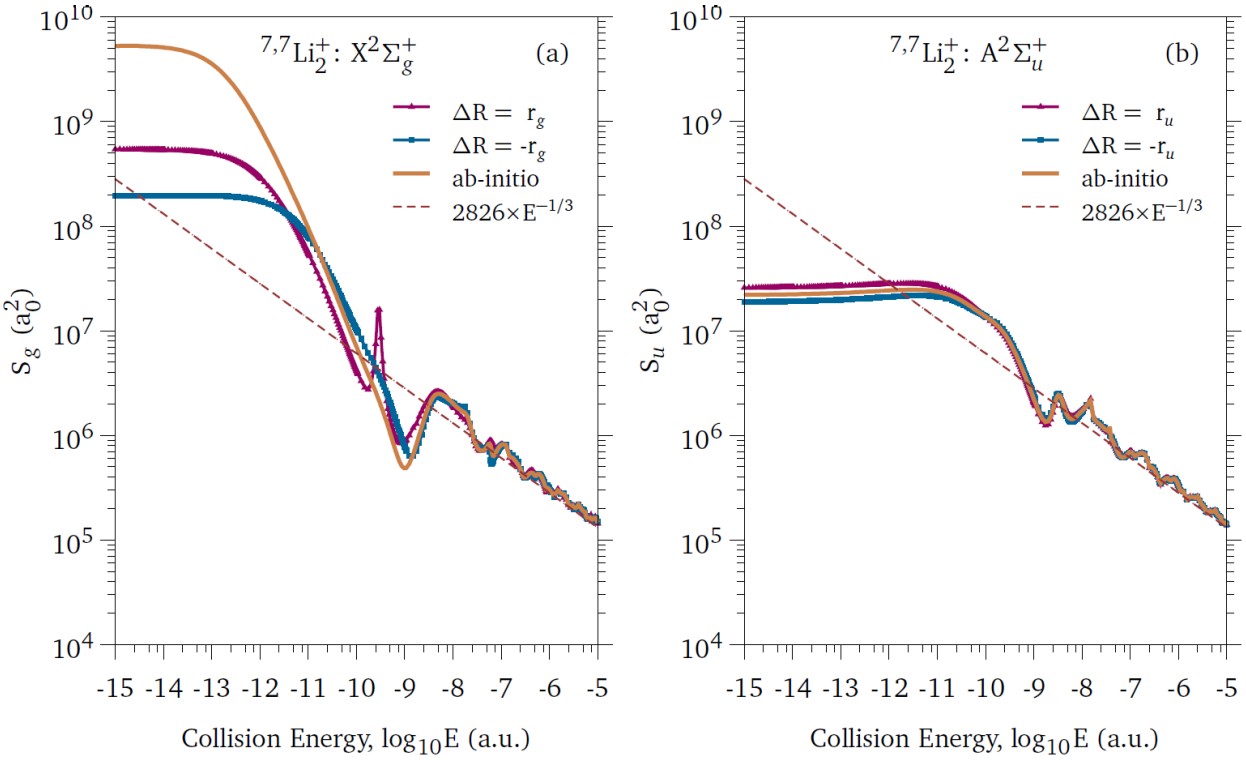

Figure 4.6: (a) S_g(E) for the generated $X^2\Sigma_g^+$:$\Delta R = \pm r_g$, and $X^2\Sigma_g^+$:$\Delta R = 0$ curves are plotted. (b) S_u(E) for the $A^2\Sigma_u^+$:$\Delta R = \pm r_u$ and $A^2\Sigma_u^+$:$\Delta R = 0$ are plotted. In (a),(b), the semi-classical cross section, $2826\times E^{-1/3}$, is shown.

In figure 4.4, the quantum phase shifts η_p^ℓ (modulo π) are shown for E $= 10^{-5}$ a.u. (or ~ 2 cm^{-1}), and E $= 10^{-6}$ a.u. (or ~ 0.2 cm^{-1}). For large ℓ, when the outer classical turning point at a given collision energy, is such that V_p^c(R) can be approximated to the leading term $-\alpha_d/2R^4$ of V_{ind}^a(R), one can define the semi-classical phase shift as $\eta_{sc}^\ell \approx (\pi\mu^2\alpha_d)/(4\hbar^4) \times E/\ell^3$ [165]. The semi-classical phase shifts are in agreement with the quantum phase shifts for $\ell > L_{sc}$, with $L_{sc} = 41$

for E = 10^{-5} a.u. and $L_{sc} = 19$ for E = 10^{-6} a.u. Around E = 10^{-8} a.u. (or ~ 0.002 cm^{-1}), the contribution to the cross section from partial waves $\ell > 10$ becomes negligible.

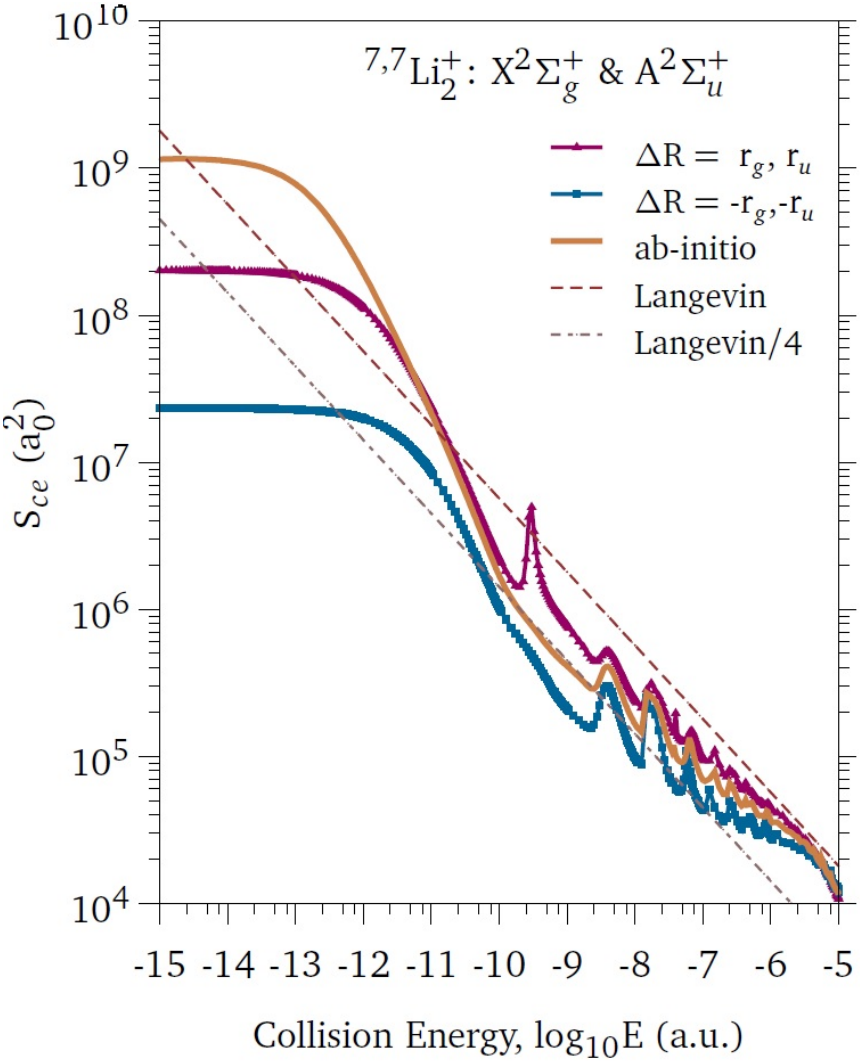

Figure 4.7: S_{ce}(E) for the two bounding modifications of PEC's, $X^2\Sigma_g^+$:ΔR = +r_g, $A^2\Sigma_u^+$:ΔR = +r_u and $X^2\Sigma_g^+$:ΔR = -r_g, $A^2\Sigma_u^+$:ΔR = -r_u, are shown along with the S_{ce} for $X^2\Sigma_g^+$:ΔR = 0, $A^2\Sigma_u^+$:ΔR = 0 curves. Langevin and Langevin/4 are also plotted for comparison.

The scattering between $^7Li^+$-^{7}Li ion-atom system has a symmetry with respect to identity exchange between the colliding partners. A scattering event when the initial identities are preserved is a direct elastic collision, whereas the event when the identities of the ion-atom pair are interchanged is termed as resonant charge exchange collision. The scattering amplitudes for $A^2\Sigma_g^+$ and the $A^2\Sigma_u^+$ potentials, are defined as f_g and f_u respectively. The scattering amplitudes for direct elastic and RCE collisions are given by $(f_g + f_u)/2$ and $f_{ce} = (f_g - f_u)/2$ respectively. We define

S_g(E) and S_u(E) in equation 4.5 and S_{ce}(E) in equation 4.6, where dΩ is the differential solid angle, as

$$S_p(E) = \int |f_p|^2 d\Omega = \frac{4\pi}{k^2} \sum_{\ell=0}^{\infty} (2\ell+1) sin^2(\eta_p^\ell)\,, \tag{4.5}$$

$$S_{ce}(E) = \int |f_{ce}|^2 d\Omega = \frac{\pi}{k^2} \sum_{\ell=0}^{\infty} (2\ell+1) sin^2(\eta_g^\ell - \eta_u^\ell)\,. \tag{4.6}$$

The average of S_g(E) and S_u(E) has been identified as total cross section and S_{ce}(E) as RCE cross section when certain high energy approximations are made. S_g(E) and S_u(E) for the $^7Li^+$-^{7}Li system as functions of the collision energy are shown along with the semi-classical scattering cross section, σ_{sc}(E), obtained using η_{sc}^ℓ, in figures 4.6.a and 4.6.b. For $^7Li^+$-^{7}Li, σ_{sc}(E) = 2826$\times$E$^{-1/3}$ a.u. The Langevin expression for $^7Li^+$-^{7}Li, 56.92$\times$E$^{-1/2}$ a.u., and Langevin/4 are shown along with S_{ce}(E) in figure 4.7. In all cases, cross sections include the sum of first 100 partial waves. It can be seen that S_{ce}(E), in this case, predominantly falls in the range defined by Langevin and Langevin/4. For low energies, S_{ce}(E) varies significantly from the expected semi-classical picture.

For homonuclear systems, in principle, individual scattering channels cannot be measured independently and therefore we compute the total cross section σ_{tot}(E), given in equation 4.7. The expression for σ_{tot}(E) differs from the one usually employed in the literature; the derivation will be discussed elsewhere. It has to be emphasized that usage of the expression in equation 4.6, or for that matter decoupling the direct elastic and RCE channels is incorrect for ultracold temperatures. The equivalences with the rightly evaluated cross sections in popular literature are accidental for those particular ion-atom species [83].

$$\sigma_{tot}(E) = \frac{4\pi}{k^2}\Bigg[x\Big[\sum_{even\,\ell's} (2\ell+1) sin^2(\eta_g^\ell) + \sum_{odd\,\ell's} (2\ell+1) sin^2(\eta_u^\ell)\Big] + (1-x)\Big[\sum_{odd\,\ell's} (2\ell+1) sin^2(\eta_g^\ell) + \sum_{even\,\ell's} (2\ell+1) sin^2(\eta_u^\ell)\Big]\Bigg]\,, \tag{4.7}$$

where x is a function of the nuclear spin I. For a half-integer nuclear spin, $x = I/(2I+1)$. For ^{7}Li, with $I = 3/2$, x is 3/8. The cross section evaluated using equation 4.7 differs significantly in the s-wave limits with the value calculated as the average of S_g(E) and S_u(E). For $^7Li^+$-^{7}Li, in the s-wave limit, cross section obtained using σ_{tot}(E) decreases by 25% of the average of S_g(E) and S_u(E). The σ_{tot}(E) for the $^7Li^+$-^{7}Li is plotted along with the semi-classical scattering cross section, σ_{sc}(E), in figure 4.8. Centrifugal barrier energies of the first few partial waves are also shown.

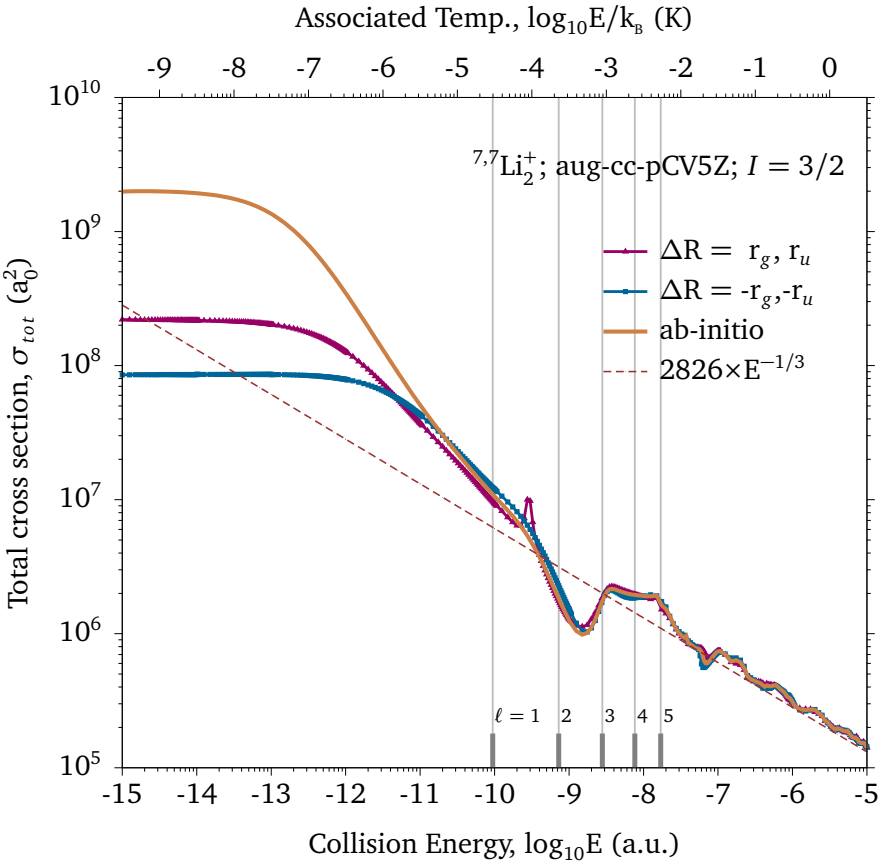

Figure 4.8: The total collision cross section, σ_{tot}(E), of the $^7Li^+$-^{7}Li system in its first asymptotic state, which involves the electronic states $X^2\Sigma_g^+$ and $A^2\Sigma_u^+$ are shown for the modified PECs X/A:ΔR = $\pm$(r_g,r_u), and X/A:ΔR = 0. The semi-classical cross section, 2826×$E^{-1/3}$ and the centrifugal barrier energies for ℓ = 1-5 are also shown.

Scattering length a_u, when compared with the characteristic interaction length scale R*, i.e. position of the ℓ = 1 barrier $(\alpha_d \times \mu/\hbar^2)^{1/2}$, which for $^7Li^+$-^{7}Li is 1024 a_0, seems typical, while a_g is very large, see table 4.3. Also, S_g(E) and a_g are more sensitive to the small-R region of the PEC and consequently to the core-electron contributions than S_u(E) and a_u. This sensitivity for the g-state

is amplified for $^7Li^+$-^7Li system, which is also noted by Schmid *et al.* [17], due to proximity of a scattering pole, i.e. the PEC has either about to acquire or just acquired a very weakly bound state.

$X^2\Sigma_g^+$, $A^2\Sigma_u^+$	$\Delta R = \pm r_{g,u}$	$\Delta R = 0$	Zhang *et al.* [171]	Schmid *et al.* [17]
a_g	-6582/3948	20465	14337	7162
a_u	1432/1227	1325	1262	–

Table 4.3: $^7Li^+$-^7Li scattering lengths for the modeled $X^2\Sigma_g^+$:$\Delta R = \pm r_g$, $X^2\Sigma_g^+$:$\Delta R = 0$ and $A^2\Sigma_u^+$:$\Delta R = \pm r_u$, $A^2\Sigma_u^+$:$\Delta R = 0$ curves are listed. For direct comparison with Zhang *et al.* [171] and Schmid *et al.* [17], the values obtained from X/A:$\Delta R = 0$ are appropriate.

The values of D_e calculated by Zhang *et al.* [171] and Schmid *et al.* [17] along with the value calculated in this work (table 4.2), fall within the experimental accuracy of 10464 $\pm$ 6 cm^{-1}. However, convergence of E_e and E_∞, and variational nature of the calculation provide additional certainty in our case. The constant shift due to relativistic corrections in the total energy does not affect the scattering calculations. This is because the absolute value of the PEC is not used in the scattering calculation, but the relative difference between the potential and E_∞ is used and therefore constant shifts do not contribute to the relative difference.

We find that $^7Li^+$-^7Li system in the $X^2\Sigma_g^+$ state is close to a scattering pole, and therefore extreme care is required in the computation of low energy scattering parameters. Scattering lengths for $X^2\Sigma_g^+$:$\Delta R = 0$, and $A^2\Sigma_u^+$:$\Delta R = 0$ are 20465 a_0 and 1325 a_0 respectively, (see table 4.3). Scattering length, a_g, reported by Zhang *et al.* [171] and Schmid *et al.* [17] are 14337 and 7162 a_0 respectively. Schmid *et al.* [17] also provides a bound on a_g as (107825 a_0; 3664 a_0) that corresponds to the potentials scaled by (0.999; 1.001) to the computed PEC.

The possible errors in the cross section are estimated by controlled variations in the small-R region of the PECs, assessing the change they bring to the phase shifts and cross sections in the low energy limit. The scattering pole for $X^2\Sigma_g^+$ occurs within the determined range of variations as shown in the figure 4.3, particularly in between the PEC models $\Delta R = +r_g$ and :$\Delta R = 0$ which is also evident in the phase shift plot, figure 4.5, which prevents us from estimating the upper limit of the total cross section.

However, the lower limit of the total cross section is given by the ΔR = -r_g,-r_u curve. The setting of this range will guard the values reported here against even more sophisticated calculations in the future. The calculated value of the total cross sections is shown by the :ΔR = 0 curve in figure 4.8. The cross sections are determined for a wide range of collision energy, from 10^{-5} to 10^{-15} a.u., which covers a large range of temperatures from few Kelvin (k) to few nano-Kelvin (nK).

S_g(E), S_u(E), S_{ce}(E), and σ_{tot}(E) in the temperature regimes below a few milli-Kelvin (mK), have contributions only from few partial waves (about 5). In this regime, we observe that the cross sections deviate from the semi-classical values, and result in the distinctive features that can be explored in the future experiments. The total cross section for $^7Li^+$-^7Li system in the low energy limit is 1.9×10^9 a_0^2. When the collision energy is larger than a few mK, many partial waves participate in the scattering and their contributions sum up to give the semi-classical value.

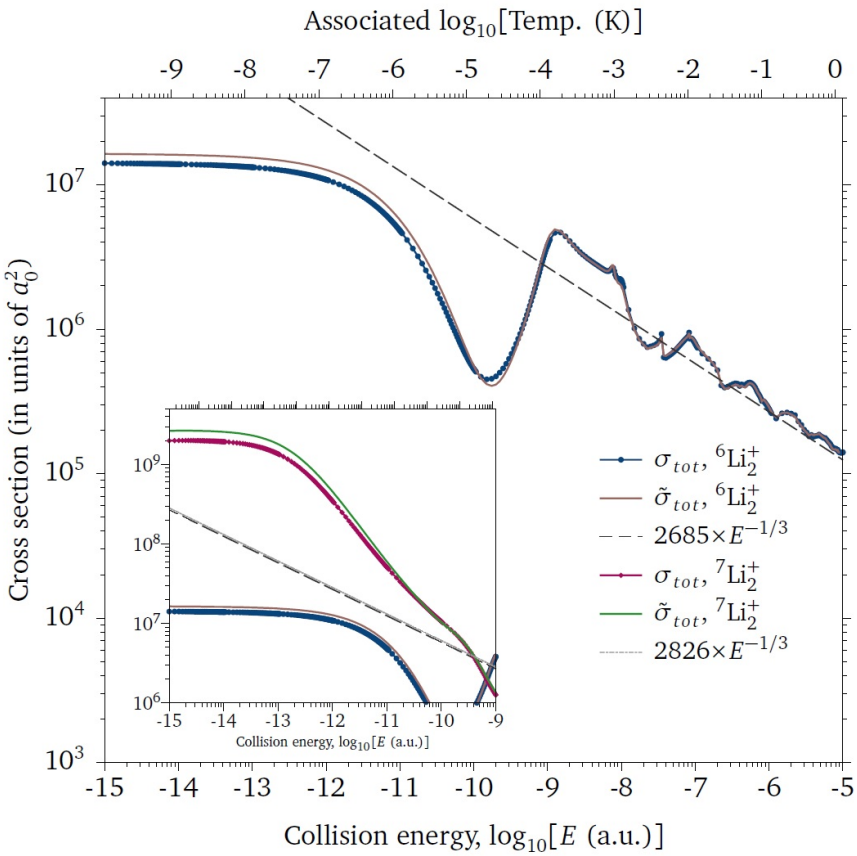

Figure 4.9: σ_{tot} obtained from partial wave method (full quantum treatment), is plotted along with the high energy approximate $\tilde{\sigma}_{tot}$, and the semi-classical result for ion-atom collision cross section for both $^7Li^+$-^7Li and $^6Li^+$-^6Li systems.

Our results for $^6Li^+$-^6Li system, on the other hand retrieve a narrow possible range for the collision parameters, see figure 4.9. This is mainly because for this isotope mass, the system is far from scattering poles. Therefore although, the same PECs with the same inaccuracies are employed for evaluating the cross sections, the allowed values for scattering length are positive definite and of the order of the characteristic collision length.

However, the ^6Li isotope is a fermion with nuclear spin 1. The right usage of equation 4.7, gives us a difference of ≈10% in the value of total collision cross section. While the agreement of the cross sections calculated by the inappropriate approximation ($\tilde{\sigma}_{tot} = (S_g + S_u)/2$), is better for the ^6Li isotope, the other popularly misapplied result of diffusion cross section being twice of $S_{ce}(E)$ is seen to be invalid over a very large range of low energies in this case, see figure 4.10.

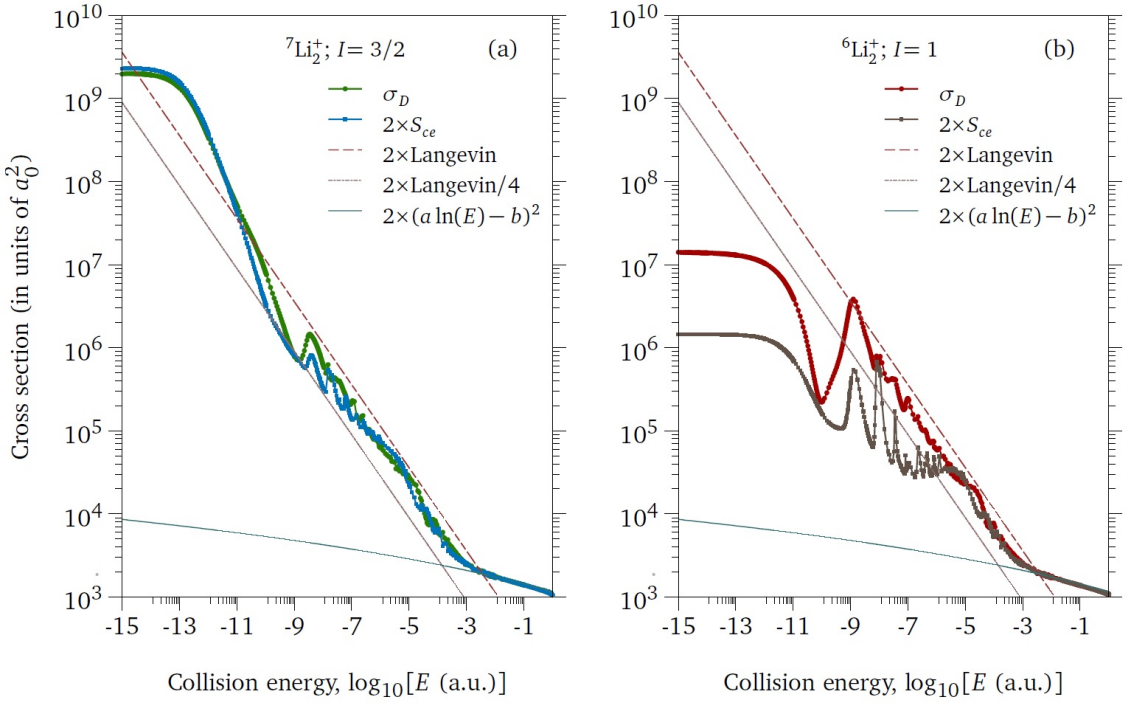

Figure 4.10: The comparison of the diffusion cross section obtained from partial wave method (full quantum treatment), with the twice of S_{ce} as done conventionally for high energy collisions, Langevin, Langevin/4, and classical high energy expression for exchange form is shown for the $^7Li^+$-^7Li system in panel (a), and for the $^6Li^+$-^6Li system in panel (b).

The remarkable differences in the shape resonances and features on the cross section curves, for

the two isotopes must be noted in figure 4.10. In fact the total cross section given by equation 4.7, is a sum over the contributions from many partial waves (l's). The contribution of the s-wave (l=0 partial wave), is constant for very low energies and it diminishes quickly as the collision energy approaches the p-wave (l=1) barrier energy. The contributions to total cross section from partial waves with nonzero l's, have a characteristic feature of being maximum for collision energies between l^{th} wave barrier energy and l+1^{th} wave barrier energy. The width of these resonances is a topic of interest and further study. When the gap between these resonances is larger than their widths, the total cross section curve features large dips and peaks, such as the ones in figure 4.10(b). Wider resonances and small gaps between them result in less pronounced shape effects in the total cross section. For collision energies much less than the l=1 wave barrier, the total cross section is just the contribution from the l=0 wave, and it is constant and isotropic. The value of this constant cross section depends on the vibrational structure of the PECs, which is a natural property of the atom we choose. For higher collision energies, the contribution of many partial wave contributions gets merged as the resonances are not well separated. In this regime, the quantum mechanical solutions to cross sections obtained through partial wave analysis show good behavioral agreement with the Langevin curves. At even higher energies there is excellent agreement with semi-classical solutions, as expected.

4.4 Experimentally relevant collision parameters

4.4.1 Collision rates

One of the measurable quantity in low energy collision experiments is the collision rate coefficient, which is defined as the collision rate per atom number density. In some well characterized experiments, measurement of atom number loss rates can be correlated to an average collision rate [75, 77, 89]. We have calculated these quantities for our lithium ion-atom systems as a function of the temperature of the atom cloud. The thermal average collision rates, plotted in figure 4.11 are evaluated using Maxwell-Boltzmann velocity distributions for the atoms.

Since the average collision rate coefficient is proportional to the cross section and the velocity of

the particles, we observe that $^7Li^+$-^7Li system which has higher low energy cross sections, has a larger collision rate. In addition, the shape resonances discussed in the previous section result in local features in the curves.

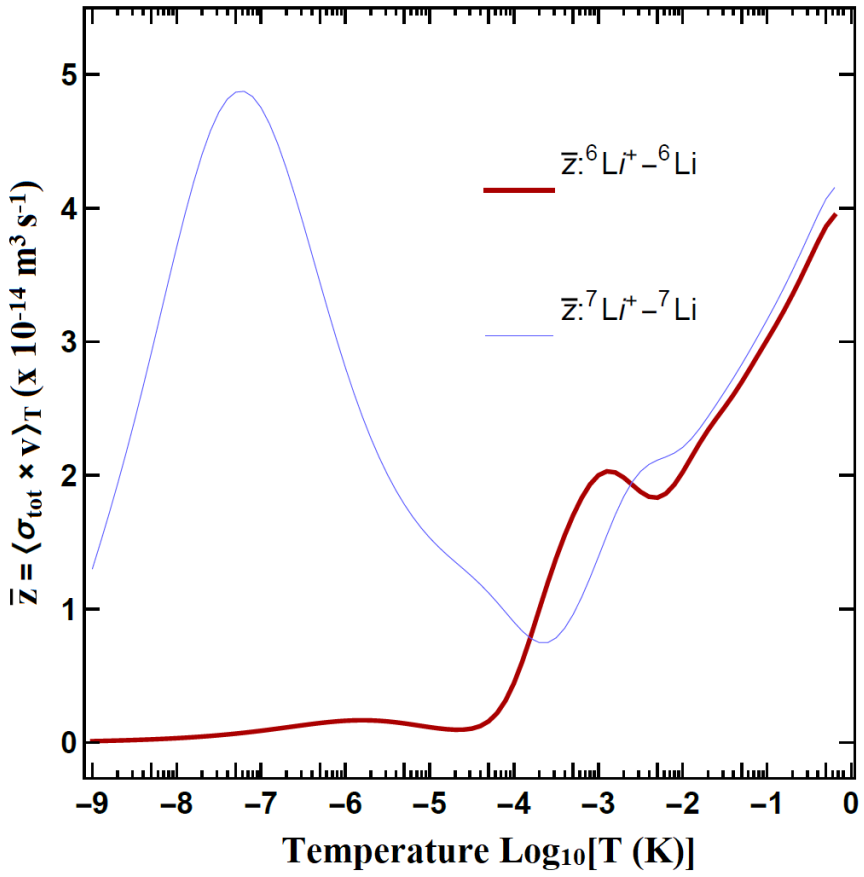

Figure 4.11: Figure shows the collision rate coefficient for $^7Li^+$-^7Li and $^6Li^+$-^6Li systems over a range of temperatures.

4.4.2 Collisions limited ion diffusion

Another experimentally measurable quantity in some scattering systems is the collisional diffusion coefficient, D_{coll}. the collision cross section which is relevant to evaluate the diffusion is called as the diffusion cross section which is different from the total collision cross section, for anisotropic collisions [83, 159]. The collisional diffusion coefficient is a measure of the limitation posed for the mobility of the ion in the medium of atoms due to collisions. This sets the maximum speeds allowed for an ion in the atomic cloud. We evaluate this quantity as a function of atom temperature,

using the thermal averaging method mentioned above and the results are shown in figure 4.12.

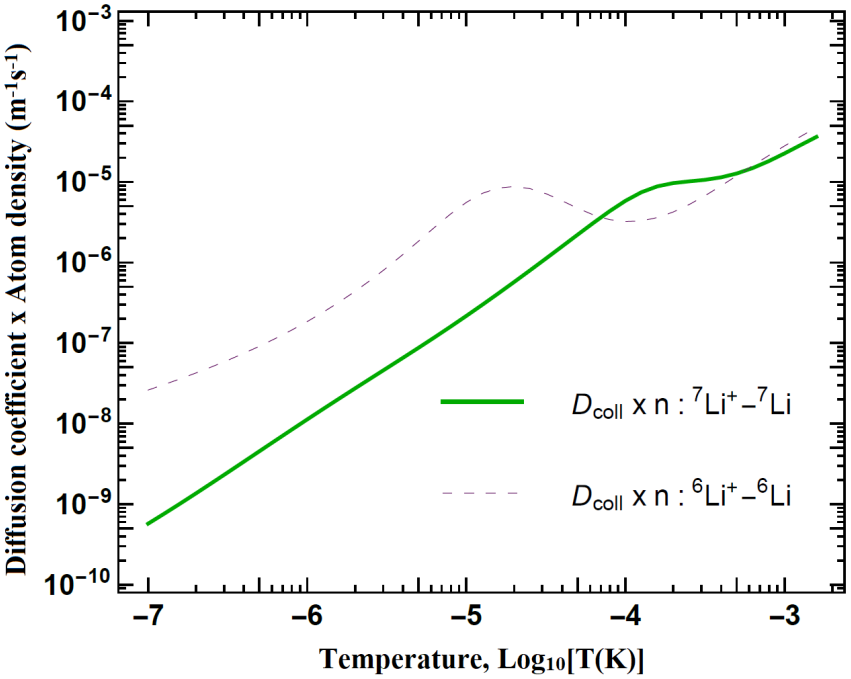

Figure 4.12: Figure shows the plot for ion diffusion coefficient due to ion-atom collisions times the atom number density as a function of temperature.

Diffusion coefficient is inversely proportional to the diffusion cross section, and therefore we see the reverse trend of the one in collision rates plotted in figure 4.11. This is expected, as the large number of collisions with atoms, restrict the ion from diffusing quickly in the atom cloud.

4.5 Summary

We calculate the isotope independent Li^+-Li potential energy curves for the electronic ground and first excited states. Scattering phase shifts and total scattering cross section for the $^7Li^+$-^7Li collision are calculated with emphasis on the ultra-low energy domain. The effect of physically motivated alterations on the calculated potential energy curves is a device used to bound the accuracy of the low energy scattering parameters for this system. It is found that the scattering length for the $A^2\Sigma_u^+$ state, a_u = 1325 a_0, is positive and has well constrained bounds. For the $X^2\Sigma_g^+$ state, the scattering length, a_g = 20465 a_0 has large magnitude as it is sensitive to the bounded

change of the potential, due to the presence of a vibrational state in the vicinity of the dissociation limit. It is easier to estimate collision cross sections for the $^6Li^+$-^6Li system with much better accuracy. The diffusion cross sections evaluated for this system makes it abundantly clear that the approximate relation between σ_D and S_{ce} does not hold even for temperatures as high as 10 Kelvin, thereby invalidating the generalizations prevalent in the literature for cold collisions.

Chapter 5

Charge Hopping in Ion-Atom Systems and its Consequences for Charge Diffusion

Interchange symmetry in particles which can swap identity, by exchanging a constituent sub-particle between them, plays critical and specific roles across physics. In the previous chapter, collisional transport properties of ions in an ultracold gas were explored. The full quantum treatment for homonuclear ion-atom scattering which is relevant below temperatures of few milli-Kelvin (mK) was described. We have demonstrated that the resonant charge exchange and direct elastic collisions are completely indistinguishable. The resulting effect on the collisional diffusion of an ion in ultracold atoms was shown. In this chapter, we explore the another kind of interaction between ions and their neutral parent atoms in the ultralow energy regime, which is not collisional in nature.

At lower temperatures and increased densities, due to increasing uncertainty in positions, partial overlap of the position distributions of different particles is achieved. The large spread of atom and ion thermal de Broglie waves allow electrons to hop from atoms to nearby ions even when they are not in collisional proximity [165]. At such low temperatures, electron hopping provides

an efficient charge diffusion in the neutral gas, as the ion-atom system becomes effectively conducting. This can be seen as analogous to hopping conductivity in doped semiconductors, where electrons hop from impurity atoms [92, 165].

The presence of this interchange symmetry has been shown to have some effect only in collisions where the ion and atom come close to each other [11, 14, 70, 75, 78, 80, 82, 162, 177]. The charge exchange for large ion-atom separations is highly improbable due to large electron binding energies in atoms. Here we theoretically study the dominance of charge hopping in the diffusion of a single ion in an ultracold parent atom gas, at appropriate temperatures and atom number densities. We compute the charge diffusion in this system for conditions where the collisional and the hop processes occur independently. The measurable signatures of the charge hopping phenomena in experiments are identified.

We present a theoretical formalism, consistent with early calculations, motivated by the state of art experimental ability to probe exotic phenomena of quantum dynamics for ion(s) in ultracold atoms [21, 31, 92, 165, 178]. This formalism of charge hopping dynamics as a result of ion and atom delocalization is purely quantum mechanical. We conclude that the experimental conditions needed to resolve this phenomena are challenging but accessible. Recent technological advances in the field of ultracold hybrid ion-atom systems [15, 29, 30, 57, 82] permit the study of such systems with precision and control. We present a first principles theoretical formalism which describes the consequences of charge hopping in 3 dimensions, motivated by the state of art experiments to probe the quantum dynamics for ion(s) in ultracold atoms [16, 19, 20, 179]. This sets the agenda for the experiments we have built at the Raman Research Institute.

This mechanism of electron hopping and its consequences for charge transport have been studied by Robin Côté [165] in 1 dimension, wherein some inconsistent application of concepts relevant only to collisional charge exchange was done. In this work, the author has outlined the possibility of seeing charge conductivity due to hopping as opposed to the ion's diffusive mobility, in an ultracold gas of atoms. The principle mechanism for such a process is proposed to be led by the quantum delocalization of ultracold particles. However, this initial study uses the length scale obtained using charge exchange cross sections (which itself is inconsistent for ultracold systems,

as argued in chapter 4), as a proxy for distance over which spontaneous exchange is allowed, to evaluate ballpark hopping based charge conductivity. This evaluation, while seminal, also implements a number of approximations which cannot be guaranteed for many real systems, apart from assuming thermal gas behaviour irrespective of temperatures and densities. In order to assess whether such a phenomenon of hopping conductivity is experimentally observable, it is important to go beyond the formalism of Côté [165], and make a complete analysis for real systems, with consistent approximations. This is described in the rest of the chapter, and its conclusions for the experiments presented.

We analyze the proposed delocalization led charge hopping, as an independent mechanism, from first principle in a self consistent way, so that it can be applied to real experimental scenarios. The results from this analysis point to important and new perspectives in dilute gas ion-atom physics. Lithium (Li) offers the best atomic choice, as it is easily laser cooled and its light mass implies that the delocalization for a given temperature is large, than for heavier atoms. This makes lithium suitable for studying ultracold homonuclear ion-atom interactions, both collisional as well as charge hopping based. For lithium ion-atom system, we show that charge hopping dominates over collisions in experimentally accessible regimes, which leads to the trapping of the ion in a 3D Gaussian distribution of atoms.

5.1 Formalism for charge hopping

Consider a single positive ion (A^+), created by threshold ionization from an ultracold, dilute, non-degenerate atomic gas ensemble of its parent atoms (A). In this case, any atom paired with the ion has inversion symmetry. The consequence of this symmetry is that the charge can hop between the components of the pair. This hopping has a probability which depends on the exchange energy of the ion-atom pair, the velocities of the ion-atom pair (or the temperature for a thermalized pair), and the distance between their mean positions. We need to use the mean measurable positions for the particles as we are dealing with delocalized quantum particles. In this situation, the charge can hop sequentially between atoms in the ensemble of atoms. This allows us to ask the question; "where will the charge be located if measured after a time t, given its mean position at $t = 0$?"

The answer to this question encompasses the stochastic scattering from both collisional diffusion as well as charge hopping led diffusion. Below we develop the formalism to study this.

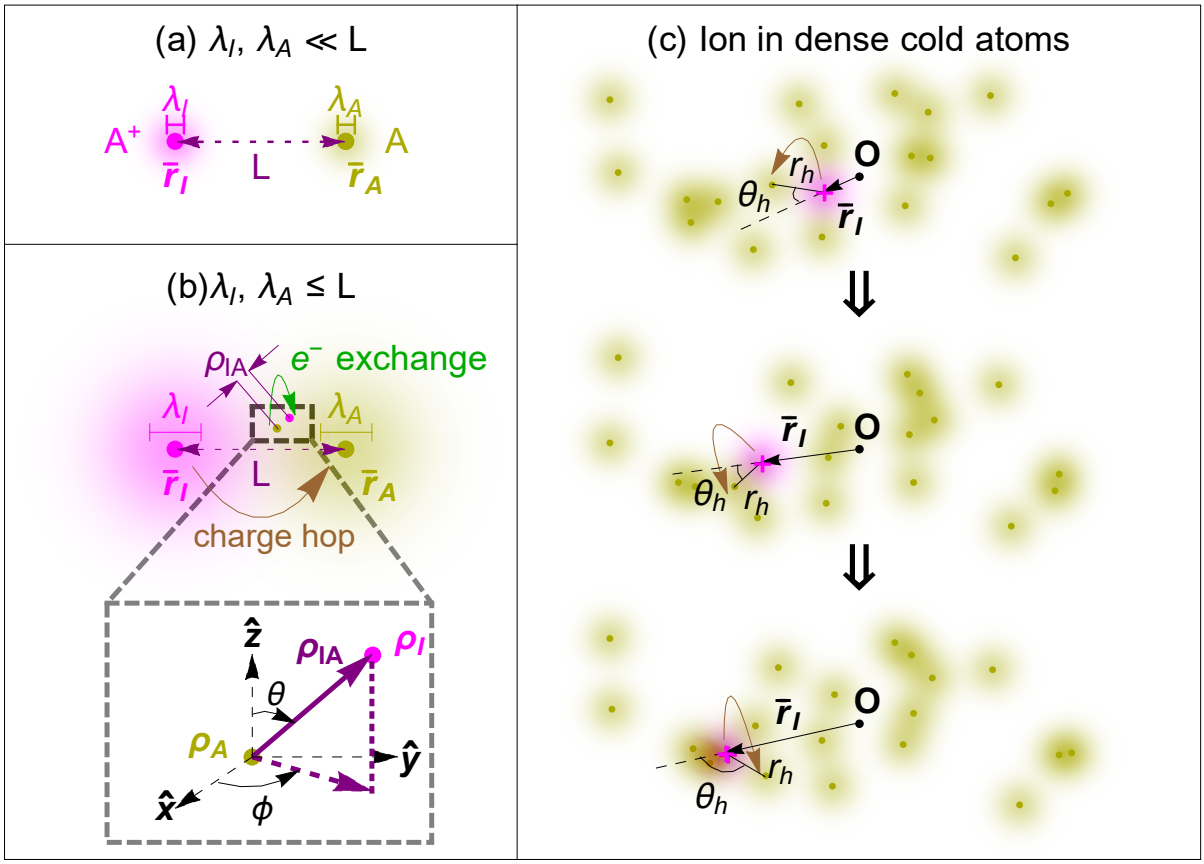

Figure 5.1: Panel (a) illustrates the condition where $\lambda_T \ll L$, where charge hopping is very unlikely as the atom and ion are well separated and although cold and delocalized, present a very small probability for charge hopping. Panel (b) illustrates the case when $\lambda_T \leq L$ where the delocalized ion and atom start overlapping and the charge hop becomes probable. The blue and red dot represents the instantaneous positions of the ion and atom at the time of charge hop, while their average separation is L. The bottom frame shows the post hop atom and ion. In panel (c) the sequential charge hops in a cloud of atoms is illustrated. In this situation charge hop with many nearby atoms is probable leading to charge transport. In successive frames in (c), the atoms are depicted in relative motion and therefore show small displacement and reordering. The symbols are self explanatory and are used in the mathematical development below.

5.1.1 Probabilistic instantaneous separation

The thermal de Broglie wavelength for atoms in a thermal ensemble, $\lambda_A = h/\sqrt{2\pi\, m\, k_B\, T_A}$, is a measure of the uncertainty in position or delocalization of an atom, where m is the mass and T_A

is the temperature of the atoms, k_B is the Boltzmann constant and h is the Planck's constant. This delocalization is isotropic and does not change in time for a thermal ensemble. Let us represent the delocalization of the ion as λ_I, see figure 5.1 for the depiction of the various length scales, conventions and parameters. The probability distribution for position of the atom and the ion, p_A and p_I, are 3 dimensional Gaussian functions centered at their respective mean positions, $\vec{r}_A$ and $\vec{r}_I$ with isotropic spread of λ_A and λ_I respectively as shown below

$$p_A(\vec{r}) = (2\pi\lambda_A^2)^{-3/2} \exp\left[-\frac{|\vec{r}-\vec{r}_A|^2}{2\lambda_A^2}\right], \tag{5.1}$$

$$p_I(\vec{r}) = (2\pi\lambda_I^2)^{-3/2} \exp\left[-\frac{|\vec{r}-\vec{r}_I|^2}{2\lambda_I^2}\right]. \tag{5.2}$$

While the separation in the mean values of the ion and the atom position distributions is $L = |\vec{r}_A - \vec{r}_I|$, the effective instantaneous separation, ρ_{IA} could vary from 0 to ∞ as a result of the Gaussian nature of delocalizations. The probability distribution for the instantaneous separation between the ion and atom, ρ_{IA} is given by combined probability that the instantaneous position of the ion is $\vec{r}$ and the instantaneous position of the atom is $\vec{r}'$ such that $|\vec{r}' - \vec{r}| = \rho_{IA}$, given by

$$P_{IA}(\rho_{IA}) = \int_0^\infty p_I(\vec{r}) \left[\int p_A(\vec{r} - \vec{\rho}_{IA})\, \rho_{IA}^2\, d\Omega\right] d^3r\,, \tag{5.3}$$

where $\vec{\rho}_{IA}$ of magnitude ρ_{IA} is directed along the unit vector $\hat{\Omega}$. Let us write the instantaneous positions as $\vec{r} = (x, y, z)$, $\vec{r}' = (x', y', z')$ and define the angles defining the unit vector $\hat{\Omega}$ as θ, ϕ such that $(x', y', z') = (x - \rho_{IA}\sin\theta\cos\phi, y - \rho_{IA}\sin\theta\sin\phi, z - \rho_{IA}2\cos\theta)$, we get

$$P_{IA}(\rho_{IA}) = \iiint_{x,y,z=-\infty}^{\infty} dx\, dy\, dz\; p_I(x,y,z) \int_{\theta=0}^{\pi}\int_{\phi=0}^{2\pi} p_A(x',y',z')\, \rho_{IA}^2\, \sin\theta\, d\theta\, d\phi\,. \tag{5.4}$$

Since this distribution does not depend explicitly on the mean position of the atom and ion, but depends only on their separation L, we set $\vec{r}_A = (0,0,0)$ and $\vec{r}_I = (L,0,0)$ and without loss of

generality, we get

$$P_{IA}(\rho_{IA}) = \iiint_{x,y,z=-\infty}^{\infty} \int_{\theta=0}^{\pi} \int_{\phi=0}^{2\pi} \exp\left[\frac{-((x-L)^2+y^2+z^2)}{2\lambda_I^2}\right] \exp\left[-\frac{x'^2+y'^2+z'^2}{2\lambda_A^2}\right] \times \frac{\rho_{IA}^2 \sin\theta}{(2\pi\lambda_I\lambda_A)^3}\, dx\, dy\, dz\, d\theta\, d\phi\,. \quad (5.5)$$

This can be rearranged as

$$P_{IA}(\rho_{IA}) = \int_{\theta=0}^{\pi} \int_{\phi=0}^{2\pi} \frac{\rho_{IA}^2 \sin\theta}{(2\pi\lambda_I\lambda_A)^3} \times I_1 \times I_2 \times I_3\, d\phi\, d\theta\,, \quad (5.6)$$

where

$$I_1 = \int_{x=-\infty}^{\infty} \exp\left[\frac{-(x-L)^2}{2\lambda_I^2} - \frac{(x-\rho_{IA}\sin\theta\cos\phi)^2}{2\lambda_A^2}\right] dx\,, \quad (5.7)$$

$$I_2 = \int_{y=-\infty}^{\infty} \exp\left[\frac{-y^2}{2\lambda_I^2} - \frac{(y-\rho_{IA}\sin\theta\sin\phi)^2}{2\lambda_A^2}\right] dy\,, \quad (5.8)$$

$$I_3 = \int_{z=-\infty}^{\infty} \exp\left[\frac{-z^2}{2\lambda_I^2} - \frac{(z-\rho_{IA}\cos\theta)^2}{2\lambda_A^2}\right] dz\,. \quad (5.9)$$

Substituting the solution to the integrals I_1, I_2 and I_3 over x, y and z in equation 5.6, we get

$$P_{IA}(\rho_{IA}) = \frac{\rho_{IA}^2}{\sqrt{4\pi\lambda_I^3\lambda_A^3}} \exp\left[\frac{-L^2-\rho_{IA}^2}{2\lambda_I^2+2\lambda_A^2}\right] \int_{\theta=0}^{\pi} \sin\theta\, \exp\left[\frac{L\times\rho_{IA}\cos\theta}{\lambda_I^2+\lambda_A^2}\right] d\theta\,. \quad (5.10)$$

Solving the θ integral in equation 5.10 gives equation 5.11, which is the exact probability distribution of effective inter-particle separation in 3D for isotropic de Broglie wavelengths.

$$P_{IA}(\rho_{IA}) = \frac{2\rho_{IA}}{L\sqrt{2\pi(\lambda_A^2+\lambda_I^2)}} \exp\left[\frac{-L^2-\rho_{IA}^2}{2\lambda_I^2+2\lambda_A^2}\right] \sinh\left[\frac{L\times\rho_{IA}}{\lambda_I^2+\lambda_A^2}\right]. \quad (5.11)$$

Integrating this probability distribution given in equation 5.11 over the full range of ρ_{IA} gives a re-

sult of 1, which is a necessary condition for a probability density function. In the low temperature limit, the condition $L \ll \lambda_A, \lambda_I$ is satisfied and therefore we get

$$\lim_{\frac{L}{\lambda_{A,I}} \to 0} P_{IA}(\rho_{IA}) = \frac{\sqrt{2}\,\rho_{IA}^2}{\sqrt{\pi(\lambda_A^2 + \lambda_I^2)^3}} \exp\left[\frac{-\rho_{IA}^2}{2\lambda_I^2 + 2\lambda_A^2}\right]. \tag{5.12}$$

From equation 5.12, we can see that at ultracold temperatures, P_{IA} is maximum at the instantaneous separation of $\rho_{IA} = 2\sqrt{\lambda_I^2 + \lambda_A^2}$. $P_{IA}(r_{IA})$ does not vary much with L for $L < \lambda_A, \lambda_I$.

5.1.2 Charge hop rate

The charge exchange rate in a binary ion-atom system is a function of the inter-nuclear separation, R, given [165] by $\nu_{ex}(R) = V_{ex}(R)/h = |V_u(R) - V_g(R)|/h$, where the two molecular potential energy curves (PEC's), V_g and V_u, have opposite symmetry [167]. The average charge hop rate between an atom and an ion with separation between mean positions L, is given by the charge exchange rate for a given ρ_{IA} weighted by the probability that the instantaneous inter-nuclear separation is ρ_{IA},

$$\langle \nu_h(L, \lambda_A, \lambda_I) \rangle = \int_{\rho_{IA}=0}^{\infty} P_{IA}(\rho_{IA})\, \frac{V_{ex}(\rho_{IA})}{h}\, d\rho_{IA}\,. \tag{5.13}$$

This integral is evaluated numerically with the lower limit replaced by the repulsive wall position of the PEC's and for the upper limit, a sufficiently large distance. We find for the case of Li that the upper limit can be 200 a_0 as the residual integral of V_{ex} is negligible beyond it. The method for creation of the ion (threshold ionization of an atom in the ultracold ensemble), ensures that the initial ion delocalization is same as λ_A. With time, wavepacket expansion for the individual ion can change the ion's delocalization and can even make it anisotropic. We assume for the calculations done in this chapter that the ion remains thermalized with the atomic ensemble and that frequent charge hops, will set the ion's delocalization to be same as that of the atoms. Therefore we assert that, $T_A = T_I = T$ and $\lambda_A = \lambda_I = \lambda_T$ as we ignore wave packet expansions and velocity effects. These are valid assumptions, given the hop rates which are obtained, as will be seen later.

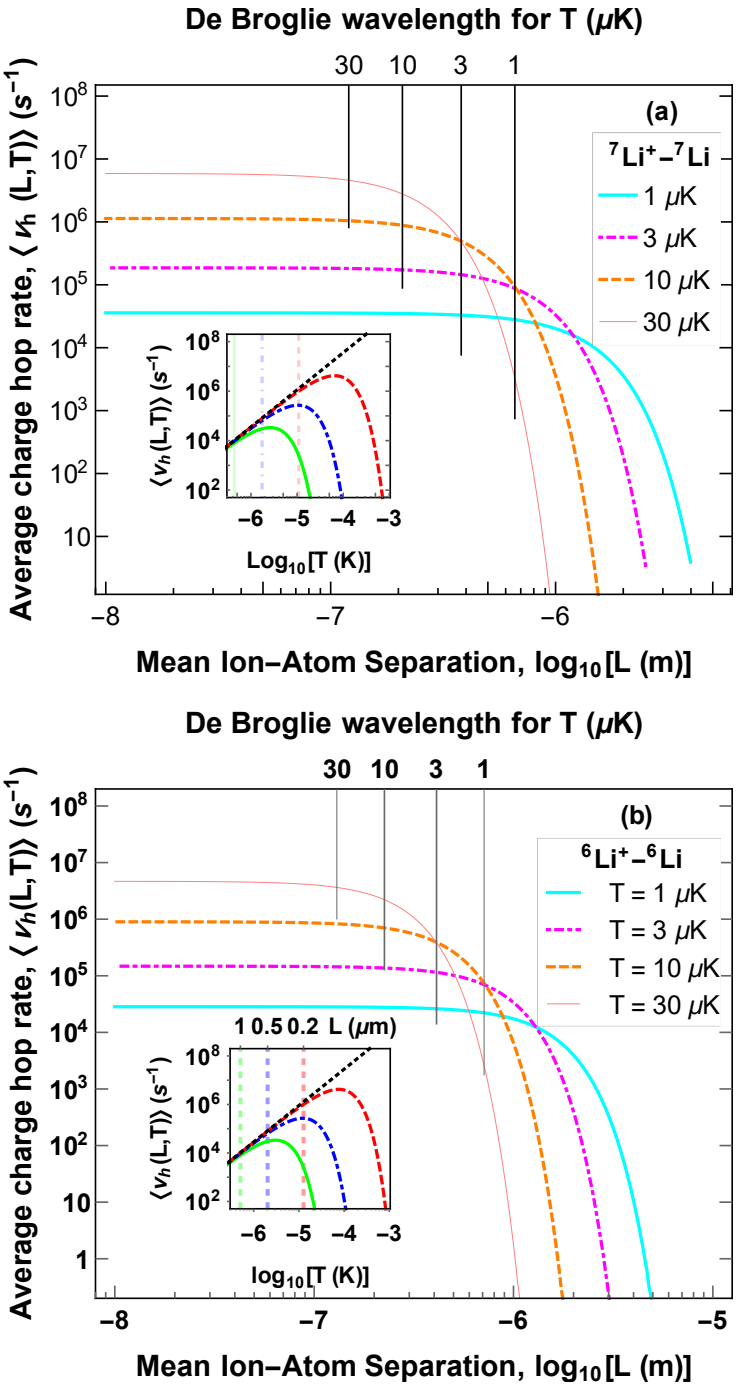

Figure 5.2: Panel (a) shows the average hop rate between an ion-atom pair of ^{7}Li as a function of their mean separation, L, plotted for different temperatures, T. The top ticks mark the L for which the condition L = λ_T is satisfied. In the inset, average hop rates for a fixed separation L= 1μm (green solid curve), L = 0.5 μm (blue dot-dashed curve), L= 0.2μm (red dashed curve) and the limiting case, L$\approx$ 0 (black dotted curve) are plotted as a function of T with the vertical grid-lines marking the $L = \lambda_T$ condition. This illustrates that the temperature range where hop rates are significant and the range where the low temperature limit holds revealing that hop rates diminish for $L > \lambda_T$. Panel (b) shows the same plots for ^{6}Li$^+$-^{6}Li system.

The results here are for $^7Li^+$-^7Li and $^6Li^+$-^6Li systems with the atom in the ground electronic state. Isotope effects for hopping mechanism are mainly due to mass dependence of λ_T. The electronic state of the atom effects charge hop rates significantly as it changes V_{ex}. Figure 5.2 shows that the average charge hop rates between a pair of ion and atom increases when L decreases, and saturates below $L = \lambda_T$. The hop rates for different values of L are equal to their $L \approx 0$ limits at very low temperatures, irrespective of the specific value of L, and deviate from the ultracold limit as λ_T becomes less than L to show temperature dependent behaviour. Our results show higher hopping rates for very small L's at higher temperatures compared to lower temperatures. This may seem non intuitive, but it is because of the smaller spread of the atom and ion wave packets, the denominator which is the normalization over the extent of the wave packets reduces. Although, the hop rates are high, it is not feasible to achieve such proximate mean separations at high temperatures, also the resulting displacement if the charge due to hopping, would be insignificant at such high temperatures.

5.2 Charge hopping in a uniform and continuous distribution of atoms

Let us first, for simplicity, assume the atom density to be described by a uniform and continuous function. In this system, as we increase the atom number density, the ion can have a wavepacket overlap simultaneously with multiple atoms which are at different mean separations as shown in figure 5.1.c. We calculate the hop rate driven ion dynamics in this system and compare it with the collisional transport of the ion in ultracold atoms with uniform density.

Solving for the limiting case where the atomic number density is continuous and homogenous with magnitude n, the effective total hop rate is given by integrating the pairwise hop rates given by equation 5.13 over the full volume,

$$\nu_{tot}^{con} = \int_{L=0}^{\infty} \langle \nu_h(L,T) \rangle \; n \, 4\pi L^2 \, dL \, . \tag{5.14}$$

Substituting equation 5.13 in equation 5.14 and applying $\lambda_A = \lambda_I = \lambda_T$, we get

$$\nu_{tot}^{con} = \int_{L=0}^{\infty} dL \int_{\rho_{IA}=0}^{\infty} \nu_{ex}(\rho_{IA})\, P_{\rho_{IA}}^{3D}(L,T)\, n 4\pi L^2 d\rho_{IA}\,. \tag{5.15}$$

Substituting equation 5.11 in equation 5.15 gives

$$\nu_{tot}^{con} = \int_{\rho_{IA}=0}^{\infty} \frac{4\sqrt{\pi}\, n\, \rho_{IA}\, \nu_{ex}(\rho_{IA})}{\lambda_T} \int_{L=0}^{\infty} L \sinh\left[\frac{L \times \rho_{IA}}{2\, lambda a_T^2}\right] \exp\left[\frac{-L^2 - \rho_{IA}^2}{4\lambda_T^2}\right] dL\, d\rho_{IA}\,. \tag{5.16}$$

Solving the integral over L gives

$$\nu_{tot}^{con} = \int_{\rho_{IA}=0}^{\infty} \frac{4\sqrt{\pi}\, n\, \rho_{IA}\, \nu_{ex}(\rho_{IA})}{\lambda_T} \times \sqrt{\pi}\, \lambda_T\, \rho_{IA}\; d\rho_{IA}\,, \tag{5.17}$$

which then gives

$$\nu_{tot}^{con} = 4\pi\, n \int_{\rho_{IA}=0}^{\infty} \rho_{IA}^2\, \nu_{ex}(\rho_{IA})\, d\rho_{IA}\,. \tag{5.18}$$

From equation 5.18 we see that ν_{tot}^{con} is independent of temperature or isotopic mass (λ), but depends only on the choice of the atom and its internal state (ν_{tot}^{con}) and scales linearly with the atomic density n. In order to estimate whether charge hopping will play a significant role in the dynamics of the system, this total hop rate must be compared to the rate of ion-atom collisions for identical parameters. The average collision rate $z = n \langle \sigma_{tot}\, v \rangle_T$, where σ_{tot} is the total ion atom collision cross section, v is the relative speed of the particles and $\langle\rangle_T$ represents the thermal average quantity for temperature T, also scales linearly with density. Since both hop rate and collision rate are directly proportional to n, the density independent functions $\overline{\nu}_{tot}^{con} = \nu_{tot}^{con}/n$ is compared with $k_{coll} = z/n$ (also known as collision rate coefficient), see figure 5.3. This figure shows that, for both the ^{7}Li and ^{6}Li systems, the hop rate dominates the two-body collision ion-atom collision rates, for the specified parameters range.

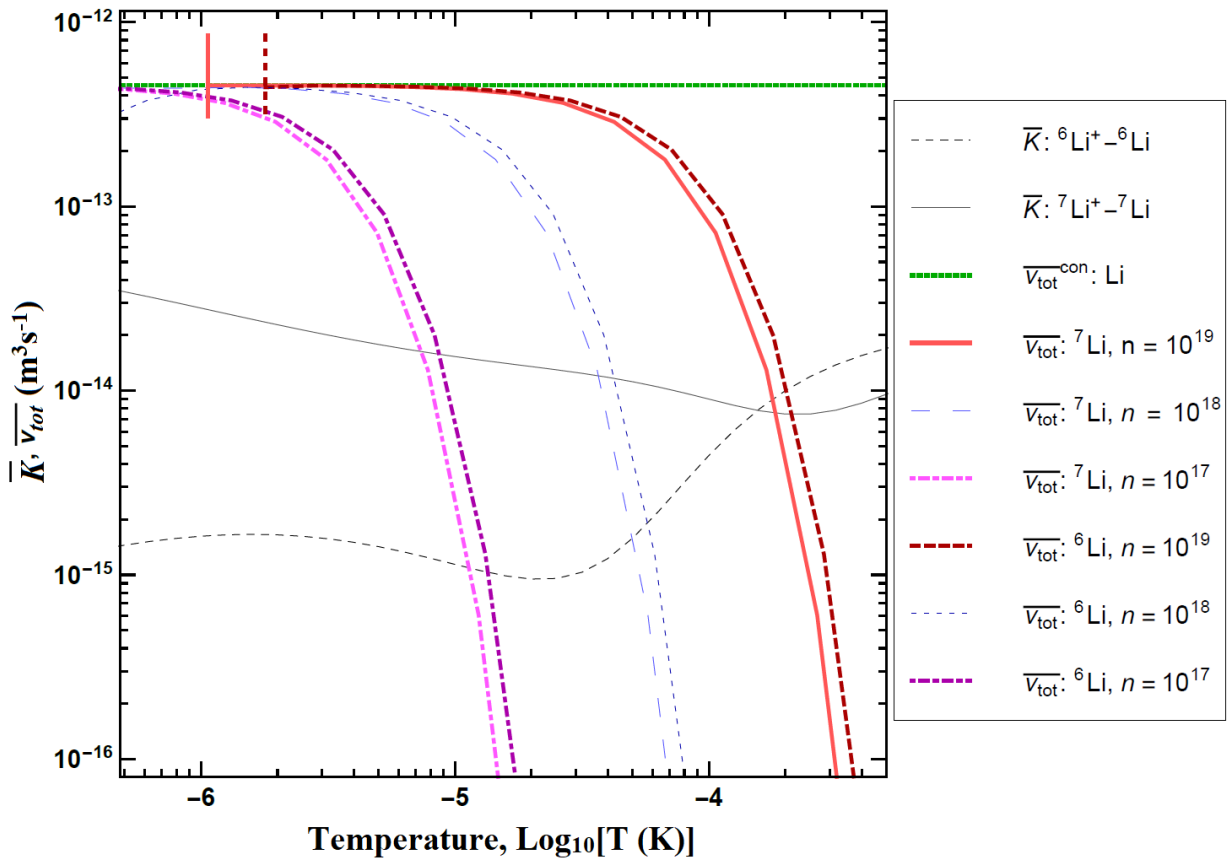

Figure 5.3: Figure illustrates the comparison of collision rates normalized by atom density k_{coll}, total hop rates per atom density for continuous atom density distribution, $\bar{v}_{tot}^{con}$ and the total hop rates per atom density for discrete atom density distribution, $\bar{v}_{tot}$ for both ^{7}Li$^+$-^{7}Li and ^{6}Li$^+$-^{6}Li systems, evaluated for atom densities $n_1 = 10^{19}$ m^{-3}, $n_2 = 10^{18}$ m^{-3} and $n_3 = 10^{17}$ m^{-3} as a function of temperature T are shown. This illustrates the large temperature where the hop rates exceed the collision rates. The corresponding free space degenerate gas transition temperatures are shown by the vertical bars.

Although the rates for hopping are much higher for ultralow temperatures and high atom number densities, whether hopping can be experimentally differentiated can be determined by computing the diffusion of the ion. By measuring charge diffusion directly in an experiment, it is possible to differentiate the effects of the new phenomenon of charge hopping from that of the known collisional phenomenon.

Merely the hop rate being higher than the collision rate is not enough to do so, if the effect produced by such hop rates remain insignificant. The diffusion coefficient for the charge due to hops is given by $D_h = \langle \Delta r_I^2 \rangle / 2d\Delta t$, where r_I is the magnitude of position of the charge in time interval

Δt for d dimensional space. For a three dimensional uniform continuous cloud of atoms, consider a time interval $\Delta t = 1/\nu_{tot}^{con}$ in which one hop happens on an average. The probability that the hop happens over a distance of L, P_L is given by

$$P_L = \langle \nu_h(L,T) \rangle \; n \, 4\pi L^2 \, dL \, . \tag{5.19}$$

Using $\left\langle \Delta r^2 \right\rangle = \int_0^\infty L^2 \, P_L \, dL$ and $d = 3$, we get

$$D_h^{con} = \int_{L=0}^{\infty} \frac{L^2}{6} \, \langle \nu_h(L,T) \rangle \; n \, 4\pi \, L^2 \, dL \, . \tag{5.20}$$

Substituting equation 5.13 in equation 5.20 and solving gives

$$D_h^{con} = \frac{2\pi}{3} n \int_{r=0}^{\infty} \rho_{IA}^2 (\rho_{IA}^2 + 6\lambda_T^2) \, \nu_{ex}(\rho_{IA}) \, d\rho_{IA} \, . \tag{5.21}$$

It can be seen from equation 5.21 that D_h^{con}/n is of the form $D_1 + D_2/T$ where D_1 and D_2 are constants which depend only on the internal state of the atoms and that D_h^{con} is directly proportional to the atom number density. On the other hand, the collisional diffusion coefficient for an ion in a thermal gas of atoms, discussed in the previous chapter, is given by [92, 159]

$$D_{coll} = \frac{3\sqrt{\pi}}{8 \, n \, \langle \sigma_D \rangle_T} \sqrt{\frac{k_B \, T}{m}} \, . \tag{5.22}$$

As $D_{coll} \propto 1/n$ and $D_h^{con} \propto n$, higher atom number densities and low temperatures favour hop mediated charge diffusion over collisional ionic diffusion, as seen in figure 5.4.

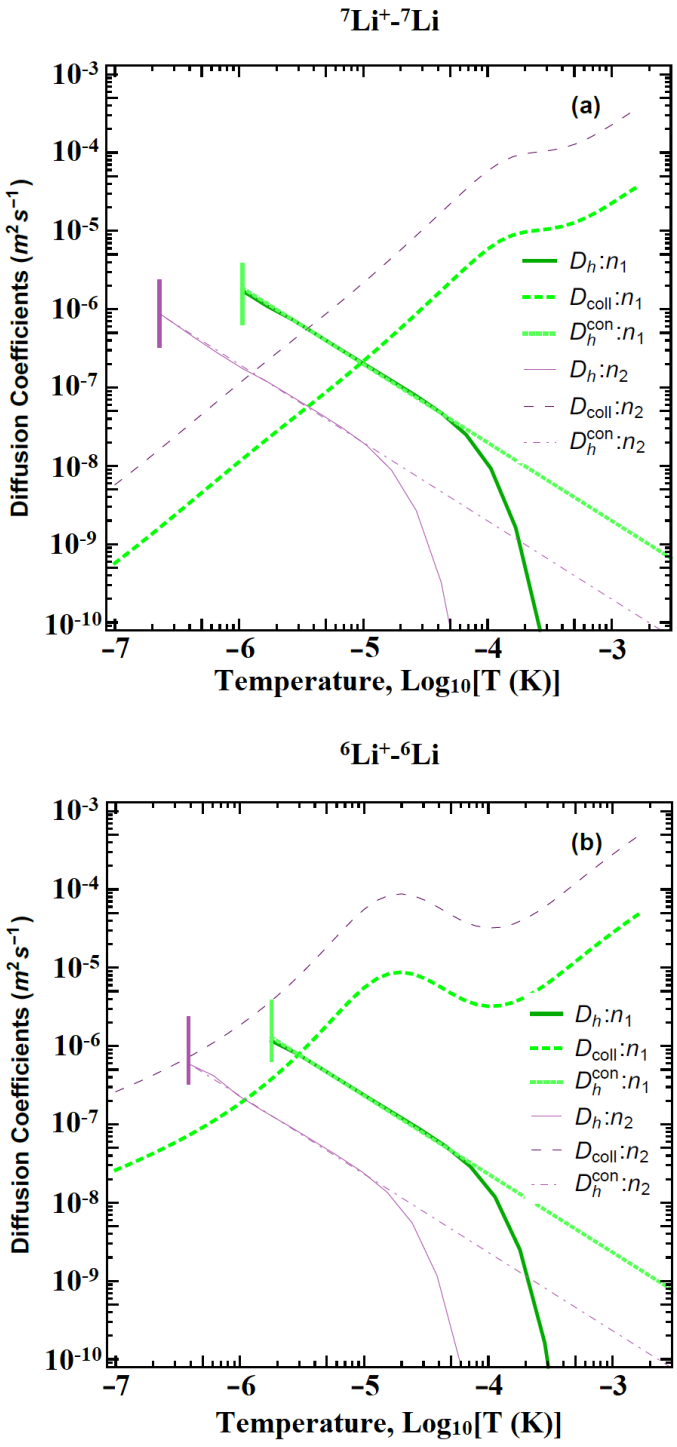

Figure 5.4: Panel (a) shows the diffusion coefficients for the, collision mediated ion transport D_{coll}, hop mediated charge transport for continuous density distribution of atoms D_h^{con} and the hop mediated charge transport for discrete density distribution of atoms D_h for ^{7}Li-^{7}Li system as function of temperature T. In both panels, $n_1 = 10^{19} m^{-3}$ and $n_2 = 10^{18} m^{-3}$. Panel (b) shows the same plots for ^{6}Li$^+$-^{6}Li system. This shows that a temperatures of few μK and densities higher than 10^{18} m^{-3} will be needed to observe the dominance of hop mediated diffusion over collisional diffusion, which is a much smaller parameter space than the one in which hop rates are higher than collision rates.

5.3 Charge hopping in discrete cloud of atoms

When the atomic number density is taken as a discrete, random, homogenous distribution with magnitude n, which is more realistic, the volume integrals used above are replaced by summations over different particles. The mean α^{th} power of the distance to the j^{th} nearest neighbour, given by (see Appendix. A)

$$\left\langle r_j^{\alpha} \right\rangle = \frac{\Gamma(j+\frac{\alpha}{3})}{(j-1)!} \left(\frac{3}{4\pi\, n} \right)^{\alpha/3} , \tag{5.23}$$

where α can be any real number, is used to get the average total charge hop rate between an ion and all the atoms around it,

$$\langle \nu_{tot} \rangle = \sum_{j=1}^{\infty} \langle \nu_h(\langle r_j \rangle, T) \rangle \ . \tag{5.24}$$

We define a quantity $\overline{\nu}_{tot} = \langle \nu_{tot} \rangle / n$ and numerically evaluate this for relevant densities as a function of T, which are compared with $\overline{\nu}_{tot}^{con}$ and k_{coll} in figure 5.3 for both $^7Li^+$-^7Li and $^6Li^+$-^6Li. The total hop rates for a discrete atom distribution are similar to that for a continuous atom distribution with the same number density for lower temperatures. At higher temperatures, they diverge and fall quickly, see figure 5.3. illustrates the range of temperatures and density where hopping rates are significantly larger than the ion-atom collision rates.

The hop mediated diffusion coefficient for the case of uniform discrete atom cloud case is

$$D_h = \sum_{j=1}^{\infty} \frac{\left\langle r_j^2 \right\rangle}{6} \langle \nu_h(\langle r_j \rangle, T) \rangle \ , \tag{5.25}$$

which is evaluated using equation 5.13 and equation 5.23, for relevant atom number densities as a function of T and plotted in figure 5.4 along with D_h^{con} and D_{coll}. Figure 5.4 shows that $n > 10^{18}$ m^{-3} give larger hop mediated transport than the collisional diffusion at few μK temperature. The equivalence of D_h^{con} and D_h for low temperatures is also seen, which illustrates the validity of the continuum approximation in the low temperature limit. The results for a continuous distribution of atoms hold in the ultracold limit for high densities. These give well defined analytical expressions which work out to give the same results as the mean values calculated for a uniform discrete

distribution. The range of temperature and atom density needed to observe a pronounced hop diffusion for a cloud of thermal lithium atoms, is restricted but experimentally accessible.

5.4 Charge trapping in density gradient of Gaussian atom distribution

One practical experimental system where these ion diffusion mechanisms can be tested is that of a localized, 3D Gaussian distribution of atoms, centered at the origin, with number density given by $n = n_0 \exp\left[-r_G^2/2\sigma^2\right]$, as a function of the magnitude of the position $\vec{r_G} = (x_G, y_G, z_G)$, where n_0 is the peak atom number density. The average charge hop rate in this non-uniform cloud depends on the position of the ion, $\vec{r_I}$ as it depends on the local atomic number density. The r_I dependent hop diffusion coefficient is given by

$$D_h(r_I) = \frac{2\pi}{6} \int_{\overline{r}_h=0}^{\infty} \int_{\theta_h=0}^{\pi} \left(\overline{r}_h^2 + 2\overline{r}_h r_I \cos\theta_h\right) \langle \nu_h(\overline{r}_h, T)\rangle \\ n_0 \exp\left[\frac{-(r_I^2 + \overline{r}_h^2 + 2r_I\overline{r}_h\cos\theta_h)}{2\sigma^2}\right] \overline{r}_h^2 \, \sin\theta_h \, d\overline{r}_h d\theta_h \quad , \tag{5.26}$$

where the average hop distance, $\overline{r}_h$, which depends on the local neighborhood at the ion position $\vec{r_I}$, is given by

$$\overline{r}_h(r_I) = \sum_{j=1}^{\infty} \frac{\langle r_j(r_I)\rangle \, \langle \nu_h(\langle r_j(r_I)\rangle, T)\rangle}{\langle \nu_{tot}(r_I)\rangle} \, . \tag{5.27}$$

In the continuum case, which is consistent with the ultracold limit for this system, taking a number density of atoms $n(r_I) = n_0 \exp -r_I^2/(2\sigma^2)$, we get

$$\overline{r}_h(r_I) = \frac{\int_{L=0}^{\infty} L \, 4\pi L^2 \, n(r_I) \, \langle \nu_h(L,T)\rangle \, dL}{\int_{L=0}^{\infty} 4\pi L^2 \, n(r_I) \, \langle \nu_h(L,T)\rangle \, dL} \, . \tag{5.28}$$

Since n_0 is in both numerator and denominator, the average hop distance at a given ion position $\overline{r}_h(r_I)$ becomes independent of the magnitude of the atom number density n_0, and depends only on the geometric parameter σ and temperature T. An interesting consequence of the anisotropic

density gradient is that $D_h(r_I)$ given in equation 5.26 can become negative in certain spatial regions. When placed in these regions, the charge moves closer to the center of the atomic cloud over time due to hopping. The condition for $D_h(r_I) < 0$ is given by

$$\int_{\theta_h=0}^{\pi/2+\theta_c} \exp\left[\frac{-2r_I\,\overline{r}_h\cos\theta_h}{2\sigma^2}\right]\sin\theta_h\,d\theta_h \;\leq\; \int_{\pi/2+\theta_c}^{\pi} \exp\left[\frac{-2r_I\,\overline{r}_h\cos\theta_h}{2\sigma^2}\right]\sin\theta_h\,d\theta_h\,, \tag{5.29}$$

where $\theta_c = \sin^{-1}(\overline{r}_h/2r_I)$, the left hand side of the equation 5.29 is the probability that the magnitude of ion position after charge hopping is greater than that of before hopping, and the right hand side of the equation 5.29 is the probability that the magnitude of ion position after charge hopping is lesser than that of before hopping. This gives the condition required for stable, diffusive trapping confining the position magnitude of the charge r_I, as

$$D_h(r_I) + D_{coll}(r_I) \leq 0\,, \tag{5.30}$$

which is demonstrated in figure 5.5 Simulations for trajectories of the ion undergoing charge hopping in 3D Gaussian atomic cloud with $\sigma = 100\,\mu$m are performed. Here we ignore collisions with atoms and allow the ion to move ballistically between hops. The results are shown in figure 5.6 where the comparison with a collision-less ballistic trajectory and collisional diffusion is shown for each case.

A random list of distances to the nearest atoms from the ion is generated using the conditional probability distribution $P(r_j|r_{j-1})$ (see Appendix. A), until the change in the total charge hop rate becomes negligible.

$$P(r_j|r_{j-1}) = 4\pi\,n\,r_j^2\,\exp\left[-4\pi n(r_j^3 - r_{j-1}^3)\right]. \tag{5.31}$$

In the interval between two hops, given by a Poisson's distribution with mean $1/\nu_{tot}$, the ion is allowed to move ballistically with a velocity taken from Maxwell Boltzmann distribution for temperature T. A hop is performed by swapping identity of the ion with one of the nearby atoms from this new location. For this a list of neighbouring atoms is made again and one of them is picked with weight factor of hop rate to that atom.

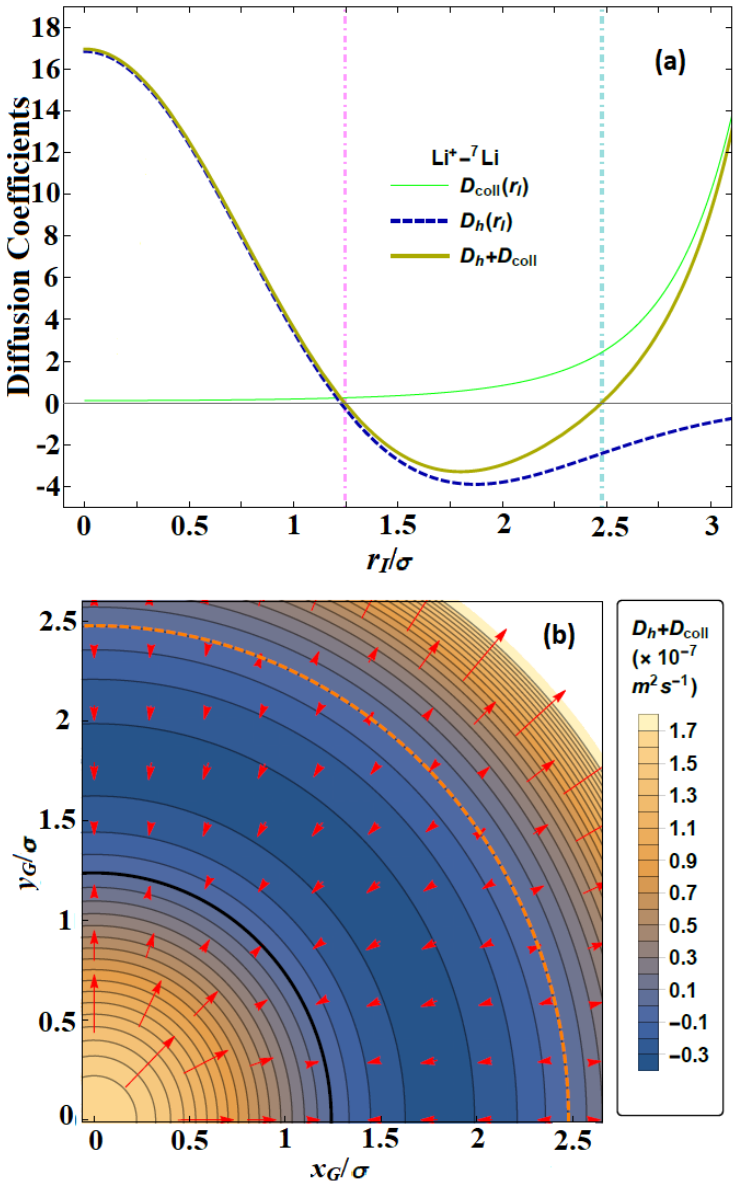

Figure 5.5: The diffusion coefficients of a single ion starting at the centre of a Gaussian distribution of atoms of peak density $n_0 = 10^{19}$ m^{-3} and $\sigma = 100\mu$m is shown in panel (a). The collisional diffusion (large dashed, green) moves the ion away from the trap centre monotonically. The hopping diffusion coefficient (small dashed, blue) first causes the ion to move outward for $r_I < 1.24\sigma$, and inwards for $r_I \geq 1.24\sigma$. The net diffusion coefficient of the ion (thick yellow) is a result of the combination of these two distinct processes. It make two intercepts at zero diffusion coefficient, one at 1.25σ and the other at 2.48σ. A thermal ion starting at $r_I < 2.48\sigma$ will move to stabilize at $\approx 1.25\sigma$ and an ion beyond 2.48σ will escape. This shows that there is a shell of diffusive stability for a ion. Panel (b) is a contour plot of the total diffusion coefficient in a plane and the red arrows show the direction and magnitude of average diffusion at each point in the plane. Here, the shell of stable equilibrium is shown by the black circle and the orange circle shows the radius beyond which inward diffusion is not likely. This shows that the presence of the hopping mechanism results in ion trapping by a gradient atom distribution and charge localization to a spherical shell. This provides a very clear experimental signature of charge hopping.

While the separations used are the same as for uniform density of value $\rho_A(\vec{r}_I)$, the density gradient is simulated by assigning the azimuth angle θ using a distribution given by

$$P_\theta = r_I\, r_j\, \sin\theta\, \exp[\frac{-(r_i^2 + r_j^2 + 2r_i r_j \cos\theta)}{2\sigma^2}]\,. \tag{5.32}$$

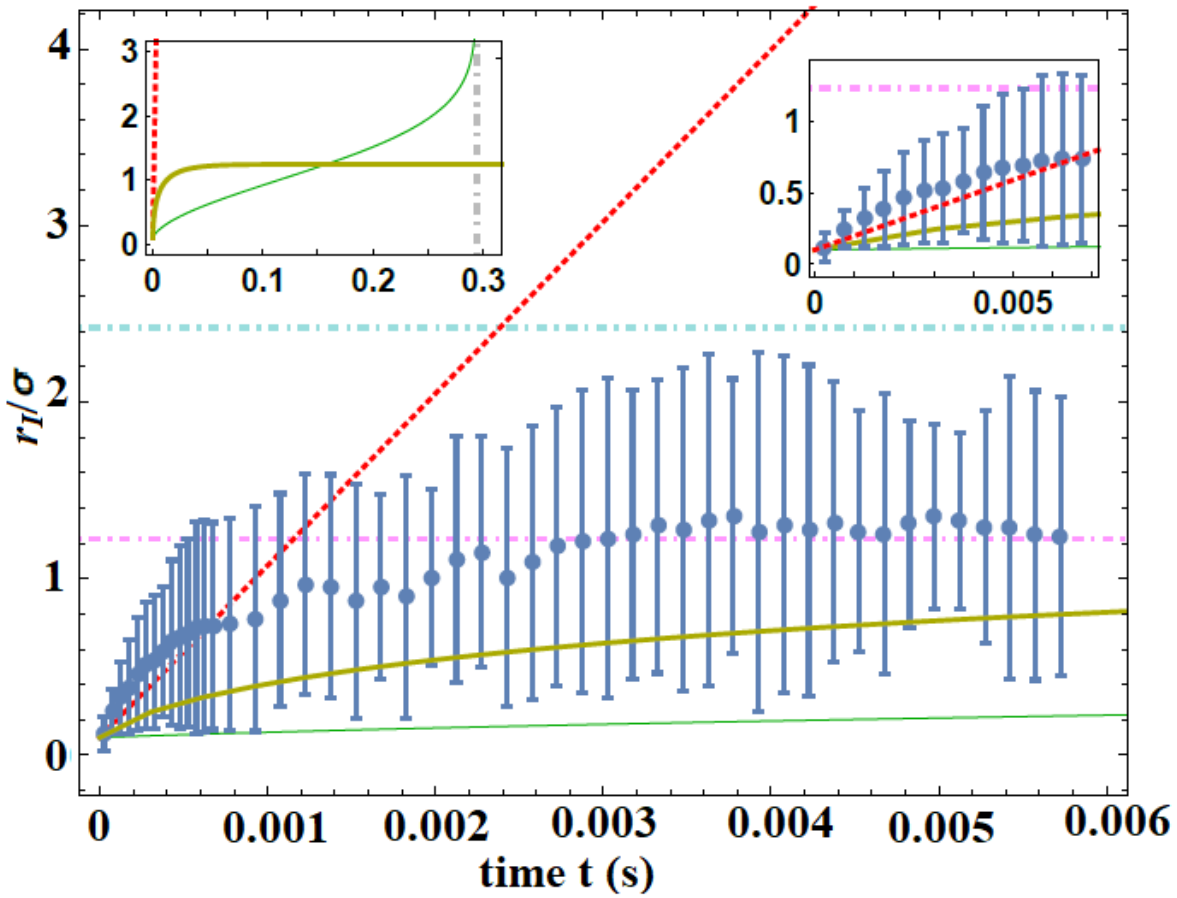

Figure 5.6: Figure illustrates the Monte-Carlo hopping trajectory calculations for 100 instances of an ion starting at the origin. The statistical average values of $\overline{r}_I$ over all trajectories, are represented by filled blue circles, and the error bars denoting one standard deviation. It is clear that the ion localizes at $\overline{r}_I \approx 1.25\sigma_G$, for long hold times. The dashed red curve is the ballistic trajectory with average thermal velocity, the thick yellow curve is the theoretical mean trajectory $\overline{r}_I(t)$ incorporating both collisional and hopping diffusion and the thin green curve is the theoretical mean trajectory $\overline{r}_I(t)$ with just the collisional diffusion coefficient. The insets show these curves in their small and large hold time limits.

These steps are repeated to form the trajectory up to a large number of hops. 100 such trajectories are generated and the averages and standard deviations are presented. The same procedure is

followed for generating trajectories in stray electric fields, except that between hops along with ballistic motion the ion is accelerated in the direction of the field.

It is clear from figure 5.5.a. that so long as the ion is in the region $r_I < 2.48\sigma$, it will move to $r_I = 1.24\sigma$ over time unless the ion's stochastic motion leads it beyond $r_I = 2.48\sigma$. Since collisions further limit the ballistic diffusion, definitive trapping of charge in the density gradients of ultracold atomic clouds results on a spherical shell of radius 1.24 σ in this case.

The solutions of equation 5.29 and equation 5.30 for r_I/σ is independent of σ. Therefore, the ratios obtained above and weather such stable solutions can be obtained, do not depend of the size of the Gaussian atomic cloud σ, and vary with T and n_0. To our knowledge, this example of trapping on a density gradient is unique.

We show the results of the diffusion coefficients as a function of radial position, for a few other values of the parameters, peak number density and temperature, for the $^7Li^+$-^7Li system in figure 5.7. The simulation results for trajectories of the $^7Li^+$ ion due to charge hopping in a thermal ensemble of ^7Li atoms is shown in figure 5.8. Some of the equivalent results for the $^6Li^+$-^6Li system, are shown in figures 5.9 and 5.10 respectively.

Figure 5.5.a shows that a charge created at the centre of the atomic distribution diffuses faster than ballistic thermal velocities initially, consistent with the computed large hop diffusion coefficients in equations 5.21, 5.25 and figure 5.4. The charge diffusion slows down to below thermal velocities as the steep density gradient comes into play as per the condition in equation 5.29. Radial diffusion stops as the ion reaches the regions where the sum of the diffusion coefficients goes to zero, beyond which the inequality in 5.30 gets satisfied.

We define the term hold time as the time up to which an ion can be found within $r_I < 3\sigma$ due to diffusion. Experimentally the confinement of charge to within the Gaussian atomic cloud for longer than collisional hold times is definitive evidence of the charge hop mechanism.

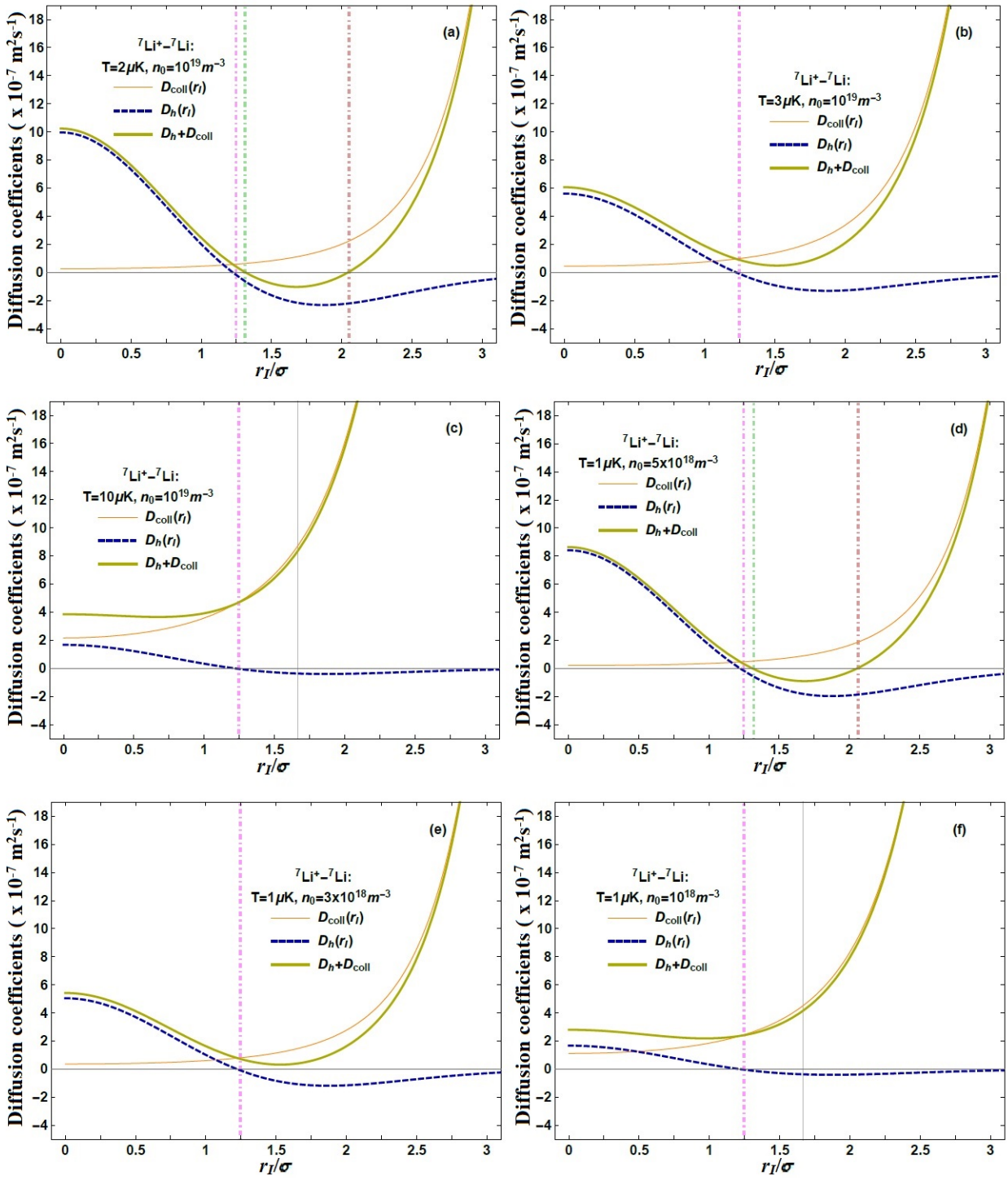

Figure 5.7: For a ^{7}Li$^+$-^{7}Li system with different conditions mentioned in the panels, the collisional diffusion coefficient (brown), hopping based diffusion coefficient (dashed blue) and their sum (thick yellow) are plotted. In the insets, the corresponding theoretical mean trajectories due to these diffusion coefficients are shown in similarly styled curves along with the ballistic trajectory with mean velocity (dotted red). It is clear that ^{7}Li system offers a few more temperature and atom number density choices to observe charge trapping due to hopping in a spherical shell. Larger the gap between the green and red vertical lines, the more stable the radial charge confinement.

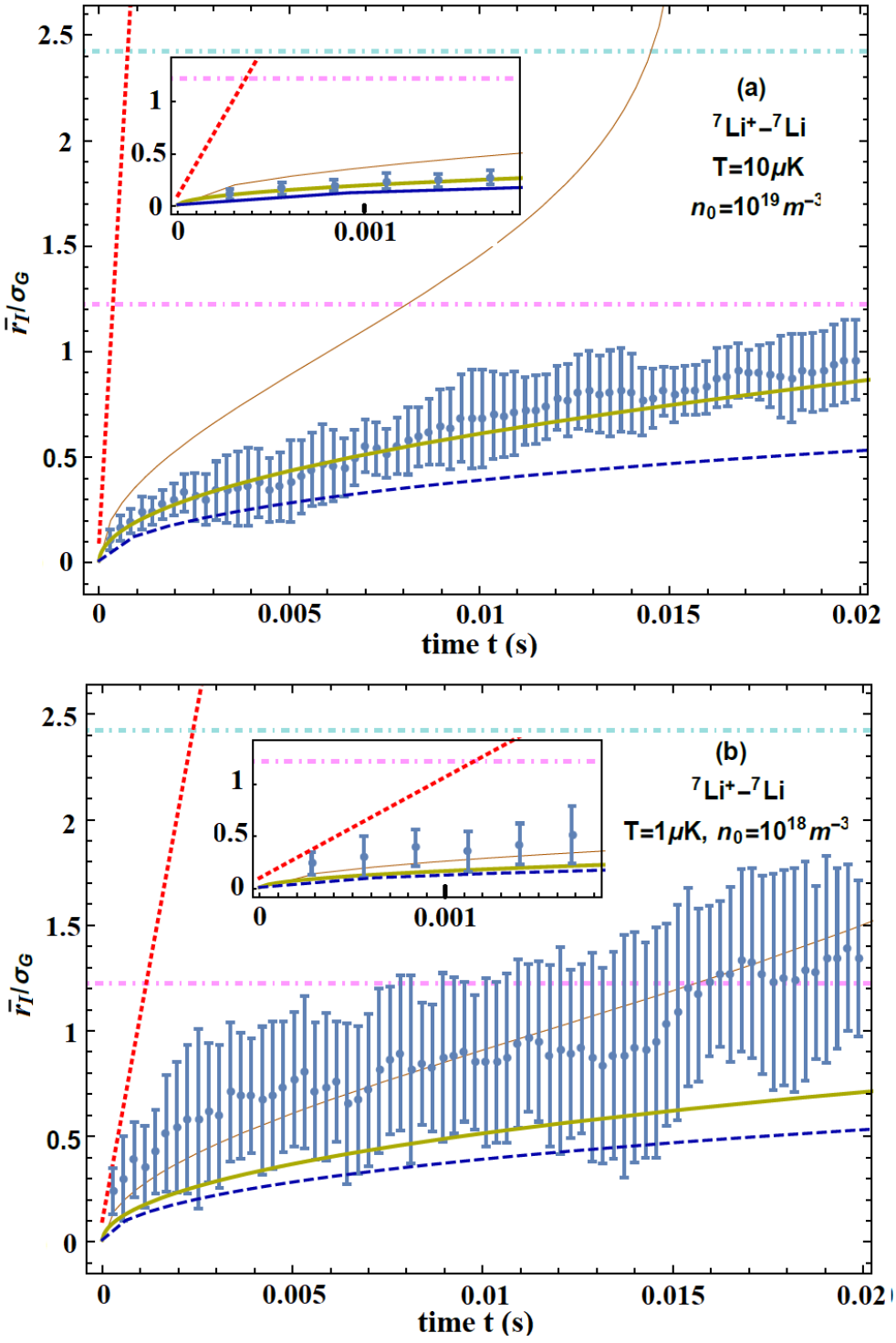

Figure 5.8: For a $^7Li^+$-^7Li system under conditions mentioned in the panels, the mean of 100 simulated trajectories with charge hopping is plotted as blue circles and the error bars represent the standard deviation. The dotted red curve is the ballistic trajectory with average thermal velocity, the thick yellow curve is the theoretical mean trajectory with the sum of collisional and hopping diffusion coefficients, the dashed dark blue curve is the average theoretical trajectory with just charge hopping and the thin brown curve is the upper limit to ion mobility allowed by just collisions. The insets show the same curves in their small hold time limits.

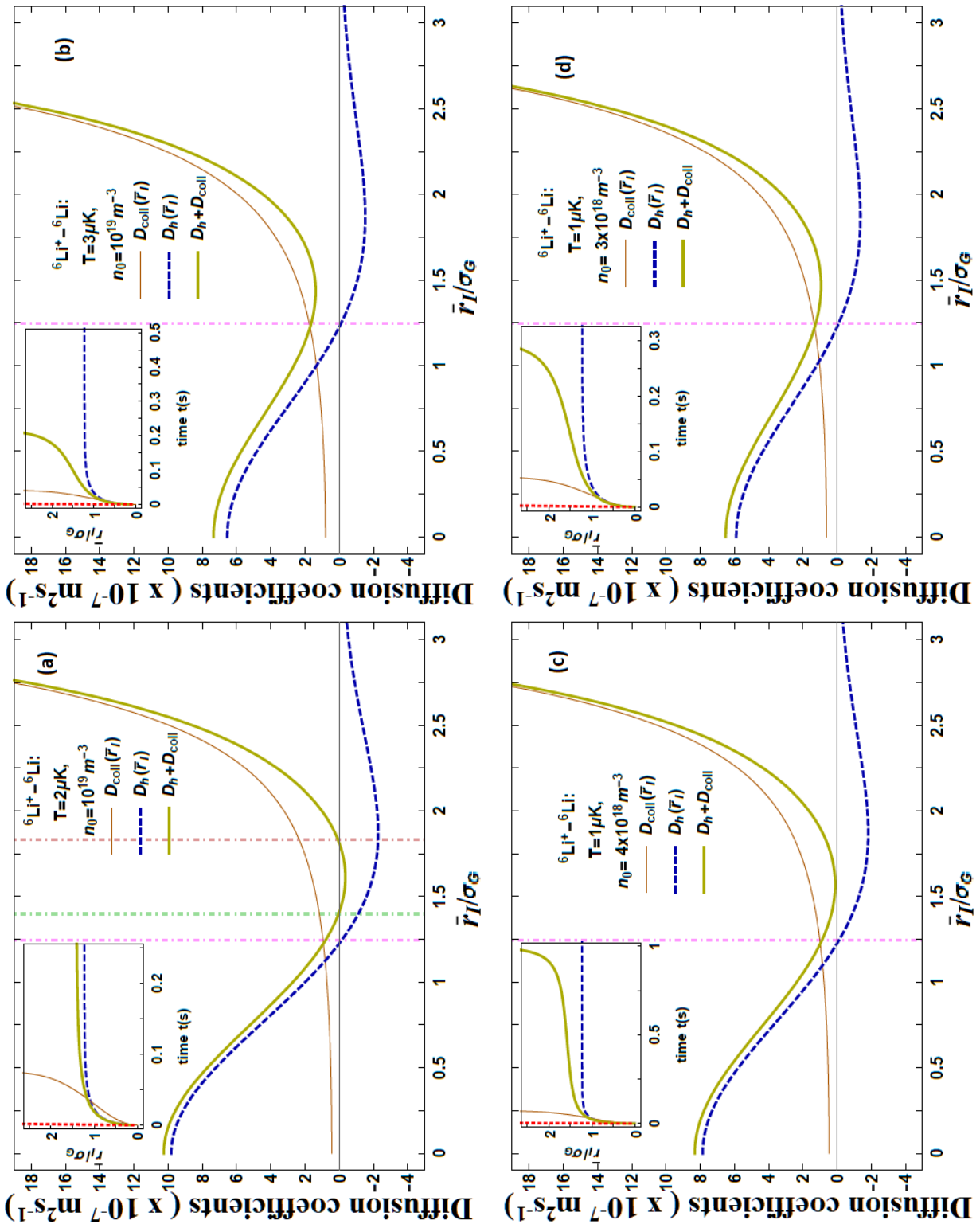

Figure 5.9: For a $^6Li^+$-^6Li system with different conditions mentioned in the panels, the collisional diffusion coefficient (brown), hopping based diffusion coefficient (dashed blue) and their sum (thick yellow) are plotted. In the insets, the corresponding theoretical mean trajectories due to these diffusion coefficients are shown in similarly styled curves along with the ballistic trajectory with mean velocity (dotted red).

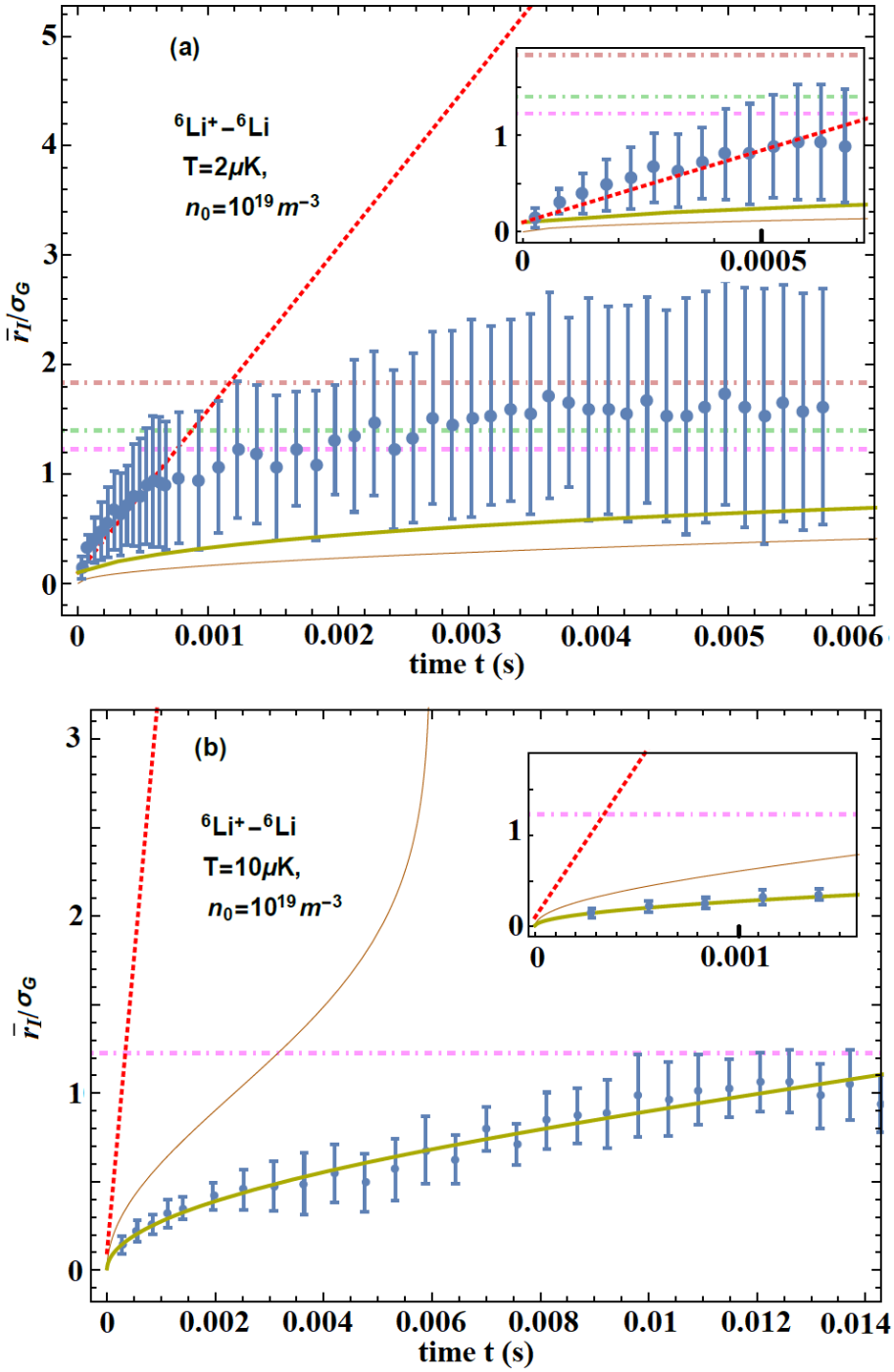

Figure 5.10: For a $^6Li^+$-^6Li system under conditions mentioned in the panels, the average of 100 simulated trajectories with charge hopping is plotted as blue circles and the error bars represent the standard deviation. The dotted red curve is the ballistic trajectory with average thermal velocity and the thick yellow curve is the theoretical mean trajectory with the sum of collisional and hopping diffusion coefficients. In panel (a), the thin brown curve represents the mean trajectory with just collisional diffusion. Whereas in panel (b), the brown curve is the thin brown curve is the upper limit to ion mobility allowed by just collisions. The physical meaning of the result of same equation (the brown curves), changes as the thermal velocities become lower than the corresponding collisional mobility limit. The insets show the same curves in their small hold time limits.

We can see from the above results that even the cases where the ion is not perpetually trapped by the gradient density of atoms, the hold times obtained upon including charge hopping, can be significantly longer than the expected hold times assuming only collisions at play. These effects are measurable in real experiments and can provide solid evidence for charge hopping and the underlying mechanism.

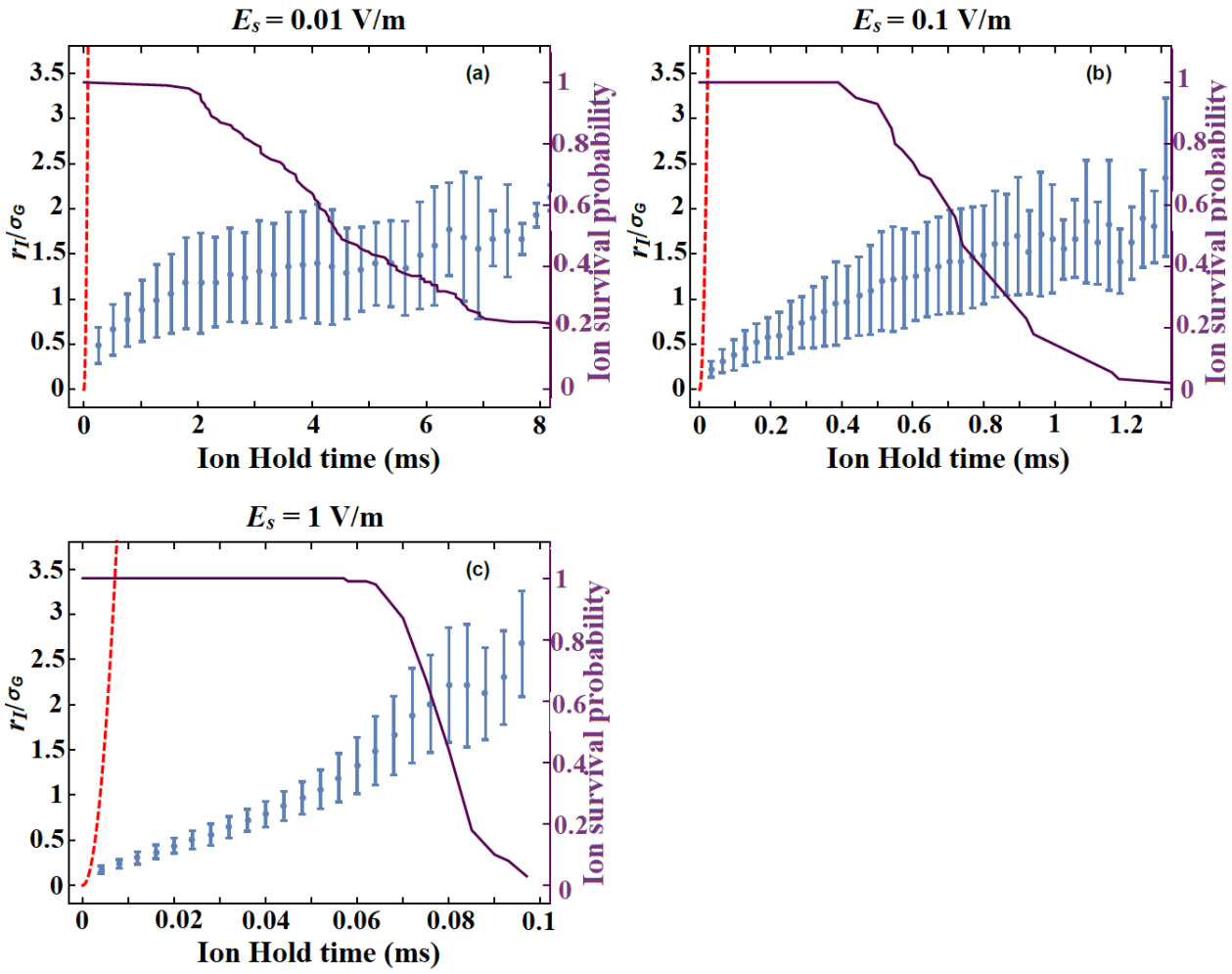

Figure 5.11: The panels show the ballistic trajectory (red, dotted) of a single ion starting at the origin at $t = 0$, the Monte-Carlo hopping trajectory calculations for 100 instances (light blue) and the survival probability (purple) of the ion within 3σ of the Gaussian atomic distribution discussed in figure 5.5. The three panels show these for different values of a constant electric field E_s imposed on the system. This is the experimentally realistic case, and once again illustrates that the prolonged survival of the ion within the atomic ensemble is the testable signature of charge hopping due to exchange symmetry.

5.5 Effect of a small electric field

In order to further connect with laboratory situations, the effects of a small, constant electric field on this system is computed. During the ion's motion between hops, no change in its delocalization or charge hop rates is considered. This is reasonable as we evaluate the expected average expansion of wave packet in between hops to be less than 1%. Figure 5.11 illustrates the survival probability of a Li ion in a Gaussian ensemble of Li atoms, at 1 μK and $n_0 = 10^{19}$ m^{-3}. The measurement of ion survival time will directly measure the diffusion in a gradient density of atoms. The large ion hold times validates the prospect of practical implementation of this atomic trapping mechanism for a homonuclear ion. As significantly longer hold times are shown with electric fields of magnitude higher than the field due to another ion at $\approx 2\sigma$ distance (0.036 V/m) and ion hold time of a few ms is experimentally measurable, this system will also allow the simultaneous diffusive trapping of more than one ion.

5.6 Discussion

In summary, we studied charge hop mechanism due to exchange symmetry in Li^+-Li system. The calculation is very general and with a few element specific changes, the formalism can be extended to any homonuclear ion-atom system in the ultracold regime. The probability distribution calculation for effective separation under Gaussian position uncertainties is general and applies to all cases with isotropic delocalizations. We ignore 3 body collisions [17, 180], as we estimate their threshold rates [181] to be at least 2 orders of magnitude lower than the binary collision rates considered. We have not considered coherent interactions as we have carefully limited the parameter space of study to within the non-degenerate gas limit. Effective trapping of the charge with a Gaussian atomic density profile in experimental conditions and the stability of such a trap against stray electric fields makes this system very exciting. Zooming out, the problem solved is one of competing diffusion mechanisms, resulting in a random walk of the charge due to various mechanisms. It is shown that the quantum symmetry enabled exchange due to particle delocalization dominates and is a measurable quantity in upcoming experiments. Details of the dynamics of

multiple ions, effects of acceleration and wave packet evolution will be explored in the future.

In the presence of excited atoms and negative ions, the hopping rates calculated can be expected to increase dramatically. In both these cases, the size of the ion/atom will be larger and therefore, the exchange energy would be relevant up to larger instantaneous ion-atom seperations. This improves the probability of ion-atom overlap significantly and thereby results large charge hopping rates. In the case of excited atoms, the coefficient A in equation 4.3, would increase proportional to the principle quantum number of the excited state. This results in large charge hopping rates and the resulting hopping-led diffusion [165, 182].

Extensions to degenerate gas systems will require the inclusion of the mean field potential and possible many body quantum effects. The work here reveals the dynamics in the full quantum regimes, and adds new vistas beyond s-wave regime to ultracold ion-atom physics while enhancing our understanding of systems with interchange symmetry in general.

In a homonuclear ion-atom system, the uncertainties in their position, given by the thermal de Broglie wavelengths, λ_T, lead to a scenario where the effective ion-atom separation has a probability distribution ranging from 0 to ∞ as shown in section 5.1.1. While the uncertainty in ion-atom separation is negligible at high temperatures, the effective ion-atom separation can be much smaller than the mean ion-atom separation, L with significant probability for the case of low temperature when $L > \lambda_T$ (low density). The ion-atom interchange symmetry which has limited effect on the collision cross sections under these conditions, can lead to an additional hopping mediated charge mobility which becomes significant for low temperatures and high densities. Further, when $L < \lambda_T$ (high density), the instantaneous ion-atom separation can be larger than the mean separation also with significant probability. In this case the charge hop rates are almost the same over a range of mean ion-atom separations, see figure 5.2. This leads to spontaneous charge hopping with beyond nearest neighbor atoms in a dense cold atomic cloud, which is computed in section 5.3, where the resulting mobility's are discussed. As the hop rates remain similar with all atoms in the neighborhood of the ion, the charge will drift towards region of higher atomic density if the ion is in a region with gradient in atomic density. We show effective trapping of the charge with a Gaussian atomic density profile with experimentally feasible parameters in section

5.4 and discuss the stability of such trap against stray electric fields in section 5.5.

As computing full quantum dynamics of a large finite interacting hybrid system is extremely difficult, we compute the dynamics using a charge hop rate, which simulates the phenomenological attributes of the quantum system. The complete theoretical formalism and experimentally relevant analytical calculations and numerical simulations have been presented without any unrealistic assumptions. With a few element specific changes, the formalism can be extended to any ion-atom system. The probability distribution calculations for effective separation under Gaussian uncertainties and j^{th} nearest neighbor distance in a uniform density, are general and could be used across fields of physics. Dynamics of multiple ions and usage of ultracold ion-atom interactions to confine ions and effects of acceleration and wave packet evolution can be explored further. This combined with the ability to measure these phenomena, which reveal the dynamics in the full quantum regimes, with experimental control, will broaden the horizons of ultracold ion-atom physics and also help enhance our understanding of systems with interchange symmetry in general.

Chapter 6

Virial Analysis for Linear Multipole Ion Traps

In order to build the next generation of experiments with hybrid ion-atom traps, it is important to settle on the design of the ion trap of choice during conception. The ion trap components will have to be inside the vacuum chambers as the electrodes have to be the closest surfaces from the ion in order for it to experience undisturbed trapping potentials. This requires us to ask basic questions about the ion trap design, keeping in mind the conceived experiments and the ion-atom systems of interest, such that the necessary ultracold atom trap can be implemented at the same location as the ion trap center. As mentioned earlier in Chapter 2, implementing a continuously loadable ultracold trap for the atom trap, like a MOT, requires large optical access to the common trap centre, making linear traps our generic choice within the various Paul trap configurations.

Whether higher order linear multi-pole trap is more favorable than a quadrupole trap, for studying ion-atom interactions, is a question for experiments with trapped ions. Historically, the hybrid traps used have been quadrupole Paul traps as ion traps, barring rare exceptions. However at this stage of evolution of the field, when a new experiment is to be constructed, it is important to study whether the quadrupole Paul trap is the best possible choice, all things considered. In this chapter, we therefore analyse and evaluate the performance of multipole, linear Paul traps for the purpose of studying cold ion-atom collisions. A combination of numerical simulations and analysis based

on the virial theorem is used to draw conclusions on the differences that result, by considering the trapping details of several multipole trap types. Starting with an analysis of how a low energy collision takes place between a fully compensated, ultracold trapped ion and an stationary atom, we show that a higher order multipole trap is, in principle, advantageous in terms of collisional heating. The virial analysis of multipole traps then follows, along with the computation of trapped ion trajectories in the quadrupole, hexapole, octopole and do-decapole radio frequency traps. A detailed analysis of the motion of trapped ions as a function of the amplitude, phase and stability of the ion's motion is used to evaluate the experimental prospects for such traps. The present analysis is published [183], and has the virtue of providing definitive answers for the merits of the various configurations, using first principles.

6.1 Scope and utility of linear Paul traps

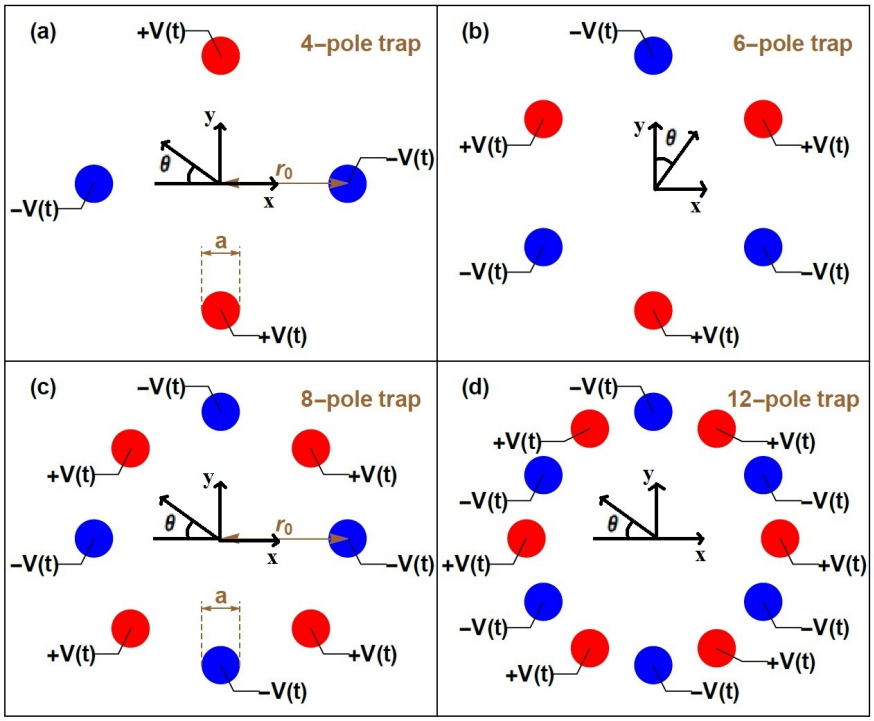

Figure 6.1: Electrode potential configuration for normal operation of (**a**) a 4-pole trap, (**b**) a 6-pole trap, (**c**) an 8-pole trap and (**d**) a 12-pole trap, where $V(t) = V_0 \sin \omega t$. We keep the parameters r_0 and a fixed for all the trap configurations. Note that the 12-pole trap in (**d**) is also equivalent to the superposition of three quadrupole traps.

Linear multipole Paul trap configurations are emerging as a natural choice for a wide range of charged particle trapping experiments [12–16, 30, 49, 56, 90, 161, 162, 180, 184]. The study of mixtures of trapped ions and atoms has spawned a variety of hybrid traps [13, 18, 21, 22, 70, 75, 88, 89, 161, 185, 186]. Such traps allow for the simultaneous and overlapped trapping of cold atoms and cold ions. The objective of such experiments is to study the interactions between the trapped ions and atoms, typically by collisions. It is therefore necessary to evaluate which trap geometry is ideal for experimental objectives to be met. The key question of interest here is whether higher order multi-pole traps (figure 6.1) are more favorable than a quadrupole trap or not, if the objective is to study the ion-atom collisions at the coldest temperatures. The wider scope of such traps ranges from single ion-based mass spectroscopy to optical spectroscopy experiments [46, 47, 187–189], and a few ion-based quantum logic and computation experiments [42, 190], experiments with coulomb crystals with many ions [8, 15, 28, 41, 118, 180] and single ions or ion clouds interacting with cold atoms [11, 21, 29, 30, 55, 82, 161, 180, 185].

Optical access for laser beams and absence of strong magnetic fields [11] make linear Paul traps a favorable choice for these experiments, apart from their relative simplicity of modeling and the ability to perform numerical and analytical calculations. So while the linear Paul trap can be used for a large number of experiments with different and ever expanding objectives, here we examine and evaluate different linear Paul trap electrode configurations, in an effort to decide which multipole radio frequency (RF) linear electrode configuration is suitable for the study of ion-atom collisions at the coldest temperatures. One of the outstanding goals for hybrid-trap experiments is the realization of the s-wave regime for the ion-atom system, when there is a single trapped ion in a cloud of ultracold atoms [16, 17, 20].

In a Paul trap, the dynamic trapping of an ion due to the RF fields applied to the electrodes results in ion motion which can be decomposed into two parts. The ion exhibits a forced motion, which is the instantaneous response of the ion to the time varying RF field (micromotion) and the slower (macro) secular motion, which is the trajectory of the trapped ion in the effective trapping field the ion experiences. In this scenario, the lowest energy of a single ion in a quadrupole ion trap can be confined within a compensated ion trap. Such an ion is insulated from micromotion due to the RF fields. Since a linear quadrupole ion trap has a nodal line, where the acceleration on the

ion vanishes, any small deviation of the ion from this spatial location results in an increase in its motional energy. If we now consider such a specially prepared ultracold ion in collision with an ultracold atom in its vicinity, the mutual interaction between these two is sufficient to pull the ion out of the compensated configuration. The resulting collision increases the kinetic energy of the ion-atom pair compared to the s-wave limit, due to the energy coupled from the trapping field via the mutual interaction [13, 82, 90].

6.2 Microscopic detail of ultracold ion-atom collision

Let us compare the scenarios of a single zero energy $^{40}Ca^{+}$ ion at the center of a quadruple and an octupole trap colliding with a zero energy ^{40}Ca atom placed proximate to the ion. The 2-dimensional potential forms of the quadrupole and octopole traps can be found in table 6.1. In this scenario, the mutual ion-atom interaction potential results in ion displacement from the compensated point and a collision initiates. On being displaced from the center, the ion starts moving under the influence of its trapping field, and the field does work on the ion in the presence of the atom, increasing the total energy of the colliding system. To model this collision we set the time of the first collision to be equal to $t = 0$, the ion-atom interaction potential is modeled by induced dipole interaction term, $-C_4/r^4$, the collision is always head on and its sense reverses when ion-atom internuclear separation approaches the repulsive wall of the ion-atom potential energy curve. This 2-dimensional collision calculation was performed by Anand Prakash and the details of the calculation can be found elsewhere [183]. The trajectories of the ion-atom pair and the kinetic energy of the ion in the respective traps during an instance of such a collision is illustrated in figure 6.2. The collision is treated classically and all quantum aspects of the collision are ignored. When the collision initiates, under the influence of the mutual ion-atom attraction, in the presence of the RF trapping field, RF energy is pumped into the collision partners, increasing the collision energy as the collision progresses. This is evident for only very low energy collisions, where the time taken for the collision spans several RF cycles. The collision is complex enough so that there can be several sequential collisions between the ion-atom pair before they eventually separate.

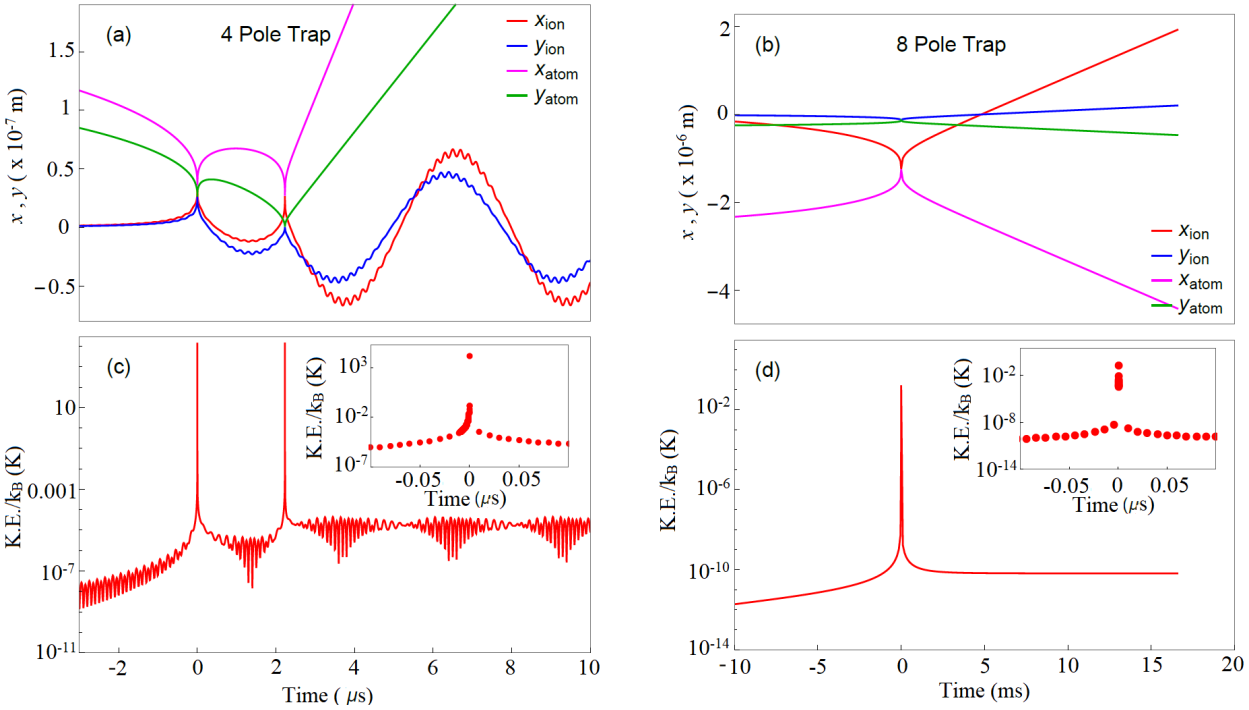

Figure 6.2: The time domain collision between a trapped and compensated stationary ion, initially located at the center of a quadrupole (**a**) and octupole (**b**) trap, with a stationary atom in its vicinity is shown. The calculation is two-dimensional. As a result of the mutual attraction of the trapped ion with the atom, in the presence of the trapping field, post collision, both the ion and the atom gain kinetic energy. The amount of kinetic energy gained in the collision in (**a**,**b**) is illustrated in (**c**,**d**), respectively.

An example of an ion-atom collision in an RF trap with quadrupole and octopole fields is shown in figure 6.2. Both traps have an RF of 5 MHz, and their RF voltages are ≈512 V and ≈256 V for the quadrupole and octopole, respectively. This ensures that the Mathieu q_r parameter is matched for the two traps, which is the appropriate condition to compare different traps for a compensated ion. The collision parameters are adjusted so that the first collision takes place at time $t = 0$ and because of the mutual interaction of the ion and the atom before the collision, the ion shifts from its compensated position and the resulting post collision energy of the ion increases. In the process of the collision, the action of the electric field on the colliding partners has made the collision more energetic than the initial ion and atom energies would suggest. The numerical treatment for this calculation closely follows that of Cetina et al. [90].

Conventionally, most experimental efforts to study cold ion-atom collisions have favored the

quadrupole trap [70], barring a few exceptions [45, 191–193]. In contrast, for RF traps with larger numbers of electrodes, six, eight and twelve, the gradient of electric field in the neighborhood of the trap center is much smaller than that of the quadrupole. Due to this, as shown in figure 6.3 a similar ion-atom collision in an octopole trap would transfer significantly less energy to the ion-atom system than in the case of the quadrupole. Although the two traps used in figure 6.2 have the same value of Mathieu parameter q_r, the secular frequencies in eight-pole trap are much smaller than that of four-pole trap. Due to the reduced RF amplitude close to the trap center, as the order of the poles increase, the energy gained by the ion during collision reduces. It should be kept in mind that the octupole trap does not have a strong restoring force at its center, resulting in the drift of the ion to regions of higher fields post collision, where the ion's micro-motion will come into play.

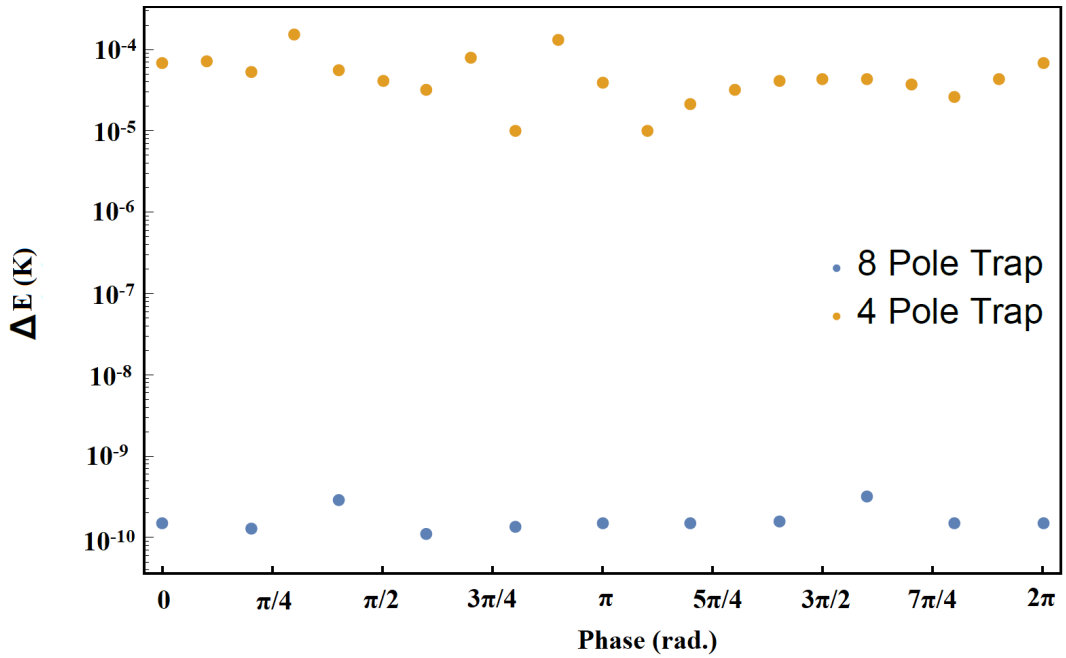

Figure 6.3: The change in the energy of the Ca ion-atom system, initially at rest, with the ion at the trap center post collision is presented. The results for the quadrupole and octopole trap configurations are shown. The energy gained is plotted against the phase of the electric field at the time of ion-atom's closest approach.

The above example illustrates that the higher multipole trap excites less collision induced heating in a single collision event based on just the collision energy change in figure 6.2, and therefore working with a higher order multipole trap appears to be advantageous. Thus, figures 6.2 and 6.3

together provide a quantitative description of ion heating in a collision which has a direct dependence on the form of the external potential in which they collide. The figures summarize the consequences of the low energy classical ion-atom scattering problem in the presence of a time-dependent field, which has a dramatic impact on the fate of the collision. While the reduced one-dimensional problem has been solved by Cetina et al. [90] for the quadrupole potential, this two dimensional treatment is important, because of the $x^m y^n$ product terms in the higher order multipole traps, to illustrate the advantage of the octopole over the quadrupole configuration, in a quantified manner.

However, when faced with building an experiment, a broader view of the requirements is needed, in order to determine the choice of permanent geometry of the trap to be built. We therefore take this analysis of comparative study of the ion trap designs, further to arrive at the good conclusion of which trap is suited best.

6.3 Ion trap configurations

A linear multi-pole Paul trap has 2*k* (*k*, integer) cylindrical electrodes of diameter a, which are all held parallel to the trap axis z, such that on the transverse plane, the centers of the electrodes are equidistant points on a circle of radius r_0. Hence, such traps are referred to as 2*k*-pole traps, the simplest of which is a linear quadrupole trap (k = 2,4-pole trap). In the common modes of operation, radio frequency electrical fields applied to the electrodes create a trap at the center of the geometry. This is achieved by applying ac voltages of opposite polarity to alternate electrodes, which spatially confine charged particles in the transverse direction. For confinement along the trap axis, another set of electrodes (end caps [75], segmented electrodes [190]) are used, to which dc voltages are applied in order to obtain the necessary trap depth and curvature along the symmetry axis of the 2k-pole trap. In what follows, we shall solve the for the ion trajectories two dimensions.

The trapped ion trajectories obey the Mathieu equation, the solution of which can be decomposed into two parts [164]. The macro-motion is characterized mainly by the pseudo-potential (proportional to r^{2k-2}, where *r* is the distance from trap center in the transverse plane) seen by the ion,

which is the time averaged trapping field over the fast RF cycles. The micro-motion of the ion is its response to the electric field at the instantaneous position of the ion. For most experiments with ion traps, micro-motion is undesirable as it limits the cooling of the ions, induces decoherence or limits ion control.

As higher order pseudo-potentials would exhibit a potential of the kind $r^n, n \geq 2$ is the potential form at the center of the electrodes, ions in a higher order 2*k*-pole trap are expected to experience a lesser electric field on average compared to ions in a four-pole trap. Thus, the magnitude and effect of micro-motion would decrease with an increase in the order of a 2*k*-pole trap, which is one of the motivations for building them. This is illustrated in figure 6.2, where the micromotion is not visible on the trajectories for the eight-pole trap but distinctly visible on the four-pole trap. In principle, the number of poles can be very large, though necessary a/r_0 ratios for optimum stability of the trap and geometrical constraints have seen experimental configurations up to 22 poles [194].

For each of the configurations in figure 6.1, we also analyze the dynamics of the ion using the virial theorem. The success and applicability of the virial approach is established and is found to be very valuable, as it reduces a complex dynamical non-linear problem with time variation of the potential and cross terms in the coordinates to one that can be solved almost by inspection. However, this approach needs to be validated carefully with explicit numerical trajectory calculations so the conclusions arrived at are shown to be reliable, once and for all. Since in a linear Paul trap and its extensions discussed above, the configuration comprises the multipoles and two DC biased, end cap electrodes, in the analysis for the optimal trap below, we confine ourselves to the plane perpendicular to the axis of the trap as illustrated in figure 6.1. This results in simplification and still allows for the problem to be analyzed in terms of mean energy.

6.4 Virial theorem for 2*k*-pole traps

Let ac voltages of $V_0 \sin \omega t$ and $-V_0 \sin \omega t$ be applied to alternate electrodes of a linear Paul trap, i.e., V_0 is amplitude and ω is the frequency. The 2-D pseudo potential (in the transverse plane)

experienced by an ion due to the 2*k* electrodes is given by

$$V^* = \frac{k^2 q^2 V_0^2}{4m\omega^2 r_0^{2k}} r^{2k-2}\,, \tag{6.1}$$

where q is the charge and m is the mass of the ion and r_0 is the size of the trap given by the distance from the center of the trap to the center of any electrode [45]. Stable trapping of ions is achieved when the amplitude of micro-motion is smaller than the distance from the geometric center, i.e., when relative change in the electric field amplitude during a micro-motion cycle is small. An adiabaticity parameter, η is used to quantify this,

$$\eta = \frac{k(k-1)2qV_0}{m\omega^2 r_0^k} r^{k-2}\,. \tag{6.2}$$

When $k = 2$, η is a constant (i.e., for a four-pole trap) and the well known Mathieu stability criteria apply [195]. It should be noted that the Mathieu parameter q_r in 2-D is the same as η and thus the four-pole ion trap is stable if $\eta \leq 0.908$. When $k > 2$, stability of the ion trajectory is probabilistic and subject to initial conditions of the ion. In higher order traps, it is found that only for $\eta \lessapprox 0.3 \equiv \eta_{max}$, stable ion trajectories exist. This limits the spatial extent to which the ion can span, r_{max} as η is a function of r (for $k > 2$),

$$r_{max} = \left[\frac{\eta_{max} m\omega^2 r_0^k}{2k(k-1)qV_0}\right]^{1/(k-2)}\,. \tag{6.3}$$

Thus, the effective trap depth for a $2k$-pole trap is given by $V^*(r_{max})$, which is very different from that of a four-pole trap. In such a scenario, the average kinetic energy of a trapped ion is described by

$$\langle T_{tot}\rangle = \langle T_s\rangle + \langle T_\mu\rangle\,, \tag{6.4}$$

where $\langle T_{tot}\rangle$ is the total kinetic energy, $\langle T_s\rangle$ is the mean secular energy and $\langle T_\mu\rangle$ the micromotion energy. The average secular kinetic energy $\langle T_s\rangle$ of a particle bound by a potential of form equation 6.1 is given by the virial theorem as

$$\langle T_s\rangle = (k-1)\,\langle V^*\rangle\,. \tag{6.5}$$

The amplitude of micromotion is proportional to the potential experienced by the ion. The average kinetic energy in the micromotion thus turns out to be the same as stochastic mean in the secular trajectory. This is given by the following two equations.

$$\langle T_\mu \rangle = \langle V^* \rangle \tag{6.6}$$

$$\langle U \rangle = 2 \langle V^* \rangle \ . \tag{6.7}$$

Therefore, the ratio between average total kinetic energy and average potential energy $\langle U \rangle$, of an ion, defined here as ν, in a 2*k*-pole trap is

$$\nu = \frac{\langle T_{tot} \rangle}{\langle U \rangle} = k/2 \, . \tag{6.8}$$

The immediate consequence of equation 6.8 is that, for the same ion energy, the larger fraction of the ion energy is kinetic. This implies that, when all other things are equal, the ion in the center of the higher order trap will be more energetic than its quadrupole counterpart, which in turn implies that the ion has to be cooled down much further in order to be centered at the trap. This is detrimental to the execution of the ion-atom collision experiment with higher order multipoles in the manner discussed in Section 6.2, where the ion has to be positioned at the trap center as precisely as possible in order for it to be well compensated. So while it is indeed true that there is an advantage to having an higher order trap, to keep collisional heating in check, there are problems with initializing the system, flagged by the virial theorem.

6.5 Results

To quantify the results, we study numerically the dynamics of a single ion in various 2*k*-pole traps. The simulations have been done for a Calcium ion, $^{40}Ca^{+}$ in 2-D. The potentials have been generated in SIMION software with $r_0 = 0.707$ cm and $a = 0.1$ cm have been used for the electrode

sizes. The RF frequency applied, ω is kept constant for all traps at $2\pi\times$ 5 MHz.

6.5.1 Dynamics of an Ion in a 2*k*-Pole Trap

An electric potential $V(t) = V_0 Sin(\omega t)$ with opposite polarity was applied to alternate electrodes. The time dependent potential energy profiles for an ion, $U_{2k}(x, y, t)$ were generated both using the ideal functional form and using SIMION [196] software and used to solve the equations of motion for the ion,

$$m\frac{d^2x}{dt^2} = -q\frac{\delta U_{2k}(x, y, t)}{\delta x}, \tag{6.9}$$

$$m\frac{d^2y}{dt^2} = -q\frac{\delta U_{2k}(x, y, t)}{\delta y}\,. \tag{6.10}$$

Using the trajectories obtained by solving the above coupled differential equations, we calculated the ratio of $\langle T_{tot}\rangle$ and $\langle U\rangle$ of the ion in the trap. The values of this ratio obtained when computed for a multiple of the period of the secular motion are shown in Table 6.1. We show, with the numerical results, that the relation, equation 6.8 derived from virial theorem holds. This is true even in the presence of damping, the motion of the ion in the trap is still consistent with the virial theorem. The damping term was added to the equation of motion of the ion, to model laser cooling.

In order to make the coefficient of the damping term realistic, it was calculated from the scattering force due to laser beams at saturation intensity. This calculation does not capture the stochastic nature of laser cooling and hence fails to provide a cooling limit as in the case of real laser cooled atoms. Using the trajectories of the ion calculated with and without damping, we calculated the ratio of $\langle T_{tot}\rangle$ and $\langle U\rangle$ in the trap. These numbers are given in Table 6.1. It can be seen that the results of the virial theorem for ion traps hold even with damping or laser cooling.

Table 6.1: Virial analysis of $2k$-pole traps in normal operation. Results for the coefficient ν, from simulated trajectories using various appropriate potentials are shown which illustrate the compliance with equation 6.8. The average values are computed over several macromotion cycles and the standard deviation is shown as the error.

Traps	Quadrupole $k = 2$	Hexapole $k = 3$	Octupole $k = 4$	Do-decapole $k = 6$
Ideal Potential	$\frac{V(t)(y^2-x^2)}{r_0^2}$	$\frac{V(t)(3x^2-y^2)y}{r_0^3}$	$\frac{V(t)(6x^2y^2-x^4-y^4)}{r_0^4}$	$\frac{V(t)(x^2-y^2)(x^4-14x^2y^2+y^4)}{r_0^6}$
ν: Theory	1	1.5	2	3
ν: Ideal potential	1.00 ± 0.05	1.50 ± 0.07	2.01 ± 0.09	3.00 ± 0.17
ν: SIMION potential	0.99 ± 0.03	1.48 ± 0.07	2.03 ± 0.08	1.01 ± 0.20
ν: constant damping	1.10 ± 0.06	1.55 ± 0.08	1.98 ± 0.09	3.04 ± 0.19

The evolution of ion trajectories in the different trap potentials throws up some interesting results. In ultracold atom physics, it is normal to evolve the ion trajectories from the origin, with an initial velocity. In addition, for laser cooled ions, the ions accumulate at the bottom of the defined secular potential. When cooling multiple ions, laser cooling of ions leads to a space charge limited density distribution of the cooled ions. In quadrupole potentials, these form ion crystals [51] and in higher order multipole potentials a dense localized distribution of ions is formed, which to the best of our knowledge has not led to ion crystals being produced [193].

In the case corresponding to the single compensated ion, it is required to first produce this ion. This will be done by ionizing an atom from a distribution of atoms contained within the trap and followed by subsequent cooling of the ion. With this motivation we consider the motion of an ion within the trap volume, for the different multipolar configurations. Unlike previous studies which deal with phase space and real space trajectories in such traps for an ion created at the trap center with finite kinetic energy, we simulate trajectories for a realistic case of an ion being created away from the trap center with zero initial kinetic energy, these trajectories are shown in figures 6.4 and 6.5. For specific initial phase relations, the probability distribution of the ion position with respect to the radial coordinate is shown in figures 6.6 and 6.7 for the multipole configurations. The insets at the top of each panel in figures 6.6 and 6.7, show the phase space plot of the ion trajectories in one direction. For each trajectory, the coefficient ν is calculated over multiple periods of the secular motion. In each case the virial theorem holds within the numerical error and its value corresponds closely to the theoretical value of the trapped ion in its secular potential [14, 87]. For all traps, the radial position distribution for the non-zero initial phase, corresponding to the ion being confined within a lower and an upper bound in r. The most limiting radial confinement is seen for an ion created equidistant from the two nearest electrodes. Another observation we make is that, in this limiting case of the initial phase, the lower bound for r overlaps with the initial radial position, in this case $0.1r_0$, for a quadrupole trap and the upper bound for r overlaps with the initial radial position for a higher order trap. The results for $k > 2$ in figures 6.6.d-f and 6.7.a-f show that the nature of the phase space trajectories varies significantly with the initial phase, thus implying that calculation of statistical averages is further complicated in higher order traps.

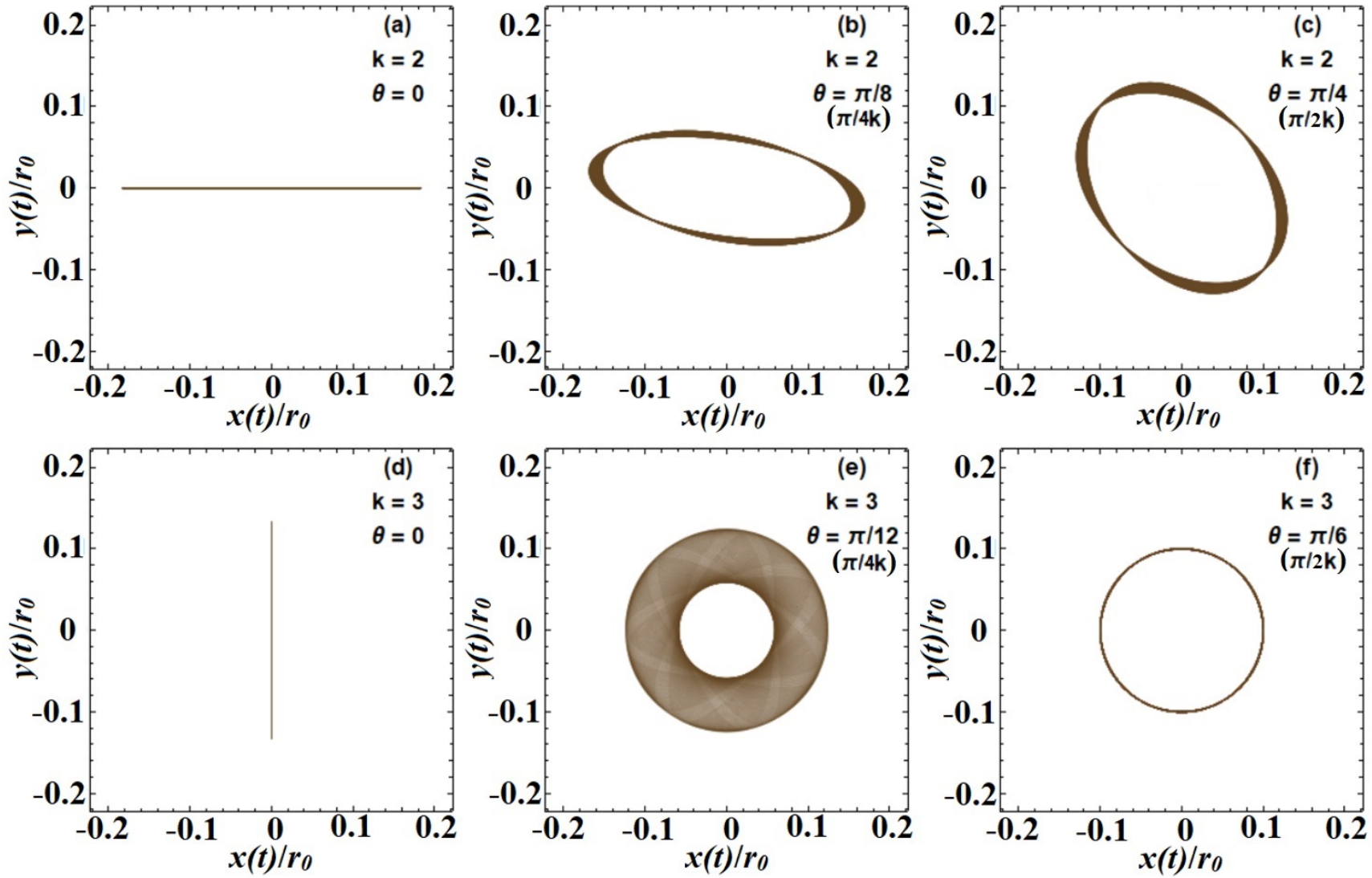

Figure 6.4: The real space trajectories for the mentioned initial position (r=0.1r_0, $\theta = 0, \pi/4 and \pi/2k$ respectively) of creation of ion in 4 and 6 pole trap configurations is shown.

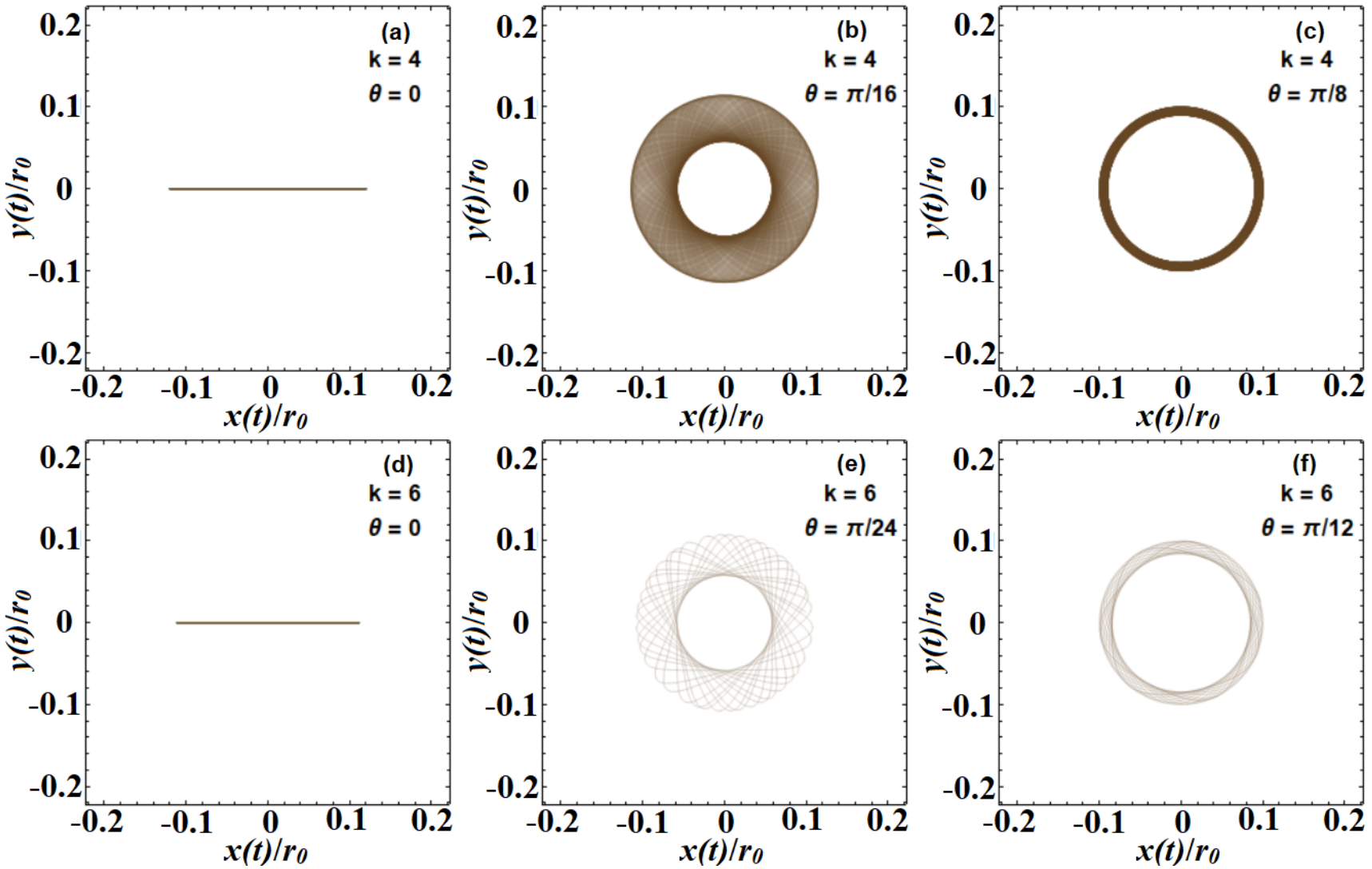

Figure 6.5: The real space trajectories for the mentioned initial position (r=0.1r_0, $\theta = 0, \pi/4k and \pi/2k$ respectively) of creation of ion in 8 and 12 pole trap configurations is shown.

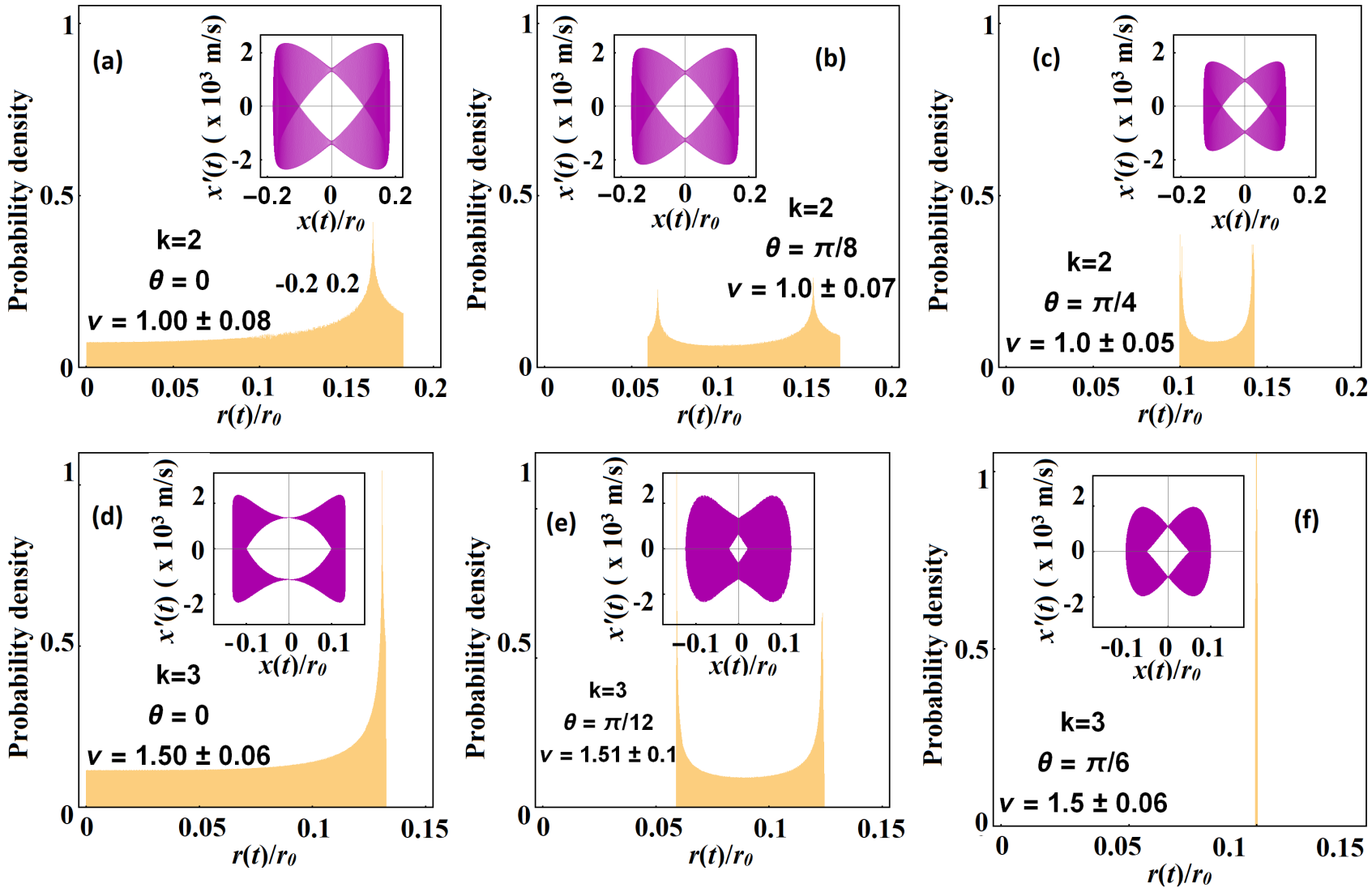

Figure 6.6: Probability distribution of finding the ion at a radial distance r from the center of the trap in 2-dimensional 4 and 6 pole traps, for an ion created at $r(0) = 0.1r_0$ and angular coordinate θ. The inset2s show the phase space trajectories associated with the respective trapping configurations and the computed value of ν, specific to each case, is shown in the panels.

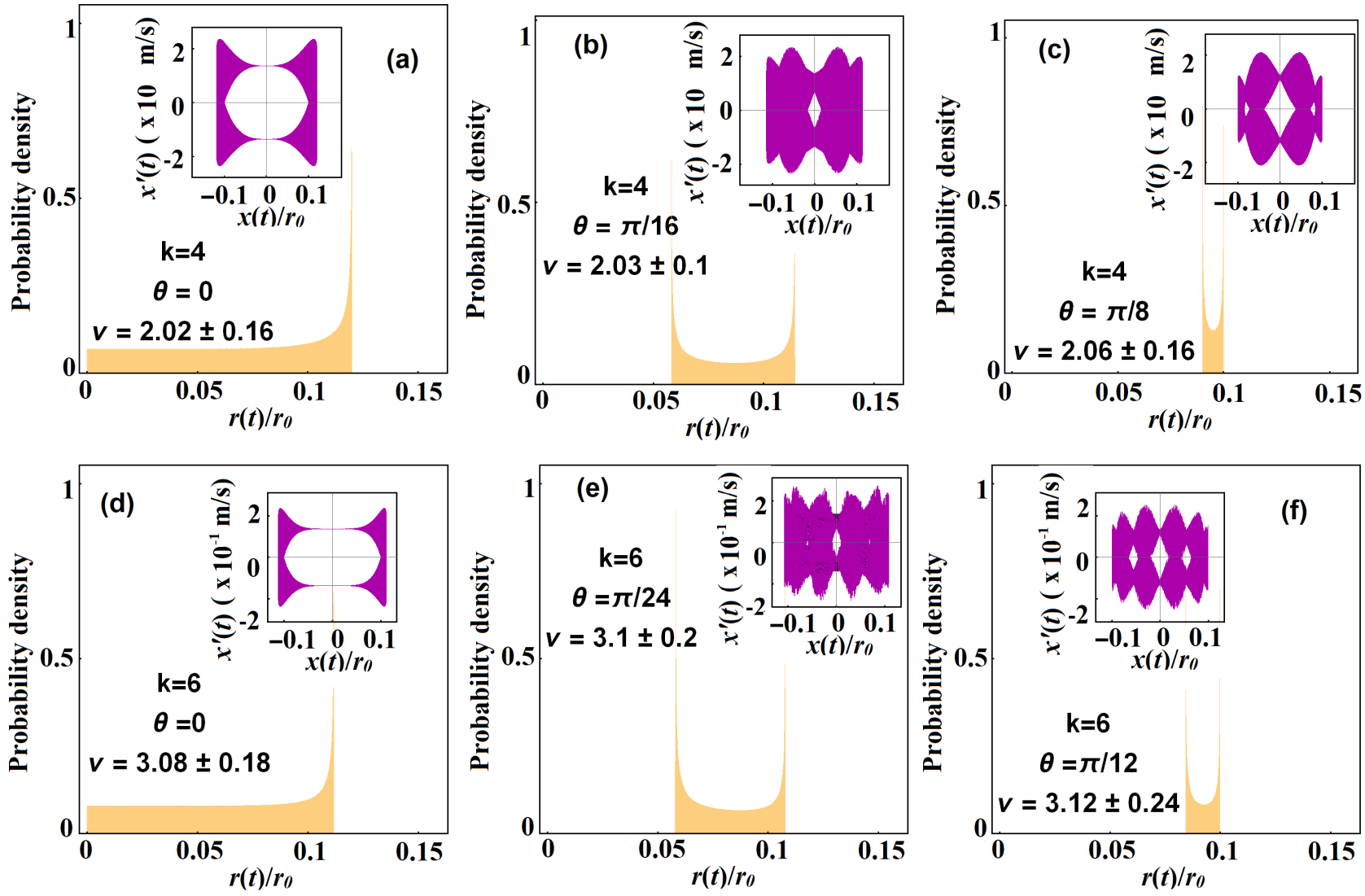

Figure 6.7: Probability distribution of finding the ion at a radial distance r from the center of the trap in 2-dimensional 8 and 12 pole traps. The insets show the phase space trajectories associated with the respective trapping configurations and the computed value of ν, specific to each case, is shown in the panels.

This dependence on the initial phase can be attributed to the presence of $x^m y^n$ terms in the potential form of higher order traps, leading to the coupling of the motion in the two dimensions. Despite the separate nature of phase space trajectories, the virial theorem result $\nu = k/2$ is found to be valid in every individual case. It can be observed consistently in all configurations that, the case where the ion is created equidistant from the nearest two electrodes, the radial position coordinate distribution is the narrowest with the least maximum ion velocities. The real space trajectory of an ion in a four-pole trap, shown in figure 6.4.a-c is close to an ellipse in two dimensions and for the case of the limiting phase, the lower bound of the radial orbit occurs at $0.1r_0$ and, due to micromotion, the upper bound of the radial coordinate appears as broadened in the probability densities shown in figure 6.6.a-c. However, the real space trajectory of an ion in traps with $k > 2$ spans a circularly symmetric region between two radial bounds, as seen in figure 6.4.d-f and figure 6.5.a-f. The inner bound occurs at $r = 0$ for $\theta = 0$ and at a finite radius for non-zero θ, this manifests as the two radial peaks, which are sharply cut-off, in the density distributions in figure 6.6.d-f and figure 6.7, for higher pole traps, at the turning points. The radial confinement for the limiting value of θ is narrowest for $k = 3$ (figure 6.6.d-f) and becomes wider for higher k traps (figure 6.7).

To address what the chance is, for finding an ion at a particular distance from the trap center, we calculated two scenarios. In the first, illustrated in figure 6.8a, the probability distribution of the ion created at a distance of 0.1 r_0 from the origin, with zero initial velocity and at different angular displacements with respect to the electrode axes was computed. As seen from the probability density plots in figure 6.6, the ion coverage of the trap volume has tremendous variety. It is therefore important to understand the statistical likelihood of the ion occupying a particular region of space. This was therefore studied with respect to the angular creation of the ion in the multipole trap in figure 6.8a and its inset. The most reasonable experimental situation is that there is an cold atom ensemble located about the ion trap center. If the ion is to be created from such an ensemble of atoms by threshold ionization, what would the spatial distribution of the ion be? This is illustrated in figure 6.8b where the probability distribution of the ion created at a distance generated from a two-dimensional Gaussian distribution of width $0.05r_0$, with zero initial velocity is plotted. The spatial density distribution of the ion, over repeated instances, is illustrated in the

inset. So, figures 6.6 and 6.8 allow us to conclude what the trapped ion distribution would be that we would have to deal with in an experiment, in particular instances and on average.

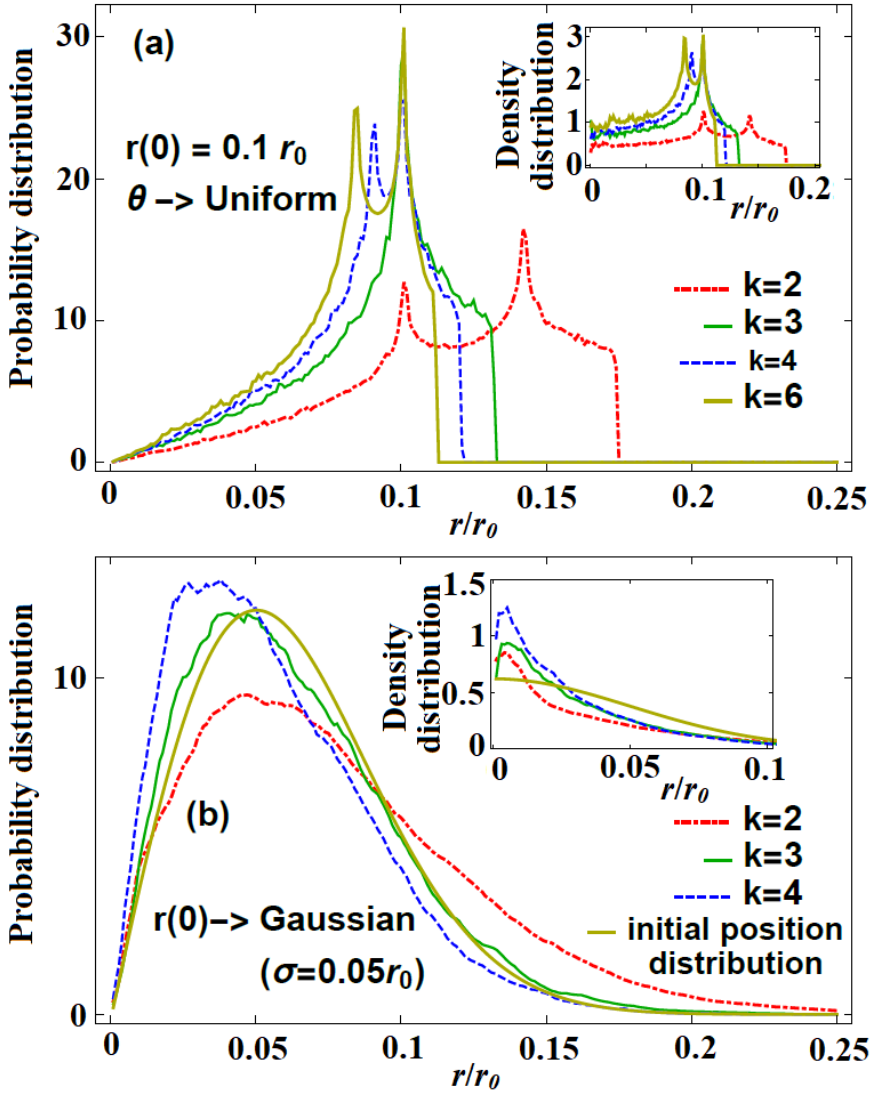

Figure 6.8: Panel (**a**) shows the probability distribution for an ion created at radial distance of 0.1 r_0, with random angular coordinate θ for various $2k$-pole traps. Panel (**b**) shows the probability distribution for an ion created with a Gaussian distribution of width $0.05r_0$, centered with the ion trap for various $2k$-pole traps. The insets show the corresponding density distribution.

The agreement of the hexapole and the do-decapole electrode configuration with the virial theorem is also shown in table 6.1. All values are as expected, except in the case for do-decapole trap using SIMION potentials, where the ratio of $\langle T_{tot} \rangle / \langle U \rangle$ is consistent with that of a quadrupole. After some investigations, we conclude that this is a finite grid and grid size numerical effect,

where the pseudo-potential is effectively decomposed into three independent quadrupole potentials, which is what is reflected in the value of the $\langle T_{tot} \rangle / \langle U \rangle$ ratio in that instance. When the potentials analytic form is used, the value of $\nu = 3$ results for the same ratio, as per expectations both with and without damping. It is therefore an instance where one has to be cautious with the results of explicit numerical calculations. This instance underlines the necessity for cross checking the qualitative and the explicit calculations against each other. Also, this result shows the possible issues with a practical do-decapole trap, as it is an idealization to preclude on the basis of a perfect analytical potential.

6.5.2 Comparison of ion cooling efficiency

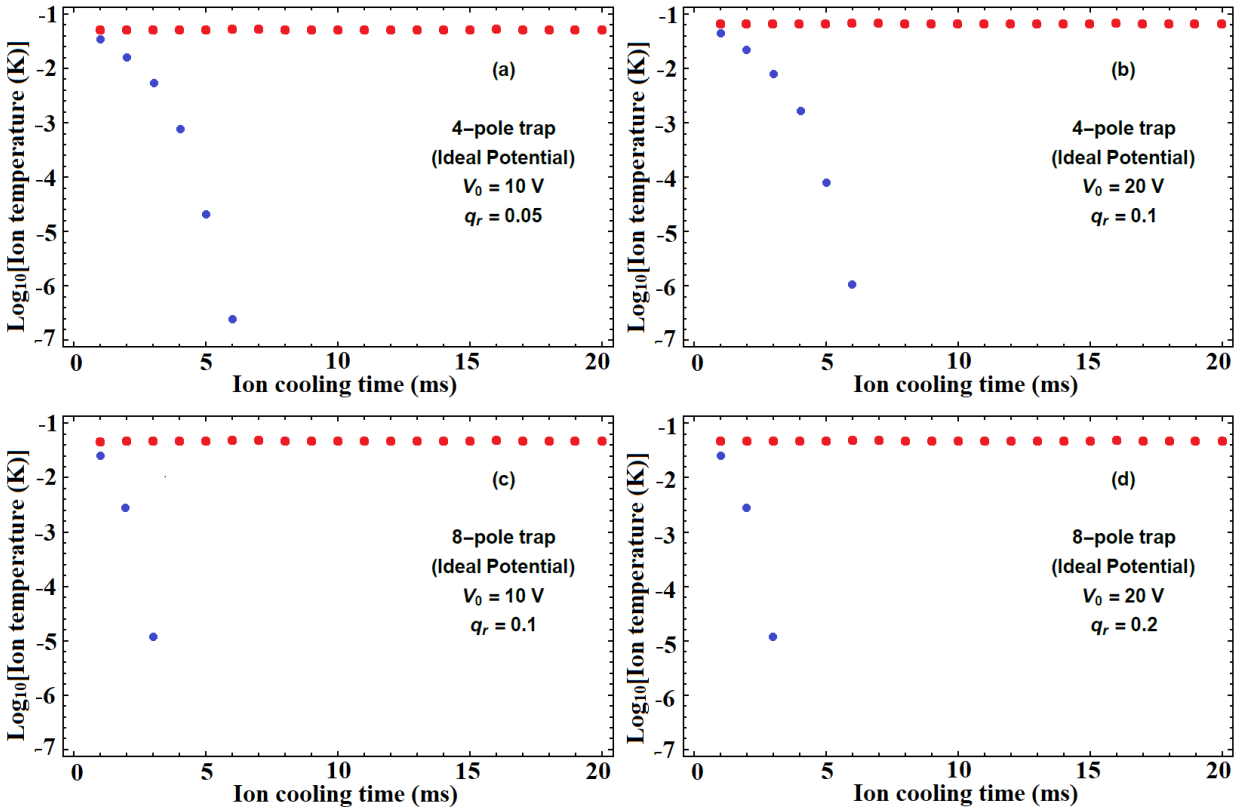

Figure 6.9: The temperature of an ion held in ideal 4-pole and 8-pole trapping potentials are shown with constant damping (blue points) and without damping (red points). The variation of cooling rates in both trap potentials with the parameter q_r can be seen. The damping coefficient is equivalent to the best achievable laser cooling for a $^{40}Ca^{+}$ ion, in all panels.

The results obtained with constant damping term for each of the configurations discussed above, allow us to deduce the effectiveness of higher order traps for laser cooling based experiments in general. The distribution of ion velocity varies significantly with the location of the ion in all linear Paul traps. Therefore, the phase space volume spanned by the ion shrinks at different rates at different times of the ion trajectory. However, it is consistently found in every macromotion period, that the relation in equation 6.8 holds for all stable traps. The start and end of macromotion cycles are identified with a micromotion cycle within which the potential energy of the ion becomes zero, one additional time, while $V(t) \neq 0$. We find that the virial relation between potential and kinetic energies hold even for unstable trajectories, when the ion is yet to exit from the trapping volume.

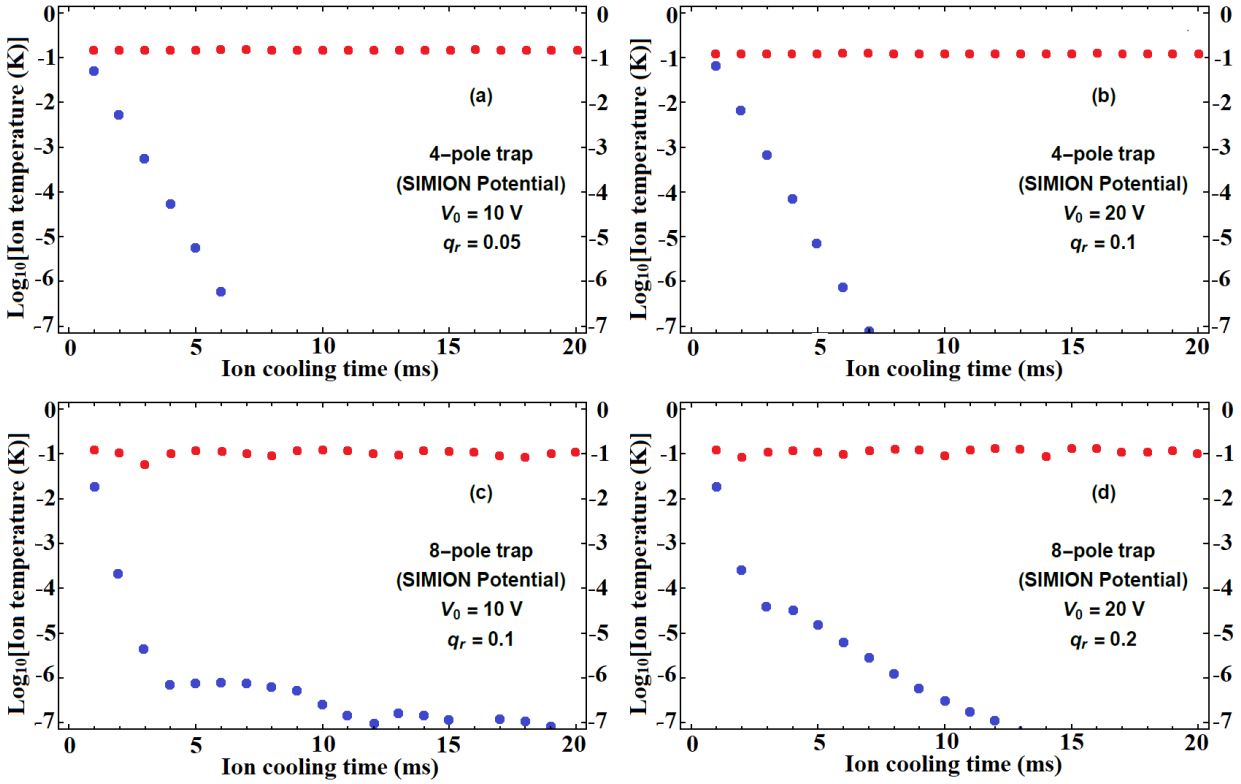

Figure 6.10: The temperature of an ion held in 4-pole and 8-pole trapping potentials, generated using SIMION software are shown with constant damping (blue points) and without damping (red points).

The coefficient of damping used to simulate these set of trajectories mimics the effect of laser cooling of a Ca^+ ion. To do this, we evaluate the optimum force imparted due to laser cooling, as given in chapter 2, and assume constant damping of this magnitude. While this ensures the magnitude

of the damping term is relevant to the application, the effect of finite momentum kicks experienced in laser cooling is not incorporated. As a result, we see that the cooling of the ion obtained here due to damping continues even below the Doppler limit to unrealistic temperatures. However, as we simulate the trajectories using SIMION potentials, we see that the residual potentials resulting from imperfections due to discretization, does not allow ion cooling to such low temperatures, see figures 6.9, 6.10.

From figure 6.9, shows that the cooling rate is better with lower q_r for both the traps, and that for equal q_r, higher pole trap provides a better rate of cooling, for ideal potentials. However, if we take the discretization effects in SIMION potentials as a proxy for imperfections in a practical trap, we obtain from figure 6.10, that the cooling rate in practical higher order traps decreases as the ion approaches ultracold temperatures. However, this is likely to be an artifact of the platform rather than a physical effect.

6.6 Inferences from the computation analysis

We first observe that the agreement of the computed ion motion with the virial theorem holds well, for all the multipole traps considered here. It is therefore reasonable to conclude that an analysis based on the proper application of the virial theorem provides a legitimate platform for discussions on what to expect of ion traps, without performing detailed computations. Since we initiate the ions at a distance from the center with zero energy, we do not have a length scale for each trap corresponding to the energy of the ions; therefore, we chose to keep the parameter q_r fixed when comparing various multipole traps. From the discussion above, given the same RF frequency and fixing the operating value of $q_r = 0.1$ for all multipole traps, we see that with increasing k, the trap depths reduce. This is the consequence of the fact that for a constant q_r, $V_0 \propto 1/k$, so, as the number of poles increases, the RF voltage required for a stable trajectory decreases. In addition $r_{max} \propto [1/k(k-1)V_0]^{(1/(k-2))}$, which means the radius for which the adiabatic operating condition of the ion trap persists, shrinking with increasing k. If the ion motion is not described by the adiabatic condition, then the conventional description of the trapped ion motion breaks down and the motion becomes sensitive to small changes. This implies that the kinetic energy of the trapped

ion has to be lower at the time of production. That is determined by the extent of cooling of the atoms from which the ion is created, which cannot be reduced arbitrarily. Creating an ion with external ionization processes needs to be performed with greater care for higher order multipole traps.

Within the regime of applicability of the virial theorem, $\langle T_{tot} \rangle / \langle U \rangle = k/2$ applies, as seen in Table 6.1. When we allow for the presence of stray fields and field inhomogeneities, the requirement of a minimum trap depth is produced. In this situation, if a certain minimum trap depth is required to hold the ion, then the kinetic energy is increases as $k/2$ times the mean trap potential energy. This can be problematic in the actual realization of a highly controlled multipole trap.

A practical issue for higher order multipole traps is that the secular motion slows down with respect to the applied RF frequency. It therefore takes the ion much more time to span the full phase space for the trapping conditions, and this time increases with the number of multipoles. While this poses a significant computational challenge, it is also detrimental to the time scales of typical dilute gas experiments. This is because the precision with which the ion's state can be known is harder to determine and therefore to set up a controlled ultracold ion-atom experiment of the kind described in the beginning without the deleterious effect of the RF excitation of the ion during collision becomes more difficult with larger k.

For the same q_r and RF frequency, higher order multi-pole ion traps have significantly lower trap depths, compared to the corresponding quadrupole trap. When $k > 2$, the spatial extent of stable trapping is much smaller than the physical size of the trap, unlike in a quadrupole trap. This result, when seen in the context of a large number of ions in the trap and relative ion density in higher order traps, is at its maximum for a finite r, and the density at $r = 0$, decreases as $2k$ increases. This is undesirable for interactions with spatially localized cold atoms.

Another problem of higher order traps is that the pseudo-potential becomes more and more flat in a higher multi-pole trap, the cooled ion is not spatially confined to the center of the trap. This is likely to be a problem for experiments where ion localization is required. Another deduction that can be made from the virial theorem analysis is that the prospects of laser cooled ion crystals in higher order multipole traps is quite bleak. This is because, for crystals to be created, multiple

points in space are required where the net force due to laser cooling, external drive fields and ion-ion repulsion become zero. Only this will allow the ions to be motionless at those locations and therefore crystallize. However the cooling requirements for the ion in higher order traps, as discussed above, is much more stringent. This is perhaps why, in higher order multipole traps, ion crystals have remained elusive, despite advances in laser cooling.

Recent studies with higher order multipole traps have shown that the flat potential is dimpled due to field imperfections and this results in a potential which has local quadrupole minimas within the higher order multipole field [193, 194]. In this scenario, the lowest point of the higher order multipole trap converts into a defined number of quadrupole traps, depending on the order of the multipole. So, in the case of really efficient cooling, it is quite likely that the ions find themselves in the dimpled quadrupole potential, which is sensitive to the local field environment. However, since these local minimas are not at the geometric center of the trap, the utility of these for interactions with a localized atomic ensemble is moot. In this case, when the ion is trapped in the local quadrupole field, the discussion accompanying figures 6.2 and 6.3 has limited applicability.

Quadrupole traps have some advantages over higher $2k$-pole traps like larger trap depths, stability, better ion loading probability and deterministic stability. In order to capitalize on the advantages of both kinds of traps when needed, one can use either two concentric traps, one four-pole and another a higher $2k$-pole trap or operate a higher $2k$-pole configuration with modified polarities on different electrodes to make it an equivalent four-pole trap. Implementation of higher order linear multipole trap setup can provide versatility for experiments. In figure 6.11, we show a few examples of alternate operation schemes for obtaining an equivalent quadrupole trap. This gives the opportunity to switch between a quadrupole and a higher order trap to exploit the best of both configurations. The large trap depths of the quadrupole trap and better shielding from stray electric fields can be accessed in the effective quadrupole schemes and relatively low electric field experienced by ions in higher order traps near the trap center can be accessed in the regular $2k$-pole trap scheme, making it a versatile tool. While the configurations shown in figure 6.11b-d lead to an effective quasi-quadrupole trap, the scheme shown in figure 6.11a leads to a pure quadrupole trap with the additional grounded electrodes ensuring the points of zero potential, thereby providing additional stability against stray fields.

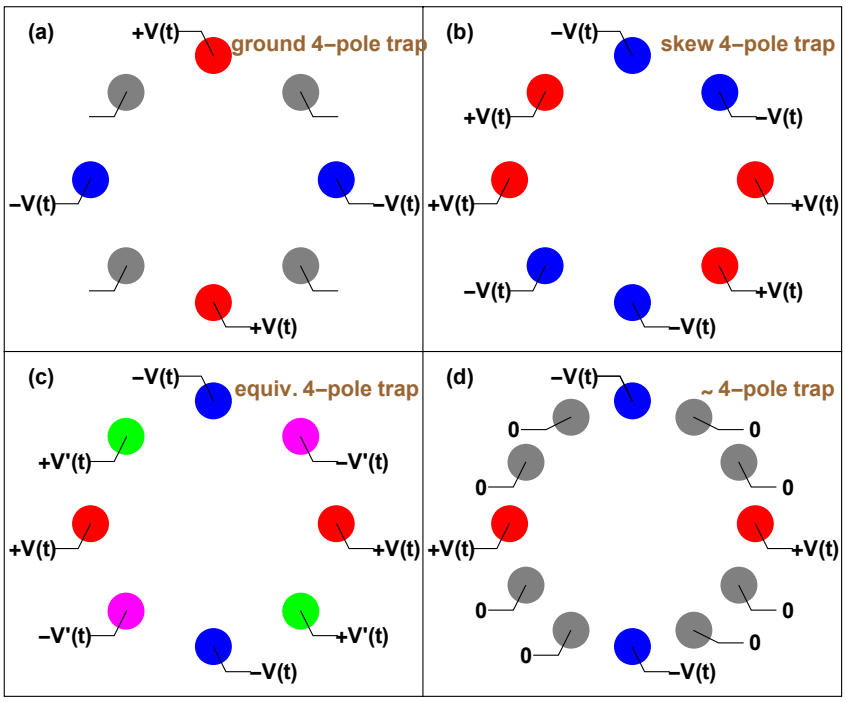

Figure 6.11: Alternate trap configurations for using an 8-pole or 12-pole setup as a modified quadrupole are shown. Panel (**a**) is an 8-pole structure with alternate electrodes explicitly grounded. Panel (**b**) shows a skewed quadrupole trap. Panel (**c**) shows an effective quadrupole trap with an 8-pole setup, where successive electrodes are at a phase difference of Pi/2. Finally, panel (**d**) shows a 12-pole structure, with a quadrupole field configuration and multiple shielding electrodes.

Putting together all the above results, it is not easy to see the practical advantage of using a higher order multipole trap to confine the ion for ultracold ion-atom physics. This is because such experiments are performed with both positional and state control of the colliding partners and the spread in position of the ion for a higher order multipole is experimentally hard to overcome. It is perhaps more advantageous to work with a very weak, well shielded quadrupole trap. The trap configurations in figure 6.11 are a path to harness the advantages of the quadrupole trap and the higher order multipole trap. However such a trap configuration may present significant operational challenges. The virial theorem and its explicit verification provides the base for quick conclusions about energetics, which is very useful for complicated potentials. On the other hand, if the objective is to study collisions at higher energy between atoms and neutrals in buffer gas regimes then higher order multipoles can be used very fruitfully for a vast array of experiments, keeping in mind the arguments made above [191, 197]. With all of these studies behind us,we

can make an informed decision to build a linear quadrupole ion trap, for investigating interaction ion-atom systems, as will be detailed in the next chapter.

Chapter 7

The Experiment for Ion Transport Studies

The outcome of the work presented in previous chapters lay the requirements and specifications for the experimental scheme. The planned method for measuring ultracold ion-atom scattering, must be in line with the theoretical developments and constraints identified in the earlier chapters. Here we detail the design and construction of the apparatus. The diverse experimental needs for implementing various schemes for the ion and atom cooling, trapping and detection combined with geometric constraints arising from the symmetry of the individual traps make this challenging. In this chapter, we first explain the schemes of measurements and their requirements and then describe the design and assembly of various components of the apparatus. We provide the details of the laser systems that have been used and their control. Finally, we will show some preliminary results obtained showing the successful operation of various constituent sub-systems of the total apparatus.

7.1 Goals and the approach for measurement

Throughout this thesis we have been consistently developing the theoretical framework, measurable distinct phenomena and optimized designs for the study and measurement of ultracold

ion-atom interactions, in their quantum regime. We have established the need for working with small number of ions to assure stability at the desired low temperatures, and the inability to use non-destructive detection schemes using optical cavities for measuring such small interactions. The theoretical studies for low energy ion-atom scattering and the hopping based scattering in earlier chapters point out that direct measurement of ion diffusion in ultracold atoms can verify the exotic and novel artifacts of these phenomena.

The first of many requirements set by these studies for the apparatus of measurement is of the vacuum environment needed in the region where ion-atom scattering is carried out. The stability of an isolated charged ion at low energies requires that stray collisions with background gas molecules has to be several orders of magnitude lesser than one, in the time interval between ion-atom collisions. This requires the ion and the ultracold cloud of atoms to be in extreme high vacuum (XHV) environment, while allowing for the discharge of atoms that have to be trapped, ionized, etc.

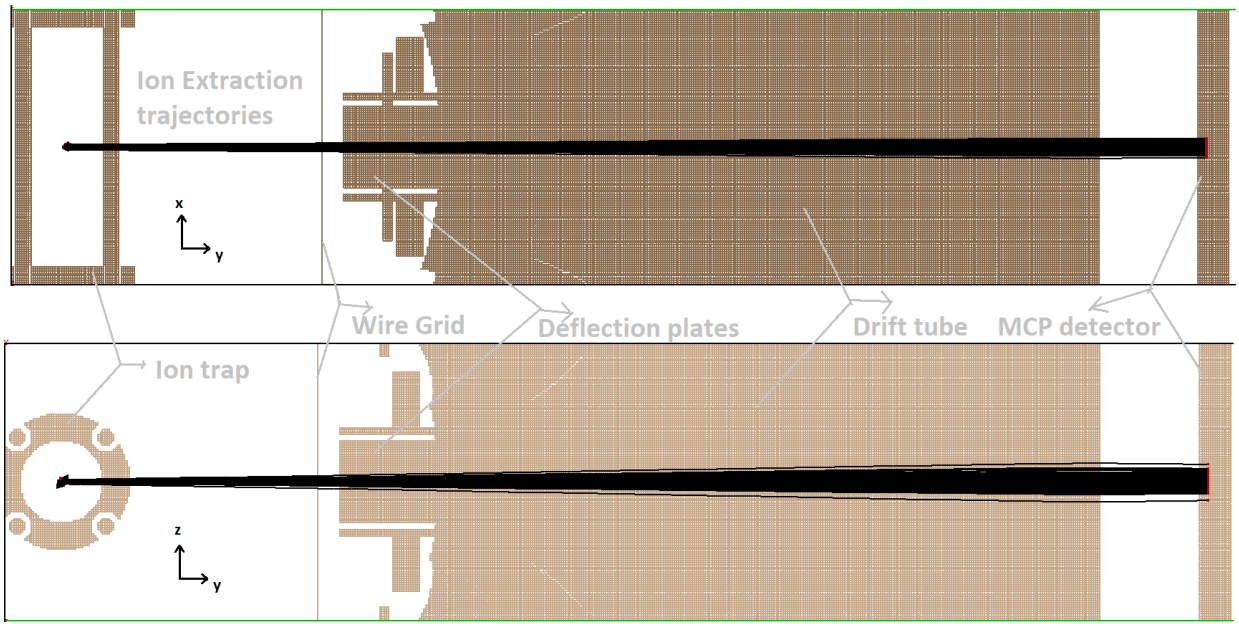

Figure 7.1: The illustration of position sensitive ion destruction is shown. For different positions of the ion at the center of the trapping region, the position of hit on the micro channel detector plane varies accordingly. The readout of the position of hit on the detector plate can be mapped to the ion position, prior to extraction.

The ion diffusion measurement requires creation of the ion at a specific initial location within the

atom cloud, and the detail of the position of the ion (charge) after a time t, over which it interacts with the atoms. Position sensitive ion detection for optically dark ions like Li^+ can be done only destructively [198–200], see illustration in figure 7.1. Therefore, the scheme of measurement involves repetition of the process of creation, evolution for a time t, and final position detection of the ion. This experimental duty cycle will be repeated several times to obtain the average position of ion after various hold times t, as the trajectory evolution of the charge is stochastic. The analysis of these multiple outcomes will result the diffusion phenomena and allow to verify the results predicted by our hopping simulations like ion confinement to a radial shell. The specifics of the components of the apparatus which are tuned to make the following measurements will be shown below.

7.2 Essentials and requisites for DiLi+hium experiment

In order to apply the above methods to study scattering in ultracold ion-atom systems, at their limiting conditions, the demands on the experimental apparatus are stringent and challenging to fulfill. As established in previous chapters, the experiment needs to be conducted with a light and laser coolable atom, which has been identified as lithium, Li. Its homonuclear ion Li^+, which will also be light and cannot be laser cooled, thereby imposes several restrictions on the components to be used in the apparatus. We will elaborate on each of these, starting with the vacuum requirements for stable operation to conduct such studies.

7.2.1 Vacuum constraints

The Vacuum requirements for studying ion-atom scattering are set by the temperatures at which we need to stabilize the ensemble of atoms and the experiments' duty cycle interval over which the incident of ion collision with the background gas must be made negligible. From the simulations discussed in chapter 5, the hold times needed to distinguish the effects of the proposed hopping mechanism, against the prevalent collisional diffusion, ranges from $1 - 20$ ms.

Therefore, we demand that the ion collision rate with background gas must be curtailed to less

than 1 s^{-1} for redundancy. The background gas collision (BGC) rate, k_{BGC} for an ion is given by [201–203]

$$k_{BGC} = \frac{P\,e}{k_B\,T}\sqrt{\frac{\pi\,\alpha_D}{\mu\,\epsilon_0}}\,, \tag{7.1}$$

where P is the background gas pressure, e is electron charge, T is the background gas temperature, α_D is the dipole polarizability of the background gas, μ is the reduced mass for the ion-background gas collision and ϵ_0 is the free space permittivity. We first estimate the pressures needed for a H_2 background gas as it is the typical dominant constituent of vacuum systems. By substituting the lab temperature, 293 Kelvin as the background gas temperature, the reduced mass of $^6Li^+$-H_2 for μ and the dipole polarizability of H_2 gas, 0.787×10^{-30} m^3 [204], in equation 7.1, we get the maximum limiting pressure to have $k_{BGC} < 1$, as 2.4×10^{-8} mbar.

However, in our experiment, we use a non evaporative getter (NEG) pump to handle the residual H_2 gas in the main chamber. Given the fact that our atom ensemble will be vapour loaded to begin with, for redundancy, we also model the background gas as Li. So, by substituting the appropriate reduced mass and the value of α_D as that of Lithium, 24.33×10^{-30} m^3 [205] for the above calculation, we get a more stringent pressure limit of 6×10^{-9} mbar.

While these limitations are estimated for the necessary hold times with the atoms, the vacuum must also be sufficient to have a stable Li atom ensemble at $\approx 1\mu$K temperature. For this we have to be able to perform sub-Doppler and/or optical cooling in the apparatus which require ultra high vacuum (UHV) environments.

7.3 Vacuum System for UHV

The strategy for achieving the estimated vacuum is to design and build a UHV compatible conflat (CF) flanged assembly. We primarily use Ionization pumps to achieve the set vacuum and monitor the pressure using ionization gauge. The choice of the main chamber for carrying out this experiments is chosen to provide ample optical access to its center via multiple optical feedthroughs.

The main chamber

The core of the apparatus is within a stainless steel (SS304) extended spherical octagon chamber of outer diameter 8 inch (Kimball physics Inc: MCF800-ExtOct-G2C8). The chamber has 16 CF16 ports, 8 CF 40 ports and 2 CF160 ports, which allows sufficient optical and electrical access. An ion trap is assembled symmetrically about the chamber diameter that passes through the center of two of the 8 CF40 ports of the chamber. To one of the port along this longitudinal axis of the ion trap, the vacuum pumps are connected, and to the opposite port, a provision to connect a Zeeman slower or a 2D-MOT is provided. We refer to the axis from the Zeeman slower (to be installed later) side to the pumps side as the x-axis. To one CF40 port in the orthogonal direction to the ion trap axis, the drift tube which leads to the MCP detector is connected and the opposite port to this one is used for primary optical imaging. This transverse axis from the optical imaging side to the MCP side is referred to as the y-axis which fixes the axis passing through the large CF160 ports from bottom to top as the z-axis. This leaves 4 CF40 ports which will be ideal for MOT laser beams and the smaller CF16 ports for electrical feedthroughs and extra optical access.

7.3.1 Pumps and plumbing

The chamber, along with the MCP detector side extension, is pumped mainly through a CF40 six way cross mounted via the CF40 port on the chamber (pump port). The arm opposite the chamber is connected with short CF40 spacer and then a fused silica optical feedthrough. A heating wire is wound around the optical feedthrough to avoid deposition of lithium vapour on it, we intend to use this port for introducing high power optical trap beams and UV beams into our setup.

The remaining 4 orthogonal arms of the six way cross connect to a 40 l/s ionization pump (Agilent Valcon plus Starcell 9191243), a titanium sublimation pump (Agilent 9160050) contained within a 300 mm long CF40 flanged tube, an ionization gauge (Agilent UHV-24) for measuring the pressure inside the apparatus and an all metal valve which can connect or disconnect the apparatus with a turbo molecular pump (Pfeiffer: TMU 071). We have attached a non-evaporative getter (NEG) pump of capacity 20 l/s (SAES D20) directly to one of the CF16 ports of our chamber, the port

directly opposite to the one on which lithium dispensers were mounted. The schematic of the full apparatus is shown in figure 7.2

7.3.2 Magnetic coils and final assembly

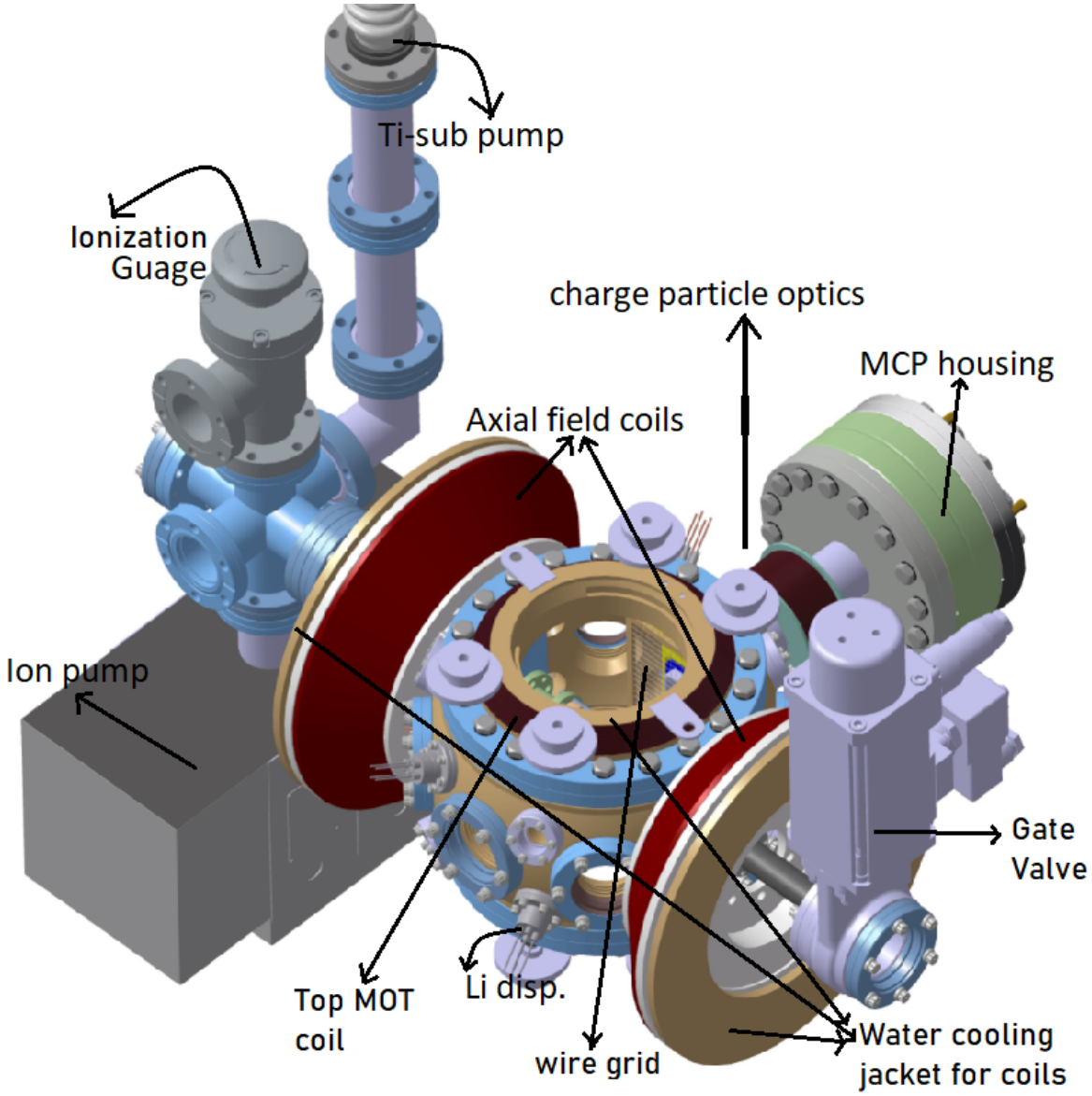

Figure 7.2: The schematic of the full vacuum setup showing the components exterior to the vacuum chamber is shown. The mounting sites of vacuum pump, Li dispensers, all the magnetic coils, and the MCP detector is shown to clarify the geometry of various ports discussed in the main text.

For the top and bottom ports, we use CF160 optical FTs with Kodial windows. Between the top of the FT flange and the Kodial window, is a gap of 10.7 mm that is ideal location for the MOT coils. The MOT coil's former is con-flat with the top of the CF160flange. Although this arrangement allows us to keep the MOT coils close to the center, it calls for a cooling mechanism for the coil so that it does not end up heating the main chamber. So, a water cooling jacket is integrated into the coil former above the flange. The shape of the water cooling jacket is tapered so that it does not further limit optical access to the trap center from this port. The water cooling jacket and the other side of the MOT coil former are used to wind an additional MOT-shim coil which can be used to offset the fields. The main MOT coil is wound using American wire gauge (AWG) 11 wire that can carry up to 16 Amperes of current and the shim coils are wound using AWG 16 wire that can take up to 19 Amperes. A pair of such MOT coils are operated to get the gradient magnetic fields needed to make a lithium MOT.

We have designed a pair of axial coils that can provide magnetic fields along the ion trap axis, so that ions confinement in the other two dimensions can be enhanced. These coils have been designed to provide axial magnetic fields as large as 350 Gauss at the trap center, and can be used to work with Feshbach resonances in Li. In order to achieve such large fields, we have made the coils large with a conical shape so that they do not obstruct the MOT laser beams. These coils are wound on segmented formers, which incorporate a water cooling jacket of their own along with the outer axial-main and inner axial-shim coils.

Since we plan to introduce a Zeeman slower later into our apparatus, we have incorporated a gate valve on the CF40 port opposite to the pump port. The pneumatic gate valve (VAT Mini UHV Gate Valve 01032-CE44) is attached via a custom made extension with CF16 tube and CF40 flanges which go on the main chamber and the valve. The other side of the gate valve is presently bears a CF40 optical FT with fused silica window as this is directly opposite to the pump side window through which we plan to introduce high power optical trap lasers and UV light.

On the CF16 tube between the main chamber and the gate valve, we have wound a small coil which acts as the negative coil for the planned Zeeman slower. Under this coil, the CF16 tube has grooves that host a heating wire to facilitate vacuum baking. The CF40 flanged CF16 tube along

with the negative Zeeman slower coil is first mounted on to the gate valve, then the first axial coil is slipped on to the custom built tube and then the other end of the tube is attached to the main chamber. The pump side axial coil is also first slipped on to the 6-way cross and then the 6-way cross is attached to the main chamber.

The chamber is mounted horizontally 30 cm above the optical table on a frame built with extruded aluminium. The MOT coils are mounted in such a way that the weight of the apparatus is transferred from the main chamber to the aluminium frame bypassing the flanges of the FTs and the MOT coils. On the pump side, the ion pump is directly placed on the table and this is sufficient to support the weight of this part of the apparatus and its overhangs. Additional supports are provided under the MCP flange and under the gate valve, and the two axial coils are independently supported so that their weight is not transferred to the tubes.

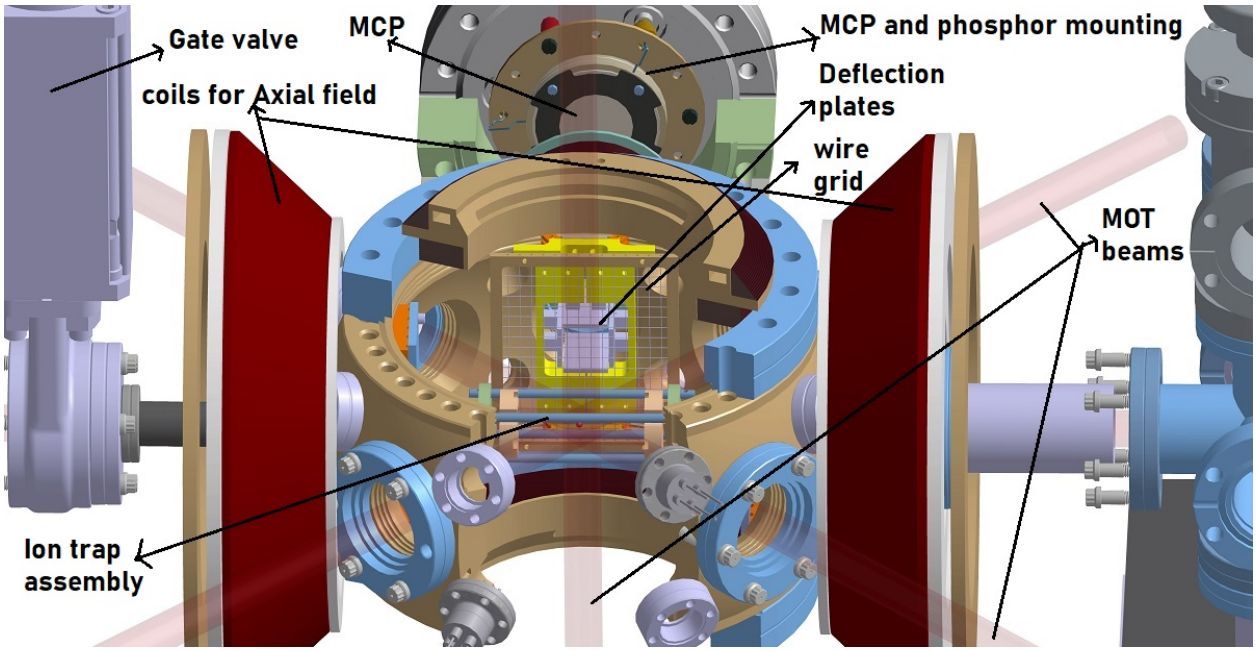

Figure 7.3: Schematic showing the mounting for axial coils, MOT coils, detector tube within the space constraints of the setup.

As a consequence of the complicated setup, we need to perform vacuum bake-outs with the coils mounted. Therefore we wind all coils with double enamel wires that can withstand temperatures above 200 °C. Also, the exterior ends of the electrical FTs will be inaccessible for soldering, etc., after the axial coils and the detector are mounted. Therefore we soldered and crimped all exterior

pins of the FTs with 2 meter long Teflon insulated cables before mounting the coils. The solder material and the epoxy used in the coils were chosen to withstand 200 °C. A schematic of all the coils, FTs and connections is shown in figure 7.3 to illustrate the proximity of the various components and the complexity involved in building this apparatus.

On the remaining CF16 ports, optical FTs with Kodial glass windows were mounted wherever optical access is permitted and CF16 blank flanges were mounted on ports which would eventually be blocked by the axial coils. Our MCP detector is rated to withstand temperatures only up to 150 °C and we can not allow contamination of the detector during bake-outs. Therefore we limit the baking temperatures to 140 °C on the detector side of the setup and maintain a temperature gradient keeping the pump side of the setup at 110° during vacuum bake-outs. We achieve ultra high vacuum (UHV) of $\approx 2 \times 10^{-10}$ mbar as measured by our vacuum gauge. We believe that the vacuum in the main chamber would be as good as measured by the gauge, if not better, due to presence of the NEG pump that is mounted directly on the main chamber.

7.4 Creation, trapping and detection of ions

The first obvious experimental requirement is to have spatially overlapped ultracold atoms atoms and ion(s), allowing the species to interact. As we are primarily interested in homo-nuclear ion-atom systems, the apt method for creation of the ion would be threshold ionization in an ultracold atomic gas. This ensures that the ion is overlapped with the atoms from the instance of its creation, along with giving rise to a zero energy ion, to begin with. When the trapped atoms are at the center of the ion trap, threshold ionization creates the ion(s) close to the ion trap potential minima. We have built a laser to utilize a non-resonant two photon threshold ionization for MOT Li atoms in the excited state.

Two photons from a focused laser beam of wavelength $\approx$ 699 nm will threshold ionize a Li atom in the excited state ($^2P_{3/2}$:F$^{'} = I + (3/2)$) of their first, closed D2 transition. We made a home built laser, using the design that will be described later in this chapter, to address this wavelength. However, initially when the characterization of ion creation, trapping and detection have to be

benchmarked, we use a broadband LED source of central wavelength 340 nm. This LED beam is first collimated and then focused to have the high enough intensities at the common center of the ion trap and the MOT.

To measure the ion diffusion, charge hopping and other effects discussed in chapters 4 and 5, we need to allow the ion to scatter within the atomic cloud in a field free or a field controlled environment. Although, this does not require active ion trapping, having an ion trap will provide some degree of confinement. Also, it may be necessary to implement cooling techniques and compensate for stray fields.

In this experiment, we need to measure the position of the ion(s) in addition to their survival, we need to incorporate a micro channel plate (MCP) based detection. An MCP is a position sensitive ion detector. We propose a process of standardizing the position detection of optically dark Li^+ ions, which needs calibration using a coulomb crystal of fluorescing ions. The plan is to first make a Ca^+ ion coulomb crystal with few ions, image it optically in the trap via cameras to precisely locate the ion position in the trap, before extraction and then map the Ca^+ ion positions in the trap and the positions of ion hits on the MCP. In the next step, we would make hybrid coulomb crystals of both Ca^+ and Li^+ ions, where the lithium ions will occupy the central region because of their lower mass and then map the hybrid crystals. The optical image of this hybrid crystal would directly give the positions of the outer Ca^+ ions, and through numerical analysis the positions of the Li^+ ions in the central dark region can be obtained. We then establish the mapping between these Li^+ ion positions with the corresponding hits on the MCP, which occur at an earlier time than the Ca^+ ions due to their lower mass. This allows us to optically locate the ion position inside the trap, and make correspondence with the detection on the MCP when the ion is extracted, before we completely rely on it. Therefore, we have built an ion trap which can simultaneously trap Ca^+ and Li^+ ions, optimized for lowest Li^+ ion temperatures, to facilitate the generation of the desired mixed species coulomb crystals.

Placing the ultracold atoms at the center of the trap is a prerequisite for threshold ionization and therefore it is desirable to prepare the cloud of atoms at the geometric center of the ion trap. This involves co-centering of ion trap and a magneto optical trap (MOT). The laser beams for the MOT

and optical detection of atoms and ions demand large optical access to the trap center. Therefore, keeping in mind the virial arguments made in chapter 6, we opt for a linear quadrupole Paul trap design with thin cylindrical rods as radio frequency (RF electrodes and circular ring end-caps electrodes (see figure B.2 in Appendix B).

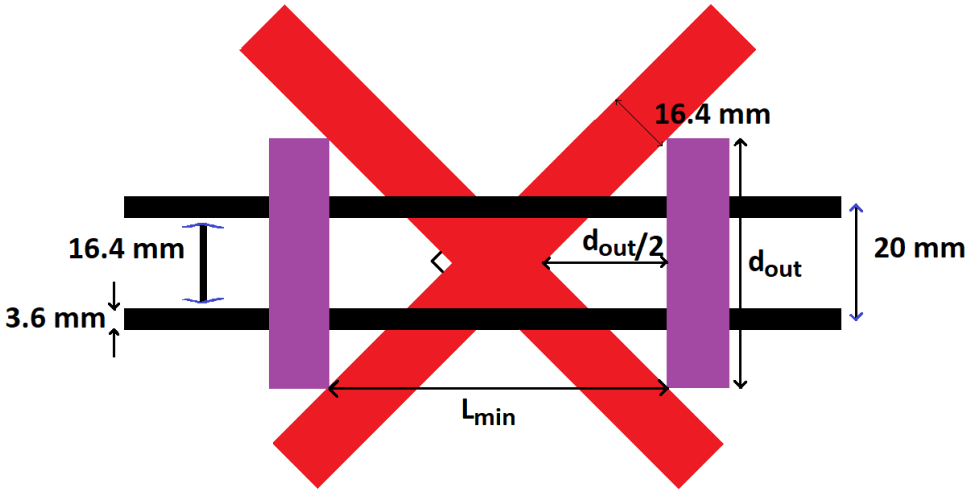

Figure 7.4: This is an illustration of the geometric constraints relating the beam diameters taken here as 16.4 mm, the outer diameter of the end caps d_{out} and the end-cap to end-cap distance l_{min}.

The size of the trap is chosen large enough to accommodate the large diameter MOT beams needed to cool Li atoms. MOT for lithium is challenging due to the not-well-resolved D2 transition, and added to this the low mass of Li atoms implies higher velocity of atoms prior to cooling, are emitted by the atomic Li gas dispenser. In order to maintain an adequate loading rate into the MOT, the cooling and repumper beams have to be larger than a centimeter to ensure a large enough volume of cooling region for the dispensed atoms. The center to center distance between two RF electrodes is kept as 20 mm. We have allowed the diameter of the electrodes to be as large as 6 mm, and have calculated 2-dimensional potential arrays using SIMION software [196], for various electrode sizes ranging from 3-6 mm. Using each of these potentials, we have simulated 2-dimensional trajectories of a $^7Li^+$ ion, for a set of voltages that satisfy the stability criterion. For the purpose of this calculation, the ions are created at the trap center with velocity equivalent to 100 μK (ballpark Li MOT temperature), and the steady state temperature of the ion in each case is obtained. We find numerically that, for the above mentioned constraints, the lowest ion temperatures are achieved with electrodes of diameter between 3.5 mm to 4 mm. So, we have used 4 mm

bare rods made of stainless steel (SS 316L) and which were turned to remove surface undulations and pits. This resulted in 3.6 mm diameter, unbent cylindrical rods with excellent surface quality, which were used as our RF trap electrodes.

Once the RF electrode diameter is fixed at 3.6 mm, keeping the electrode to electrode distance 20 mm, we get a clear optical access for up to 16.4 mm diameter MOT beams. In order to allow orthogonal beams of diameter 16.4 mm, and keep a similar optical access of 16.4 mm through the end-cap rings, the constraints for the dimensions of the end caps are obtained, see figure 7.4. While the inner diameter of the end-cap rings, d_{in} has to be at least 16.4 mm, the maximum outer diameter of the end-cap rings, d_{out} is determined by its axial distance from the trap center. The end-cap to end-cap distance has to be at least $l_{min} = d_{out} + (16.4\sqrt{2})$. Also, in this design, the end-caps need 4 circular cutouts to allow the RF electrodes through them without making contact. Through holes of 4 mm diameter have been made for this purpose (see Figure B.2 in Appendix B).

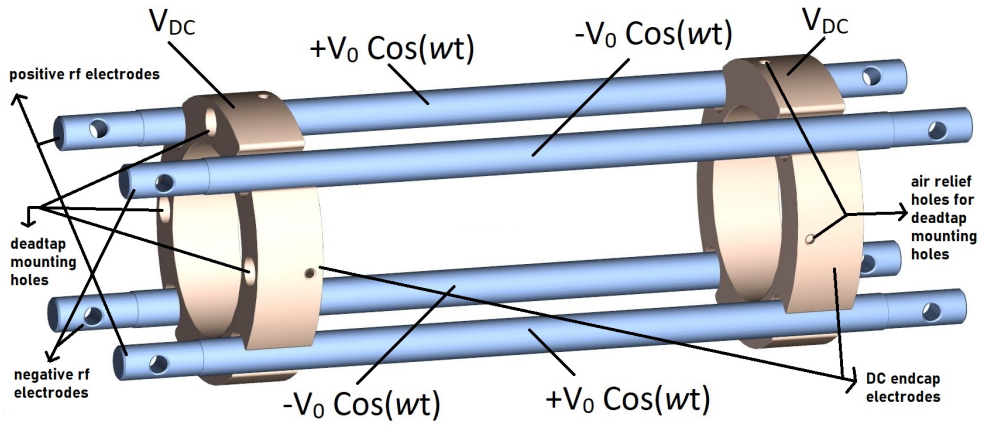

Figure 7.5: This is a design render of the functional elements of the Paul trap with optimized dimensions for the purpose of our hybrid ion-atom experiments. The various parts have been labelled and the electrode voltages to be applied in the normal operation are mentioned.

We have simulated 3-dimensional potential arrays using SIMION software for configurations with different values of d_{out}, keeping $d_{in} = 16.4$ mm, subject to the constraint discussed above. In each case, we evaluate the parameter space for simultaneous stable trapping of Ca^+ and Li^+ ions. The intention is to select the dimension d_{out}, and thereby the end-cap to end-cap distance, such that the parameter space with for simultaneous trapping of Ca^+ and Li^+ ions is large and the resulting temperatures for the ions in the trap are low. We obtain that end cap size of 32 mm outer diameter

provide optimum results and therefore fix this length scale, and the resulting end-cap to end-cap distance becomes 54 mm. The thickness of the end caps is chosen as 8 mm, see figure 7.5 in order to incorporate all the design requirements of the ion trap mounting which will be discussed below.

In the previous experiments built in our group [75, 89], channel electron multipliers were used to detect number of ions. These have been shown to reliably detect the number, temperature and mass of the ions [14, 77, 78, 87, 206]. However, as we have established earlier, measurement of phenomena related to charge hopping and the resulting diffusion, require the read out of position of the optically dark ion prior to destructive detection. This is facilitated by the use of MCP based detectors.

MCP based detectors, which can provide good resolution for position of the ion detection, come in two basic variations. The first kind provide an electronic readout of the time of arrival of the detected ion and with a integration of a delay-line, allow the estimation of the location of ion hit(s) on the detector. This method is popular with experiments where both location of hit as well as the time of arrival need to be measured, despite its complexity and difficulty to operate. The second kind of MCP detectors have a phosphor screen on the rear end which produces a glow at the site of ion hit. The grain size of the phosphor element determines the size of the glowing spot, which affects the resolution for position of hit determination. The decay time characteristics of the phosphor element determine resolution for time of arrival and limit the usage of the detector. This is because, a second ion hit in the same location can not be differentiated if the time difference in the arrivals is less than the phosphor's decay time. Phosphor elements with low decay time and high gain are developed for such applications, which turn out to be very expensive. We have used a widely available kind of phosphor screen and MCP detector by determining the size that allows the required resolution of ion position detection.

Our experiment needs to determine the position of a single ion and in a cloud of size $\approx 400\mu$m, with a resolution of up to 1μm. If we use the widely used variety of phosphor, P43, which has ample gain and a grain size of $\approx 1\mu$m. The detector size is 40 mm in diameter to provide ample resolution for position determination. The job of magnifying the region of interest of $\approx 400\mu$m to the detector size of 40 mm, must be done by the charged particle lenses and the ion extraction

mechanism. The detector we used is a two stage (Chevron) detector with P43 phosphor screen, purchased as a (CF100) flange mounted system from Surface Concept - part number MCP-45-60-P43-CF100, who in turn source the MCPs from Photonis, see schematic in Figure 7.6.

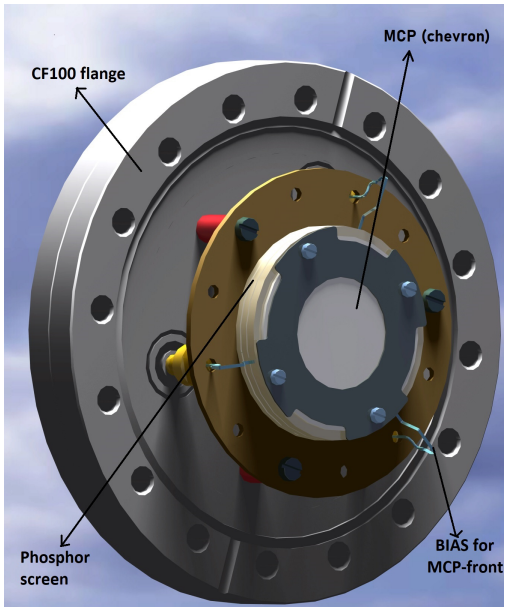

Figure 7.6: A rendered image of the assembled ion detector with 2 MCPs in Chevron configuration and P43 phosphor screen mounted on a CF100 flange with CF63 glass window to image the phosphor screen.

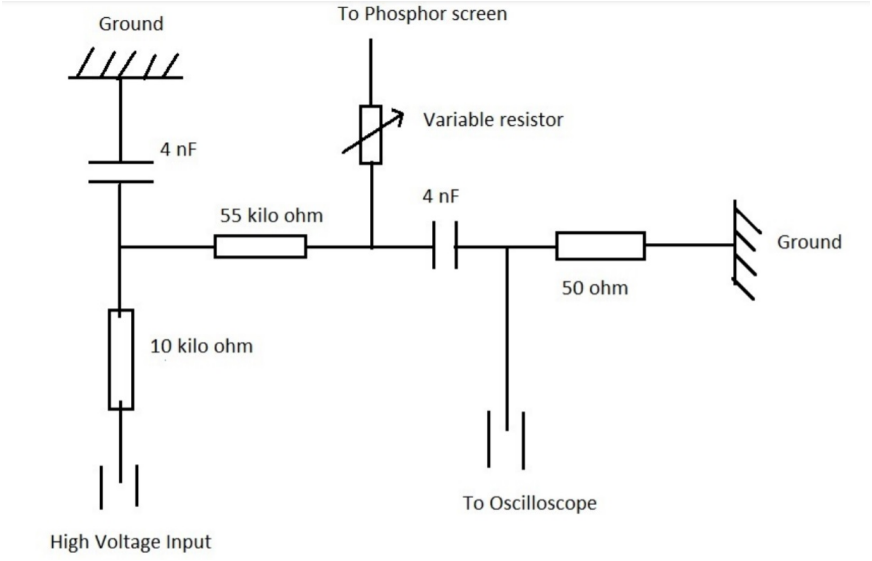

Figure 7.7: Circuit diagram for appending the detector power supply to provide electronic signal for ion time of arrival measurement.

The large decay time of P43 limits the accurate determination of the time of arrival of the ions. Although Surface Concept does not provide an electronic signal readouts, we have modified the power supply circuit to obtain an analog output of the phosphor screen signal, the circuit diagram is shown in figure 7.7.

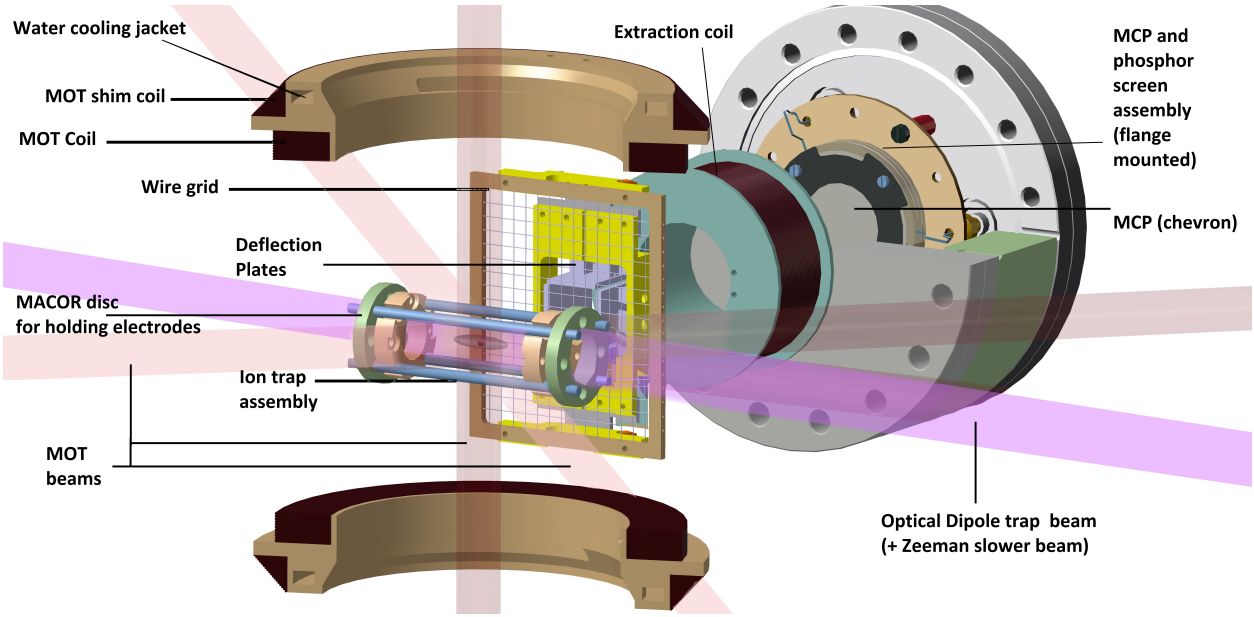

Figure 7.8: schematic showing the designed elements of the hybrid ion-atom trap, the assembled ion detector along with the components for ion extraction.

Between the detector and ion trap, a drift tube of 127 mm length is used to increase the time of flight of the extracted ions, sufficiently to be manipulated by the extraction fields. On the ion trap side of this drift tube, we place a wire grid to electrically isolate the ion trap region from the detector side. Within the drift tube, adjacent to the wire grid, we have placed 4 deflection plates, two for each direction, to tweak the trajectory of the ions and aid in providing the magnification needed.

Finally, a magnetic coil is mounted around the drift tube to provide the magnification during ion extraction onto the detector. Figure 7.8 shows the schematic with the designed functional elements of the hybrid trap, the ion detector and functional components for the ion extraction.

7.4.1 Ion trap assembly and mounting

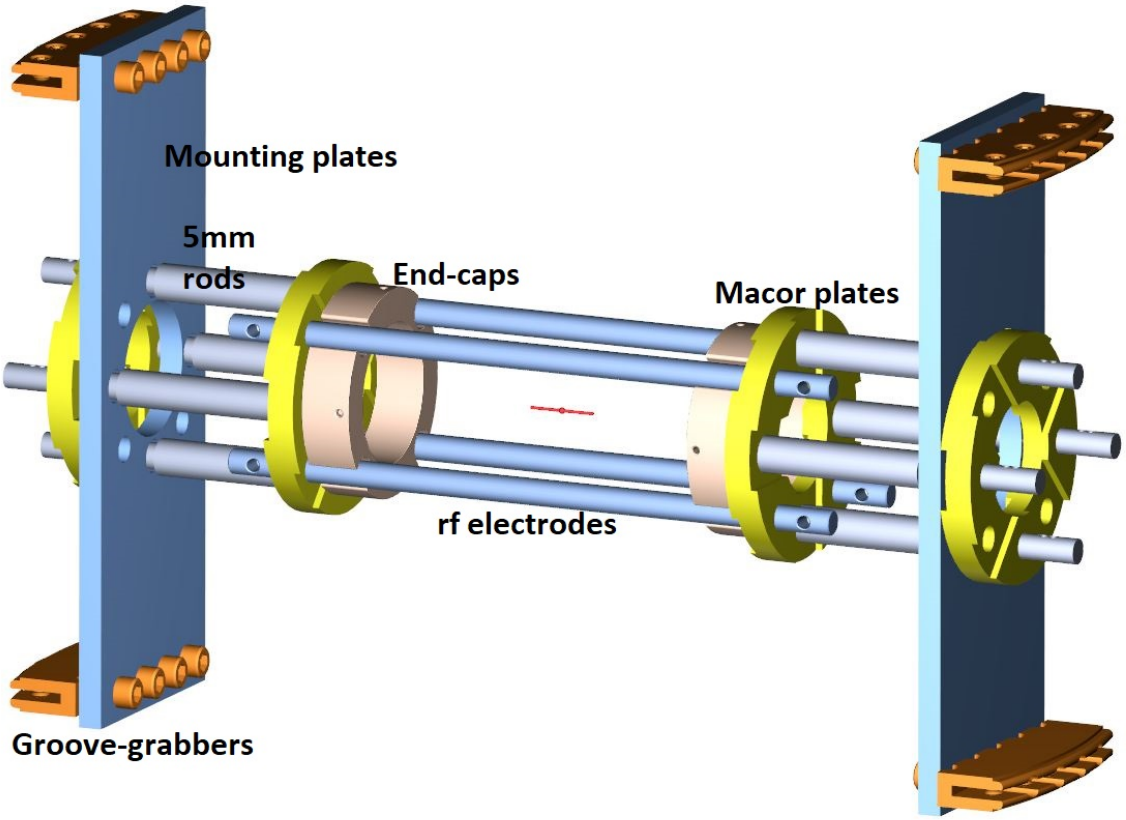

Figure 7.9: The full mounting assembly of the ion trap to the main chamber is shown. The ion trap electrodes are held by the two central Macor plates, which also insulate all of the electrodes from each other. The wider mounting rods connect to the rear side of the end caps (see Figure B.2 in Appendix B) through the Macor plates. These mounting rods are held without touching the mounting plates by use of another set of similar design Macor plates, behind the mounting plates. Finally the whole assembly mounts to the grooves on the chamber with the help of the groove grabbers attached to the mounting plates.

The central ion trap electrode assembly has 4 stainless steel rods of 3.6 mm diameter held in a quadruple configuration, with adjacent rods at a center to center distance of 20 mm. The ion trap electrode rods are electrically isolated as well as mechanically supported by two Macor(machinable ceramic) plates of 5 mm thickness. The plates are 40 mm in diameter and have a central hole of 16 mm diameter for optical access to the ion trap center. Circular cut outs of 3.64 mm are provided to allow the RF electrodes to pass through and 5.04 mm holes are made on these plates (see Figure B.3 in Appendix B) to allow the diagonal mounting rods, which connect and

thread into the end caps. Both the surfaces of the Macor plates are structured so that the regions with 3.64 mm holes and the regions with 5.04 mm holes can not be short by deposition of metallic vapours during the operation of the experiment.

The ion trap electrodes extend beyond the Macor plates, where they have M4 threads and with the help of a washer and double nuts, they hold the Macor plate flush with the rear surface of the end-cap electrodes and apply an inward pull on the ion trap assembly. On the end-cap electrodes, 4 mm semi-circular cutouts are provided to allow the RF electrodes (Rods) to pass through (see figure B.2 in Appendix B) and in the gap between the end cap electrode and the linear rod electrodes, a thin Macor bush is placed to ensure electric insulation.

The surface of the end caps facing the ion trap center are plane and smooth, but on the opposite side, there are 4 end tapped holes with M4 of depth 7 mm. Air relief holes are provided at the ends of these tapped holes towards the larger diameter side of the rings to improve vacuum (see figure B.2 in Appendix B). 4 stainless steel (SS316L) rods of 5 mm diameter with M4 threads at the end are threaded into the rear side of each end-cap electrode. These rods pass through the Macor plate behind the end-caps as described above and connect the ion trap assembly to the mounting plates (see figure B.3 in Appendix B).

The mounting plates made out of stainless steel (SS316L) are 5 mm thick and have 5.5 mm holes to allow the 5 mm rods to pass through (see figure B.3 in Appendix B). Behind the mounting plates another pair of Macor plates, one for each side, are used to tighten the whole assembly via double nuts to apply an outward push on the trap assembly. The Macor plates behind the mounting plates insulate the rods from the mounting plate, and are bolted to them using the 4 mm through holes.

The mounting plates are attached to the chamber wall by means of groove-grabbers (Kimball Physics: MCF800-GrvGrb-C01). Each plate is attached to a pair of stainless steel (SS) groove-grabber (top and bottom) by means of gold plated SS screws. The mounting plates also have a central 20 mm hole to allow optical access to the center of the ion trap in the longitudinal direction (see figure B.3 in Appendix B). The complete ion trap assembly looks as shown in figure 7.9.

7.4.2 Ion extraction and detection assembly

The MCP detector, as described earlier is mounted on a CF100 flange with a window, and the detector assembly extends 35 mm beyond the flange. This is attached to a CF100-40 straight reducing nipple (Kurt J Lesker), through a 40 mm thick SS304 CF100 spacer to accommodate the detector. The CF100-40 straight reducing nipple has a 127 mm tube of diameter 40 mm that acts as our drift tube for the ions and its CF40 flange is mounted to the main chamber. As for the magnetic coil around the drift tube, it was wound around the tube before attaching it to the main chamber. Also, between the tube and the coil, insulated NiChrome heating wire was wound on the tube which would be needed to perform vacuum bake-outs.

At the main chamber side of the drift tube, the wire grid and deflection plates are assembled as a single unit which are mounted to the main chamber using 2 groove-grabbers. This assembly is done using Macor insulating pieces (see figure B.4 in Appendix B) and SS bolt-plates (see figure B.6 in Appendix B). The frame for the wire grid is made of 3 mm wide and thick aluminium, and the wire itself is made of 80 μm diameter tungsten. The wire grid is weaved as vertical and horizontal lines of 5 mm spacing, and positioned such that the center of the grid, where most of the ions pass through has no wires. The length of the grid in x-direction is, 54 mm, long enough to electrically shield the deflection plates, and all the wires up to the electrical feedthoughs (2 CF16 ports) behind it. The deflection plates are 19 mm long and 14 mm wide (see figure B.5 in Appendix B), bolted to Macor mounts and the end taps are provided with air relief holes. We designed special jigs made of Nylon and brass, to mount the ion trap assembly and the wire grid assembly to the chamber, so that axes are well matched. Laser beams along the axes were used as reference during the processes to ensure proper alignment.

7.4.3 Feedthroughs and electrical connections

There are two 4 pin (Kurt J Lesker, 5 kV, 10 A), CF16 electrical feed-through (FT) directly attached to the chamber to two CF16 ports adjacent to the MCP detector port. Of the 4 pins on each FT, two are connected to two nearest deflection plates, one is connected to the grid frame and one to the

SS piece in the mounting to explicitly ground it during operation.

We use two 4 pin (Kurt J Lesker, 5 kV, 20 A) FTs to provide electrical connections to the 4 ion trap RF and 2 end-cap electrodes as well as to two ends of a Rb dispenser. The Rb dispenser is included in the setup to keep an option of using the easily laser coolable atoms for heteronuclear and mixed species in this setup in the future. These FTs are mounted on 2 CF16 ports on either side of the ion trap. On 2 CF16 ports diagonally opposite to these, two FTs, one for a pair of Li dispensers and another for a pair of Ca dispensers, are attached.

The electrodes, grid and deflection plates are connected to the respective FTs using silver wires of 0.4 mm diameter. The specialty of the silver wires are that they are flexible but can not be corroded by reactive elements like lithium, in addition to excellent UHV and conduction property. The wires providing connections are bent and placed in the shadow region behind the SS rods in such a manner that the voltage applied on them are screened from the center of the trap by the trap electrodes. These silver wires connect to all electrodes between their washer and the nut(s).

A set of specially designed gold plated copper beads are used to attach the silver wires to the copper FT pins. The beads have an off-axis through hole along with two radially threaded M2 holes on two ends to connect the FT pin in one and the silver wires on the other. It is also slotted axially to provide air-relief for the end taps through which gold plated SS screws secure the connections. These slots are also used to attach the dispensers on the other FTs.

We had also gold plated the copper CF gaskets used on the main chamber, the (future) zeeman slower side and the pump side. The dispensers are mounted on FTs facing away from the MCP detector port. Detailed mechanical drawings of the internal components of the apparatus are provided in the appendix.

7.5 Laser systems and control

We have used home built (see figure B.1 in Appendix B) external cavity diode lasers (ECDLs) with Toptica diode laser controllers for the lithium MOT. Since it is difficult to source high power laser

diodes at the required wavelengths ≈ 671 nm, we use 660 nm diodes (Thorlabs L660P120) which give up to 120 mW of optical power. The ECDL design, shown in figure 7.10, permits variation of the wavelength of the laser by more than 10 nm by changing the temperature of the internal mount and grating angle. The grating mount allows the angle adjustment needed for this, so that the stimulation via the external cavity can help in stabilizing a larger range of wavelengths. The internal mounts which hold the laser diode and the grating are made of brass to accommodate the temperature changes and the grating mount is designed to allow large mode hop free wavelength scans up to 10 GHz around any central wavelength between 655-675 nm at the corresponding temperatures.

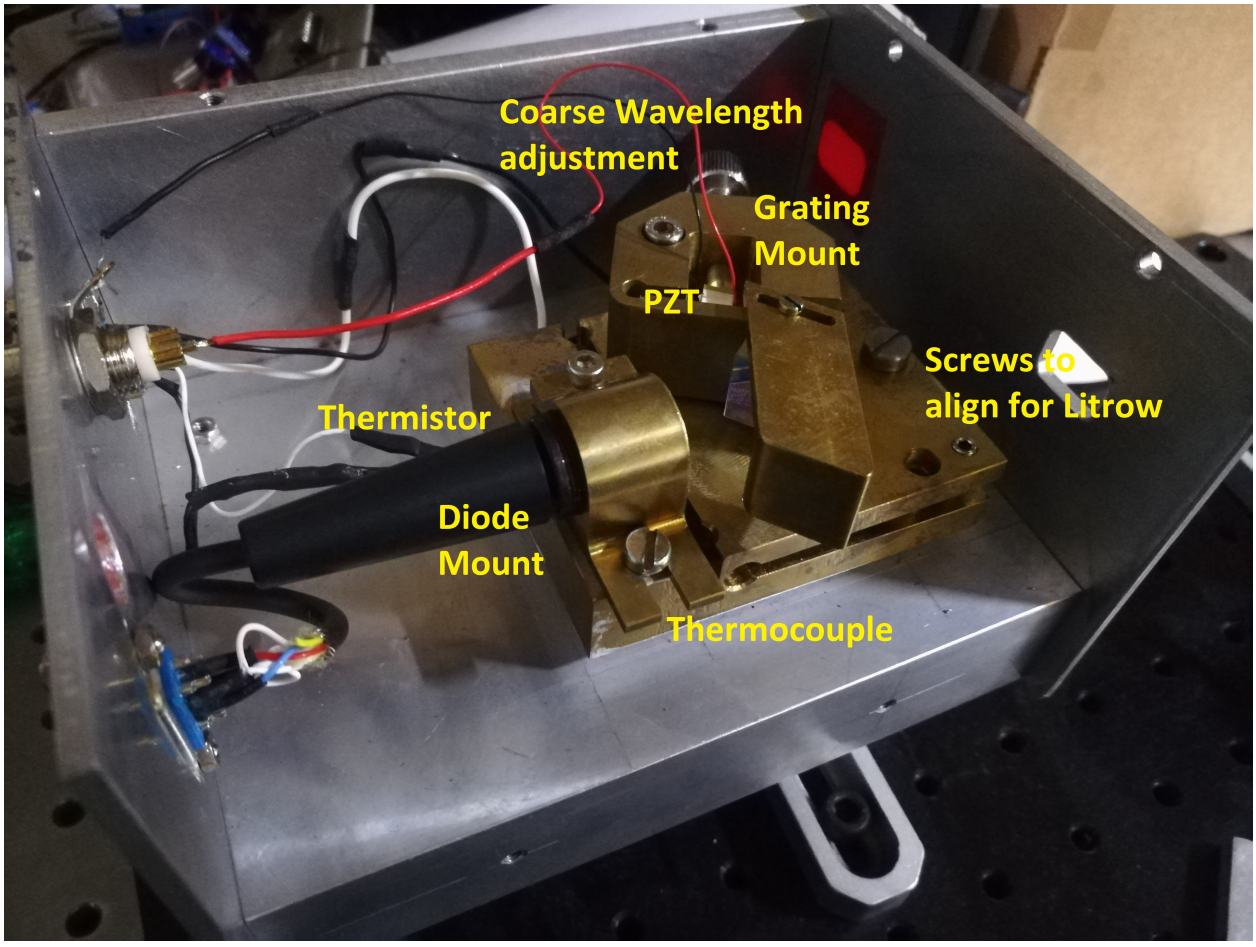

Figure 7.10: A photograph showing the schematic of the home-built laser mounts for high temperature ECDL application. The components are labelled and the mechanical drawings for the parts are provided in Appendix B.

The L660P120 diodes will have to be operated at temperatures of 65-75°C in order to emit the

required wavelengths. This is beyond their rated range of temperatures. We had heated the diodes for more than 24 hours at 80°C before using them in our ECDLs. We found that the diodes which survive this heat treatment will later emit 671 nm wavelength, at manageable temperatures of ≈ 60°C for regular use.

We use holographic gratings rated for UV wavelengths to make the ECDLs. These are less efficient in creating a first order diffraction beam, leaving more power in the zero order beam which is the output of the laser. Also, low first order pump powers lead to more stable laser performance. The base for the laser mount and its casing on all sides are made of aluminium and we paste acoustic grade Styrofoam sheets on the aluminium casing to thermally and acoustically isolate the laser housings.

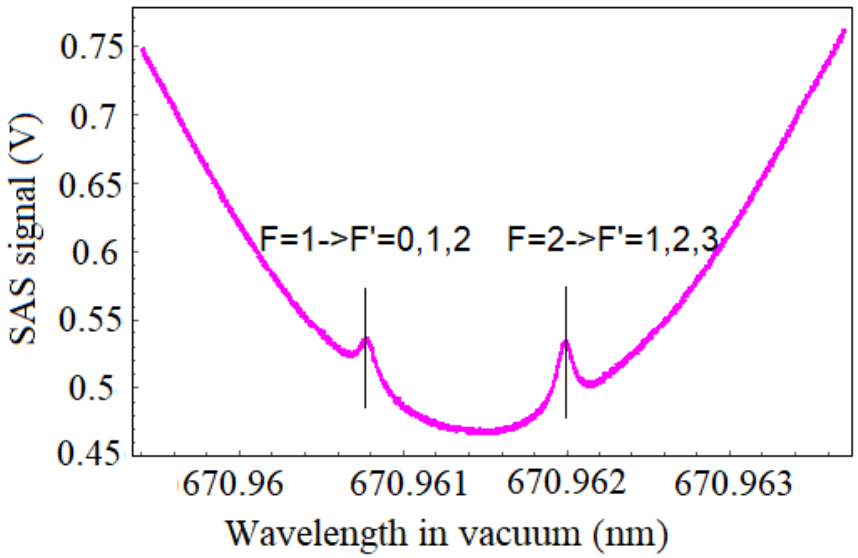

Figure 7.11: Figure shows the saturation absorption spectrum for ^{7}Li obtained using home-built lasers. The setup involves a hollow cathode lamp which results a different spectrum from the ones obtained using heat pipes. We do not see any pronounced ground state cross over peaks. The excited state hyperfine levels are unresolved.

An optical isolator (Thorlabs IOT-5-670-VLP) is used to ensure protection against destabilizing reflected light. A small fraction of the output beam is directed into a lithium see-through hollow cathode lamp (Hamamatsu L2783-38Ne-Li) around which the necessary optical circuit for saturated absorption spectroscopy (SAS) is setup. Another small fraction of the output beam is coupled to the wavemeter optical fiber for measurement of the wavelength. By using the SAS

signal (power vs time) and the wavemeter readout (wavelength vs time), we obtain the saturation absorption spectrum (power vs wavelength), shown in figure 7.11. The rest of the output beam is coupled to a polarization maintaining fiber. At the output end of the polarization maintaining fiber, the required amount of power is branched out and the MOT beams are generated with the respective polarizations. In order to generate ample cooling beam power, we use a tapered amplifier (Toptica BoosTA Pro 670).

The Toptica DLC110 diode laser controllers can be used to lock the laser wavelengths either to the obtained SAS signal or to the signal generated using the wavemeter's PID module. The wavemeter model we use is High Finesse WSU2, which is capable of measuring wavelengths of 350-1100 nm with an accuracy of 2 MHz and a precision of few 100 kHz, when continuously calibrated with a reference laser within ± 2 nm from the wavelength to be measured.

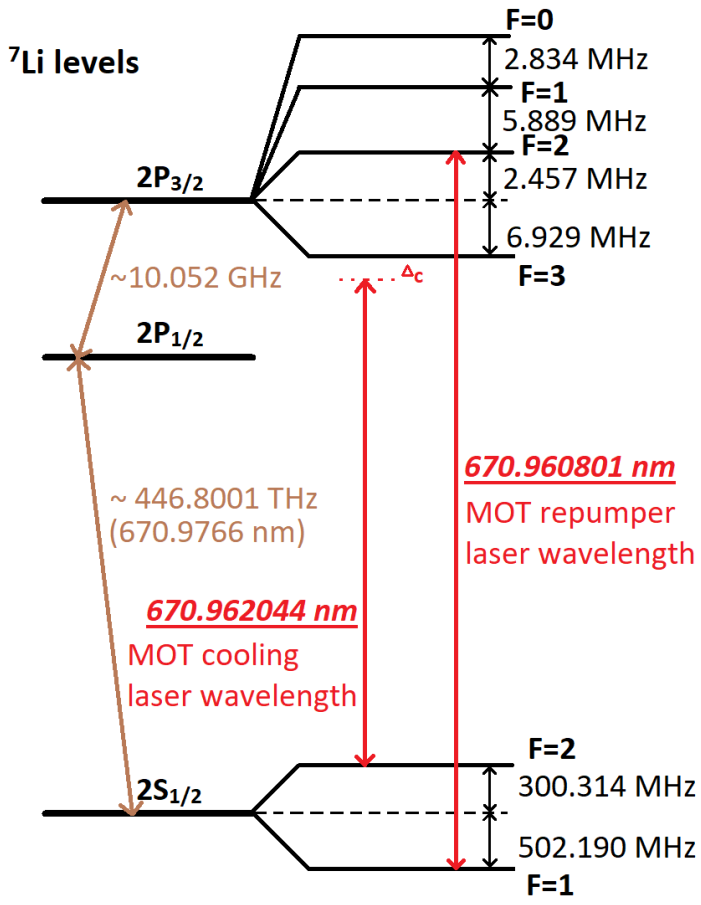

Figure 7.12: The atomic levels relevant for ^{7}Li MOT are shown with the various level seperations labelled and the measured values of cooling and repumper MOT laser beams, on our wavemeter are also given.

Figure 7.13: A photograph of the lasers on the optical table, taken in our lab.

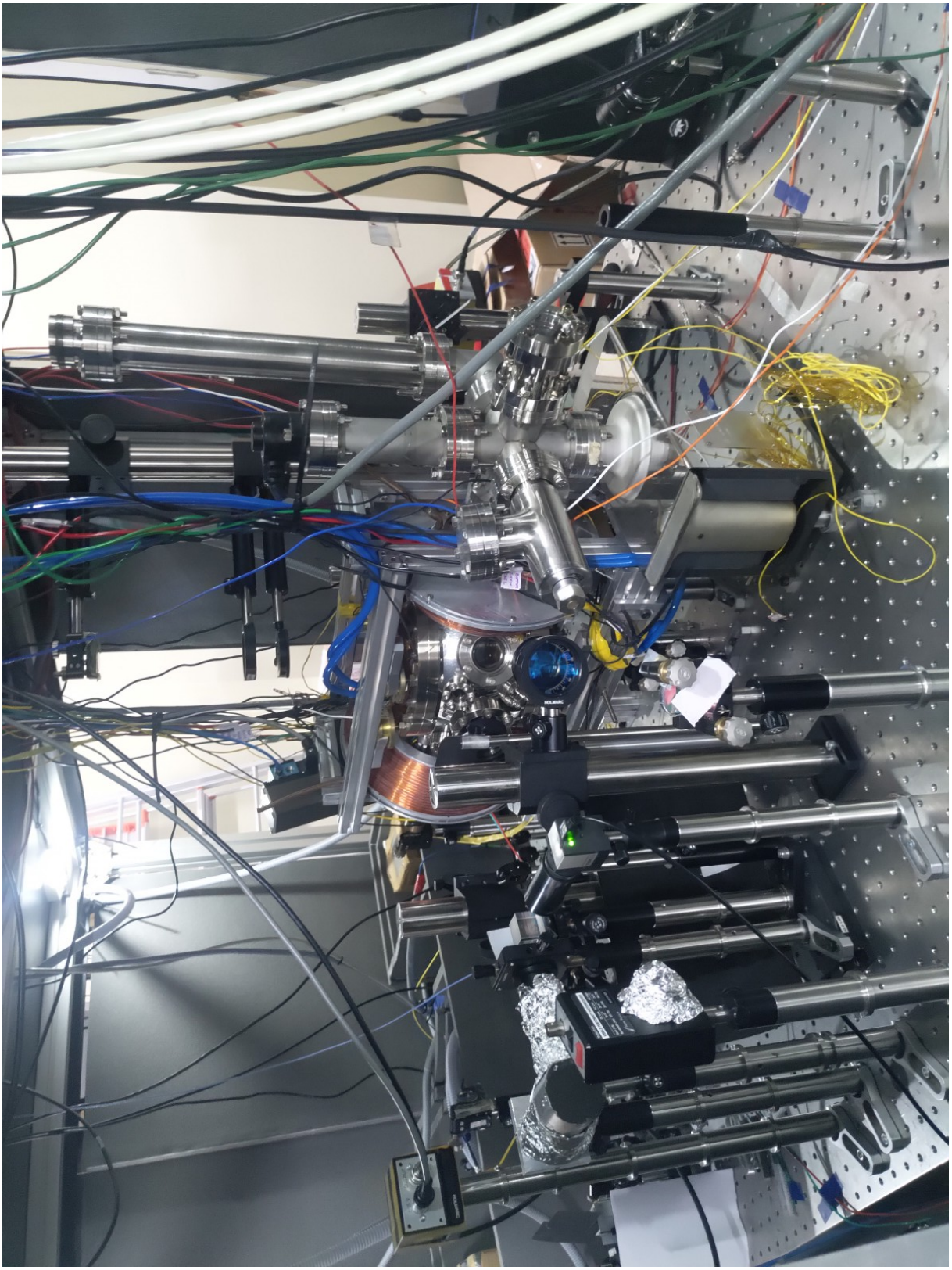

Figure 7.14: A photograph of the experimental chamber and the associate optical circuitry on the optical table, taken in our lab.

We do not have any good reference laser sources around the lithium wavelengths, making it impossible to rely on the absolute values of wavelengths measured by the wavelength. We choose a 852 nm laser locked on the most resolved and accurately known Cs atomic transition for continuous calibration of the wavemeter. This along with the HCL spectroscopy, gives the Li wavelengths accurately which are shown in the ^{7}Li atomic levels diagram, in figure 7.12. A photograph of the lasers on our optical table is shown in figure 7.13 and another photograph of the apparatus on the other half of the same optical table is shown in figure7.14.

7.6 Characterization and results

For MOT lasers, the detuning from natural transitions must be well known to be able to determine the number of atoms from the measured fluorescence. We employ the following method for reliable determination or setting of MOT laser detunings. First, we lock the laser using to the top of the unresolved peak in the saturated absorption spectroscopy signal and note the wavelength measured by the calibrated wavemeter, λ_1. Then the wavelength of the MOT beam, λ_2 is measured with the same wavemeter calibration. Although the absolute values of λ_1 and λ_2 are not accurate, the value of $\lambda_{12} = \lambda_1 - \lambda_2$ will be correct to few 100 kHz.

We model the unresolved SAS peak using known natural linewidths, relative intensities, and some floating parameters which we fix by fitting to the measured unresolved SAS peak. The energy separation between the unresolved excited state hyperfine levels is taken from available literature [207]. From the best fit model, the offset between the underlying natural transitions and the top of the overall unresolved peak is obtained. The relevant offset is added to λ_{12} to get the detuning of the MOT beam(s), which are used to accurately measure the number of trapped atoms in a ^{7}Li MOT.

We adjust the wavelengths of the cooling and repumper laser beams, and the coil currents to attain the brightest, symmetric and well behaved MOT at the center of the ion trap electrode geometry. We ensure this by imaging the center of the main chamber from two orthogonal directions, the primary imaging port (-y direction) and the gate valve port (-x direction). The fluorescence collected

from -y port is split into two equal halves and sent to a CMOS camera and a PMT, to measure the density distribution from the camera image and the total atom number from the PMT signal.

The MOT density distribution is measured to be close to a Gaussian standard deviations $\sigma_x = 1.04 \pm 0.05$ mm and $\sigma_z = 0.95 \pm 0.05$ mm, see figure 7.15. The total number of atoms in the MOT is determined to be $\approx 7.8 \times 10^5$. Assuming $\sigma_y = \sigma_x$, we obtain the peak MOT density to be $\approx 2.4 \times 10^{14}$ atoms/m^3, the MOT loading time is measures to be 7 seconds and the atom loading rate for the MOT is determined to be $\approx 1.6 \times 10^5$ atoms per second.

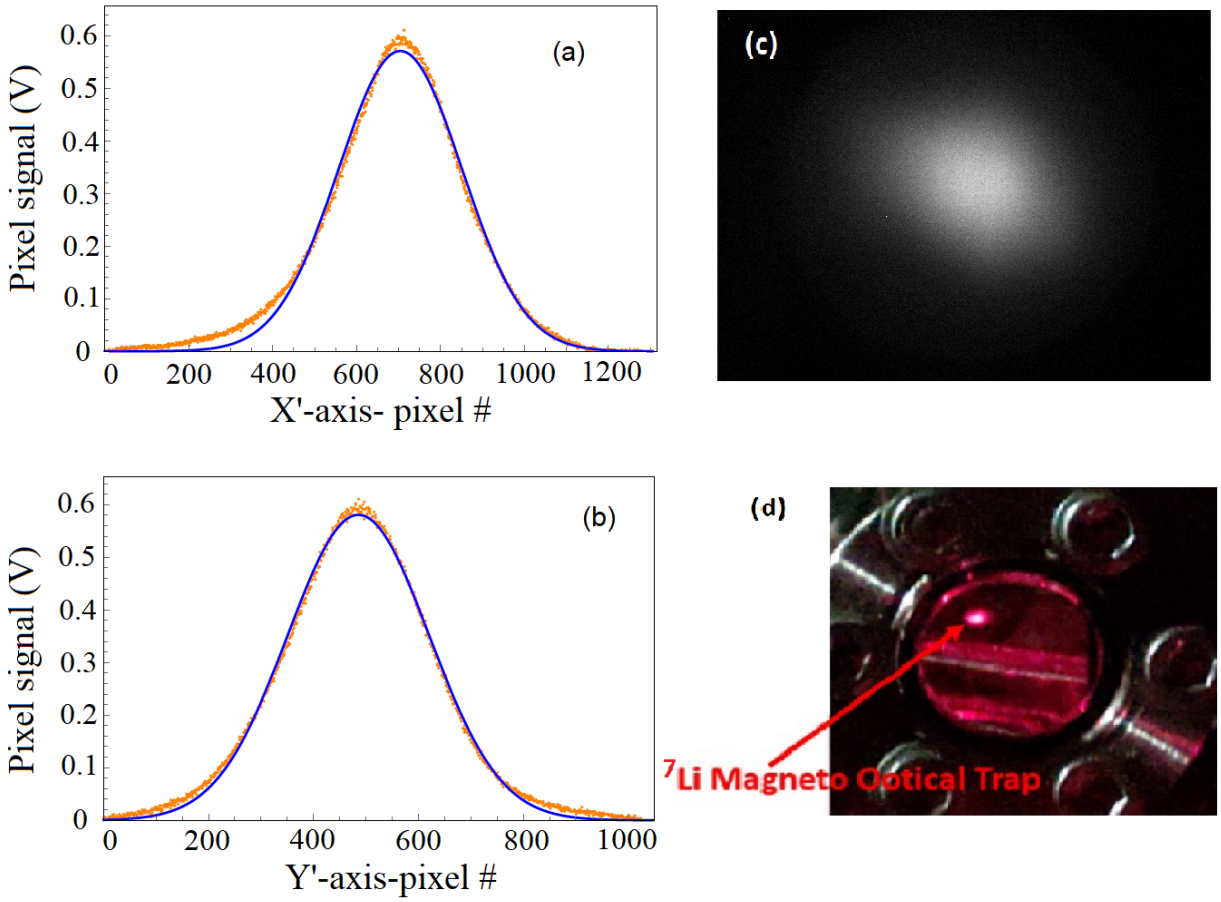

Figure 7.15: Panel (a) and (b) show intensity profiles measured by the CMOS camera pixels in the two directions x and z, along with the obtained best fits for a Gaussian of widths $\sigma_x = 1.04$ mm and $\sigma_z = 0.95$ mm respectively. Panel (c) is the full gray scale image of the MOT from the from the camera. Panel (d) shows a photograph of the ^{7}Li MOT fluorescing red light, taken with a handheld mobile camera through one of the CF16 view ports. Since the wavelength emitted by lithium is visible red, one can directly see such a MOT without much difficulty.

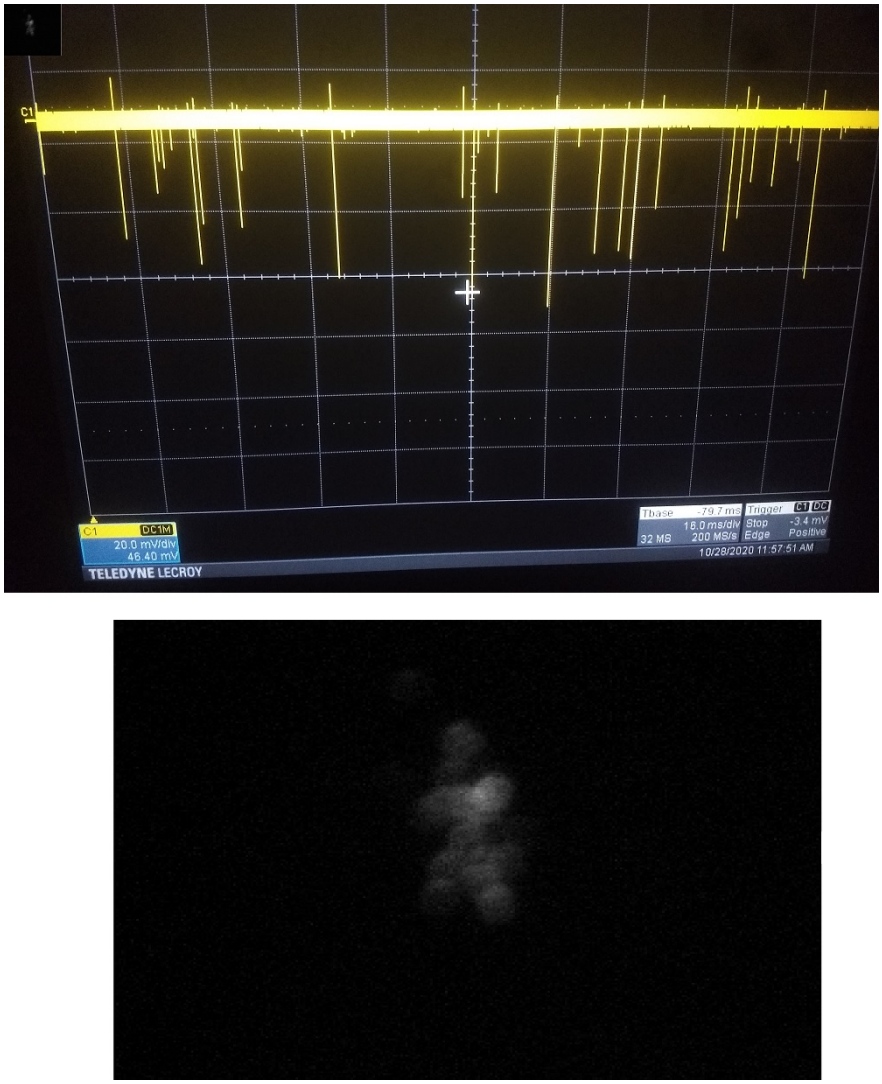

Figure 7.16: The top panel shows the image of the electronic readout from the MCP detector illustrating the pulses obtained for each ion hit and the availability of the ions' time of arrival information and ion count. The bottom panel shows a long time integrated image of the phosphor screen behind the detector, that replicates the MOT atom density profile as it is an overlap of glows from hits of multiple ions originating from different regions of the MOT.

We ionized theses MOT atoms using a UV led of 340 nm central wavelength. A single photon of the UV light should be able to ionize an excited Li atom which made available by the cooling cycle of the MOT. We do not measure any significant change in the MOT atom numbers due to the additional loss rate introduced by ionization. To confirm the creation of ions, we have used the MCP detector and the trap electrodes in continuous extraction and detection mode. We see an easily measurable number of ion hits on the detector. While the phosphor screen image shows

an overlap of numerous glows, corresponding to many previous ion hits, replicating the MOT density distribution, the electronic readout clearly provides time of arrival of the ions and allows to count the number of ions detected in a given interval of time, see figure 7.16.

7.7 Concluding remarks

In this chapter we have discussed in detail, the design and construction of the hybrid trap apparatus. With the requirements of the apparatus in mind and the constraints arising from combining the optical, electric and magnetic fields for trapping, probing and for detection, the whole system has been devised. This experiment, will enable the study of interaction between multiple species along with the novel investigations of homonuclear ion-atom systems, that have been studied throughout this thesis. We have also discussed about the lasers and the optical arrangements that have been used for the experiments. The preliminary experiments performed in the hybrid apparatus to establish its functioning have been discussed.

There are a few substitutes to this system which can be thought about. A 2D-MOT instead of a Zeeman slower may help improve the atom loading rate. This can be implemented on our present setup with some extension. A thinner main chamber will reduce the complexity of both internal and external apparatus assembly significantly. All coils can then be placed closer and the direct contact between the coils and the chamber can be avoided. With some customization, if coils can be mounted in place after vacuum bake-out, the vacuum assembly can be considerably eased, better vacuum and reliable operations can be achieved. Modern but expensive technologies such as NEG coatings, Bitter coils, high power lasers, etc. can be utilized for the best benefit.

Chapter 8

Summary and Future Prospects

8.1 Summary of results

A versatile and effective platform for experimental study of ultracold ion-atom interactions is developed. We first considered an optical cavity as a non-destructive probe for ultracold systems and show prospective implementations to enhance its utility. However the limitations of cavity based detection, with respect to weak interactions and small number of ions, and the requirements imposed by the theoretical calculations, demanded an alternate scheme.

To lay down the parameters needed to study the unexplored regimes of interest, theoretical calculations of ion atom interactions were adapted to our system. We found the widely used theoretical recipes for ion atom scattering suffered from inconsistencies, particularly when applied to ultracold homonuclear ion-atom systems. This called for a rework of the theoretical framework from first principles, which has been presented in detail. The possible range for scattering outcomes in any particular system, can be estimated using the methods we have applied.

The theoretical study is extended to quantify quantum phenomena of charge hopping in thermal gas regimes. The challenging but achievable demands for measuring such well characterized phenomena have been established. We then work towards a consistent scheme of measuring charge transport which links to all aspects of ultracold ion-atom scattering. Design optimization,

including detail analysis for the choice of the type of trap to use, the detectors, the tricks for integrating and extracting the most out of them have been presented. All the elements of work, both theoretical and experimental have been developed with versatile formalism and methods, and their relevance to a lot of applications and other systems has been explored, some of which has also been published.

Finally, we demonstrate stable trapping of ultracold lithium atoms in a MOT, using some of our lab-developed methods and devices. Li^+ ions are created and detected, and their time of arrival and position mapping are shown to be feasible, using the customised readout mechanisms.

8.2 Future prospects

A direct next step in the experiment is to establish a protocol for reliable measurement of the position of a $^7Li^+$ ion using the time of arrival and position of striking the detector. To calibrate this protocol for optically dark lithium ions, as we discussed earlier, a calcium ion crystal will be implemented. Then the transition to an optical dipole trap to get to the desired densities and temperatures will have to be worked on before being able to measure the ultracold phenomena that are sought-after.

The usage of axial magnetic fields and studying charge hopping-led confinement of multiple ions is of specific interest to us. This is expected to show emergence of symmetric configurations for the confined ions through a random, stochastic quantum mechanism. The theoretical frame work can be further extended to incorporate hyperfine interactions and study the effects of cooling the system further into degenerate gas regimes.

Appendix A

Near neighbor distances for discrete distributions

Consider N point particles uniformly distributed in a D dimensional volume, V. The number density is given by n = N/V and the volume per particle v = V/N. Let us define a characteristic length r_c, which is the radius of a D dimensional hyper-sphere with volume v. Using the known volume of sphere, V_D of radius r in D dimensional Euclidean space, 2

$$V_D(r) = \frac{\pi^{\frac{D}{2}}}{\Gamma(\frac{D}{2}+1)} r^D \,, \tag{A.1}$$

we get

$$r_c = \frac{(\Gamma(\frac{D}{2}+1) \times \frac{V}{N})^{\frac{1}{D}}}{\sqrt{\pi}} \,, \tag{A.2}$$

where Γ is the gamma function. Let $P_k(r)$ dr denote the probability that the k^{th} nearest neighbour to a particle is at a distance between r and r+dr. This is the product of the probability that one particle is in the shell of radius r and thickness dr, the probability that k-1 particles are within a hyper-sphere of radius r and the probability that the remaining N-k particles are outside the hyper-sphere of radius r [208],

$$P_k(r)\,dr = N\,\frac{V_D'(r)dr}{V} \times {}^{N-1}C_{k-1} \times \left(\frac{V_D(r)}{V}\right)^{k-1} \times \left(1 - \frac{V_D(r)}{V}\right)^{N-k}. \tag{A.3}$$

Substituting V = N V_D(r_c) and the expression for V_D'(r) which is the derivative of V_D with r, we get

$$P_k(r) = \frac{{}^{N-1}C_{k-1}}{N^{k-1}}\frac{D}{r}\left(\frac{r}{r_c}\right)^{D\times k}\left(1 - \frac{1}{N}\left(\frac{r}{r_c}\right)^{D}\right)^{N-k}. \tag{A.4}$$

In the limit N $\gg$ k, we obtain

$$P_k(r) = \frac{D\,r^{kD-1}\,\exp\left(-(\frac{r}{r_c})^D\right)}{(k-1)!\;\;r_c^{kD}} \tag{A.5}$$

and substituting equation A.2 in equation A.5, we can write the probability density for the distance to the k^{th} nearest neighbour in terms of the number density n. The mean distance to the k^{th} neighbour $\langle r_k \rangle$, the mean square distance to the k^{th} nearest neighbour $\langle r_k^2 \rangle$, etc., can be obtained using P_k(r). The general expression for $\langle r_k^\alpha \rangle$ is given by

$$\langle r_k^\alpha \rangle = \int_0^\infty r^\alpha\,P_k(r)\,dr = \frac{\Gamma\left(k + \frac{\alpha}{D}\right)}{(k-1)!}\,r_c. \tag{A.6}$$

Let $P_{k|k-1}$(r) dr denote the conditional probability for the k^{th} nearest neighbour being at a distance r, given that the (k-1)th nearest neighbour distance is r_{k-1}. This is the product of the probability that a particle is found in a shell of radius r and thickness dr and the probability that none of the remaining N-k particles is found in the excluded volume between the sphere of radius r and the sphere of radius r_{k-1}. Since the k^{th} nearest neighbour has to be more distant than the (k-1)th nearest neighbour, this is for r$\geq r_{k-1}$.

$$P_{k|k-1}(r)dr = (N-k+1)\,\frac{V_D'(r)\,dr}{V - V_D(r_{k-1})} \times \left(\frac{V - V_D(r)}{V - V_D(r_{k-1})}\right)^{N-k} \quad : r \geq r_{k-1} \tag{A.7}$$

Using V = N $V_D(r_c)$, we get

$$P_{k|k-1}(r) = \frac{(N-k+1)D}{r} \times \frac{r^D}{N r_c^D - r_{k-1}^D} \times \left(1 - \frac{r^D - r_{k-1}^D}{N r_c^D - r_{k-1}^D}\right)^{N-k} \quad : r \geq r_{k-1}. \tag{A.8}$$

In the limit N $\gg$ k, we get obtain the expression

$$P_{k|k-1}(r) = \frac{D\,r^{D-1}}{r_c^D}\,\exp\left(\frac{r_{k-1}^D - r^D}{r_c^D}\right) \quad : r \geq r_{k-1}. \tag{A.9}$$

Appendix B

Mechanical drawings

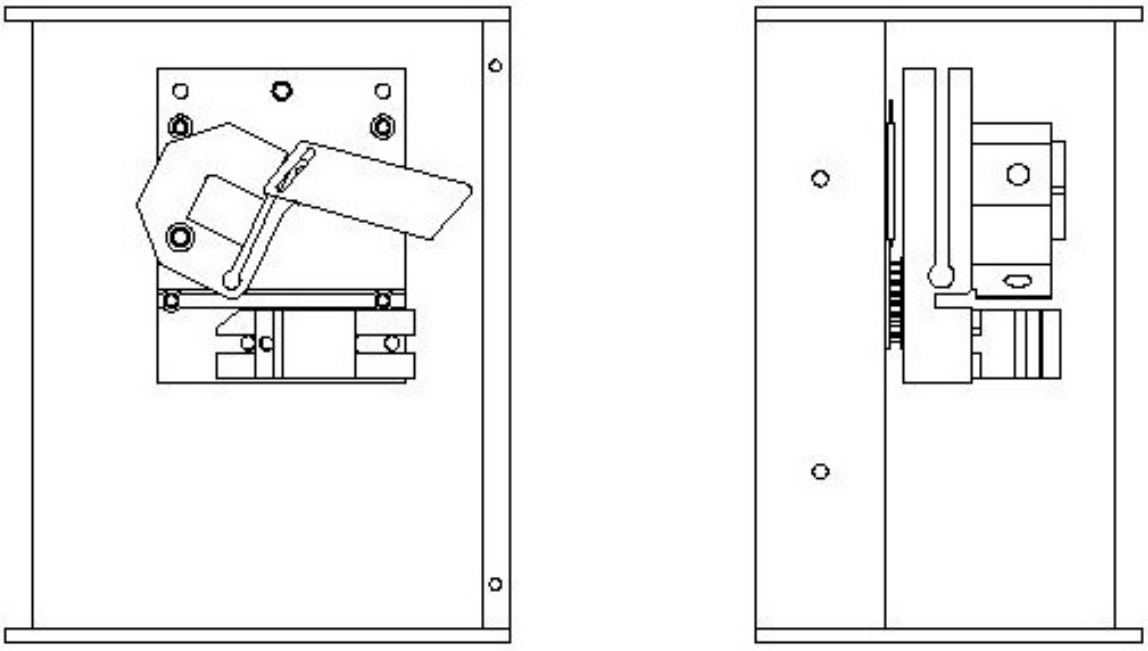

Figure B.1: Laser mount showing diode and grating mounts.

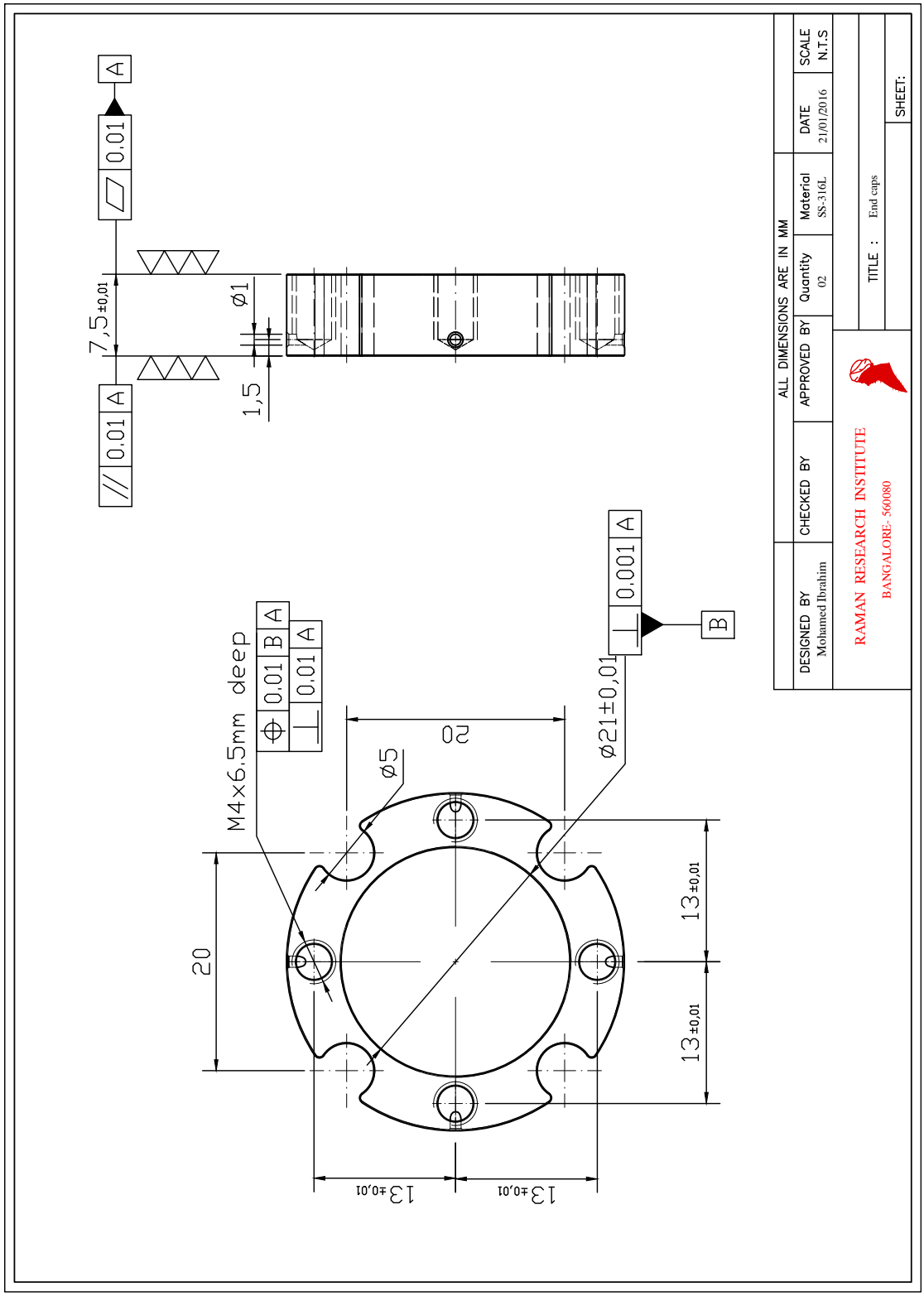
A
0,01
7,5±0,01
ø1
1,5
// 0.01 A
M4x6.5mm deep
⌖ 0,01 B A
⊥ 0,01 A
ø5
R2
ø21±0,01
⊥ 0.001 A
B
20
13±0,01
13±0,01
13±0,01
13±0,01
ALL DIMENSIONS ARE IN MM
DESIGNED BY
Mohamed Ibrahim
CHECKED BY
APPROVED BY
Quantity
02
Material
SS-316L
DATE
21/01/2016
SCALE
N.T.S
TITLE : End caps
SHEET:
RAMAN RESEARCH INSTITUTE
BANGALORE- 560080

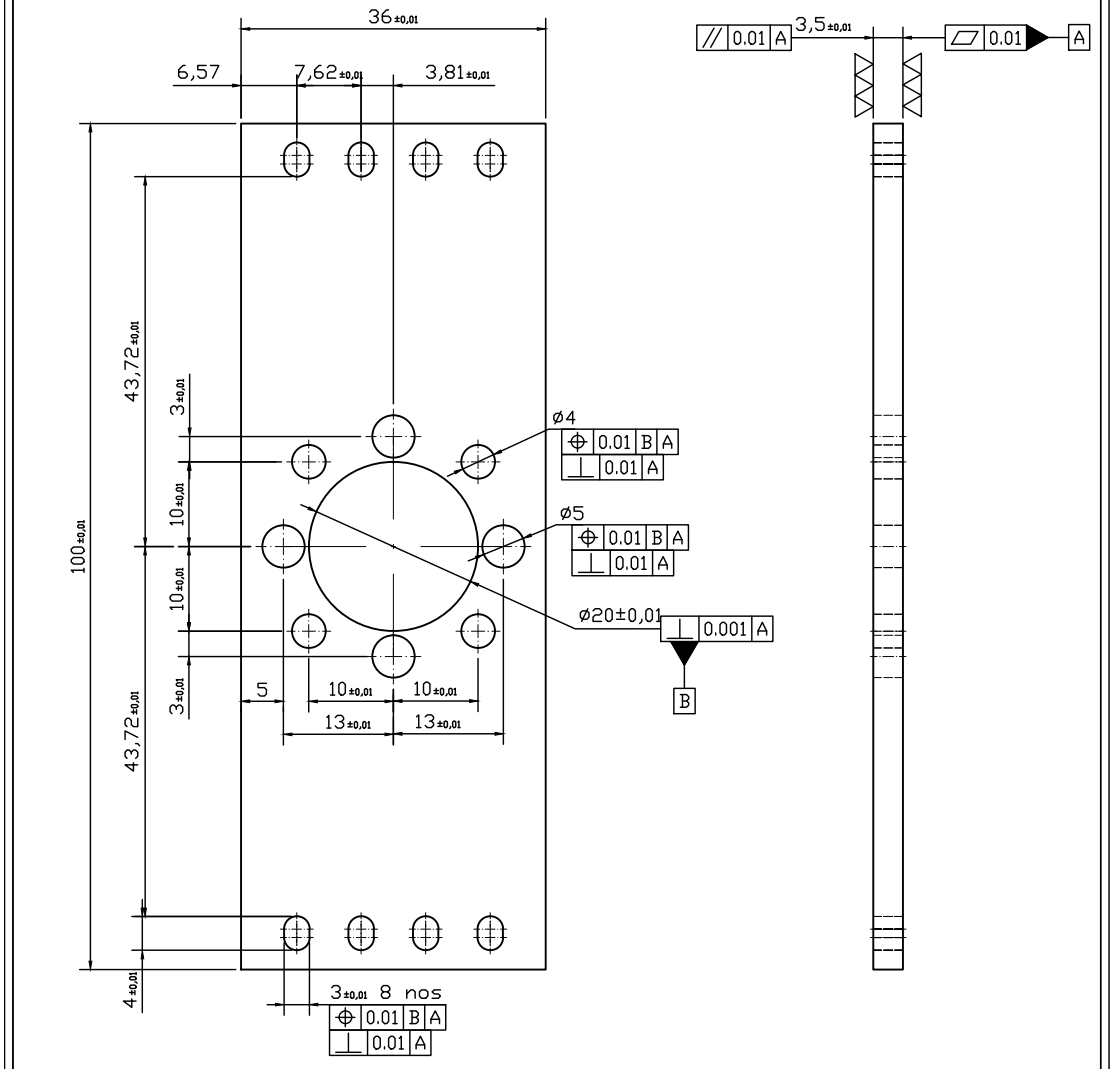

	ALL DIMENSIONS ARE IN MM					
DESIGNED BY Mohamed Ibrahim	CHECKED BY	APPROVED BY	Quantity 02	Material SS-316L	DATE 21/01/2016	SCALE N.T.S

RAMAN RESEARCH INSTITUTE
BANGALORE- 560080

TITLE : SS mounting plate

SHEET:

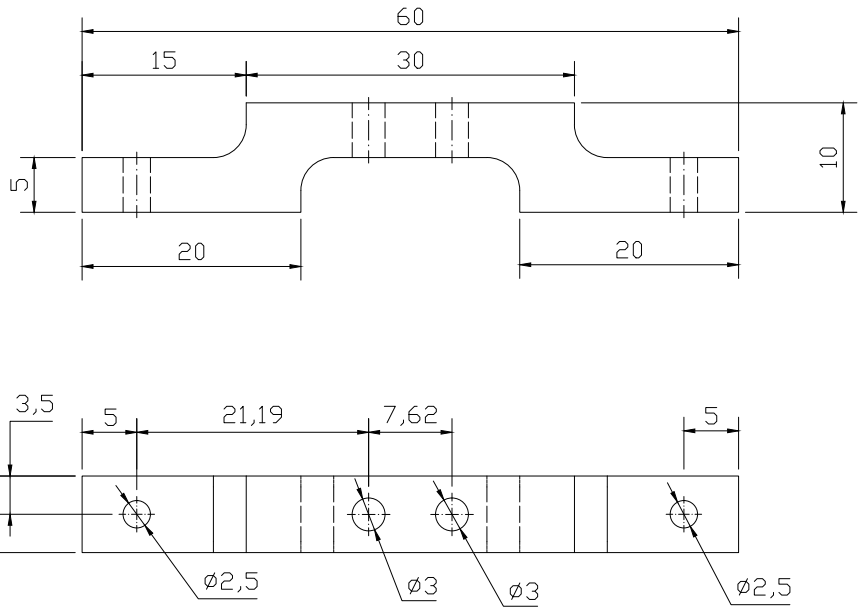

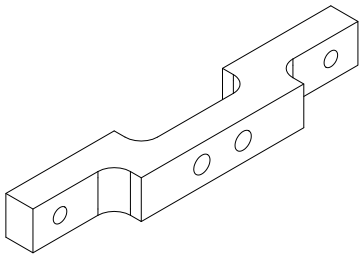

	ALL DIMENSIONS ARE IN MM					
DESIGNED BY Mohamed Ibrahim	CHECKED BY	APPROVED BY	Quantity 02	FILE NAME	DATE 18/09/2015	SCALE N.T.S

RAMAN RESEARCH INSTITUTE
BANGALORE- 560080

TITLE : Ceramic seperator

SHEET:

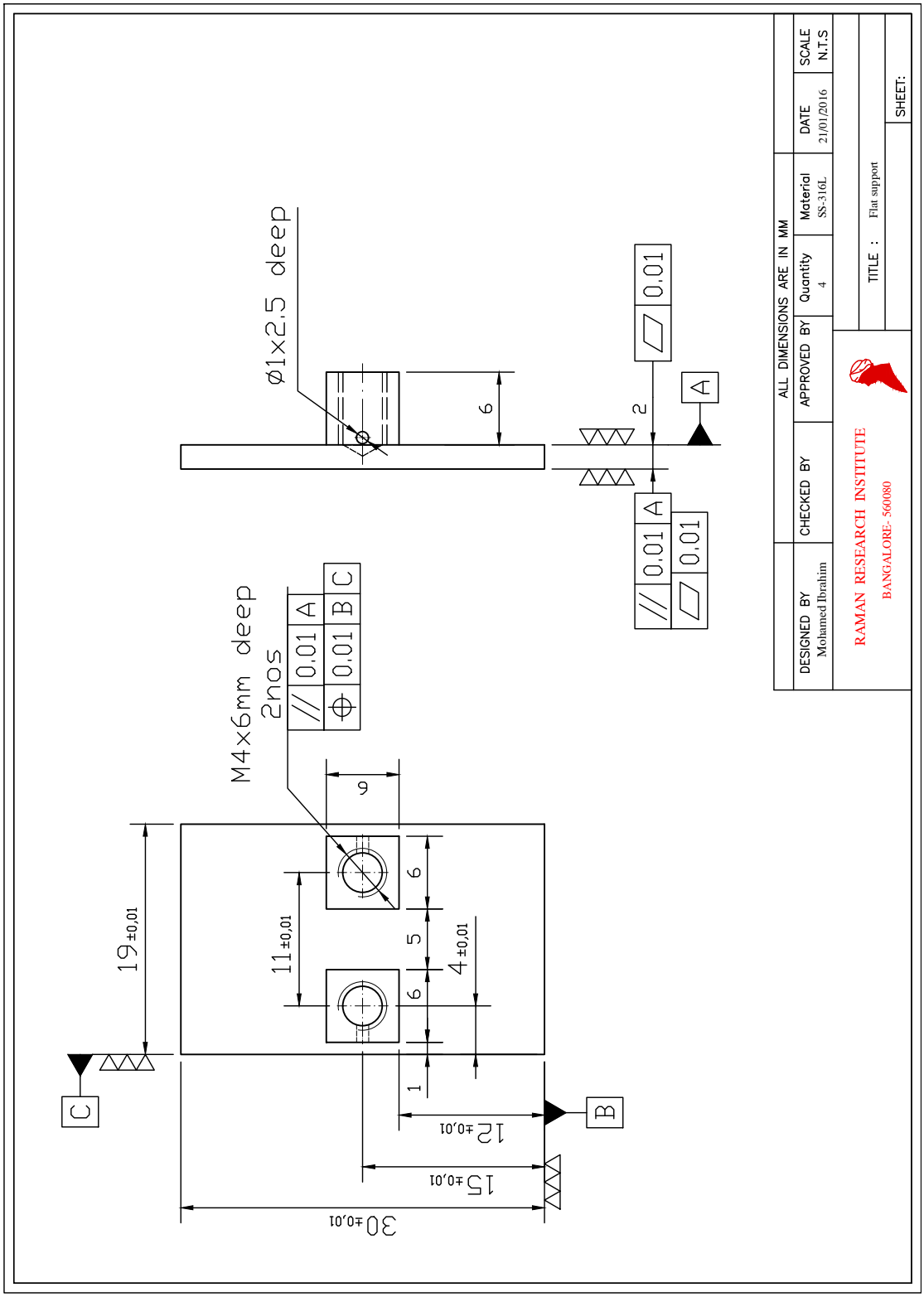
ALL DIMENSIONS ARE IN MM
DESIGNED BY
Mohamed Ibrahim
CHECKED BY
APPROVED BY
Quantity
4
Material
SS-316L
DATE
21/01/2016
SCALE
N.T.S
TITLE : Flat support
SHEET:
RAMAN RESEARCH INSTITUTE
BANGALORE- 560080
ø1x2.5 deep
6
2
0.01 A
0.01
0.01 A
0.01
M4x6mm deep
2nos
0.01 A
0.01 B C
9
19±0,01
11±0,01
6
5
6
4±0,01
1
12±0,01
15±0,01
30±0,01
C
B
A

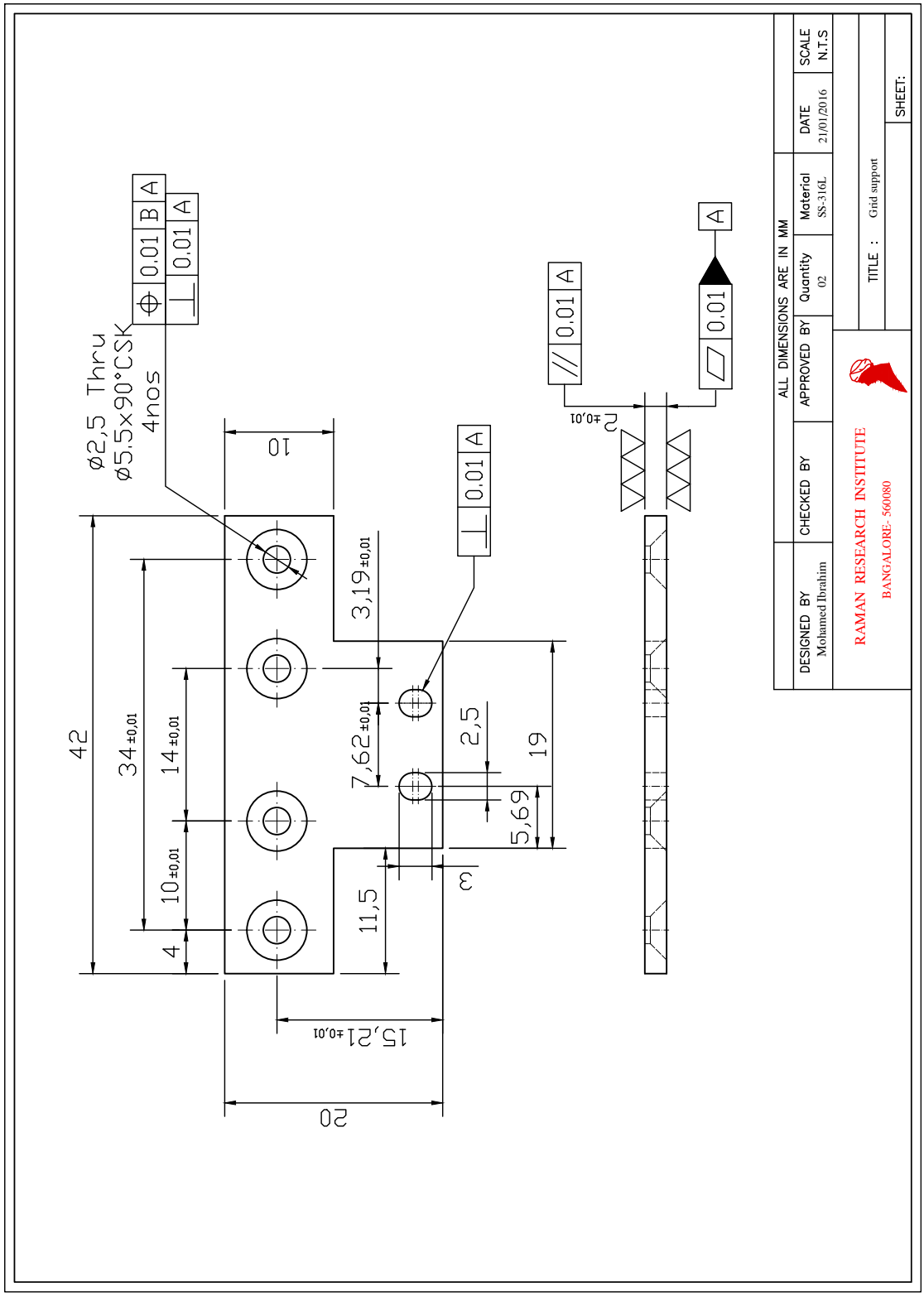
ø2,5 Thru
ø5,5x90°CSK
4nos
⌖ 0.01 B A
⊥ 0.01 A
10
42
34 ±0,01
14 ±0,01
10 ±0,01
4
3,19 ±0,01
7,62 ±0,01
2,5
19
5,69
3
11,5
15,21 ±0,01
20
⊥ 0.01 A
// 0.01 A
2 ±0,01
0.01 A
ALL DIMENSIONS ARE IN MM
DESIGNED BY
Mohamed Ibrahim
CHECKED BY
APPROVED BY
Quantity
02
Material
SS-316L
DATE
21/01/2016
SCALE
N.T.S
TITLE : Grid support
SHEET:
RAMAN RESEARCH INSTITUTE
BANGALORE- 560080

Appendix C

Mathematica code for charge hop rates

All numerical codes for arriving at the main results of this thesis have been made available with a google drive link given below. Any further details can be requested by contacting the author via email: niranjanmyneni2004@gmail.com.

Here we have provided a one of these numerical codes, which clarifies the methodology which is conceived and conceptualized by the author in this thesis, for obtaining the charge hopping rates between an ion and an atom at ultracold temperatures. Also the extension of the hopping rate between an pair, to obtain charge hopping rates for an ion in a uniform ensemble of ultracold atoms can be found below. The code provided here has been written for Mathematica 11.0 version and comments have been placed to make the code self explanatory.

$h = 6.62607015 * (10^{-34})$;(*Planck's constant in SI*)

$hcut = h/(2\pi)$;

$Eh = 4.35974465054 * 10^{-18}$; (*Hartree/Joule*)

$a0 = 5.291772106712 * (10^{-11})$; (*Bohr radius in m*)

$e = 1.602176620898 * (10^{-19})$; (*proton charge in C*)

$kB = 1.3806485279 * (10^{-23})$; (*Boltzmann constant in SI*)

$m6 = 6.01512279516 * 1.66053904020 * (10^{-27})$; (*mass of ^{6}Li*)

$m7 = 7.016003436645 * 1.66053904020 * (10^{-27}$; (*mass of ^{7}Li*)

$x6 = 2/3; x7 = 3/8;$

$Ta = T$; (*Temp. of atoms*)

$Ti = T$; (*Temp. of ion, used to apply a corresponding delocalization (via de Broglie wavelength)*)

$\lambda Ta6 = Sqrt[h^2/(2\pi\, m6\, kB\, Ta)];$

$\lambda Ti6 = Sqrt[h^2/(2\pi\, m6\, kB\, Ti)];$

$k6 = 2(\lambda Ta6^2 + \lambda Ti6^2);$

$\lambda Ta7 = Sqrt[h^2/(2\pi\, m7\, kB\, Ta)]$;(*de Broglie wavelengths*)

$\lambda Ti7 = Sqrt[h^2/(2\pi\, m7\, kB\, Ti)];$

$\Delta r = .005a0$; (*half-step size for integrating probability density*)

$k7 = 2(\lambda Ta7^2 + \lambda Ti7^2);$

$Pria3d6 = (r/Sqrt[\pi\, k6\, L^2])\,(Exp[-(L-r)^2/k6] - Exp[-(L+r)^2/k6])$; (*probability density functions for instantaneous ion-atom separation to be ria*)

$Pria3d7 = (r/Sqrt[\pi\, k7\, L^2])\,(Exp[-(L-r)^2/k7] - Exp[-(L+r)^2/k7]);$

$\Delta Pria3d6 = 1/(2L\, Sqrt[\pi])((Exp[-((L - ria + \Delta r)^2/k6)] - Exp[-((L + ria - \Delta r)^2/k6)]$
$- Exp[-((-L + ria + \Delta r)^2/k6)] + Exp[-((L + ria + \Delta r)^2/k6)])Sqrt[k6]$
$+ L\, Sqrt[\pi](Erf[Sqrt[(L - ria + \Delta r)^2/k6]] - Erf[Sqrt[(-L + ria + \Delta r)^2/k6]]$
$- Erf[Sqrt[(L + ria - \Delta r)^2/k6]] + Erf[Sqrt[(L + ria + \Delta r)^2/k6]]));$

$\Delta Pria3d7 = 1/(2L\, Sqrt[\pi])((Exp[-((L - ria + \Delta r)^2/k7)) - Exp[-((L + ria - \Delta r)^2/k7)]$
$- Exp[-((-L + ria + \Delta r)^2/k7)] + Exp[-((L + ria + \Delta r)^2/k7)])Sqrt[k7]$
$+ L\, Sqrt[\pi](Erf[Sqrt[(L - ria + \Delta r)^2/k7]] - Erf[Sqrt[(-L + ria + \Delta r)^2/k7]]$

$$- Erf[Sqrt[(L + ria - \Delta r)^2/k7]] + Erf[Sqrt[(L + ria + \Delta r)^2/k7]]);$$

(*pobability that instantaneous ion-atom separation is between $ria - \Delta r$ and $ria + \Delta r$, $\Delta Pria3d = Integrate[Pria3d, \{r, ria - \Delta r, ria + \Delta r\}]$*)

$$Vg6 = ReadList[OpenRead["folderaddress//2\Sigma_g.ext"], \{Real, Character, Real\}];$$

(*Import PEC data, R is in atomic units*)

$$Vu6 = ReadList[OpenRead["folderaddress//2\Sigma_u.ext"], \{Real, Character, Real\}];$$

$$Vg7 = ReadList[OpenRead["folderaddress//2\Sigma_g.ext"], \{Real, Character, Real\}];$$

(*Import PEC data, R is in atomic units*)

$$Vu7 = ReadList[OpenRead["folderaddress//2\Sigma_u.ext"], \{Real, Character, Real\}];$$

(*Potentials are in units of Hartree *)

$$vex6 = Table[\{Vg6[[i, 1]], (Vu6[[i, 3]] - Vg6[[i, 3]])\}, \{i, 1, Length[Vg6]\}];$$

$$vex7 = Table[\{Vg7[[i, 1]], (Vu7[[i, 3]] - Vg7[[i, 3]])\}, \{i, 1, Length[Vg7]\}];$$

(*table of exchange energies from PEC data*)

$$Clear[Vg6, Vu6, Vg7, Vu7]$$

(*

$$Tabk6collTby\rho = Table[\{T = 10^{lT}, (kB\,T)^{-2}\, Sqrt[16kB\,T/(\pi\, m6)] \times$$
$$Integrate[Exp[-EE/(kB\,T)]\, EE\, Interpolation[\sigma tot6][EE]$$
$$, \{EE, \eta g6[[-1, 1]]\, Eh, \eta g6[[1, 1]]\, Eh\}]\}, \{lT, -9, -.2, .1\}];$$

$$Tabk7collTby\rho = Table[\{T = 10^{lT}, (kB\,T)^{-2}\, Sqrt[216kB\,T/(\pi\, m7)] \times$$
$$Integrate[Exp[-EE/(kB\,T)]\, EE\, Interpolation[\sigma tot7][EE]$$
$$, \{EE, \eta g7[[-1, 1]]\, Eh, \eta g7[[1, 1]]\, Eh\}]\}, \{lT, -9, -.2, .1\}];$$

*)

$$Tab\nu 6hopTby\rho cont = Table[\{T = 10^{lT}, 4\pi Sum[rIA^2\, vex6[[Round[(rIA - 2a0)/(.01a0) + 1], 2]] \times .01a0, \{rIA, 2a0, 1000a0, .01a0\}]\, Eh/h\}, \{lT, -7, -2, .1\}];$$

$$Tab\nu 7hopTby\rho cont = Table[\{T = 10^{lT}, 4\pi Sum[rIA^2\, vex7[[Round[(rIA - 2a0)/(.01a0) + 1], 2]] \times .01a0, \{rIA, 2a0, 1000a0, .01a0\}] * Eh/h\}, \{lT, -7, -2, .1\}];$$

$$Tab\nu 7T3d19by\rho = Table[\{T = 10^{lT}, Sum[(L = Gamma[k + 1/3](3/(4\pi\, 10^{19}))^{(1/3)}/(k - 1)) \times Sum[\Delta Pria3d7 \times vex7[[Round[(ria - 2a0)/(.01a0) + 1], 2]], \{ria, 2a0, 50a0, .01a0\}]\, Eh/(L\, h\, 10^{19}), \{k, 1, If[lT < -5, 500, 200]\}]\}, \{lT, Log_{10}[3.3125\, hcut^2 (10^{19})^{(2/3)}/(m7\, kB)], -2, .2\}];$$

$$Tab\nu 7T3d18by\rho = Table[\{T = 10^{lT}, Sum[(L = Gamma[k + 1/3](3/(4\pi\, 10^{18}))^{(1/3)}/(k - 1)) \times Sum[\Delta Pria3d7 \times vex7[[Round[(ria - 2a0)/(.01a0) + 1], 2]], \{ria, 2a0, 50a0, .01a0\}]\, Eh/(L\, h\, 10^{18}), \{k, 1, If[lT < -5, 500, 200]\}]\}, \{lT, Log_{10}[3.3125\, hcut^2 (10^{18})^{(2/3)}/(m7\, kB)], -2, .2\}];$$

$$Tab\nu 7T3d17by\rho = Table[\{T = 10^{lT}, Sum[(L = Gamma[k + 1/3](3/(4\pi\, 10^{17}))^{(1/3)}/(k - 1)) \times Sum[\Delta Pria3d7 \times vex7[[Round[(ria - 2a0)/(.01a0) + 1], 2]], \{ria, 2a0, 50a0, .01a0\}]\, Eh/(L\, h\, 10^{17}), \{k, 1, 60\}]\}, \{lT, Log_{10}[3.3125\, hcut^2 (10^17)^{(2/3)}/(m7\, kB)], -2, .2\}];$$

$$Tab\nu 6T3d19by\rho = Table[\{T = 10^{lT}, Sum[(L = Gamma[k + 1/3](3/(4\pi\, 10^{19}))^{(1/3)}/(k - 1)) \times Sum[\Delta Pria3d6 \times vex6[[Round[(ria - 2a0)/(.01a0) + 1], 2]], \{ria, 2a0, 50a0, .01a0\}]\, Eh/(L\, h\, 10^{19}), \{k, 1, If[lT < -5, 500, 200]\}]\}, \{lT, Log10[4.7854\, hcut^2 (10^{19})^{(2/3)}/(m6\, kB)], -2, .2\}];$$

$$Tab\nu 6T3d18by\rho = Table[\{T = 10^{lT}, Sum[(L = Gamma[k + 1/3](3/(4\pi\, 10^{18}))^{(1/3)}/(k - 1)) \times Sum[\Delta Pria3d6 \times vex6[[Round[(ria - 2a0)/(.01a0) + 1], 2]], \{ria, 2a0, 50a0, .01a0\}]\, Eh/(L\, h\, 10^{18}), \{k, 1, If[lT < -5, 500, 200]\}]\}, \{lT, Log10[4.7854\, hcut^2 (10^{18})^{(2/3)}/(m6\, kB)], -2, .2\}];$$

$$Tab\nu 6T3d17by\rho = Table[\{T = 10^{lT}, Sum[(L = Gamma[k + 1/3](3/(4\pi\, 10^{17}))^{(1/3)}/(k - 1)) \times Sum[\Delta Pria3d6 \times vex6[[Round[(ria - 2a0)/(.01a0) + 1], 2]], \{ria, 2a0, 50a0, .01a0\}]\, Eh/(L\, h\, 10^{17}), \{k, 1, If[lT < -5, 500, 200]\}]\}, \{lT, Log10[4.7854\, hcut^2 (10^{17})^{(2/3)}/(m6\, kB)], -2, .2\}];$$

(*These codes result the hop rates used.*)

The other important codes that can be found in the google drive link provided below include the following, as separate folders:

- Vacuum Rabi splitting (VRS) with a MOT in cavity code and its implementation with different cavity modes.
- ion-atom collision cross sections codes
- ion hopping diffusion simulations
- Ion trap stability codes
- Virial analysis of $2k$-pole traps codes

Please visit for accessing additional numerical codes:

`https://drive.google.com/drive/folders/1R2c8PW2q9lpNpqlZtdd0Jz7NluHX6q-A?usp=sharing`

References

[1] T W Hänsch and A L Schawlow. "Cooling of gases by laser radiation". In: *Optics Communications* 13.1 (1975), pp. 68–69. ISSN: 0030-4018. DOI: https://doi.org/10.1016/0030-4018(75)90159-5.

[2] A Ashkin. "Trapping of Atoms by Resonance Radiation Pressure". In: *Physical Review Letters* 40.12 (Mar. 1978), pp. 729–732. DOI: 10.1103/PhysRevLett.40.729.

[3] D J Wineland, R E Drullinger, and F L Walls. "Radiation-Pressure Cooling of Bound Resonant Absorbers". In: *Physical Review Letters* 40.25 (June 1978), pp. 1639–1642. DOI: 10.1103/PhysRevLett.40.1639.

[4] A Aspect, E Arimondo, R Kaiser, N Vansteenkiste, and C Cohen-Tannoudji. "Laser Cooling below the One-Photon Recoil Energy by Velocity-Selective Coherent Population Trapping". In: *Physical Review Letters* 61.7 (Aug. 1988), pp. 826–829. DOI: 10.1103/PhysRevLett.61.826.

[5] Peter Horak, Gerald Hechenblaikner, Klaus M Gheri, Herwig Stecher, and Helmut Ritsch. "Cavity-Induced Atom Cooling in the Strong Coupling Regime". In: *Physical Review Letters* 79.25 (Dec. 1997), pp. 4974–4977. DOI: 10.1103/PhysRevLett.79.4974.

[6] William D Phillips. “Nobel Lecture: Laser cooling and trapping of neutral atoms”. In: *Reviews of Modern Physics* 70.3 (July 1998), pp. 721–741. DOI: 10.1103/RevModPhys.70.721.

[7] Hans Dehmelt. “Experiments with an isolated subatomic particle at rest”. In: *Reviews of Modern Physics* 62.3 (July 1990), pp. 525–530. DOI: 10.1103/RevModPhys.62.525.

[8] A Bermudez, T Schaetz, and M B Plenio. “Dissipation-Assisted Quantum Information Processing with Trapped Ions”. In: *Phys. Rev. Lett.* 110.11 (Mar. 2013), p. 110502. DOI: 10.1103/PhysRevLett.110.110502.

[9] E A Cornell and C E Wieman. “Nobel Lecture: Bose-Einstein condensation in a dilute gas, the first 70 years and some recent experiments”. In: *Reviews of Modern Physics* 74.3 (Aug. 2002), pp. 875–893. DOI: 10.1103/RevModPhys.74.875.

[10] Wayne M Itano, J C Bergquist, J J Bollinger, and D J Wineland. “Cooling methods in ion traps”. In: *Physica Scripta* T59 (1995), pp. 106–120. ISSN: 0031-8949. DOI: 10.1088/0031-8949/1995/t59/013.

[11] F G Major and H G Dehmelt. “Exchange-Collision Technique for the rf Spectroscopy of Stored Ions”. In: *Phys. Rev.* 170.1 (June 1968), pp. 91–107. DOI: 10.1103/PhysRev.170.91.

[12] F. G. Major, Viorica N. Gheorghe, and Günther Werth. *Charged Particle Traps*. 1st ed. Berlin: Springer-Verlag Berlin Heidelberg, 2005. ISBN: 1615-5653. DOI: 10.1007/b137836.

[13] Andrew T. Grier, Marko Cetina, Fedja Oručević, and Vladan Vuletić. “Observation of Cold Collisions between Trapped Ions and Trapped Atoms”. In: *Phys. Rev. Lett.* 102.22 (June 2009), p. 223201. DOI: 10.1103/PhysRevLett.102.223201.

[14] K Ravi, Seunghyun Lee, Arijit Sharma, G Werth, and S A Rangwala. “Cooling and stabilization by collisions in a mixed ion–atom system”. In: *Nature Communications* 3.1 (2012), p. 1126. ISSN: 2041-1723. DOI: 10.1038/ncomms2131.

[15] Felix H J Hall, Pascal Eberle, Gregor Hegi, Maurice Raoult, Mireille Aymar, Olivier Dulieu, and Stefan Willitsch. “Ion-neutral chemistry at ultralow energies: dynamics of reactive collisions between laser-cooled Ca+ ions and Rb atoms in an ion-atom hybrid trap”. In: *Molecular Physics* 111.14-15 (2013), pp. 2020–2032. DOI: 10.1080/00268976.2013.780107.

[16] Ziv Meir, Meirav Pinkas, Tomas Sikorsky, Ruti Ben-shlomi, Nitzan Akerman, and Roee Ozeri. “Direct Observation of Atom-Ion Nonequilibrium Sympathetic Cooling”. In: *Phys. Rev. Lett.* 121.5 (Aug. 2018), p. 53402. DOI: 10.1103/PhysRevLett.121.053402.

[17] T Schmid, C Veit, N Zuber, R Löw, T Pfau, M Tarana, and M Tomza. “Rydberg Molecules for Ion-Atom Scattering in the Ultracold Regime”. In: *Phys. Rev. Lett.* 120.15 (Apr. 2018), p. 153401. DOI: 10.1103/PhysRevLett.120.153401.

[18] Steven J Schowalter, Alexander J Dunning, Kuang Chen, Prateek Puri, Christian Schneider, and Eric R Hudson. “Blue-sky bifurcation of ion energies and the limits of neutral-gas sympathetic cooling of trapped ions”. In: *Nature Communications* 7.1 (2016), p. 12448. ISSN: 2041-1723. DOI: 10.1038/ncomms12448.

[19] T Feldker, H Fürst, H Hirzler, N V Ewald, M Mazzanti, D Wiater, M Tomza, and R Gerritsma. “Buffer gas cooling of a trapped ion to the quantum regime”. In: *Nature Physics* (2020). ISSN: 1745-2481. DOI: 10.1038/s41567-019-0772-5.

[20] Julian Schmidt, Alexander Lambrecht, Pascal Weckesser, Markus Debatin, Leon Karpa, and Tobias Schaetz. “Optical Trapping of Ion Coulomb Crystals”. In: *Phys. Rev. X* 8.2 (May 2018), p. 21028. DOI: 10.1103/PhysRevX.8.021028.

[21] Stefan Schmid, Arne Härter, and Johannes Hecker Denschlag. "Dynamics of a Cold Trapped Ion in a Bose-Einstein Condensate". In: *Phys. Rev. Lett.* 105.13 (Sept. 2010), p. 133202. DOI: 10.1103/PhysRevLett.105.133202.

[22] T Dieterle, M Berngruber, C Hölzl, R Löw, K Jachymski, T Pfau, and F Meinert. "Transport of a Single Cold Ion Immersed in a Bose-Einstein Condensate". In: *Phys. Rev. Lett.* 126.3 (Jan. 2021), p. 33401. DOI: 10.1103/PhysRevLett.126.033401.

[23] Krzysztof Tomza Michaland Jachymski, Rene Gerritsma, Antonio Negretti, Tommaso Calarco, Zbigniew Idziaszek, and Paul S Julienne. "Cold hybrid ion-atom systems". In: *Rev. Mod. Phys.* 91.3 (July 2019), p. 35001. DOI: 10.1103/RevModPhys.91.035001.

[24] Steven Chu. "Nobel Lecture: The manipulation of neutral particles". In: *Reviews of Modern Physics* 70.3 (July 1998), pp. 685–706. DOI: 10.1103/RevModPhys.70.685.

[25] A J Moerdijk, H M J M Boesten, and B J Verhaar. "Decay of trapped ultracold alkali atoms by recombination". In: *Physical Review A* 53.2 (Feb. 1996), pp. 916–920. DOI: 10.1103/PhysRevA.53.916.

[26] K W Madison, Y Wang, C Cohen-Tannoudji, and A M Rey. *Annual Review of Cold Atoms and Molecules*. Annual Review of Cold Atoms and Molecules v. 1. World Scientific, 2012. ISBN: 9789814440394.

[27] David R Leibrandt, Jaroslaw Labaziewicz, Vladan Vuletić, and Isaac L Chuang. "Cavity Sideband Cooling of a Single Trapped Ion". In: *Phys. Rev. Lett.* 103.10 (Aug. 2009), p. 103001. DOI: 10.1103/PhysRevLett.103.103001.

[28] N V Ewald, T Feldker, H Hirzler, H A Fürst, and R Gerritsma. “Observation of Interactions between Trapped Ions and Ultracold Rydberg Atoms”. In: *Phys. Rev. Lett.* 122.25 (June 2019), p. 253401. DOI: 10.1103/PhysRevLett.122.253401.

[29] Limei Wang, Markus Deißand Georg Raithel, and Johannes Hecker Denschlag. “Optical control of atom-ion collisions using a Rydberg state”. In: *Journal of Physics B: Atomic, Molecular and Optical Physics* 53.13 (June 2020), p. 134005. DOI: 10.1088/1361-6455/ab7d24.

[30] I Rouse and S Willitsch. “Superstatistical Energy Distributions of an Ion in an Ultracold Buffer Gas”. In: *Phys. Rev. Lett.* 118.14 (Apr. 2017), p. 143401. DOI: 10.1103/PhysRevLett.118.143401.

[31] Y Sherkunov, B Muzykantskii, N D’Ambrumenil, and B D Simons. “Probing ultracold Fermi atoms with a single ion”. In: *Phys. Rev. A* 79.2 (Feb. 2009), p. 23604. DOI: 10.1103/PhysRevA.79.023604.

[32] Claude N Cohen-Tannoudji. “Nobel Lecture: Manipulating atoms with photons”. In: *Reviews of Modern Physics* 70.3 (July 1998), pp. 707–719. DOI: 10.1103/RevModPhys.70.707.

[33] Wolfgang Ketterle. “Nobel lecture: When atoms behave as waves: Bose-Einstein condensation and the atom laser”. In: *Rev. Mod. Phys.* 74.4 (Nov. 2002), pp. 1131–1151. DOI: 10.1103/RevModPhys.74.1131.

[34] John Weiner, Vanderlei S Bagnato, Sergio Zilio, and Paul S Julienne. “Experiments and theory in cold and ultracold collisions”. In: *Reviews of Modern Physics* 71.1 (Jan. 1999), pp. 1–85. DOI: 10.1103/RevModPhys.71.1.

[35] Maciej Lewenstein, Anna Sanpera, Veronica Ahufinger, Bogdan Damski, Aditi Sen(De), and Ujjwal Sen. "Ultracold atomic gases in optical lattices: mimicking condensed matter physics and beyond". In: *Advances in Physics* 56.2 (Mar. 2007), pp. 243–379. ISSN: 0001-8732. DOI: 10.1080/00018730701223200.

[36] Immanuel Bloch, Jean Dalibard, and Wilhelm Zwerger. "Many-body physics with ultracold gases". In: *Reviews of Modern Physics* 80.3 (July 2008), pp. 885–964. DOI: 10.1103/RevModPhys.80.885.

[37] Immanuel Bloch, Jean Dalibard, and Sylvain Nascimbène. "Quantum simulations with ultracold quantum gases". In: *Nature Physics* 8.4 (2012), pp. 267–276. ISSN: 1745-2481. DOI: 10.1038/nphys2259.

[38] Hannes Bernien, Sylvain Schwartz, Alexander Keesling, Harry Levine, Ahmed Omran, Hannes Pichler, Soonwon Choi, Alexander S Zibrov, Manuel Endres, Markus Greiner, Vladan Vuletić, and Mikhail D Lukin. "Probing many-body dynamics on a 51-atom quantum simulator". In: *Nature* 551.7682 (2017), pp. 579–584. ISSN: 1476-4687. DOI: 10.1038/nature24622.

[39] Kensuke Inaba, Yuuki Tokunaga, Kiyoshi Tamaki, Kazuhiro Igeta, and Makoto Yamashita. "High-Fidelity Cluster State Generation for Ultracold Atoms in an Optical Lattice". In: *Phys. Rev. Lett.* 112.11 (Mar. 2014), p. 110501. DOI: 10.1103/PhysRevLett.112.110501.

[40] Christopher Monroe. "Atomic physics Shaping atoms in optical lattices". In: *Nature* 388.6644 (1997), pp. 719–720. ISSN: 1476-4687. DOI: 10.1038/41885.

[41] J D Sterk, L Luo, T A Manning, P Maunz, and C Monroe. "Photon collection from a trapped ion-cavity system". In: *Phys. Rev. A* 85.6 (June 2012), p. 062308. DOI: 10.1103/PhysRevA.85.062308.

[42] Harvey B Kaplan, Lingzhen Guo, Wen Lin Tan, Arinjoy De, Florian Marquardt, Guido Pagano, and Christopher Monroe. "Many-Body Dephasing in a Trapped-Ion Quantum Simulator". In: *Phys. Rev. Lett.* 125.12 (Sept. 2020), p. 120605. DOI: 10.1103/PhysRevLett.125.120605.

[43] Th. Udem, R Holzwarth, and T W Hänsch. "Optical frequency metrology". In: *Nature* 416.6877 (2002), pp. 233–237. ISSN: 1476-4687. DOI: 10.1038/416233a.

[44] Andrew D Ludlow, Martin M Boyd, Jun Ye, E Peik, and P O Schmidt. "Optical atomic clocks". In: *Rev. Mod. Phys.* 87.2 (June 2015), pp. 637–701. DOI: 10.1103/RevModPhys.87.637.

[45] J D Prestage, R L Tjoelker, and L Maleki. "Mercury-ion clock based on linear multi-pole ion trap". In: *Proceedings of the 2000 IEEE/EIA International Frequency Control Symposium and Exhibition (Cat. No.00CH37052)*. 2000, pp. 706–710. ISBN: 1075-6787 VO -. DOI: 10.1109/FREQ.2000.887441.

[46] Jae C Schwartz, Michael W Senko, and John E P Syka. "A two-dimensional quadrupole ion trap mass spectrometer". In: *Journal of the American Society for Mass Spectrometry* 13.6 (2002), pp. 659–669. DOI: 10.1021/jasms.8b01797.

[47] Donald J Douglas, Aaron J Frank, and Dunmin Mao. "Linear ion traps in mass spectrometry". In: *Mass Spectrometry Reviews* 24.1 (2005), pp. 1–29. DOI: https://doi.org/10.1002/mas.20004.

[48] Felix H.J. Hall, Mireille Aymar, Maurice Raoult, Olivier Dulieu, and Stefan Willitsch. "Light-assisted cold chemical reactions of barium ions with rubidium atoms". In: *Molecular Physics* 111.12-13 (July 2013), pp. 1683–1690. ISSN: 00268976. DOI: 10.1080/00268976.2013.770930.

[49] M Albert, J P Marler, P F Herskind, A Dantan, and M Drewsen. “Collective strong coupling between ion Coulomb crystals and an optical cavity field: Theory and experiment”. In: *Phys. Rev. A* 85.2 (Feb. 2012), p. 023818. DOI: 10.1103/PhysRevA.85.023818.

[50] Peter F Herskind, Aurélien Dantan, Joan P Marler, Magnus Albert, and Michael Drewsen. “Realization of collective strong coupling with ion Coulomb crystals in an optical cavity”. In: *Nature Physics* 5 (June 2009), p. 494.

[51] Richard C Thompson. “Ion Coulomb crystals”. In: *Contemporary Physics* 56.1 (Jan. 2015), pp. 63–79. ISSN: 0010-7514. DOI: 10.1080/00107514.2014.989715.

[52] J I Cirac and P Zoller. “Quantum Computations with Cold Trapped Ions”. In: *Physical Review Letters* 74.20 (May 1995), pp. 4091–4094. DOI: 10.1103/PhysRevLett.74.4091.

[53] Marko Cetina, Alexei Bylinskii, Leon Karpa, Dorian Gangloff, Kristin M Beck, Yufei Ge, Matthias Scholz, Andrew T Grier, Isaac Chuang, and Vladan Vuletić. “One-dimensional array of ion chains coupled to an optical cavity”. In: *New Journal of Physics* 15.5 (2013), p. 53001.

[54] Carlo Sias, Lothar Ratschbacher, Christoph Zipkes, Michael Koehl, and AMOP Team. “A hybrid quantum system of ultracold atoms and trapped ions”. In: *APS Division of Atomic, Molecular and Optical Physics Meeting Abstracts*. Vol. 42. Cambridge, May 2011, OPJ.10.

[55] Leon Karpa, Alexei Bylinskii, Dorian Gangloff, Marko Cetina, and Vladan Vuletić. “Suppression of Ion Transport due to Long-Lived Subwavelength Localization by an Optical Lattice”. In: *Phys. Rev. Lett.* 111.16 (Oct. 2013), p. 163002. DOI: 10.1103/PhysRevLett.111.163002.

[56] Christoph Zipkes, Stefan Palzer, Carlo Sias, and Michael Köhl. "A trapped single ion inside a Bose–Einstein condensate". In: *Nature* 464.7287 (2010), pp. 388–391. ISSN: 1476-4687. DOI: 10.1038/nature08865.

[57] Ziv Meir, Tomas Sikorsky, Ruti Ben-Shlomi, Nitzan Akerman, Yehonatan Dallal, and Roee Ozeri. "Dynamics of a Ground-State Cooled Ion Colliding with Ultracold Atoms". In: *Physical Review Letters* 117.24 (Dec. 2016). DOI: 10.1103/PhysRevLett.117.243401.

[58] M H Anderson, J R Ensher, M R Matthews, C E Wieman, and E A Cornell. "Observation of Bose-Einstein Condensation in a Dilute Atomic Vapor". In: *Science* 269.5221 (1995), pp. 198–201. DOI: 10.1126/science.269.5221.198.

[59] B DeMarco and D S Jin. "Onset of Fermi Degeneracy in a Trapped Atomic Gas". In: *Science* 285.5434 (1999), pp. 1703–1706. DOI: 10.1126/science.285.5434.1703.

[60] S Inouye, M R Andrews, J Stenger, H.-J. Miesner, D M Stamper-Kurn, and W Ketterle. "Observation of Feshbach resonances in a Bose–Einstein condensate". In: *Nature* 392.6672 (1998), pp. 151–154. ISSN: 1476-4687. DOI: 10.1038/32354.

[61] T Loftus, C A Regal, C Ticknor, J L Bohn, and D S Jin. "Resonant Control of Elastic Collisions in an Optically Trapped Fermi Gas of Atoms". In: *Phys. Rev. Lett.* 88.17 (Apr. 2002), p. 173201. DOI: 10.1103/PhysRevLett.88.173201.

[62] K Dieckmann, C A Stan, S Gupta, Z Hadzibabic, C H Schunck, and W Ketterle. "Decay of an Ultracold Fermionic Lithium Gas near a Feshbach Resonance". In: *Phys. Rev. Lett.* 89.20 (Oct. 2002), p. 203201. DOI: 10.1103/PhysRevLett.89.203201.

[63] Cindy A Regal, Christopher Ticknor, John L Bohn, and Deborah S Jin. "Creation of ultracold molecules from a Fermi gas of atoms". In: *Nature* 424.6944 (2003), pp. 47–50. ISSN: 1476-4687. DOI: 10.1038/nature01738.

[64] Markus Greiner, Cindy A Regal, and Deborah S Jin. "Emergence of a molecular Bose–Einstein condensate from a Fermi gas". In: *Nature* 426.6966 (2003), pp. 537–540. ISSN: 1476-4687. DOI: 10.1038/nature02199.

[65] M W Zwierlein, C A Stan, C H Schunck, S M F Raupach, S Gupta, Z Hadzibabic, and W Ketterle. "Observation of Bose-Einstein Condensation of Molecules". In: *Phys. Rev. Lett.* 91.25 (Dec. 2003), p. 250401. DOI: 10.1103/PhysRevLett.91.250401.

[66] S Jochim, M Bartenstein, A Altmeyer, G Hendl, S Riedl, C Chin, J Hecker Denschlag, and R Grimm. "Bose-Einstein Condensation of Molecules". In: *Science* 302.5653 (2003), pp. 2101–2103. DOI: 10.1126/science.1093280.

[67] C. Cohen-Tannoudji. "Theory of atomic motion in laser light". In: 2008. DOI: 10.1063/1.36783.

[68] Igor B Mekhov, Christoph Maschler, and Helmut Ritsch. "Probing quantum phases of ultracold atoms in optical lattices by transmission spectra in cavity quantum electrodynamics". In: *Nature Physics* 3 (Mar. 2007), p. 319.

[69] Robert Jördens, Niels Strohmaier, Kenneth Günter, Henning Moritz, and Tilman Esslinger. "A Mott insulator of fermionic atoms in an optical lattice". In: *Nature* 455.7210 (2008), pp. 204–207. ISSN: 1476-4687. DOI: 10.1038/nature07244.

[70] Michaland Tomza, Krzysztof Jachymski, Rene Gerritsma, Antonio Negretti, Tommaso Calarco, Zbigniew Idziaszek, and Paul S. Julienne. "Cold hybrid ion-atom

systems". In: *Reviews of Modern Physics* 91.3 (July 2019). ISSN: 0034-6861. DOI: 10.1103/revmodphys.91.035001.

[71] Sara Shadmehri and Vladimir S Melezhik. "Confinement-induced resonances in two-center problem via a pseudopotential approach". In: *Phys. Rev. A* 99.3 (Mar. 2019), p. 32705. DOI: 10.1103/PhysRevA.99.032705.

[72] Lincoln D Carr, David DeMille, Roman V Krems, and Jun Ye. "Cold and ultracold molecules: science, technology and applications". In: *New Journal of Physics* 11.5 (May 2009), p. 55049. DOI: 10.1088/1367-2630/11/5/055049.

[73] Goulven Quéméner and Paul S Julienne. "Ultracold Molecules under Control!" In: *Chemical Reviews* 112.9 (Sept. 2012), pp. 4949–5011. ISSN: 0009-2665. DOI: 10.1021/cr300092g.

[74] John L Bohn, Ana Maria Rey, and Jun Ye. "Cold molecules: Progress in quantum engineering of chemistry and quantum matter". In: *Science* 357.6355 (2017), pp. 1002–1010. ISSN: 0036-8075. DOI: 10.1126/science.aam6299.

[75] K Ravi, S Lee, A Sharma, G Werth, and S A Rangwala. "Combined ion and atom trap for low-temperature ion–atom physics". In: *Applied Physics B* 107.4 (2012), pp. 971–981. ISSN: 1432-0649. DOI: 10.1007/s00340-011-4726-6.

[76] Sourav Dutta, Rahul Sawant, and S A Rangwala. "Collisional Cooling of Light Ions by Cotrapped Heavy Atoms". In: *Phys. Rev. Lett.* 118.11 (Mar. 2017), p. 113401. DOI: 10.1103/PhysRevLett.118.113401.

[77] Sourav Dutta and S A Rangwala. "Nondestructive detection of ions using atom-cavity collective strong coupling". In: *Phys. Rev. A* 94.5 (Nov. 2016), p. 053841. DOI: 10.1103/PhysRevA.94.053841.

[78] Sourav Dutta and S A Rangwala. “Cooling of trapped ions by resonant charge exchange”. In: *Phys. Rev. A* 97.4 (Apr. 2018), p. 41401. DOI: 10.1103/PhysRevA.97.041401.

[79] S Jyothi, Kisra N Egodapitiya, Brad Bondurant, Zhubing Jia, Eric Pretzsch, Piero Chiappina, Gang Shu, and Kenneth R Brown. “A hybrid ion-atom trap with integrated high resolution mass spectrometer”. In: *Review of Scientific Instruments* 90.10 (2019), p. 103201. DOI: 10.1063/1.5121431.

[80] William Lichten. “Resonant Charge Exchange in Atomic Collisions”. In: *Phys. Rev.* 131.1 (July 1963), pp. 229–238. DOI: 10.1103/PhysRev.131.229.

[81] N D Bhaskar, J Pietras, J Camparo, W Happer, and J Liran. “Spin Destruction in Collisions between Cesium Atoms”. In: *Phys. Rev. Lett.* 44.14 (Apr. 1980), pp. 930–933. DOI: 10.1103/PhysRevLett.44.930.

[82] Ruti Ben-shlomi, Romain Vexiau, Ziv Meir, Tomas Sikorsky, Nitzan Akerman, Meirav Pinkas, Olivier Dulieu, and Roee Ozeri. “Direct observation of ultracold atom-ion excitation exchange”. In: *Phys. Rev. A* 102.3 (Sept. 2020), p. 31301. DOI: 10.1103/PhysRevA.102.031301.

[83] R Côté and A Dalgarno. “Ultracold atom-ion collisions”. In: *Phys. Rev. A* 62.1 (June 2000), p. 12709. DOI: 10.1103/PhysRevA.62.012709.

[84] R Hackam. “Mobility and diffusion cross section of atomic xenon ion in xenon”. In: *Journal of Physics B: Atomic and Molecular Physics* 2.7 (July 1969), pp. 790–797. DOI: 10.1088/0022-3700/2/7/309.

[85] Robin Côté. *From Classical Mobility to Hopping Conductivity: Charge Hopping in an Ultracold Gas*. Tech. rep. 2000.

[86] E.R. Christensen, A. Camacho-Guardian, and G.M. Bruun. "Charged polarons and molecules in a Bose-Einstein condensate". In: *arXiv* 2.2 (2020), pp. 1–8. ISSN: 23318422.

[87] Seunghyun Lee. *The study of trapped ion collisions with cold atoms and cold molecules*. Ph.D. Thes. 2014.

[88] S Jyothi, Tridib Ray, Bhargava Ram, and Sadiqali Rangwala. "Hybrid ion, atom and light trap". In: *Proceedings of the International School of Physics "Enrico Fermi"* 189 (2015), pp. 269–278.

[89] Tridib Ray, S Jyothi, N Bhargava Ram, and S A Rangwala. "A thin wire ion trap to study ion–atom collisions built within a Fabry–Perot cavity". In: *Applied Physics B* 114.1 (Jan. 2014), pp. 267–273. ISSN: 1432-0649. DOI: 10.1007/s00340-013-5686-9.

[90] Marko Cetina, Andrew T. Grier, and Vladan Vuletić. "Micromotion-induced limit to atom-ion sympathetic cooling in Paul traps". In: *Physical Review Letters* 109.25 (Dec. 2012). ISSN: 00319007. DOI: 10.1103/PhysRevLett.109.253201.

[91] Ludwig Boltzmann. "Zur Integration der Diffusionsgleichung bei variabeln Diffusionscoefficienten". In: *Annalen der Physik* 289.13 (Jan. 1894), pp. 959–964. ISSN: 0003-3804. DOI: https://doi.org/10.1002/andp.18942891315.

[92] Alexander Dalgarno and David Robert Bates. "The mobilities of ions in their parent gases". In: *Philosophical Transactions of the Royal Society of London. Series A, Mathematical and Physical Sciences* 250.982 (1958), pp. 426–439. DOI: 10.1098/rsta.1958.0003.

[93] Serge Haroche and Jean-Michel Raimond. "Unveiling the quantum". eng. In: *Exploring the Quantum*. Oxford: Oxford University Press, 2006. ISBN: 9780198509141. DOI: 10.1093/acprof:oso/9780198509141.003.0001.

[94] J Dalibard and C Cohen-Tannoudji. “Laser cooling below the Doppler limit by polarization gradients: simple theoretical models”. In: *J. Opt. Soc. Am. B* 6.11 (Nov. 1989), pp. 2023–2045. DOI: 10.1364/JOSAB.6.002023.

[95] Paul D Lett, Richard N Watts, Christoph I Westbrook, William D Phillips, Phillip L Gould, and Harold J Metcalf. “Observation of Atoms Laser Cooled below the Doppler Limit”. In: *Phys. Rev. Lett.* 61.2 (July 1988), pp. 169–172. DOI: 10.1103/PhysRevLett.61.169.

[96] E L Raab, M Prentiss, Alex Cable, Steven Chu, and D E Pritchard. “Trapping of Neutral Sodium Atoms with Radiation Pressure”. In: *Phys. Rev. Lett.* 59.23 (Dec. 1987), pp. 2631–2634. DOI: 10.1103/PhysRevLett.59.2631.

[97] Hidetoshi Katori, Tetsuya Ido, Yoshitomo Isoya, and Makoto Kuwata-Gonokami. “Magneto-Optical Trapping and Cooling of Strontium Atoms down to the Photon Recoil Temperature”. In: *Phys. Rev. Lett.* 82.6 (Feb. 1999), pp. 1116–1119. DOI: 10.1103/PhysRevLett.82.1116.

[98] Jon Goldwin, Scott B Papp, Brian Demarco, and Deborah S Jin. “Two-species magneto-optical trap with 40K and 87Rb”. In: *Physical Review A* 65 (2002), p. 21402.

[99] M Taglieber, A.-C. Voigt, F Henkel, S Fray, T W Hänsch, and K Dieckmann. “Simultaneous magneto-optical trapping of three atomic species”. In: *Phys. Rev. A* 73.1 (Jan. 2006), p. 11402. DOI: 10.1103/PhysRevA.73.011402.

[100] Sebastian Kraft, Felix Vogt, Oliver Appel, Fritz Riehle, and Uwe Sterr. “Bose-Einstein Condensation of Alkaline Earth Atoms: $ˆ{40}\mathrm{Ca}$”. In: *Phys. Rev. Lett.* 103.13 (Sept. 2009), p. 130401. DOI: 10.1103/PhysRevLett.103.130401.

[101] Marcin Witkowski, Bartłomiej Nagórny, Rodolfo Munoz-Rodriguez, Roman Ciuryło, Piotr Szymon Żuchowski, Sławomir Bilicki, Marcin Piotrowski, Piotr Morzyński, and

MichałZawada. “Dual Hg-Rb magneto-optical trap”. In: *Opt. Express* 25.4 (Feb. 2017), pp. 3165–3179. DOI: 10.1364/OE.25.003165.

[102] William D Phillips and Harold Metcalf. “Laser Deceleration of an Atomic Beam”. In: *Phys. Rev. Lett.* 48.9 (Mar. 1982), pp. 596–599. DOI: 10.1103/PhysRevLett.48.596.

[103] K Dieckmann, R J C Spreeuw, M Weidemüller, and J T M Walraven. “Two-dimensional magneto-optical trap as a source of slow atoms”. In: *Phys. Rev. A* 58.5 (Nov. 1998), pp. 3891–3895. DOI: 10.1103/PhysRevA.58.3891.

[104] Sourav Dutta and S A Rangwala. “All-optical switching in a continuously operated and strongly coupled atom-cavity system”. In: *Applied Physics Letters* 110.12 (2017), p. 121107. DOI: 10.1063/1.4978933.

[105] M. Niranjan, Sourav Dutta, Tridib Ray, and S. A. Rangwala. “Measuring spatially extended density profiles using atom-cavity collective strong coupling to higher-order modes”. In: *Physical Review A* 99.3 (Mar. 2019). ISSN: 24699934. DOI: 10.1103/PhysRevA.99.033617.

[106] Robert Weinstock. “On a fallacious proof of Earnshaw’s theorem”. In: *American Journal of Physics* 44.4 (Apr. 1976), pp. 392–393. ISSN: 0002-9505. DOI: 10.1119/1.10449.

[107] Hans Dehmelt. “A Single Atomic Particle Forever Floating at Rest in Free Space: New Value for Electron Radius”. In: *Physica Scripta* T22 (Jan. 1988), pp. 102–110. DOI: 10.1088/0031-8949/1988/t22/016.

[108] Wolfgang Paul. “Electromagnetic Traps for Charged and Neutral Particles (Nobel Lecture)”. In: *Angewandte Chemie International Edition in English* 29.7 (July 1990), pp. 739–748. ISSN: 0570-0833. DOI: https://doi.org/10.1002/anie.199007391.

[109] Winthrop W Smith, Oleg P Makarov, and Jian Lin. "Cold ion–neutral collisions in a hybrid trap". In: *Journal of Modern Optics* 52.16 (Nov. 2005), pp. 2253–2260. ISSN: 0950-0340. DOI: 10.1080/09500340500275850.

[110] Yulin Huang, Guo-Zhong Li, Shenheng Guan, and Alan G Marshall. "A Combined Linear Ion Trap for Mass Spectrometry". In: *Journal of the American Society for Mass Spectrometry* 8.9 (1997), pp. 962–969. ISSN: 1044-0305. DOI: https://doi.org/10.1016/S1044-0305(97)82945-5.

[111] T Nakamura, S Ohtani, M Wada, K Okada, I Katayama, and H A Schuessler. "Ion dynamics and oscillation frequencies in a linear combined trap". In: *Journal of Applied Physics* 89.5 (2001), pp. 2922–2931. DOI: 10.1063/1.1345514.

[112] D J Bate, K Dholakia, R C Thompson, and D C Wilson. "Ion Oscillation Frequencies in a Combined Trap". In: *Journal of Modern Optics* 39.2 (1992), pp. 305–316. DOI: 10.1080/09500349214550301.

[113] A Perot and Charles Fabry. "On the Application of Interference Phenomena to the Solution of Various Problems of Spectroscopy and Metrology". In: *apj* 9 (Feb. 1899), p. 87. DOI: 10.1086/140557.

[114] Alessio Palavicini and Chumin Wang. "Ab initio design and experimental confirmation of Fabry–Perot cavities based on freestanding porous silicon multilayers". In: *Journal of Materials Science: Materials in Electronics* 31.1 (2020), pp. 60–64. ISSN: 1573-482X. DOI: 10.1007/s10854-019-01037-1.

[115] Rahul Sawant, Olivier Dulieu, and S A Rangwala. "Detection of ultracold molecules using an optical cavity". In: *Physical Review A* 97.6 (June 2018), p. 63405. DOI: 10.1103/PhysRevA.97.063405.

[116] Vladan Vuletić, James K. Thompson, Adam T. Black, and Jonathan Simon. "External-feedback laser cooling of molecular gases". In: *Physical Review A - Atomic, Molecular, and Optical Physics* 75.5 (2007), pp. 1–4. ISSN: 10502947. DOI: 10.1103/PhysRevA.75.051405.

[117] A Dombi, T W Clark, F I B Williams, F Jessen, J Fortágh, D Nagy, A Vukics, and P Domokos. "Collective self-trapping of atoms in a cavity". In: 23.8 (Aug. 2021), p. 83036. DOI: 10.1088/1367-2630/ac1a3c.

[118] A Dantan, P Herskind, J P Marler, M Albert, and M Drewsen. "Collective strong coupling with ion Coulomb crystals in an optical cavity". In: *CLEO/Europe - EQEC 2009 - European Conference on Lasers and Electro-Optics and the European Quantum Electronics Conference*. June 2009, p. 1. DOI: 10.1109/CLEOE-EQEC.2009.5191653.

[119] Hilton W. Chan, Adam T. Black, and Vladan Vuletić. "Observation of collective-emission-induced cooling of atoms in an optical cavity". In: *Physical Review Letters* 90.6 (2003), p. 063003. DOI: 10.1103/PhysRevLett.90.063003.

[120] Hilton W Chan, Adam T Black, and Vladan Vuletić. "Observation of Collective-Emission-Induced Cooling of Atoms in an Optical Cavity". In: *Phys. Rev. Lett.* 90.6 (Feb. 2003), p. 063003. DOI: 10.1103/PhysRevLett.90.063003.

[121] Monika H Schleier-Smith, Ian D Leroux, Hao Zhang, Mackenzie A Van Camp, and Vladan Vuletić. "Optomechanical Cavity Cooling of an Atomic Ensemble". In: *Phys. Rev. Lett.* 107.14 (Sept. 2011), p. 143005. DOI: 10.1103/PhysRevLett.107.143005.

[122] J McKeever, A Boca, A D Boozer, R Miller, J R Buck, A Kuzmich, and H J Kimble. "Deterministic Generation of Single Photons from One Atom Trapped in a Cavity". In: *Science* 303.5666 (2004), pp. 1992–1994. ISSN: 0036-8075. DOI: 10.1126/science.1095232.

[123] A K Tuchman, R Long, G Vrijsen, J Boudet, J Lee, and M A Kasevich. "Normal-mode splitting with large collective cooperativity". In: *Phys. Rev. A* 74.5 (Nov. 2006), p. 053821. DOI: 10.1103/PhysRevA.74.053821.

[124] Tridib Ray, Arijit Sharma, S Jyothi, and S A Rangwala. "Temperature measurement of laser-cooled atoms using vacuum Rabi splitting". In: *Phys. Rev. A* 87.3 (Mar. 2013), p. 033832. DOI: 10.1103/PhysRevA.87.033832.

[125] Jinjin Du, Wenfang Li, Ruijuan Wen, Gang Li, Pengfei Zhang, and Tiancai Zhang. "Precision measurement of single atoms strongly coupled to the higher-order transverse modes of a high-finesse optical cavity". In: *Applied Physics Letters* 103.8 (2013), p. 83117. DOI: 10.1063/1.4819228.

[126] E A Hinds. "Cavity Quantum Electrod Ynamics". In: ed. by David Bates and Benjamin Bederson. Vol. 28. Advances In Atomic, Molecular, and Optical Physics Supplement C. Academic Press, 1990, pp. 237–289. DOI: https://doi.org/10.1016/S1049-250X(08)60201-3.

[127] C J Hood, M S Chapman, T W Lynn, and H J Kimble. "Real-Time Cavity QED with Single Atoms". In: *Phys. Rev. Lett.* 80.19 (May 1998), pp. 4157–4160. DOI: 10.1103/PhysRevLett.80.4157.

[128] A D Boozer, A Boca, R Miller, T E Northup, and H J Kimble. "Cooling to the Ground State of Axial Motion for One Atom Strongly Coupled to an Optical Cavity". In: *Phys. Rev. Lett.* 97.8 (Aug. 2006), p. 083602. DOI: 10.1103/PhysRevLett.97.083602.

[129] P Münstermann, T Fischer, P.W.H Pinkse, and G Rempe. "Single slow atoms from an atomic fountain observed in a high-finesse optical cavity". In: *Optics Communications* 159.1-3 (Jan. 1999), pp. 63–67. ISSN: 0030-4018. DOI: 10.1016/S0030-4018(98)00596-3.

[130] P Münstermann, T Fischer, P Maunz, P W H Pinkse, and G Rempe. "Dynamics of Single-Atom Motion Observed in a High-Finesse Cavity". In: *Phys. Rev. Lett.* 82.19 (May 1999), pp. 3791–3794. DOI: 10.1103/PhysRevLett.82.3791.

[131] H Mabuchi, J Ye, and H J Kimble. "Full observation of single-atom dynamics in cavity QED". In: *Applied Physics B* 68.6 (June 1999), pp. 1095–1108. ISSN: 1432-0649. DOI: 10.1007/s003400050751.

[132] J M Raimond, M Brune, and S Haroche. "Manipulating quantum entanglement with atoms and photons in a cavity". In: *Rev. Mod. Phys.* 73.3 (Aug. 2001), pp. 565–582. DOI: 10.1103/RevModPhys.73.565.

[133] T Fischer, P Maunz, P W H Pinkse, T Puppe, and G Rempe. "Feedback on the Motion of a Single Atom in an Optical Cavity". In: *Phys. Rev. Lett.* 88.16 (Apr. 2002), p. 163002. DOI: 10.1103/PhysRevLett.88.163002.

[134] P Horak, H Ritsch, T Fischer, P Maunz, T Puppe, P W H Pinkse, and G Rempe. "Optical Kaleidoscope Using a Single Atom". In: *Phys. Rev. Lett.* 88.4 (Jan. 2002), p. 043601. DOI: 10.1103/PhysRevLett.88.043601.

[135] Vladan Vuletić, James K Thompson, Adam T Black, and Jonathan Simon. "External-feedback laser cooling of molecular gases". In: *Phys. Rev. A* 75.5 (May 2007), p. 051405. DOI: 10.1103/PhysRevA.75.051405.

[136] D E Chang, J D Thompson, H Park, V Vuletić, A S Zibrov, P Zoller, and M D Lukin. "Trapping and Manipulation of Isolated Atoms Using Nanoscale Plasmonic Structures". In: *Phys. Rev. Lett.* 103.12 (Sept. 2009), p. 123004. DOI: 10.1103/PhysRevLett.103.123004.

[137] Markus Koch, Christian Sames, Alexander Kubanek, Matthias Apel, Maximilian Balbach, Alexei Ourjoumtsev, Pepijn W H Pinkse, and Gerhard Rempe. "Feedback Cooling of a Single Neutral Atom". In: *Phys. Rev. Lett.* 105.17 (Oct. 2010), p. 173003. DOI: 10.1103/PhysRevLett.105.173003.

[138] Matthias Keller, Birgit Lange, Kazuhiro Hayasaka, Wolfgang Lange, and Herbert Walther. "Continuous generation of single photons with controlled waveform in an ion-trap cavity system". In: *Nature* 431 (Oct. 2004), p. 1075.

[139] R Miller, T E Northup, K M Birnbaum, A Boca, A D Boozer, and H J Kimble. "Trapped atoms in cavity QED: coupling quantized light and matter". In: *Journal of Physics B: Atomic, Molecular and Optical Physics* 38.9 (2005), S551.

[140] Gessler Hernandez, Jiepeng Zhang, and Yifu Zhu. "Vacuum Rabi splitting and intracavity dark state in a cavity-atom system". In: *Phys. Rev. A* 76.5 (Nov. 2007), p. 053814. DOI: 10.1103/PhysRevA.76.053814.

[141] Christine Guerlin, Etienne Brion, Tilman Esslinger, and Klaus Mølmer. "Cavity quantum electrodynamics with a Rydberg-blocked atomic ensemble". In: *Phys. Rev. A* 82.5 (Nov. 2010), p. 053832. DOI: 10.1103/PhysRevA.82.053832.

[142] Helmut Ritsch, Peter Domokos, Ferdinand Brennecke, and Tilman Esslinger. "Cold atoms in cavity-generated dynamical optical potentials". In: *Rev. Mod. Phys.* 85.2 (Apr. 2013), pp. 553–601. DOI: 10.1103/RevModPhys.85.553.

[143] A Wickenbrock, M Hemmerling, G R M Robb, C Emary, and F Renzoni. "Collective strong coupling in multimode cavity QED". In: *Phys. Rev. A* 87.4 (Apr. 2013), p. 043817. DOI: 10.1103/PhysRevA.87.043817.

[144] Stephen Begley, Markus Vogt, Gurpreet Kaur Gulati, Hiroki Takahashi, and Matthias Keller. "Optimized Multi-Ion Cavity Coupling". In: *Phys. Rev. Lett.* 116.22 (May 2016), p. 223001. DOI: 10.1103/PhysRevLett.116.223001.

[145] G Goubau and F Schwering. "On the guided propagation of electromagnetic wave beams". In: *IRE Transactions on Antennas and Propagation* 9.3 (May 1961), pp. 248–256. ISSN: 0096-1973. DOI: 10.1109/TAP.1961.1144999.

[146] E. T. Jaynes and F. W. Cummings. "Comparison of Quantum and Semiclassical Radiation Theories with Application to the Beam Maser". In: *Proceedings of the IEEE* 51.1 (1963), pp. 89–109. ISSN: 15582256. DOI: 10.1109/PROC.1963.1664.

[147] Michael Tavis and Frederick W Cummings. "Exact Solution for an N-Molecule Radiation-Field Hamiltonian". In: *Phys. Rev.* 170.2 (June 1968), pp. 379–384. DOI: 10.1103/PhysRev.170.379.

[148] Paul R Berman, ed. *Cavity Quantum Electrodynamics (Advances in Atomic, Molecular and Optical Physics)*. Academic Press, Jan. 1994.

[149] D Meschede, H Walther, and G Müller. "One-Atom Maser". In: *Phys. Rev. Lett.* 54.6 (Feb. 1985), pp. 551–554. DOI: 10.1103/PhysRevLett.54.551.

[150] Gerhard Rempe, Herbert Walther, and Norbert Klein. "Observation of quantum collapse and revival in a one-atom maser". In: *Phys. Rev. Lett.* 58.4 (Jan. 1987), pp. 353–356. DOI: 10.1103/PhysRevLett.58.353.

[151] R J Thompson, G Rempe, and H J Kimble. "Observation of normal-mode splitting for an atom in an optical cavity". In: *Phys. Rev. Lett.* 68.8 (Feb. 1992), pp. 1132–1135. DOI: 10.1103/PhysRevLett.68.1132.

[152] K M Birnbaum, A Boca, R Miller, A D Boozer, T E Northup, and H J Kimble. “Photon blockade in an optical cavity with one trapped atom”. In: *Nature* 436 (July 2005), p. 87.

[153] Magnus Albert. “A light-matter interface based on ion Coulomb crystals in an optical cavity”. PhD thesis. 2011.

[154] Magnus Albert, Aurélien Dantan, and Michael Drewsen. “Cavity electromagnetically induced transparency and all-optical switching using ion Coulomb crystals”. In: *Nature Photonics* 5 (Sept. 2011), p. 633.

[155] Rahul Sawant and S A Rangwala. “Lasing by driven atoms-cavity system in collective strong coupling regime”. In: *Scientific Reports* 7.1 (2017), p. 11432. ISSN: 2045-2322. DOI: 10.1038/s41598-017-11799-5.

[156] J Gripp, S L Mielke, and L A Orozco. “Evolution of the vacuum Rabi peaks in a detuned atom-cavity system”. In: *Phys. Rev. A* 56.4 (Oct. 1997), pp. 3262–3273. DOI: 10.1103/PhysRevA.56.3262.

[157] Da Steck. “Rubidium 85 D line data”. In: *Physics* (2001), p. 31. ISSN: 00301299. DOI: 10.1029/JB075i002p00463.

[158] J Gripp, S L Mielke, L A Orozco, and H J Carmichael. “Anharmonicity of the vacuum Rabi peaks in a many-atom system”. In: *Phys. Rev. A* 54.5 (Nov. 1996), R3746–R3749. DOI: 10.1103/PhysRevA.54.R3746.

[159] W McDaniel. *Collision phenomena in ionized gases*. Wiley series in plasma physics. Wiley, 1964.

[160] Shinsuke Haze, Sousuke Hata, Munekazu Fujinaga, and Takashi Mukaiyama. "Observation of elastic collisions between lithium atoms and calcium ions". In: *Phys. Rev. A* 87.5 (May 2013), p. 52715. DOI: 10.1103/PhysRevA.87.052715.

[161] I Sivarajah, D S Goodman, J E Wells, F A Narducci, and W W Smith. "Evidence of sympathetic cooling of Na+ ions by a Na magneto-optical trap in a hybrid trap". In: *Phys. Rev. A* 86.6 (Dec. 2012), p. 63419. DOI: 10.1103/PhysRevA.86.063419.

[162] Felix Hall, Mireille Aymar, Nadia Bouloufa, Olivier Dulieu, and Stefan Willitsch. "Light-Assisted Ion-Neutral Reactive Processes in the Cold Regime: Radiative Molecule Formation versus Charge Exchange". In: *Physical review letters* 107 (Dec. 2011), p. 243202. DOI: 10.1103/PhysRevLett.107.243202.

[163] Arne Härter, Artjom Krükow, Andreas Brunner, Wolfgang Schnitzler, Stefan Schmid, and Johannes Hecker Denschlag. "Single Ion as a Three-Body Reaction Center in an Ultracold Atomic Gas". In: *Physical Review Letters* 109.12 (Sept. 2012), p. 123201. DOI: 10.1103/PhysRevLett.109.123201.

[164] A Härter, A Krükow, A Brunner, and J Hecker Denschlag. "Long-term drifts of stray electric fields in a Paul trap". In: *Applied Physics B* 114.1 (2014), pp. 275–281. ISSN: 1432-0649. DOI: 10.1007/s00340-013-5688-7.

[165] Robin Côté. "From Classical Mobility to Hopping Conductivity: Charge Hopping in an Ultracold Gas". In: *Phys. Rev. Lett.* 85.25 (Dec. 2000), pp. 5316–5319. DOI: 10.1103/PhysRevLett.85.5316.

[166] Hans-Joachim Werner, Peter J Knowles, Gerald Knizia, Frederick R Manby, and Martin Schütz. "Molpro: a general-purpose quantum chemistry program package". In: *WIREs Computational Molecular Science* 2.2 (2012), pp. 242–253. DOI: 10.1002/wcms.82.

[167] A Pandey, M Niranjan, N Joshi, S A Rangwala, R Vexiau, and O Dulieu. “Interaction potentials and ultracold scattering cross sections for the 7Li+ – 7Li ion-atom system”. In: *Phys. Rev. A* 101.5 (May 2020), p. 52702. DOI: 10.1103/PhysRevA.101.052702.

[168] R A Bernheim, L P Gold, T Tipton, and D D Konowalow. “The ionization potential of 7Li2 and bond energy of 7Li2+”. In: *Chemical Physics Letters* 105.2 (1984), pp. 201–204. ISSN: 0009-2614. DOI: https://doi.org/10.1016/0009-2614(84)85650-X.

[169] R A Bernheim, L P Gold, and T Tipton. “Rydberg states of 7Li2 by pulsed optical–optical double resonance spectroscopy: Molecular constants of 7Li2+”. In: *The Journal of Chemical Physics* 78.6 (1983), pp. 3635–3646. DOI: 10.1063/1.445192.

[170] Monika Musiał, Magdalena Medrek, and Stanisław A Kucharski. “Potential energy curves of Li+2 from all-electron EA-EOM-CCSD calculations”. In: *Molecular Physics* 113.19-20 (2015), pp. 2943–2951. DOI: 10.1080/00268976.2015.1059514.

[171] Peng Zhang, Enrico Bodo, and Alexander Dalgarno. “Near Resonance Charge Exchange in Ion-Atom Collisions of Lithium Isotopes”. In: *The Journal of Physical Chemistry A* 113.52 (Dec. 2009), pp. 15085–15091. ISSN: 1089-5639. DOI: 10.1021/jp905184a.

[172] P Jasik, J Wilczyński, and J E Sienkiewicz. “Calculation of adiabatic potentials of Li2+”. In: *The European Physical Journal Special Topics* 144.1 (2007), pp. 85–91. ISSN: 1951-6401. DOI: 10.1140/epjst/e2007-00111-2.

[173] H Bouzouita, Chedli Ghanmi, and Hamid Berriche. “Ab initio study of the alkali-dimer cation Li 2 +”. In: *Journal of Molecular Structure-theochem - J MOL STRUC-THEOCHEM* 777 (2006), pp. 75–80. DOI: 10.1016/j.theochem.2006.08.003.

[174] Djamal Rabli and Ronald McCarroll. “A revised study of the Li2+ alkali-dimer using a model potential approach”. In: *Chemical Physics* 487 (2017). DOI: 10.1016/j.chemphys.2017.02.005.

[175] S Magnier, S Rousseau, A. R. Allouche, G Hadinger, and M Aubert-Frécon. “Potential energy curves of 58 states of Li $_{2}$$^{+}$”. In: *Chemical Physics* 246.1 (July 1999), pp. 57–64. DOI: 10.1016/S0301-0104(99)00084-1.

[176] Saeed Nasiri and Mansour Zahedi. “A benchmark study of Li 2 + , Li 2 - , LiH + and LiH - :Quantum Monte-Carlo, Coupled-Cluster computations”. In: *Computational and Theoretical Chemistry* 1114 (2017). DOI: 10.1016/j.comptc.2017.05.015.

[177] V Lefevre-Seguin and M Leduc. “Metastability-exchange and depolarising collisions in xenon and krypton”. In: *Journal of Physics B: Atomic and Molecular Physics* 10.11 (1977), pp. 2157–2164. ISSN: 0022-3700. DOI: 10.1088/0022-3700/10/11/016.

[178] Bo Gao. “Universal Properties in Ultracold Ion-Atom Interactions”. In: *Phys. Rev. Lett.* 104.21 (May 2010), p. 213201. DOI: 10.1103/PhysRevLett.104.213201.

[179] J Schmidt, P Weckesser, F Thielemann, T Schaetz, and L Karpa. “Optical Traps for Sympathetic Cooling of Ions with Ultracold Neutral Atoms”. In: *Phys. Rev. Lett.* 124.5 (Feb. 2020), p. 53402. DOI: 10.1103/PhysRevLett.124.053402.

[180] A Härter and J Hecker Denschlag. “Cold atom–ion experiments in hybrid traps”. In: *Contemporary Physics* 55.1 (2014), pp. 33–45. DOI: 10.1080/00107514.2013.854618.

[181] B D Esry, Chris H Greene, and H Suno. “Threshold laws for three-body recombination”. In: *Phys. Rev. A* 65.1 (Dec. 2001), p. 10705. DOI: 10.1103/PhysRevA.65.010705.

[182] J N Bardsley˜, T Holstein, B R Junker, and Swati Sinha. *Calculations of ion-atom interactions relating to resonant charge-transfer comsions˜*. Tech. rep. 6. 1975.

[183] M Niranjan, Anand Prakash, and S A Rangwala. "Analysis of Multipolar Linear Paul Traps for Ion–Atom Ultracold Collision Experiments". In: *Atoms* 9.3 (2021). ISSN: 2218-2004. DOI: 10.3390/atoms9030038.

[184] Wolfgang Paul. "Electromagnetic traps for charged and neutral particles". In: *Reviews of Modern Physics* 62.3 (July 1990), pp. 531–540. DOI: 10.1103/RevModPhys.62.531.

[185] W W Smith, D S Goodman, I Sivarajah, J E Wells, S Banerjee, R Côté, H H Michels, J A Mongtomery, and F A Narducci. "Experiments with an ion-neutral hybrid trap: cold charge-exchange collisions". In: *Applied Physics B* 114.1 (2014), pp. 75–80. ISSN: 1432-0649. DOI: 10.1007/s00340-013-5672-2.

[186] Christoph Zipkes, Lothar Ratschbacher, Stefan Palzer, Carlo Sias, and Michael Köhl. "Hybrid quantum systems of atoms and ions". In: *Journal of Physics: Conference Series* 264 (2011), p. 12019. ISSN: 1742-6596. DOI: 10.1088/1742-6596/264/1/012019.

[187] Dieter Gerlich. *Inhomogeneous RF Fields: A Versatile Tool for the Study of Processes with Slow Ions*. Ed. by Cheuk-Yiu Ng Baer and Michael Baer. vol. 82. Advances in Chemical Physics. New York: John Wiley & Sons, Inc., Jan. 1992, pp. 1–176. ISBN: 9780470141397. DOI: 10.1002/9780470141397.

[188] Oskar Asvany, Sandra Brünken, Lars Kluge, and Stephan Schlemmer. "COLTRAP: a 22-pole ion trapping machine for spectroscopy at 4 K". In: *Applied Physics B* 114.1 (2014), pp. 203–211. ISSN: 1432-0649. DOI: 10.1007/s00340-013-5684-y.

[189] Yuan Tian, Trevor K Decker, Joshua S McClellan, Linsey Bennett, Ailin Li, Abraham De la Cruz, Derek Andrews, Stephen A Lammert, Aaron R Hawkins, and

Daniel E Austin. “Improved Miniaturized Linear Ion Trap Mass Spectrometer Using Lithographically Patterned Plates and Tapered Ejection Slit”. In: *Journal of The American Society for Mass Spectrometry* 29.2 (2018), pp. 213–222. ISSN: 1879-1123. DOI: 10.1007/s13361-017-1759-z.

[190] Simon Ragg, Chiara Decaroli, Thomas Lutz, and Jonathan P Home. “Segmented ion-trap fabrication using high precision stacked wafers”. In: *Review of Scientific Instruments* 90.10 (2019), p. 103203. DOI: 10.1063/1.5119785.

[191] Roland Wester. “COLD MOLECULAR IONS IN TRAPS”. In: *Trapped Charged Particles*. Advanced Textbooks in Physics. WORLD SCIENTIFIC (EUROPE), Sept. 2015, pp. 321–334. ISBN: 978-1-78634-011-5. DOI: doi:10.1142/9781786340139{_}0016.

[192] M Debatin, M Kröner, J Mikosch, S Trippel, N Morrison, M Reetz-Lamour, P Woias, R Wester, and M Weidemüller. “Planar multipole ion trap”. In: *Physical Review A* 77.3 (Mar. 2008), p. 33422. DOI: 10.1103/PhysRevA.77.033422.

[193] J Pedregosa-Gutierrez, C Champenois, M Houssin, M R Kamsap, and M Knoop. “Correcting symmetry imperfections in linear multipole traps”. In: *Review of Scientific Instruments* 89.12 (2018), p. 123101. DOI: 10.1063/1.5075496.

[194] Rico Otto, Petr Hlavenka, Sebastian Trippel, Jochen Mikosch, Kilian Singer, Matthias Weidemüller, and Roland Wester. “How can a 22-pole ion trap exhibit 10 local minima in the effective potential?” In: *Journal of Physics B-atomic Molecular and Optical Physics - J PHYS-B-AT MOL OPT PHYS* 42 (2009). DOI: 10.1088/0953-4075/42/15/154007.

[195] R.E. Todd J.F.J. & March. *Practical Aspects of Trapped Ion Mass Spectrometry, Volume V: Applications of Ion Trapping Devices (1st ed.)*. Boca Raton: CRC press, 2009. ISBN: 9781420083736. DOI: 10.1201/9781420083743.

[196] D. Manura Dahl. and D. *SIMION (R) 8.1 User Manual (Adaptas Solutions, LLC, Palmer, MA 01069, <http://simion.com/>, January 2008).* 2008.

[197] Bogdan M Mihalcea, Liviu C Giurgiu, Cristina Stan, Gina T Vişan, Mihai Ganciu, Vladimir Filinov, Dmitry Lapitsky, Lidiya Deputatova, and Roman Syrovatka. "Multipole electrodynamic ion trap geometries for microparticle confinement under standard ambient temperature and pressure conditions". In: *Journal of Applied Physics* 119.11 (Mar. 2016), p. 114303. ISSN: 0021-8979. DOI: 10.1063/1.4943933.

[198] Joseph Ladislas Wiza. "Microchannel plate detectors". In: *Nuclear Instruments and Methods* 162.1 (1979), pp. 587–601. ISSN: 0029-554X. DOI: https://doi.org/10.1016/0029-554X(79)90734-1.

[199] G Gräff, H Kalinowsky, and J Traut. "A direct determination of the proton electron mass ratio". In: *Zeitschrift für Physik A Atoms and Nuclei* 297.1 (1980), pp. 35–39. ISSN: 0939-7922. DOI: 10.1007/BF01414243.

[200] H C Straub, M A Mangan, B G Lindsay, K A Smith, and R F Stebbings. "Absolute detection efficiency of a microchannel plate detector for kilo-electron volt energy ions". In: *Review of Scientific Instruments* 70.11 (1999), pp. 4238–4240. DOI: 10.1063/1.1150059.

[201] John Weiner. "Experiments in cold and ultracold collisions". In: *J. Opt. Soc. Am. B* 6.11 (Nov. 1989), pp. 2270–2278. DOI: 10.1364/JOSAB.6.002270.

[202] K Nanbu and Y Kitatani. "An ion-neutral species collision model for particle simulation of glow discharge". In: 28.2 (Feb. 1995), pp. 324–330. DOI: 10.1088/0022-3727/28/2/015.

[203] Krzysztof Jachymski, Paul S Krych Micha\land Julienne, and Zbigniew Idziaszek. "Quantum Theory of Reactive Collisions for $1/{r}^{n}$ Potentials". In: *Phys. Rev. Lett.* 110.21 (May 2013), p. 213202. DOI: 10.1103/PhysRevLett.110.213202.

[204] Terry N Olney, N M Cann, Glyn Cooper, and C E Brion. "Absolute scale determination for photoabsorption spectra and the calculation of molecular properties using dipole sum-rules". In: *Chemical Physics* 223.1 (1997), pp. 59–98. ISSN: 0301-0104. DOI: https://doi.org/10.1016/S0301-0104(97)00145-6.

[205] Thomas M Miller and Benjamin Bederson. "Atomic and Molecular Polarizabilities-A Review of Recent Advances". In: ed. by D R Bates and Benjamin Bederson. Vol. 13. Advances in Atomic and Molecular Physics. Academic Press, 1978, pp. 1–55. DOI: https://doi.org/10.1016/S0065-2199(08)60054-8.

[206] S. Jyothi, Kisra N. Egodapitiya, Brad Bondurant, Zhubing Jia, Eric Pretzsch, Piero Chiappina, Gang Shu, and Kenneth R. Brown. "A hybrid ion-atom trap with integrated high resolution mass spectrometer". In: *Review of Scientific Instruments* 90.10 (Oct. 2019), p. 103201. ISSN: 0034-6748. DOI: 10.1063/1.5121431.

[207] Dipankar Das and Vasant Natarajan. "Absolute frequency measurement of the lithium D lines: Precise determination of isotope shifts and fine-structure intervals". In: *Phys. Rev. A* 75.5 (May 2007), p. 52508. DOI: 10.1103/PhysRevA.75.052508.

[208] Pratip Bhattacharyya and Bikas K Chakrabarti. "The mean distance to the n th neighbour in a uniform distribution of random points: an application of probability theory". In: *European Journal of Physics* 29.3 (2008), pp. 639–645. ISSN: 0143-0807. DOI: 10.1088/0143-0807/29/3/023.